

*Advances in*  
**G E O P H Y S I C S**

*Edited by*

**RENATA DMOWSKA**

*Division of Engineering and Applied Sciences  
Harvard University  
Cambridge, Massachusetts, USA*

*VOLUME 47*



**ELSEVIER**

Amsterdam • Boston • Heidelberg • London • New York • Oxford  
Paris • San Diego • San Francisco • Singapore • Sydney • Tokyo

ADVANCES IN  
G E O P H Y S I C S

VOLUME 47

**This page is intentionally left blank**

ELSEVIER B.V.  
Radarweg 29  
P.O. Box 211, 1000 AE Amsterdam  
The Netherlands

**ELSEVIER Inc.**  
**525 B Street, Suite 1900**  
**San Diego, CA 92101-4495**  
**USA**

ELSEVIER Ltd  
The Boulevard, Langford Lane  
Kidlington, Oxford OX5 1GB  
UK

ELSEVIER Ltd  
84 Theobalds Road  
London WC1X 8RR  
UK

© 2004 Elsevier Inc. All rights reserved.

This work is protected under copyright by Elsevier Inc., and the following terms and conditions apply to its use:

#### Photocopying

Single photocopies of single chapters may be made for personal use as allowed by national copyright laws. Permission of the Publisher and payment of a fee is required for all other photocopying, including multiple or systematic copying, copying for advertising or promotional purposes, resale, and all forms of document delivery. Special rates are available for educational institutions that wish to make photocopies for non-profit educational classroom use.

Permissions may be sought directly from Elsevier's Rights Department in Oxford, UK: phone (+44) 1865 843830, fax (+44) 1865 853333, e-mail: [permissions@elsevier.com](mailto:permissions@elsevier.com). Requests may also be completed on-line via the Elsevier homepage (<http://www.elsevier.com/locate/permissions>).

In the USA, users may clear permissions and make payments through the Copyright Clearance Center, Inc., 222 Rosewood Drive, Danvers, MA 01923, USA; phone: (+1) (978) 7508400, fax: (+1) (978) 7504744, and in the UK through the Copyright Licensing Agency Rapid Clearance Service (CLARCS), 90 Tottenham Court Road, London W1P 0LP, UK; phone: (+44) 20 7631 5555; fax: (+44) 20 7631 5500. Other countries may have a local reprographic rights agency for payments.

#### Derivative Works

Tables of contents may be reproduced for internal circulation, but permission of the Publisher is required for external resale or distribution of such material. Permission of the Publisher is required for all other derivative works, including compilations and translations.

#### Electronic Storage or Usage

Permission of the Publisher is required to store or use electronically any material contained in this work, including any chapter or part of a chapter.

Except as outlined above, no part of this work may be reproduced, stored in a retrieval system or transmitted in any form or by any means, electronic, mechanical, photocopying, recording or otherwise, without prior written permission of the Publisher. Address permissions requests to: Elsevier's Rights Department, at the fax and e-mail addresses noted above.

#### Notice

No responsibility is assumed by the Publisher for any injury and/or damage to persons or property as a matter of products liability, negligence or otherwise, or from any use or operation of any methods, products, instructions or ideas contained in the material herein. Because of rapid advances in the medical sciences, in particular, independent verification of diagnoses and drug dosages should be made.

First edition 2004

ISBN: 0 12 018847 3

ISSN: 0065-2687 (Series)

© The paper used in this publication meets the requirements of ANSI/NISO Z39.48-1992 (Permanence of Paper).  
Printed in The Netherlands.

Working together to grow  
libraries in developing countries

[www.elsevier.com](http://www.elsevier.com) | [www.bookaid.org](http://www.bookaid.org) | [www.sabre.org](http://www.sabre.org)

**ELSEVIER**

**BOOK AID**  
International

**Sabre Foundation**

# CONTENTS

CONTRIBUTORS .....	ix
--------------------	----

## Crustal Deformation in the Southcentral Alaska Subduction Zone

STEVEN C. COHEN AND JEFFREY T. FREYMUELLER

1. Introduction .....	1
2. Tectonic, Geologic, and Seismologic Setting .....	8
3. Observed Crustal Motion .....	13
3.1. Coseismic Crustal Motion .....	14
3.2. Preseismic and Interseismic (Pre-1964) Crustal Motion .....	26
3.3. Postseismic and Interseismic (Post-1964) Crustal Motion .....	27
3.4. Multidecadal Postseismic Uplift Deduced from Comparisons of GPS and Leveling Observations .....	37
3.5. Contemporary GPS Observations of Crustal Motion: Spatial and Temporal Variability .....	40
4. Models of Southcentral Alaska Preseismic and Postseismic Crustal Deformation .....	45
5. Summary .....	57
Acknowledgements .....	57
References .....	58

## Relating Fault Mechanics to Fault Zone Structure

RONALD L. BIEGEL AND CHARLES G. SAMMIS

1. Introduction .....	66
2. Fault Zone Rocks .....	67
3. The Structure of Mature, Large Displacement Strike-Slip Faults .....	67
3.1. The Punchbowl and San Gabriel Faults in Southern California .....	67
3.2. The Idealized Punchbowl Model .....	72
3.3. The Nojima Fault, Japan .....	78
3.4. The Median Tectonic Line, Japan .....	82
3.5. The Carboneras Fault, Southeastern Spain .....	82

4. The Structure of Mature, Large Displacement Dip-Slip Faults .....	83
4.1. The Badwater Turtleback Normal Faults, Death Valley, CA .....	83
4.2. The Chelungpu Fault, Taiwan .....	85
5. Formation of Fault Zone Structure .....	88
5.1. Fault Zone Formation in Low Porosity Jointed Rock .....	88
5.2. Fault Zone Formation in High Porosity Sandstones .....	90
5.3. Fractal Fragmentation and Shear Localization .....	91
5.4. Fragmentation and Off-Fault Damage in the Process Zone of Large Earthquakes .....	92
5.5. Wear .....	93
5.6. Pseudotachylytes .....	94
6. Effects of Fault Zone Structure on Dynamic Rupture .....	95
6.1. Effects of Fault Zone Structure on the Nucleation of an Earthquake .....	96
6.2. Effect of Fault Zone Structure on the Propagation of an Earthquake Rupture .....	97
6.3. Effect of Fault Zone Structure on the Arrest of an Earthquake Rupture .....	102
7. Discussion .....	103
Acknowledgements .....	104
References .....	104

## Past Surface Temperature Changes as Derived from Continental Temperature Logs—Canadian and Some Global Examples of Application of a New Tool in Climate Change Studies

JACEK MAJOROWICZ, JAN SAFANDA AND WALTER SKINNER

1. Introduction .....	114
2. Basic Features of Ground Surface Temperature Reconstruction .....	116
3. Heat Gain by the Earth due to Climatic Warming .....	120
4. Temperature Profiles with Depth .....	123
5. Thermal Conductivity and Diffusivity .....	127
6. Inversions .....	129
7. Joint Inversions .....	132
8. Alternative Approach—Determining the Pre-observational Mean Level .....	133
9. Method Limitations .....	133
10. Case Studies Demonstrating the Basic Features of the Inversion Method .....	134
11. Case Studies Demonstrating the Basic Features of the “POM” Approach .....	144

12. Hemispheric and Continental Reconstructions of GST from Well Temperatures .....	148
13. Canadian Examples .....	151
14. Circumpolar Warming .....	160
15. Obscuring Factors .....	162
16. Comparison of Well Temperature Derived GST Histories with Observations and Other Proxy Climate Information .....	164
17. Conclusions .....	168
Acknowledgements .....	169
References .....	169

## Instability and Structural Failure at Volcanic Ocean Islands and the Climate Change Dimension

BARBARA H. KEATING AND WILLIAM J. MCGUIRE

1. Introduction .....	176
1.1. Volcanic Edifice Instability .....	177
2. Factors and Mechanisms Affecting Instability and Failure at Volcanic Ocean Islands .....	182
2.1. The Role of Intra-Edifice Water .....	182
2.2. The Dike Injection Process .....	184
2.3. Rock Type .....	185
2.4. Rheology .....	185
2.5. Rock Density .....	189
2.6. Landslide Structural Characteristics and Depth of Initiation .....	192
2.7. Landslide Form and Dimensions .....	195
2.8. Slope Angle (Bathymetry) .....	198
2.9. Dynamics .....	199
2.10. Change in Pore Properties Associated with Liquefaction .....	199
3. Post-Failure Debris Movement .....	200
3.1. A Review of Transport Mechanisms .....	200
3.2. Submarine Mass Movement Classification, Terminology, and Facies Concepts .....	201
3.3. Runout .....	203
4. Transport .....	204
4.1. Overview of Laboratory Experiments .....	204
4.2. Sonar Surveys .....	208
4.3. Seismic Surveys .....	210
5. Landslides as Tsunami Generators .....	210
5.1. Introduction and Recent Research Trends .....	210
5.2. Hypothetical Events .....	216

5.3. Quantification .....	218
5.4. New Areas of Tsunami Research .....	220
6. Climate Change and Landslides in Ocean Basin Environments .....	222
6.1. Climate Change as a Landslide Trigger .....	222
6.2. Gas Hydrates .....	226
6.3. Canary Islands .....	228
6.4. The Hawaiian Islands and Climate Change .....	229
6.5. Age Dating Correlations .....	230
6.6. Arguments for Climate Correlations: Rainfall and Landslides .....	235
7. Conclusions .....	239
Acknowledgements .....	243
References .....	243
INDEX .....	273

## CONTRIBUTORS

*Numbers in parentheses indicate the pages on which the authors' contributions begin*

- BIEGEL, RONALD L. (65) Department of Earth Sciences, University of Southern California, Los Angeles, CA 90089-0740, USA
- COHEN, STEVEN C. (1) Geodynamics Branch, Goddard Space Flight Center, Greenbelt, MD 20771, USA
- FREYMUELLER, JEFFREY T. (1) Geophysical Institute, University of Alaska, Fairbanks, AK 99775, USA
- KEATING, BARBARA. H. (175) Hawaii Institute of Geophysics and Planetology, University of Hawaii, 2525 Correa Road, Honolulu, HI, USA
- MAJOROWICZ, JACEK (113) NGC, 105 Carlson Close, Edmonton, Alta., Canada T6R 2J8
- MAJOROWICZ, JACEK (113) Northern Plains Climate Research Center, University of North Dakota, Grand Forks, ND 58202-8358, USA
- MCGUIRE, WILLIAM. J. (175) Benfield Hazard Research Centre, Research School of Geological and Geophysical Sciences, University College London, Gower Street, London WC1E 6BT, UK
- SAFANDA, JAN (113) Geophysical Institute, Czech Academy of Sciences, Bocni II, Sporilov, Czech Republic
- SAMMIS, CHARLES G. (65) Department of Earth Sciences, University of Southern California, Los Angeles, CA 90089-0740, USA
- SKINNER, WALTER (113) Climate Research Branch, Environment Canada, Downsview, Ont., Canada M3H 5T4

# CRUSTAL DEFORMATION IN THE SOUTHCENTRAL ALASKA SUBDUCTION ZONE

STEVEN C. COHEN<sup>a</sup> AND JEFFREY T. FREYMUELLER<sup>b</sup>

<sup>a</sup>*Geodynamics Branch, Goddard Space Flight Center, Greenbelt, MD 20771, USA*

<sup>b</sup>*Geophysical Institute, University of Alaska, Fairbanks, AK 99775, USA*

## ABSTRACT

The study of crustal deformation in the subduction zone of the 1964 Prince William Sound, Alaska earthquake reveals a temporally and spatially complex pattern of surface motions and interplate coupling. This temporal–spatial pattern provides fundamental information on the elastic and inelastic processes associated with strain energy accumulation and release in the seismic cycle and development of geological structures in southcentral Alaska. Essential data on the crustal deformation comes from seismological, geological and geodetic observations. The most salient observed features are: (1) large along-strike variations in both the coseismic moment release and the postseismic and interseismic surface deformation and (2) a complicated history of postseismic and interseismic deformation characterized by both steady-state deformation and transient motion occurring over several time scales and involving different deformation mechanisms. Numerical models give insight into the relationship between the observed crustal motions and tectonic plate motion, fault zone processes, and the Earth's rheology.

## 1. INTRODUCTION

The  $M_w = 9.2$  Prince William Sound (PWS) earthquake that struck southcentral Alaska on March 28, 1964, was one of the important earthquakes in history. While the human losses in the PWS earthquake were certainly tragic, the death toll was not high when compared to that of great earthquakes that have struck heavily populated locations. Rather, it is the impact that the earthquake had on scientific understanding that made it such a significant occurrence. The early 1960s was an important time for both seismology and tectonophysics. Seismic instrumentation and analysis techniques were undergoing considerable modernization. For example, the VELA UNIFORM program for nuclear test detection resulted in the deployment of the World Wide Standard Seismographic Network in the late 1950s and early 1960s (Lay and Wallace, 1995). Correspondingly, considerable effort was being devoted by the scientific

community to the understanding seismic source properties, characteristics of seismic signals, and interior structure of the Earth. The study of the PWS earthquake benefited from this attention to global as well as local seismological issues and, reciprocally, the study of the PWS earthquake contributed much to the research efforts of the time. In the early 1960s the paradigm of plate tectonics was in its infancy. Many fundamental plate tectonics investigations, such as the study of marine magnetic anomalies by Vine and Mathews (1963), were newly reported in the scientific literature. Indeed the structure of subduction zones and their overall importance in the scheme of seismotectonics were barely appreciated. However, investigations into the relationship between seismic and tectonic phenomena were well underway and culminated in a surge of fundamental results in the mid and late 1960s and early 1970s. The early studies of the PWS earthquake gave credence to the idea that strain is accumulated and released across shallow dipping megathrusts at plate boundaries such as the one in southcentral Alaska and the Aleutians.

Crustal deformation is an important, measurable phenomenon related to the cycle of stress accumulation and release at tectonic plate boundaries. Thus, crustal deformation measurements, along with seismological and geological investigations, have provided vital information for understanding earthquake processes. In southcentral Alaska, geodetic observations span the coseismic epoch and a postseismic/interseismic interval of a few decades. In addition, a limited number of geodetic observations provide information about the deformation that was occurring before the earthquake. This chapter is a critical review of these surface observations and of the numerical models that have been employed to explain them.

Most, although not all, of the deformations that are relevant to the earthquake cycle have been observed through the use of geodetic survey techniques. Thus, our primary focus will be on the time scales associated with these observations, typically a few months to several decades. We will also consider the much shorter time scale associated with the earthquake itself and the somewhat longer time scale associated with the recurrence of great earthquakes. Although we will not be primarily concerned with processes that occur over millions of years, we recognize that geological features are the product of both seismotectonic and geomorphological processes; thus, the insights provided by geological investigations supplement what can be learned from geodetic and seismological investigations.

Since we are discussing the 1964 PWS earthquake, it is appropriate to begin this review with a few basic facts about the earthquake itself. The earthquake was, and remains, the second largest seismic event to have occurred during the modern instrumental era. Its moment magnitude ( $M_w = 9.2$ ) is exceeded only by that of

the 1960 Chile earthquake ( $M_w = 9.5$ ). The rupture extended over a zone that was 600–800 km long and 200–250 km wide (Fig. 1). The shaking produced by the earthquake was felt at some locations for 4–5 min. The rupture began just north of PWS; the epicenter was  $61.04 \pm 0.05^\circ\text{N}$  and  $147.73 \pm 0.07^\circ\text{W}$  (Sherburne *et al.*, 1972). The motion was primarily a thrust on a low dip-angle plane, but there may have been a strike-slip component to the motion. As there were no seismometers located close to the epicenter and the initial seismic signals saturated many of the high-gain seismographic instruments in the global network, the determination of the focal depth was challenging (Stauder, 1972). The focal depth estimate of  $25 \pm 10$  km by Oleskevich *et al.* (1999) is probably as good an estimate as can be derived from seismic wave data.

The best constraints on the source depth may come from a combination of the horizontal position of the aftershock zone and depth profile of the downgoing plate. This gives a depth of 20–25 km. Certainly, the down-dip limit of the coseismic rupture surface appears to have been no deeper than about 40 km,

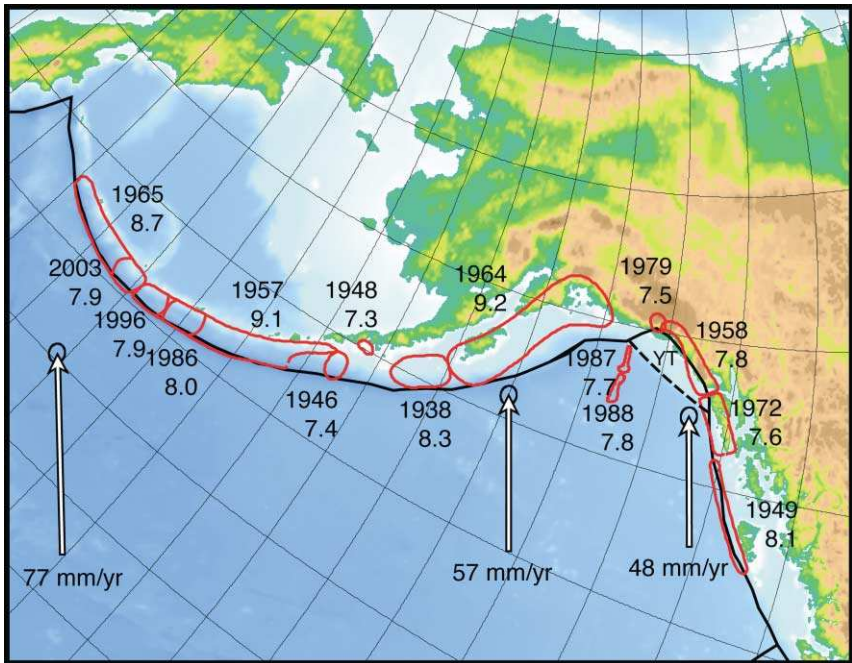


FIG. 1. Rupture areas of large historic earthquakes in Alaska and the Nuvel 1A plate velocity of the Pacific Plate relative to the North America Plate.

in agreement with the depth for a magnitude 6.9 aftershock that occurred in 1965 (Tichelaar and Ruff, 1993). This limit is shallower than the 350–450°C temperature contour computed and used by Oleskevich *et al.* (1999) as the down-dip limit for great earthquakes. The up-dip depth limit was about 4–6 km, corresponding to the 100–150°C temperature contour suggested by the same authors as an appropriate temperature limit.

The rupture lasted about 100 s in the PWS area and about 40 s at Kodiak Island (Christiensen and Beck, 1994). For the first 44 s of the event, the rupture propagated in different directions, but afterwards it propagated primarily to the southwest (Wyss and Brune, 1972).

The region of the eastern Aleutian-Alaska arc that ruptured in 1964 had not experienced a great earthquake within the historical instrumental period dating back about 65 years. Four earthquakes of magnitude 7.8–8.3 did occur near Yakutat Bay during the 13-month period from September 1899 to October 1900; however, Yakutat Bay is to the east of the 1964 rupture zone and its tectonic environment is different. Five earthquakes of magnitude 7.0–7.2 occurred between 1928 and 1957 within the 1964 rupture zone. We will discuss the paleoseismic record of great earthquakes in this region later in this article.

The 1964 earthquake produced static coseismic displacements estimated to have exceeded 20 m horizontally and 10 m vertically, although the greatest horizontal and vertical displacements were not at the same locations (Parkin, 1972; Plafker, 1972; Tocher, 1972). Most of the crustal deformation was associated with slip on the megathrust, although some of the larger vertical motions were associated with slip on subsidiary faults (Plafker, 1972). In particular, thrust slip on subsidiary faults uplifted the southeast portion of Montague Island in PWS by 10 m. The megathrust itself exhibits considerable geometric complexity; not only does the dip angle vary along strike, but the nature of the boundary itself also changes. In the western and central portions of the rupture zone, the megathrust is the boundary between the North America and Pacific Plates, while in the PWS region the megathrust is the interface between the North America Plate and the Yakutat Block (Fig. 2), an allochthonous terrane incompletely welded to the top of the Pacific Plate (Brocher *et al.*, 1994; Von Huene *et al.*, 1999).

Among the geodetic techniques that have been used to measure crustal deformation in southcentral Alaska are triangulation, leveling, very-long-baseline interferometry (VLBI) and the global positioning system (GPS) techniques. As later discussions will illustrate, GPS observations are providing an especially detailed picture of the contemporary 3-D surface crustal movement. This picture reveals aspects of the crustal deformation cycle that have not been appreciated until recently, and may be important in other subduction zones as

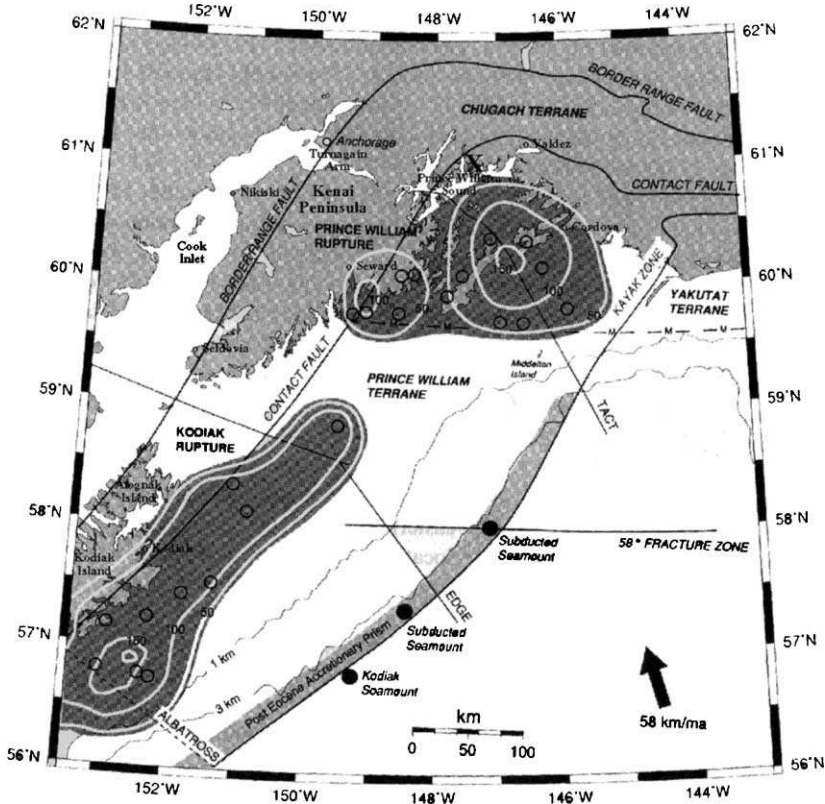


FIG. 2. Contemporary tectonic setting and features. Among the features shown are the relative velocity vector between the Pacific and North America Plates, the locations of the Prince William and Kodiak asperities (defined by intense aftershock occurrence with the aftershock strain energy being indicated by contours of the number of equivalent  $M = 3$  earthquakes), the Chugach, Prince William and Yakutat Terranes, and the Border Ranges and Contact Faults. The Peninsular Terrane lies north of the Border Ranges Fault. The open circles are the locations of aftershocks that occurred within the first 5 h of the main shock and had  $M > 6$ . Also shown are the TACT, EDGE, and ALBATROSS seismic reflection and refraction lines and several cities mentioned in the text. Modified from Von Huene *et al.* (1999).

well as Alaska. While GPS measurements are providing much of today's data, other measurements have value from both a contemporary and historical perspective. For example, tide gauge observations can be used to study crustal movements in those locations where the apparent change in sea level is primarily due to vertical movement of the land on which the instrument is located rather

than a change in the ocean. In many cases, tide gauge measurements give the longest record of crustal movement. For example, at Seward and the city of Kodiak the tide observations began in 1925 and 1950, respectively, and provide a record of preseismic, coseismic, and postseismic vertical motions. Several permanent tide gauge stations were installed shortly after the earthquake and yield good postseismic records. Other tide gauge sites were occupied for only a limited time before and after the earthquake, but their records contain valuable information about the coseismic motion.

The geodetic measurements of crustal movement span a time interval that is only a fraction of the typical recurrence time for a great earthquake. Additional information about crustal movements come from geological studies that estimate such long-term parameters as slip rates on faults and uplift rates for geologic features, as well as surface displacements in specific earthquakes. In the case of the PWS earthquake, the mapping of barnacle and algae lines have provided much of the information about the coseismic vertical motion while alternating deposits of mud and peat have provided information on both interseismic sedimentation and coseismic uplift or submergence (Carver and McCalpin, 1996). Paleoseismic information is also invaluable for developing the chronology of past earthquakes (Bartsch-Winkler and Schmoll, 1992).

There are at least two compelling scientific reasons for undertaking the types of crustal deformation studies reviewed in this article. The first is to improve the understanding of how the Earth prepares for an earthquake and relieves accumulated stress. The second is to infer geophysical parameters describing the interior of the Earth. These parameters, such as viscosity and crustal thickness, are important in both seismological and other geophysical studies.

Concerning the first of these objectives, there are two major paradigms that provide the conceptual framework for contemporary crustal deformation studies. The older of these treats the earthquake cycle as a deterministic process with the slow accumulation and sudden release of stress at a fault or within a fault system (Thatcher, 1995). The second, more recent paradigm, is that earthquakes are better understood by considering the statistical properties of a nonlinear chaotic system in a near critical state (Rundle *et al.*, 2000). To some extent the paradigm most useful for a specific study depends on the spatial and temporal scale of interest. The spatial scale involved in earthquake studies ranges from the microscope scale ( $10^{-6}$ – $10^1$  m) associated with rock frictional properties to the tectonic plate boundary scale ( $10^5$ – $10^7$  m). At the spatial scales involved in most of the studies reviewed here, the deterministic paradigm usually applies, but the chaotic paradigm can provide some insight into the temporal evolution.

The most elementary form of the deterministic paradigm is the elastic rebound theory in which both stress and strain accumulate at a constant rate

across a fault locked by frictional resistance between earthquakes. Sudden fault rupture and slip relieve the stress and strain. Studies such as those in Alaska that have revealed temporal variability and spatial heterogeneity in the deformation processes, suggest significant modifications to this simple paradigm.

The complex temporal and spatial characteristics of the southern Alaska subduction zone manifest themselves in the occurrence of secular and transient strain accumulation, quasi-static slip processes, a variety of relaxation times for postseismic rebound, and various strengths of coupling between the overthrust and subducting plates.

The rest of this article is arranged as follows. In Section 2, we describe the tectonic, geologic, and seismological framework for understanding crustal deformation in southcentral Alaska. In Section 3, we review in considerable detail the observed crustal motion, focusing first on the coseismic displacements, then on the preseismic, postseismic, and interseismic motions. In Section 4, we critically review the numerical models that have been advanced to explain the observed surface motions. Our review emphasizes the physics underlying the models and the parameters needed to describe them. This section is followed by a summary and an extensive reference list. We have tried to be fairly comprehensive in our presentation of the results from various studies; however, we have not been content to merely summarize the results as given by the authors. Rather, we have tried to indicate where there are uncertainties in the results or where conclusions should be altered or extended based on the subsequent information. We have also offered a few speculations when current results hint at behavior that has not yet been verified. Hopefully, we have clearly identified those comments that are speculative or strongly model-dependent.

Comprehensive study of the PWS earthquake began shortly after the earthquake. Many of the early studies were later compiled into an eight-volume report, "The Great Alaska Earthquake of 1964" that was published by the National Academy of Sciences in 1972. The report has distinct volumes devoted to Geology, Seismology and Geodesy, Hydrology, Biology, Oceanography and Coastal Engineering, Engineering, Human Ecology, and Summary and Recommendations. We note that several of the papers cited in this chapter can be found in the second of these volumes, although in some cases the papers are copies or updates of earlier publications. As an examination of the extensive reference list of this article will confirm, studies of the crustal deformation associated with the earthquake cycle in southcentral Alaska have continued to engage the attention of the scientific community in the decades since the earthquake.

## 2. TECTONIC, GEOLOGIC, AND SEISMOLOGIC SETTING

The contemporary tectonic environment of southern Alaska appears in Fig. 2. West of PWS, the Pacific Plate subducts under the North American Plate. Near the eastern end of the Alaska/Aleutian Trench, at  $57.5^{\circ}\text{N}$ ,  $148^{\circ}\text{W}$ , the velocity of the Pacific Plate relative to the North American Plate is about 55 mm/yr at  $119^{\circ}\text{W}$ , as estimated from the geological data (DeMets *et al.*, 1990, 1994). Newer estimates of the Pacific-North America relative plate motion based on contemporary geodetic observations give a similar velocity (DeMets and Dixon, 1999; Sella *et al.*, 2002). The magnitude of the velocity vector increases as one progresses along the plate boundary to the south and west and reaches about 57 mm/yr near  $56^{\circ}\text{N}$ ,  $152^{\circ}\text{W}$ . The strike of the Alaska-Aleutian trench varies with location (Beckman, 1980), but gradually rotates from a southwest–northeast orientation near its eastern terminus, southeast of Cordova, to an east–west orientation near the middle Aleutian Island chain. The obliquity of the plate motion vector relative to the trench normal is about  $27^{\circ}$  at the Kenai Peninsula, but is less than half that at Kodiak Island. Thus, the relative plate motion in southcentral Alaska is oriented approximately normal to the trench.

There is general agreement that the normal component of the plate motion is accommodated by slip on the megathrust and splay faults. There is, however, some debate about the extent to which the residual motion that is parallel to the plate boundary is partitioned between slip on the megathrust and strike-slip crustal faults. Such slip partitioning was noted for Sumatra by Fitch (1972) and McCaffrey (1992) presented a general model for slip partitioning. The 1964 earthquake may well have had some left-lateral slip, as well as the dip-slip motion, on both the megathrust and offshore faults. If slip partitioning were active, left-lateral strike-slip faulting would occur in the overriding North American plate. However, most crustal strike-slip faults in Alaska display right-lateral motion. Thus, most researchers have concluded that slip partitioning is not active in this region (Williams *et al.*, 2001). This issue will be discussed in more detail when we summarize observations and models of the coseismic motion.

The geometry of the plate interface varies along the strike of the plate boundary. In the PWS region, the plate interface dips at a shallow angle, the dip being  $3\text{--}4^{\circ}$  (Brocher *et al.*, 1994; Doser *et al.*, 1999). There the plate interface is the contact between the North America Plate and the Yakutat Block, an allochthonous continental terrane lying over the Pacific plate and partly welded to it (Perez and Jacob, 1980; Plafker *et al.*, 1994). The top of the Pacific Plate dips at a somewhat steeper angle than the megathrust, i.e., at  $8\text{--}10^{\circ}$  from the horizontal. To the west, the Yakutat block disappears, and the plate interface is between the North America Plate and the Pacific Plate itself. The dip angle of the interface is

about 8° near Kodiak Island (Von Huene *et al.*, 1987; Fletcher *et al.*, 2001), a location that is hundreds of kilometers west of the western edge of the Yakutat Block.

Inland, the Denali fault is a right-lateral crustal fault that extends for 500 km from near the Fairweather fault system southeast of the rupture zone of the PWS earthquake to under Denali Mountain (Mt McKinley), well to the north of the 1964 rupture zone. Slip on this fault has been ~10 mm/yr in geologically recent times (Plafker *et al.*, 1994). GPS measurements show a similar rate of 7–11 mm/yr for the present motion (Fletcher, 2002). Line length measurements from the 1980s showed a slower rate (Savage and Lisowski, 1991), but these earlier results are not entirely inconsistent with the GPS and geological estimates because there were rather large uncertainties in the line length data. In 2002, a magnitude 7.9 right-lateral strike-slip earthquake occurred on a portion of the Denali Totschunda fault system located south of Fairbanks (Eberhart-Phillips *et al.*, 2003; Hreinsdóttir *et al.*, 2003). The Denali fault is located far inboard of the subduction zone, and slip on the Denali fault is probably related to the counter-clockwise rotation of the large block of southern Alaska south of the fault (Lahr and Plafker, 1980; Fletcher, 2002).

Several other right-lateral faults in southern Alaska that lie north of the subduction zone accommodate block rotation and/or shearing within interior Alaska. As with the Denali fault, their relationship to the contemporary tectonic regime is not yet understood in full detail (Yeats *et al.*, 1996).

The geometry of the plate interface is important for describing the subduction zone structure. Zweck *et al.* (2002) derived a detailed description of the plate interface in southcentral Alaska by applying a 2-D cubic spline interpolation (with a resolution of 5 km) to the combined plate interface depth information of Moore *et al.* (1991), Page *et al.* (1991), Wolf *et al.* (1991), and Doser *et al.* (1999). They used the digital elevation/bathymetry model, ETOPO5, to estimate the interface depth near the trench. The interface depth contours from their analysis are shown in Fig. 3. These contours bend around the Kenai Peninsula. The mid-depth contours near Kodiak Island exhibit a much stronger gradient than those at the Kenai Peninsula. The 20 km depth contour passes near PWS, through portions of the eastern and central Kenai Peninsula, then under the trenchward coastline of Kodiak Island. The steepness of the plate interface increases rapidly once the subducting slab surface reaches 40–50 km depth (Ponko and Peacock, 1995).

Another important parameter of the subduction zone is the thickness of the subducting lithospheric plate. Zhao *et al.* (1995) estimated that the Pacific Plate thickness near the plate boundary is 45–55 km based on seismic tomography. This exceptional thickness may reflect a smearing-out of the Pacific slab's

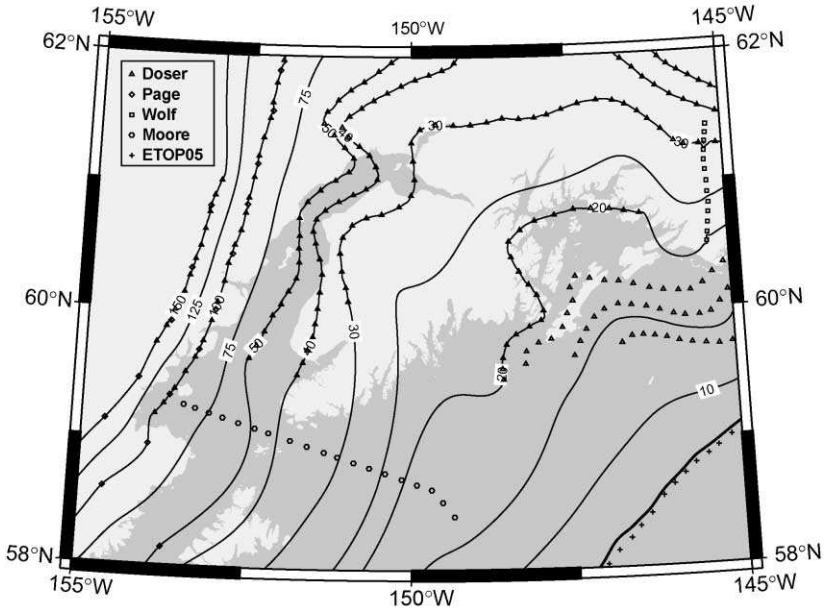


FIG. 3. Contours of plate interface depth (in km). Note the shallower dip of the Pacific Plate under the Kenai Peninsula than under Kodiak Island (to the southwest). The original data sources are indicated. From Zweck *et al.* (2002).

high-velocity anomaly due to limits on data resolution, although recent passive-source seismic imaging suggests that some portions of the downgoing slab may be anomalously thick (Ferris *et al.*, 2003).

The geology and tectonic framework of the Alaskan plate boundary region and the interior is comprehensively discussed in the compendium publication, “The Geology of Alaska,” published by the Geological Society of America. Here, we summarize some salient features of the southcentral Alaska region, as presented primarily in the chapter by Plafker *et al.* (1994). During the past 55 million years, the Pacific plate (early, the Kula plate) has been moving northwest relative to North America. The motion in southcentral Alaska has been accommodated primarily by underthrusting along the Aleutian Arc and by right-lateral to oblique-right-lateral slip on the Queen Charlotte–Fairweather fault system to the east. Some motion has also been taken up by slip on the bounding faults of the Yakutat block within Alaska. The crust of the Pacific Plate is progressively older going from east to west along the plate boundary. The oceanic crustal age is about

37 Ma at the eastern end of Aleutian trench and 45 Ma near Kodiak Island (Atwater and Severinghouse, 1989).

The continental crust is made up of a variety of terranes accreted onto the North America margin. The border ranges fault system (BRFS) separates the Chugach terrane to the south from the Peninsular terrane to the north (Fig. 2). The terranes north of the BRFS originated as an island arc and oceanic plateau (Pavlis and Crouse, 1989 and references therein) while those to the south are from a subduction-related accretionary complex. The BRFS played a role in accommodating the subduction during the early Jurassic and late Cretaceous and may have later been a site of lateral transport (Oldow *et al.*, 1989), although this latter point is disputed (Little and Naeser, 1989). The northern portion of the fault bent in response to the counterclockwise rotation of western Alaska in the Eocene. While the BRFS is a major structural boundary marking a sudden change from a mountainous to flat environment on the Kenai Peninsula, it exhibits little or no contemporary seismic activity. No fully conclusive evidence for Holocene displacement has been found (Wolf and Davies, 1986), although there is some limited evidence for motion near Anchorage within the past few hundred years (Updike and Schmoll, 1985). The major features of the Chugach terrane are the Chugach and Kenai Mountains and most of Kodiak Island. South of the Chugach terrane is the Prince William terrane with the contact fault system (CFS) marking much of the boundary. Moving to the eastern side of the region considered in this chapter, one finds the Queen Charlotte–Fairweather fault system, along which the Yakutat block has been displaced to the northwest by about 600 km (Plafker *et al.*, 1994).

Most of the geophysically interesting features shown in Fig. 2 are discussed by Von Huene *et al.* (1999). They include the aforementioned crustal faults and terranes and several subducting seamounts, some of which act as asperities. The major asperities are reflected in the coseismic slip pattern and in the location of aftershocks. Although some of the details on the asperity geometry are not well constrained or universally accepted, there is some evidence from seismic data that the length scale for the Prince William asperity was 140–200 km (Ruff and Kanamori, 1983). The subduction zone in the Kodiak region is characterized by a large accretionary prism, but there is no correspondingly large accretionary wedge in the PWS region. Figure 2 also shows the location of three seismic reflection and refraction lines (TACT, EDGE, and ALBATROSS) from which much of the information about the structure of the southcentral Alaska subduction zone has been derived (Moore *et al.*, 1991).

To illustrate the contemporary seismicity of southcentral Alaska, Fig. 4 shows the locations of large earthquakes with focal depths less than 60 km. We note a number of events near Kodiak Island. There is a scarcity of major earthquakes

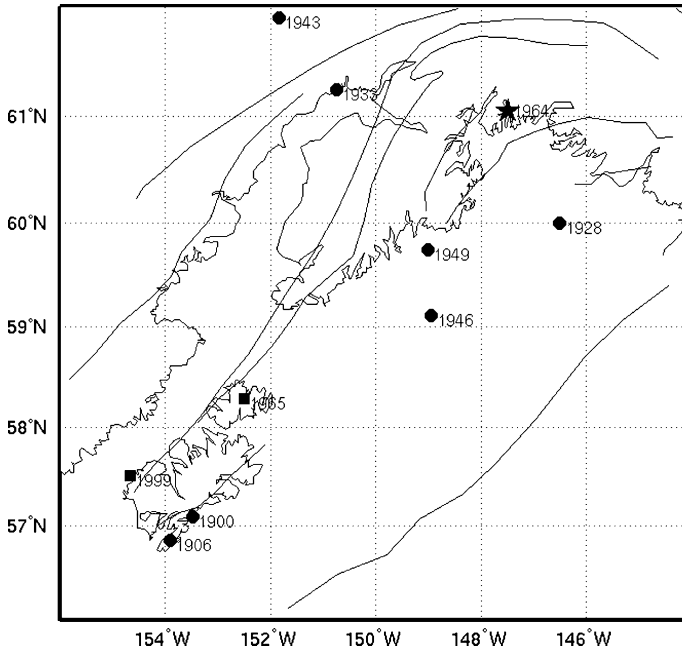


FIG. 4. Large (magnitude 7 or greater), shallow (focal depth less than 60 km) earthquakes in southcentral Alaska since 1900 from the catalog of the Alaska Earthquake Information Center. The epicenter of the 1964 earthquake is shown as a star. Earthquakes that occurred prior to 1964 are shown as filled circles, those occurring since 1964 are shown as filled squares.

between the Kenai Peninsula and the Afognak and Kodiak Islands. Both Page *et al.* (1991) and Doser *et al.* (1999) have noted that since the PWS earthquake there have been few earthquakes on the portion of the plate interface that slipped during the 1964 event. They found three clusters of moderate-size earthquakes that were associated with the subduction zone, but did not occur on the plate interface. The first two clusters were in the vicinity of the PWS asperity. One involved reverse or low angle thrusts and the other, normal to oblique faulting within the subducted Pacific Plate. The third cluster of events was in the Cook Inlet at depths below the plate interface. There is widespread seismicity within the overriding continental plate. Page *et al.* (1991) noted a band of seismicity (earthquakes with magnitude 3.0 or greater and depths less than 40 km occurring from 1967 to June 1988) north of and parallel to the Castle Mountain fault east of 151°W. They noted another seismic belt along the volcanic axis west of Cook Inlet and a diffuse north–northeast trending band of earthquakes near 150°W

longitude between Cook Inlet and the Denali Fault. On the Kenai Peninsula, the shallow seismicity does not correlate well with mapped fault traces. The shocks tend to be concentrated beneath the Kenai mountains and are, therefore, east of the Border Ranges Fault (Stephens *et al.*, 1990).

Some of the seismic asperities in the southcentral Alaska subduction zone may be associated with subducting seamounts. Estabrook *et al.* (1994) have noted that the northeast limit of five magnitude 7 earthquakes that occurred in 1938 appeared to coincide with the southwest limit of the 1964 rupture. They suggest that this seismic segmentation boundary is associated with a warping of the Pacific Plate and a change in dip angle from around  $8^\circ$  near Kodiak Island to about  $19^\circ$  to the southwest. However, the evidence for such a dramatic change in dip angle is not totally compelling. Fletcher *et al.* (2001), using the reflection profiles of Von Huene *et al.* (1987) and Moore *et al.* (1991) and source models of the 1938 Mw 8.3 earthquake, estimated a subducting plate dip angle of  $6^\circ$  for the region southwest of Kodiak Island. Von Huene *et al.* (1999) suggested that the differences between the Prince William and Kodiak asperities are related to differences in the surface properties of the lower (i.e., subducting) plate in the two regions. These authors argued for a relationship between the Kodiak asperity and the subducted Kodiak–Bowie hot spot swell. They also related the region of low aftershock moment release between the Kodiak and Prince William asperities to the thickened trench sediment adjacent to the trailing edge of the Yakutat block. The region around PWS, near the 1964 epicenter, is particularly complex from a seismotectonic perspective with the direction of maximum horizontal compression showing considerable variability (Estabrook and Jacob, 1991). Recently, additional insights concerning stress regimes on interior Alaska, based on stress tensor inversion from focal mechanisms, were presented by Ratchkovski and Hansen (2002).

### 3. OBSERVED CRUSTAL MOTION

Although there is a certain logic to discussing the observed crustal motion in temporal sequence by considering the preseismic motion followed by the coseismic, postseismic, and interseismic motion, we prefer the alternative of discussing the coseismic motion first. This approach is pedagogically useful for an awareness of the deformations that accompanied the earthquake and provides a useful conceptual basis for understanding the motions that preceded and followed the event. The coseismic displacements also define the initial conditions for the postseismic motion.

### 3.1. Coseismic Crustal Motion

Several workers have discussed the coseismic motion associated with the 1964 earthquake. Primary information about the earthquake and the associated aftershocks come from seismological studies, many of which are summarized in Christiensen and Beck (1994). Stauder and Bollinger (1966) studied the polarity of the  $P$  wave for the primary shock,  $P$  wave first motion and  $S$  wave polarizations for the aftershocks, the spatial distribution of aftershock foci, and dislocation model considerations to tentatively conclude that the Alaska earthquake occurred on a shallow thrust with a dip of about  $10^\circ$ . Kanamori (1970) used Love and Rayleigh wave records to estimate source parameters: a seismic moment of  $7.5 \times 10^{29}$  dyne cm, average slip dislocation 7 m, strain energy release  $5 \times 10^{25}$  erg, and dip direction for the reverse dip-slip event,  $N24^\circ W$ . Christiensen and Beck (1994) obtained a seismic moment of  $3 \times 10^{29}$  dyne cm from  $P$  wave data. There were only a few usable  $P$  waveforms for the 1964 earthquake because most teleseismic recordings of direct  $P$  wave arrivals were clipped due to the tremendous size of the earthquake. Most usable recordings came from diffracted  $P$  waves, and only 13 seismograms were both on scale and not contaminated by arrivals of secondary phases with 210 s of the first arrival. Christiensen and Beck (1994) noted that their estimate of the seismic moment agreed with the estimate of  $1.8 \times 10^{29}$  dyne cm obtained by Kikuchi and Fukao (1987), but warned that the  $P$  waves accounted for only one-third of the total seismic moment.

One of the earliest hints that the coseismic rupture consisted of a sequence of subevents came from the observations of multiple  $P$  wave phases whose arrival could not be predicted by travel-time curves (Wyss and Brune, 1972).

Geodetic observations gave quantitative estimates for the permanent surface deformation due to the earthquake. Parkin (1972) provided information on triangulation data and Small and Wharton (1972) discussed leveling observations. The coseismic horizontal displacements were obtained by comparing post-earthquake site coordinates, derived from triangulation observations made in 1964 and 1965, to pre-earthquake coordinates, derived from measurements made between the early 1900s and the late 1940s. There is considerable spatial variation in the quality of the pre-earthquake survey data. The region running east from Anchorage to Glennallen and then south to Valdez was surveyed to first-order standards (about  $4 \mu\text{rad}$  or 200 mm over a 50 km line). By contrast, an arc across northern PWS to Perry Island (south of Valdez) was surveyed to second-order standards and an arc from Perry Island to Anchorage was surveyed to only third-order standards. A portion of the Kenai Peninsula, including an arc from Seward to Turnagain Arm, was also surveyed to third-order standards. These surveys were made primarily for chart control, so little, if any, consideration was

given to the measurement precision needed for crustal movement studies. There are substantial misclosures for some of the triangulation arcs. Because the pre-earthquake data span four decades, part of the misclosure error is due to deformation that occurred before the earthquake. Data from a third order arc along Turnagain Arm are particularly suspect (Parkin, 1972). The scale for the pre-earthquake network was provided by a limited number of taped distance observations and a single microwave (tellurometer) distance observation. Orientation was provided by several Laplace azimuth observations. Uncertainties in the pre-earthquake survey positions may be as large as 2–3 m at the edge of the network in outer PWS, and dominate the uncertainty in the coseismic displacements.

The quality of the post-earthquake observations is more uniform than that of the pre-seismic measurements. The observations are a mixture of first-order triangulation and tellurometer observations. Parkin (1972) made a free adjustment of the network to determine the magnitude and direction of coseismic slip vectors. He used 1476 observed directions at 292 stations, 5 Laplace azimuths for orientation, and 8 geodimeter and 146 tellurometer observations for scale. The errors in the station positions estimated from an examination of residuals are 2–3 m in the PWS region.

The displacement results that were presented by Parkin (1972), and are replotted here as Fig. 5, are relative to a fixed site (Fishhook) north of Palmer, Alaska, at  $61^{\circ}43.0'N$  and  $149^{\circ}14.0'W$ . The maximum observed displacements were in excess of 20 m and were directed south–southeastward. Displacements were generally largest near the trench and smaller inland, as expected. There were some exceptions to the systematic variations in displacement vectors with distance from the trench. For example, the displacement at Middleton Island, the most southerly location at which observations were made, did not follow the general pattern. The displacement there suggested that the coseismic slip along the shallow portions of the megathrust was less than the average slip in the earthquake. The present GPS velocity from Middleton Island is also smaller than the velocity for sites farther from the trench (Savage *et al.*, 1998), so this observation is probably reliable. Slip on the Patton Bay fault also affected this coseismic displacement near Montague Island. Furthermore, the absolute motion of the entire geodetic network has some ambiguity as the displacements were calculated assuming no motion at Fishhook, a site that may have moved during the earthquake by as much as a few meters (Suito *et al.*, 2003). As Whitten (1972) mentions, “In Parkin’s investigation the western end of this scheme was held fixed... The eastern end was permitted to seek its most probable position.” It appears that many of the coseismic slip vectors were aligned with the relative plate motion vector and that there was an easterly component to the motion at

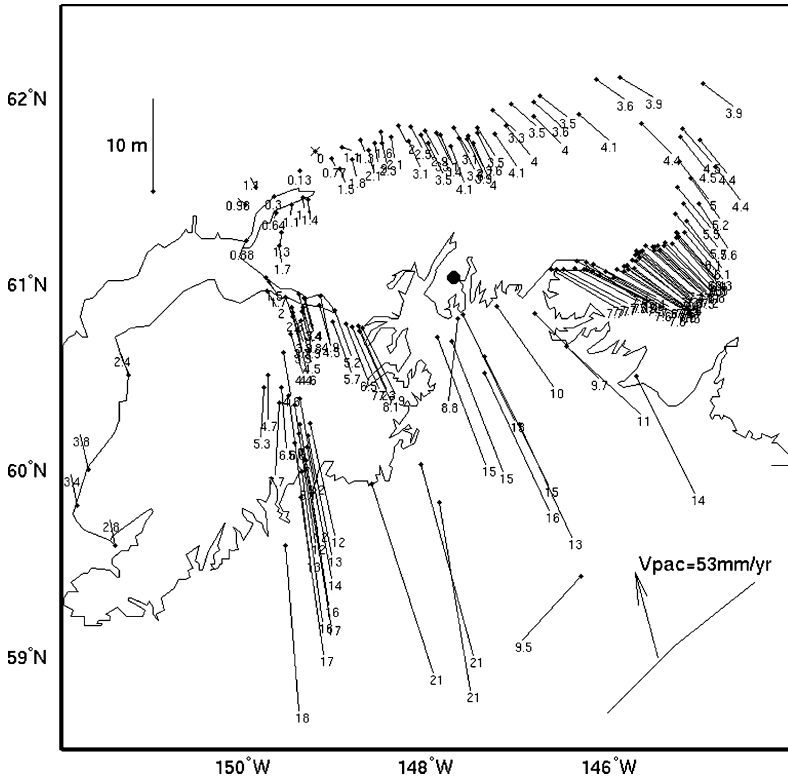


FIG. 5. Coseismic horizontal displacements for the 1964 Prince William Sound earthquake. The displacements are relative to site Fishhook, located at  $61^{\circ}43.0'N$ ,  $149^{\circ} 14.0'W$ . The data are from Parkin (1972).

sites on the eastern side of the network. This alignment may have been a consequence of the assumptions. If, alternatively, the displacement of the easterly sites were in the direction of plate motion, then there would have been a left-lateral component to the largest of the displacement vectors, and quite possibly a change in rake. The rotation in the displacement vectors between PWS and the region to the east seen in Fig. 5 matches a similar rotation in the present GPS data (Fletcher and Freymueller, 2002) suggesting it reflects a true change in fault slip vector, possibly due to the differential motion of the Pacific Plate and Yakutat block.

It is not known whether the apparent northwesterly coseismic motion of sites on the western side of the Kenai Peninsula was real or an artifact of a weak

network connection to this region. This orientation of displacement vectors might also result from the coseismic motion of Fishhook; if the sites in the western Kenai Peninsula moved seaward less than Fishhook did, they would show a residual NW-directed displacement. However, there is also a dramatic difference in the direction of interseismic motions of the eastern and western portions of the Kenai Peninsula as well. Later, we will discuss in detail this difference in the direction of interseismic motion.

An illustrative example of the geodetic network geometry, specifically that of the southcentral portion of the triangulation network, is shown in Fig. 6. Data from this and other portions of the triangulation network were used by Pope (1972) to compute strains. The network geometry was less than ideal because some segments of the network consisted of a thin band of nearly linearly arrayed sites and other segments were made up of intersite triangles with long sides. However, the general results from the analysis of the network are probably reliable. The direction of the principal coseismic compressive strain axis was north–northwest in the Seward region, but north–northeast in the tectonically complex region near PWS.

The coseismic vertical motion was studied using five repeated leveling profiles and apparent sea-level heights as measured by tide gauges at Homer, Seward, Whittier, and Valdez (Small and Wharton, 1972). Among the leveling profiles, the most interesting one ran from Matanuska through Anchorage, then southward through Portage along the Turnagain Arm. It extended southward from there to Seward along the Alaska railroad right-of-way. The pre-earthquake survey was conducted in 1922 and the post-earthquake survey was done in 1964. Coseismic subsidence was noted along the entire profile, with a vertical height change of  $\sim 1$  m occurring at Seward and a maximum subsidence of  $\sim 2$  m occurring south of Portage (Fig. 7). Another line, first surveyed in 1944, then resurveyed after the earthquake, ran west–northwest from Matanuska through Glennallen then turned to the north. Along this route the typical coseismic subsidence was about  $\sim 0.5$  m with only a modest variation along the route. This small variation in subsidence is not surprising since the survey line ran roughly parallel to the trench. Along a profile running southward from Glennallen and then turning eastward toward Valdez that was first surveyed in 1923, the maximum coseismic subsidence exceeded 1.2 m. The measured subsidence was less than 1 m at Valdez, but there was a 2–3 m difference in the tidal datum as determined in May through July of 1964 vs. July through November. The difference is too large to be attributable to postseismic motion.

Plafker (1972) developed a contour map of the vertical coseismic displacements throughout southcentral Alaska by combining leveling data, tide gauge observations, changes in the upper growth level of intertidal organisms, changes

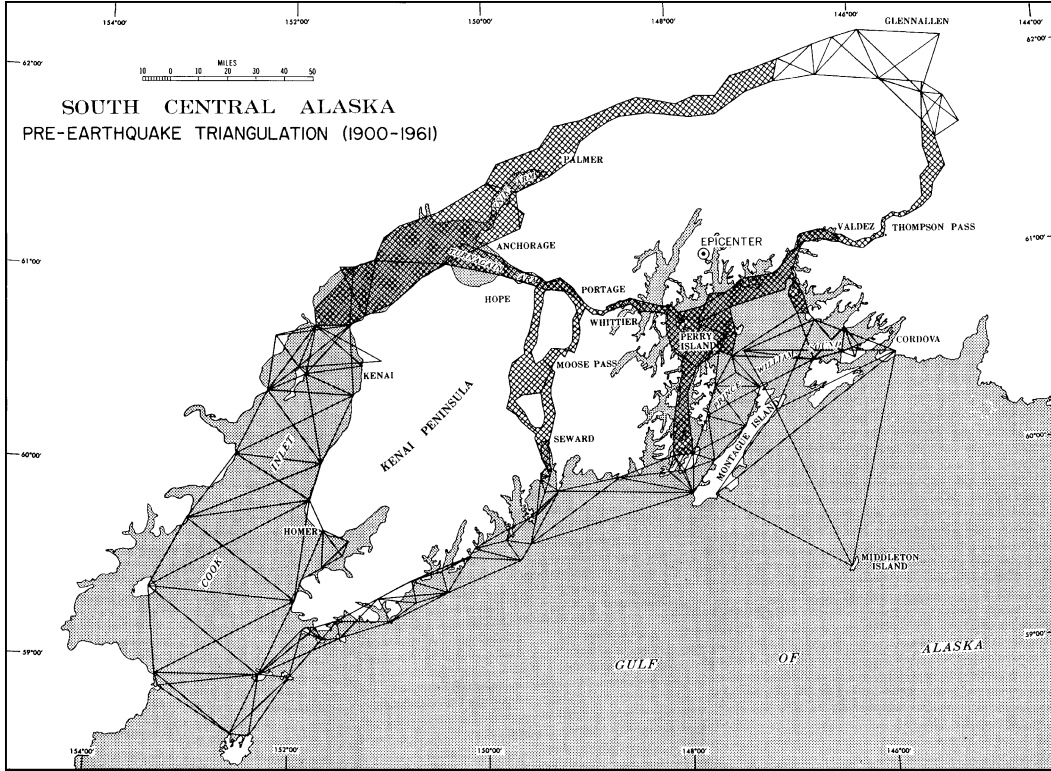


FIG. 6. Portions of the geodetic networks used to deduce coseismic displacements and strain changes. The top panel shows the pre-earthquake network for southcentral Alaska; the bottom panel shows the post-earthquake network for the same region. From Parkin (1972).

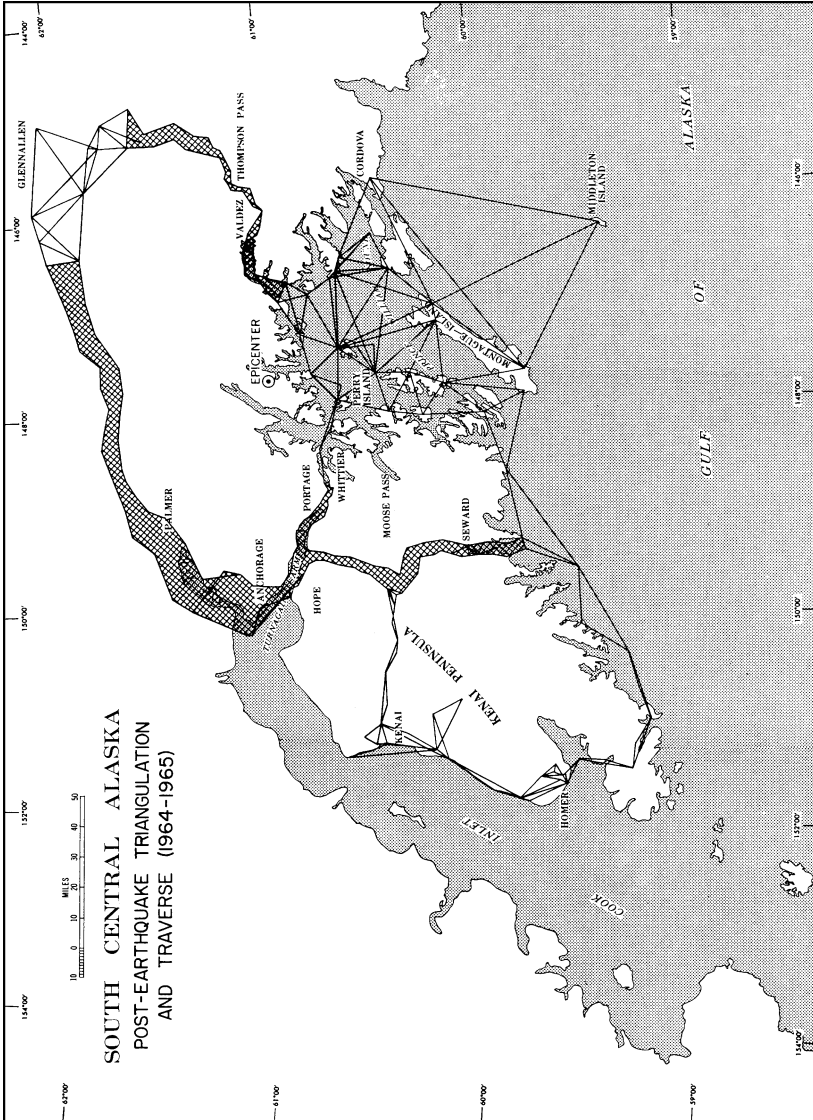


Fig. 6. Continued.

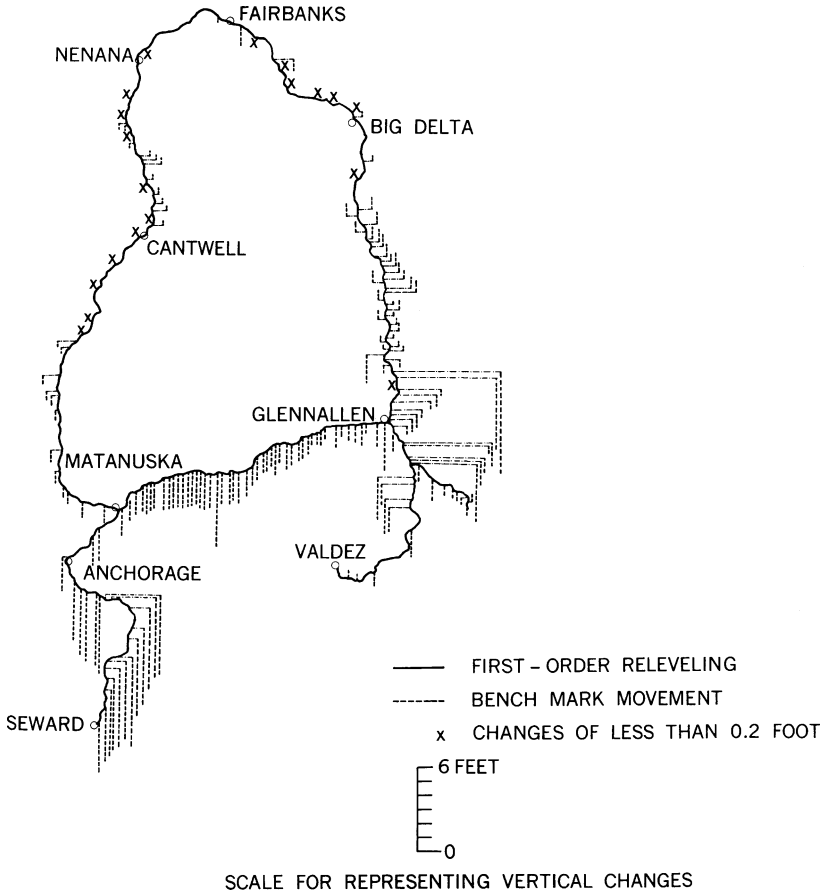


FIG. 7. Coseismic vertical displacements from leveling observations. The leveling segments and the dates of the pre-earthquake and post-earthquake surveys are as follows: Seward to Matanuska: 1922/23, 1964; Matanuska to north of Glennallen: 1944, 1964; Glennallen to Valdez: 1923, 1964; North of Glennallen to Fairbanks: 1923, 1964; Matanuska to Fairbanks: 1922, 1965. From Small and Wharton (1972).

in the heights of storm beaches, changes in the tidal benchmark heights relative to sea level, and changes in the location of the shoreline as estimated by local residents. His generalized map (Fig. 8) shows several interesting features. The contours are oriented southwest to northeast, a direction consistent with the strike of the trench, the trend of the surface geological features, and the orientation of

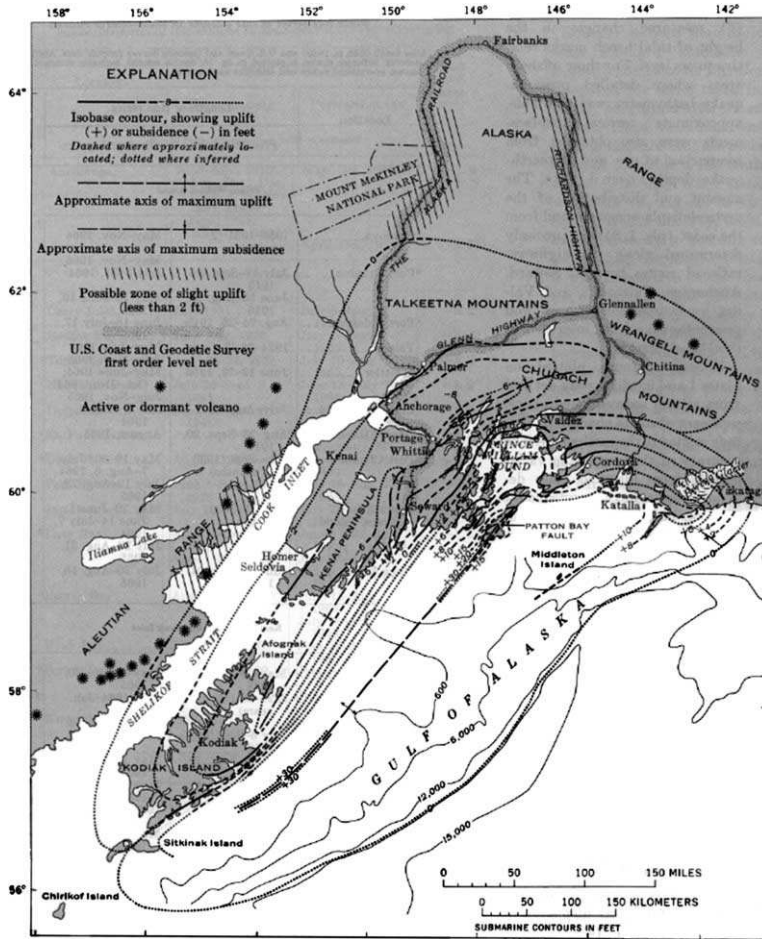


FIG. 8. Coseismic uplift contours (in feet) as deduced from both geodetic and geologic information. Note that the oceanward portion of the zero uplift contour crosses the southeastern Kenai Peninsula and southern Kodiak Island. The maximum local uplift lies near the Patton Bay fault; the maximum subsidence lies further inland and is about 2 m (6 ft). From Plafker (1972).

magnetic and gravitational anomalies. The oceanward portion of the zero uplift contour passes near the southern edge of Kodiak Island, south of most of the Kenai Peninsula and near Valdez. Cordova, Middleton Island, and much of the Gulf of Alaska are in the region of coseismic uplift. The maximum coseismic

uplift was around 10 m (n.b., the Plafker map units are feet). The uplift contours are influenced by localized slip on the Patton Bay and other shallow reverse faults. Most of Kodiak and Afognak Islands, the Kenai Peninsula, the Matanuska Valley and the region north of PWS were in the zone of coseismic subsidence. The width of the subsidence region broadened considerably around Anchorage. The maximum coseismic subsidence was around 2 m. Plafker (1972) suggested that a region of modest uplift occurred inland beyond the zone of subsidence, notably in the Aleutian range northwest of Cook Inlet and north of the Talkeetna Mountains between Anchorage and Fairbanks.

One of the intriguing aspects of the coseismic vertical deformation pattern comes from terrace data at Middleton Island. The observed 3.3 m uplift (Plafker, 1972) is apparently only about half that for the preceding three earthquakes. There has been speculation that additional uplift will occur in a future rupture of the eastern segment of the 1964 earthquake zone or that the distribution of slip between the interface and crustal faults was different in the 1964 earthquake than in preceding events (Carver and McCaLpin, 1996).

Information on the coseismic and horizontal surface coseismic displacements have been used to develop models of fault slip during the earthquake. Hastie and Savage (1970) performed a least-squares analysis using an elastic dislocation model with a single fault plane on the plate interface and a subsidiary slip surface on Montague Island. They estimated the slip on the main thrust to be 10 m. Their work, along with that of many others (Plafker, 1965; Stauder and Bollinger, 1966; Kanamori, 1970), helped establish that the main fault plane was a low-dip angle megathrust. The alternative, then under consideration, was that slip had occurred on a nearly vertical fault extending to 100–200 km depth (Press, 1965; Press and Jackson, 1965). Although the speculation that the earthquake occurred on a vertical fault extending to considerable depth might seem strange to the present-day reader, it was a viable hypothesis in 1964 because plate tectonics concepts were not well established (Harding and Algermissen, 1972).

Miyashita and Matsu'ura (1978) developed a coseismic deformation model based on vertical displacement data. Their major contribution was to consider four fault segments rather than a single surface. Three of the slip planes were along the main thrust and were laterally adjacent to one another; the fourth was at Montague Island. The three main thrust fault planes were centered on Kayak Island (on the eastern side of the rupture), PWS, and the Kenai Peninsula–Kodiak Island region. Miyashita and Matsu'ura (1978) estimated slip, dip angle, strike, and fault segment extent. The Kodiak–Kenai segment had the largest estimated slip, nearly 19 m, while the Montague Island segment had an estimated slip of

11.5 m. This model should be considered preliminary as more recent studies have included more data and tectonic complexity and have resulted in a modification to the estimated slip distribution. For example, Holdahl and Sauber (1994) developed a more spatially detailed coseismic model. Their analysis was based on a variety of previously published data including: (1) changes in coastal heights from barnacle, vegetation, storm beach, and marker observations, (2) changes in tidal datum planes, (3) pre- and postseismic leveling, (4) pre- and postseismic bathymetry, and (5) horizontal displacements. Their inversion allowed for both strike-slip and dip-slip components of the motion, but the inferred strike-slip displacements were generally small except in segments near PWS and northeast of there. There was an area of high slip near the coast and offshore from the PWS region through the eastern Kenai Peninsula. The highest slip was about 30 m, near Montague Island. Since the Holdahl and Sauber (1994) model included 68 fault patches, the slip on some of them may not have been well resolved by the data. Johnson *et al.* (1996, see also Johnson, 1999) updated and improved on the Holdahl and Sauber (1994) analysis, conducting a joint inversion using 23 tsunami waveforms as well as 188 vertical and 292 horizontal geodetic observations in their inversion. Their model had only 18 fault segments, but the dip angles and depths for the segments near the Yakutat block were consistent with the megathrust being at the top of that terrane rather than at the top of the Pacific plate, as had been assumed in some other work. They adopted Holdahl and Sauber's (1994) estimate of 8.5 m slip on the Patton Bay fault at Montague Island. Despite some differences in detail, the slip distribution deduced by Johnson *et al.* (1996), shown in Fig. 9, closely resembles that of Holdahl and Sauber (1994). The peak fault displacement was  $22.1 \pm 4.4$  m. One of the most important aspects of the Johnson *et al.* (1996) analysis was that they gave full consideration to the tsunami data using these data as constraints along the coast. A significant portion of the slip occurred offshore, i.e., beyond where geodetic measurements could be made. Thus, geodetic survey data alone do not provide sufficient constraints on the slip pattern, particularly at locations near the trench. Holdahl and Sauber (1994) used tsunami information as *a priori* inputs to their model, but Johnson *et al.* (1996) used the full strength of the tsunami data.

Both Kikuchi and Fukao (1987) and Christiensen and Beck (1994) studied the seismic moment release of the 1964 earthquake, as previously mentioned. Both pairs of authors identified an area of large moment release near PWS, centered away from the earthquake epicenter. In addition, Christiensen and Beck (1994) identified a secondary region of moment release near Kodiak Island. They found only modest moment release between the two locations (Fig. 10). Similarly, Johnson *et al.* (1996) estimated large slip at the PWS asperity and

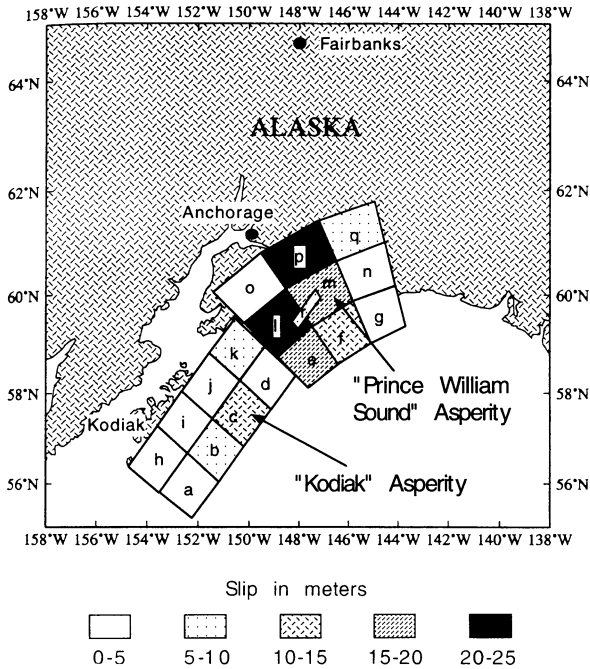


FIG. 9. Coseismic slip distribution as deduced from an elastic dislocation model using geodetic and tsunami data. From Johnson *et al.* (1996).

secondary, but still substantial, slip at the Kodiak asperity. The comparatively small moment release between the PWS and Kodiak asperities may be related to a tear in the subducting Pacific Plate. Pulpan and Frohlich (1985) argued for such a tear underneath Cook Inlet at about 59°N.

One issue that remains a matter of debate is whether significant strike-slip motion occurred during the PWS earthquake. Hastie and Savage (1970) considered slip on both the main thrust and a subsidiary fault running through Montague Island. They estimated left-lateral slip of nearly 10 m on the main thrust and 12 m on the subsidiary fault. Miyashita and Matsu'ura (1978) also found significant left-lateral motion on the subsidiary fault but relatively little lateral motion on any of the three faults in their main thrust. Holdahl and Sauber (1994) found right-lateral slip on the main thrust in the vicinity of PWS, but this result appears anomalous. Johnson *et al.* (1996) constrained the slip to be in the dip direction along much of the plate interface, but to be in the direction of plate motion in the vicinity of PWS. This gave a left-lateral component to the slip.

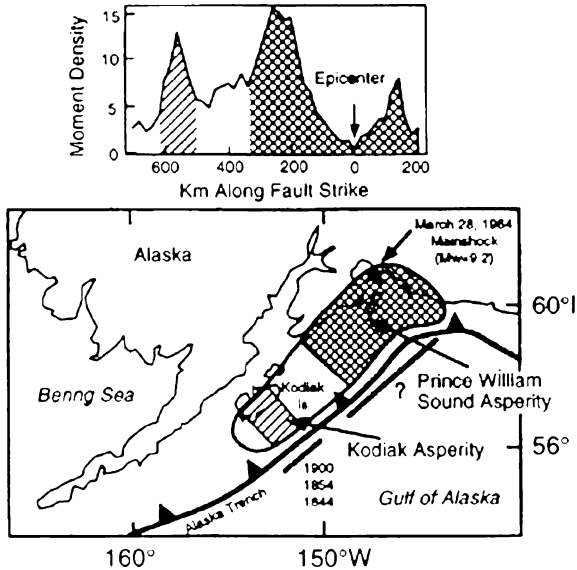


FIG. 10. Asperity distribution as determined by Christiensen and Beck (1994) and presented in Johnson *et al.* (1996). The upper figure shows the along-strike moment density release in units of  $10^{26}$  dyne cm/km. The lower figure shows the map view of the asperities. The dates of historical earthquakes in the Kodiak segment are listed.

Thus, the PWS earthquake was primarily a dip-slip event on the shallow megathrust. There may have been some left lateral slip, but its magnitude is not well determined. The weak constraints on the slip direction are a consequence of the limitations of the horizontal geodetic data, which is substantially less precise than the vertical data. Additionally, there was locally significant, subsidiary slip, on crustal faults.

The recurrence time between major earthquakes is a key parameter for assessing earthquake hazards as well as for modeling the temporal evolution of the crustal deformation. Based on an average coseismic displacement of 14 m and a somewhat too rapid estimate of North America-Pacific relative plate velocity of 65 mm/yr, Nishenko and Jacob (1990) derived a recurrence interval of 233 yr for the PWS segment of the plate boundary. Using a peak displacement of 30 m, rather than the average displacement, they derived an alternative recurrence period of 462 yr. This second estimate is closer to the geological estimate, as we will summarize later, but might still be low if some of the convergent motion between North America and the Pacific is accommodated aseismically.

These recurrence times are based on a simple time-predictable model in which the recurrence time is the coseismic slip divided by the interseismic velocity. This model is almost certainly oversimplified, but is commonly used to help interpret geodetic observations.

Using radiocarbon dating of terraces, notably at Middleton Island, Nishenko and Jacob (1990) estimated an earthquake recurrence interval of  $1021 \pm 362$  yr. The most recent terrace at Middleton Island dates from 1300 years ago. However, the Middleton Island estimate may not be representative. Along Turnagain and Knik Arms of Cook Inlet, Combellick (1993) estimated an average recurrence interval of 590–780 yr, in closer agreement with the longer of the estimates from geodetic data. Similarly, Plafker *et al.* (1992) reported an age of 665–895 yr for the most recent earthquake uplift in the Copper River delta. Combellick (1992) obtained evidence from Girdwood, along the Turnagain Arm, that the penultimate great earthquake in the Anchorage region occurred 700–900 yr ago. There is evidence from peat stratigraphy in a borehole near Portage that significant earthquakes may have occurred within a century of one another (Combellick, 1991).

For the Kodiak Island segment of the plate boundary, Nishenko and Jacob (1990) derived a recurrence interval of only 50–60 yr. The magnitudes of the Kodiak Island earthquakes were in the range  $M_s = 7.5-8$ , while the PWS earthquake was much larger, so the different recurrence intervals are associated with earthquakes of different magnitudes. Furthermore, the earthquake history of the Kodiak segment is complex, as this segment appears to have ruptured with the PWS segment, by itself, and also with the Peninsula segment located to the southwest of it (Nishenko and Jacob, 1990).

### 3.2. Preseismic and Interseismic (Pre-1964) Crustal Motion

Tide gauges located at Seward and Kodiak city give some insight into the vertical motion that occurred in southcentral Alaska in the decades preceding the 1964 earthquake. The tide gauge at Seward was installed in 1925 and the one near Kodiak city in 1950. Savage and Plafker (1991) examined the pre-earthquake tide gauge records at these two locations. They deduced that the mean crustal uplift rate before the earthquake was  $2.7 \pm 1.5$  mm/yr at Seward and  $4.8 \pm 1.6$  mm/yr at Kodiak. The slow preseismic uplift rate at Kodiak is particularly interesting in light of the rapid uplift there after the earthquake. Either there is a time-dependence to the uplift rate, or the deformation rates during the interseismic periods before and after the 1964 earthquake are very different. The slow preseismic uplift rates seen in the tide gauge data are

consistent with Plafker's (1972) claim that "no change in mean sea level attributable to tectonic movement was detected in a 21 year tidal record at Seward and a 15 year record at Kodiak." The expression, "no change" must be taken in proper context. The statement was written when its author was studying the large vertical motions associated with the earthquake. The coseismic vertical movements were orders of magnitude larger than any known preseismic ones; thus, preseismic motion was not considered to be of consequence. However, Shennan *et al.* (1999) recently documented evidence for preseismic subsidence from a study of microfossil assemblages along Turnagain Arm.

Plafker (1972) also discussed the recent Holocene record of shoreline movements. The record is quite complex. A large number of shoreline samples have radiocarbon dates of less than 1000 years before the 1964 earthquake and thus may be associated with preseismic and interseismic deformation. The sites in the coseismic uplift zone appeared to have been located below the pre-1964 sea level. This suggests that these shoreline points gradually submerged during the interseismic period. However, samples with older carbon dates reflect a pattern similar to the coseismic deformation. For example, several points on the Kenai Peninsula and Turnagain Arm that subsided during the earthquake show Holocene subsidence as well. Similarly, there is long-term emergence at Middleton Island and at Bering Lake (between Cordova and Yakataga), locations that also rose during the earthquake. It appears that the geologically recent vertical motions are due more to tectonic processes than post-glacial rebound at most locations. The net emergence or submergence is, of course, a combination of the coseismic and interseismic motions. Plafker (1972) states that this interplay has resulted in the net emergence of part of the continental margin and submergence of part of the Kenai-Kodiak mountains.

### 3.3. Postseismic and Interseismic (Post-1964) Crustal Motion

#### 3.3.1. *Postseismic Uplift Observed from Repeated Leveling Surveys*

One of the earliest reports of significant postseismic motion based on definitive geodetic observations was published by Small and Wharton (1972). They compared leveling observations along Turnagain Arm made in October 1964 to those made in May and June of the same year. As shown in Fig. 11 the observed motion was a trenchward tilting. Small and Wharton (1972) interpreted the tilting as subsidence at Portage, citing as additional evidence the results of a survey taken in 1965 that they felt demonstrated further subsidence at Anchorage and

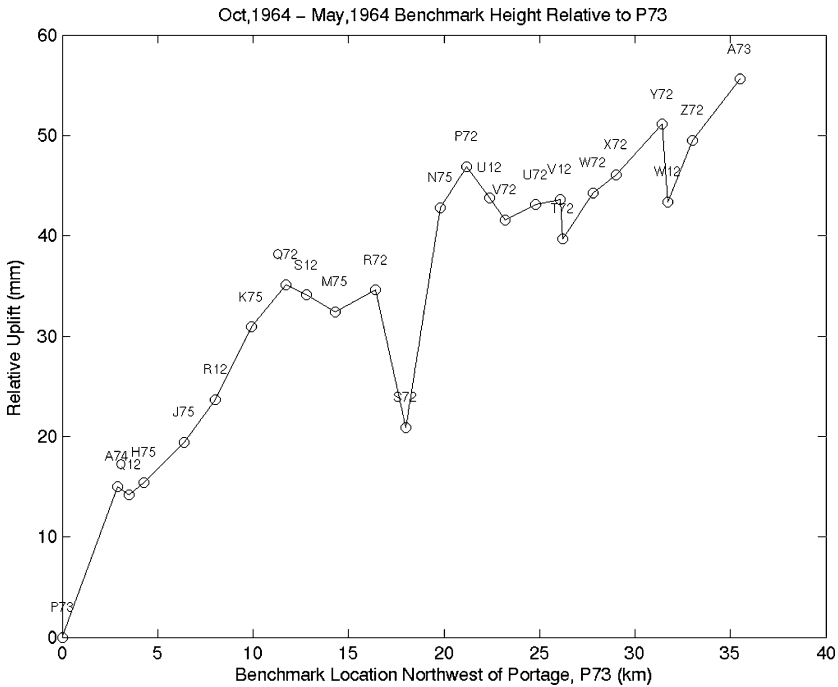


FIG. 11. Postseismic uplift relative to site P73, near Portage, as determined from leveling differences deduced from surveys along Turnagain Arm in May and October, 1964. Portage is located near the southern end of Turnagain Arm (Fig. 2). From Small and Wharton (1972).

Portage. However, as Brown *et al.* (1977) later argued, the Turnagain Arm observations are more convincingly interpreted as postseismic uplift along much of the route between Portage and Anchorage. Cohen (1998) showed that the uplift deduced from the two surveys made six months apart in 1964 could be extrapolated to predict the uplifts observed over a year as derived from the initial survey and one made in 1965. This indicates that the rapid, early postseismic uplift proceeded at a roughly constant rate for at least one year following the earthquake. The maximum relative uplift rate along Turnagain Arm in this first year was about 150–160 mm/yr, although the absolute uplift rate might have been somewhat less. Brown *et al.* (1977) examined leveling data from surveys made along Turnagain Arm in 1964, 1965, 1968, and 1975. The observations (Fig. 12) indicated a maximum uplift between 1964 and 1975 of 0.37 m relative to the tide gauge station at Anchorage. The maximum uplift occurred at D73,

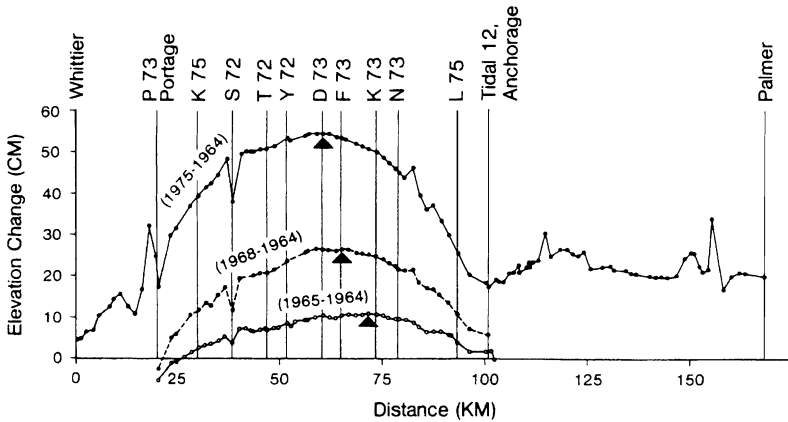


FIG. 12. Postseismic uplift derived from repeated leveling along a route beginning at Whittier and extending northwest along Turnagain Arm between Portage and Anchorage, then mostly northeast toward Palmer. The absolute values of the uplift may be biased. They are based on the assumption that Anchorage was moving upward at a constant rate of 16.3 mm/yr. (see text for discussion). From Brown *et al.* (1977).

a site located approximately 40 km southeast of Anchorage along the 100-km long Turnagain Arm profile. The relative uplift dropped to about zero near Portage, located 75 km southeast of Anchorage. Modest relative subsidence occurred between there and Whittier. To estimate absolute motion, Brown *et al.* (1977) used tide gauge observations of the uplift rate of Anchorage and a tie between the tide gauge and leveling benchmark. They deduced that the Anchorage tide gauge site was moving upward at a constant velocity of 16.3 mm/yr in the years following the earthquake. If this were correct, then the absolute uplift of D73 by 1975 would have exceeded 0.50 m. However, it is not certain that Anchorage actually experienced the rapid upward movement that Brown *et al.* (1977) thought they detected. Savage and Plafker (1991) examined the tide gauge records at Anchorage over a much longer time span than was available to Brown *et al.* (1977). The Savage and Plafker (1991) study concluded that the average uplift rate at Anchorage since the earthquake was quite small. They estimated a vertical velocity of  $-0.7 \pm 1.3$  mm/yr for the period from immediately after the earthquake through 1973 and  $1.0 \pm 2.2$  mm/yr for the entire postseismic period through 1988. Given these slow uplift rates, we may reasonably assume little or no postseismic uplift at Anchorage. In this case, the aforementioned relative uplifts are absolute. Thus, the maximum absolute uplift, through 1975, was about 0.37 m. There may have been transient motions,

particularly in the years immediately following the earthquake, that are not reflected in the long term averages. We will return to this issue briefly later.

The time dependence of the uplift (Fig. 13) is another intriguing aspect of the leveling observations. Again taking Anchorage as a reference point, we find that the maximum uplift rate for the first year after the earthquake was 80–90 mm/yr (150–160 mm/yr relative to Portage). Averaged over the four years between 1964 and 1968, the maximum uplift rate was about 50 mm/yr, and averaged over the 11 years between 1964 and 1975, the maximum rate was about 30 mm/yr. The maximum uplift rate did not occur at a fixed location, rather, its location appeared to migrate trenchward. The time histories of the relative motion between pairs of sites provide important constraints on the time scale for the postseismic

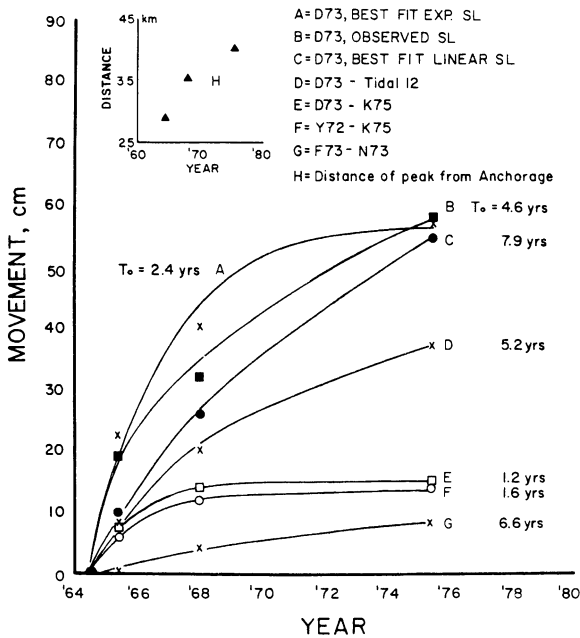


FIG. 13. Time dependence of postseismic uplift as deduced from leveling data along Turnagain Arm. In each case the data are fit (in a least squares sense) to an exponential function with time constant,  $T_0$ . Curves A, B, and C refer to the motion of site D73 in Fig. 12. In A, an exponential uplift function is also assumed for the sea level tide gauge site in Anchorage. In B, the observed uplift function is also assumed for the sea level tide gauge site in Anchorage. In C, a linear, i.e., constant rate, uplift is assumed for the tide gauge. Curves D, E, F, and G are relative uplifts assuming that the uplifts of the points being considered have the same time constant. The inset shows the migration of the point of maximum uplift in Fig. 12. From Brown *et al.* (1977).

relaxation. For example, the uplift rate of site D73 relative to Anchorage decayed with an exponential relaxation time of 5.2 yr. That the transient decayed over a few years is important because other data reveal longer-lived postseismic transients, as we will discuss later. The different transient time constants may indicate that there are several mechanisms for the postseismic relaxation or that the parameters governing the relaxation vary with locality.

Prescott and Lisowski (1977, 1980) examined a set of leveling observations on Middleton Island, located about 60 km northwest of the Alaska-Aleutian Trench. The observations were made in 1966, 1974, and 1975. They indicate a down-to-the-northwest tilt. The tilt rate derived from the first two surveys was  $11.5 \pm 5.3 \mu\text{rad/yr}$  and that derived from the last two surveys was  $5.0 \pm 0.8 \mu\text{rad/yr}$ . The smaller uncertainty in the second time interval resulted from the use of substantially more precise leveling techniques in the 1974 and 1975 surveys. Although the tilt rate may have decreased with time, the details of the temporal evolution are not resolved. The deformation may be strongly influenced by strain accumulation and release on secondary faults rather than the main thrust. The main thrust should contribute little to the vertical motion because the dip angle is only about 3–4 degrees below Middleton Island. However since Middleton Island is located very close to the up-dip end of the locked zone, as shown by the distribution of 1964 aftershocks, some of the vertical motion may be due to edge effects.

### 3.3.2. Vertical Motion Measured at Tide Gauges

Brown *et al.* (1977) examined crustal uplift as indicated by tide gauge stations at Seward, Seldovia, St. Paul's Harbor (Kodiak), and Cordova as well as Anchorage, but the deduced rates are suspect due to the limited time span and the noisy observations (as we hinted earlier). A longer set of tide gauge data was used by Savage and Plafker (1991). They analyzed sea-level observations at seven southcentral Alaska sites (Anchorage, Kodiak Cordova, Seldovia, Seward, Nikiski, and Valdez) that were affected by the 1964 earthquake; five southeast Alaska sites (Juneau, Ketchikan, Sitka, Skagway, and Yakutat) that were unaffected by the earthquake; and one southwest site (Sand Point) that was also unaffected by the earthquake. The rates of uplift they deduced for the southcentral Alaska locations are summarized in Table 1. Locations that subsided during the earthquake, notably Seldovia, Seward, and Nikiski, showed postseismic uplift, whereas Cordova, which rose during the earthquake, showed postseismic subsidence. Despite this apparent relationship, the quantitative correlation between the coseismic vertical displacement and the postseismic

TABLE 1. Uplift Rate (mm/yr) and Rate Change (mm/yr<sup>2</sup>) Estimates at Tide Gauge Sites in Southcentral Alaska

Tide Gauge Site	Rate: SP91 <sup>a</sup>	Rate: CF00 <sup>b</sup>	Rate: LET02 <sup>c</sup>	Rate Change: CF00 <sup>b</sup>	Rate Change: LET02 <sup>c</sup>
Anchorage	1.0 ± 2.2	2.7 ± 0.9	3.1 ± 0.3		0.48 ± 0.08
Cordova	-6.8 ± 1.1	-4.7 ± 1.0	-3.65 ± 0.12	0.39 ± 0.06	0.48 ± 0.04
Kodiak	20.4 ± 1.3	16.5 ± 0.7	16.4 ± 0.2	-0.67 ± 0.11	-0.66 ± 0.04
Nikiski	21.6 ± 2.0	11.9 ± 0.8	15.6 ± 0.4		-0.80 ± 0.08
Seldovia	10.1 ± 1.8	11.3 ± 0.8	10.0 ± 0.2	0.16 ± 0.18	
Seward	2.8 ± 1.5	3.2 ± 0.7	2.7 ± 0.2	0.09 ± 0.15	0.54 ± 0.04
Valdez	-2.6 ± 1.4	2.2 ± 0.2	1.66 ± 0.14	0.76 ± 0.14	0.78 ± 0.04

<sup>a</sup>SP91—Savage and Plafker (1991) used a eustatic sea level rise of  $2.4 \pm 0.9$  mm/yr and assumed the effect of post-glacial rebound to be  $0.5 \pm 0.5$  mm/yr.

<sup>b</sup>CF00—Cohen and Freymueller (2001) assumed that the combined effect of eustatic sea level rise and post-glacial rebound is 2 mm/yr.

<sup>c</sup>LET02—Larsen *et al.* (2002) used a eustatic sea level rise of  $1.09 \pm 0.21$  mm/yr.

uplift rates was poor. Some of the postseismic uplift rates were particularly rapid: Kodiak— $17.7 \pm 1.2$  mm/yr, Seldovia— $9.9 \pm 2.3$  mm/yr, and Nikiski— $21.6 \pm 2.0$  mm/yr. The rate at Nikiski is suspect because that tide gauge did not operate between 1984 and 1996; however, the rates at Kodiak and Seldovia are more reliable because they are based on long data sets.

In contrast to sites with rapid uplifts, other sites, such as Anchorage, showed relatively slow motion. At Seward, the post-1973 uplift rate was  $0.0 \pm 2.0$  mm/yr. Presumably, slow vertical movement occurs at Seward because it lies near the transition between subsidence and uplift while the slow uplift at Anchorage is due to its distance from the plate boundary. Savage and Plafker (1991) adjusted the apparent annual sea-level heights by removing fluctuations that were correlated with those at sites in southeastern Alaska, a region not affected by the 1964 earthquake. The removal of the oceanographic signal resulted in a considerable reduction in the interannual noise in sea-level height at some of the tide gauge locations (Fig. 14). Nevertheless, the residuals show an oscillatory signature over the first few years following the earthquake at Anchorage and, to a lesser extent, Seward. Cohen and Freymueller (2001) suggested that this oscillation might be an artifact of the data. They noted that some of the annual sea-level height averages used by Savage and Plafker (1991) were based on an incomplete record of monthly sea-level heights. Since the sea-level height has a strong annual signal, having incomplete monthly data could bias the annual mean. However, Larsen *et al.* (2003) showed that the oscillating signature remains when the analysis is based on monthly rather than annual sea-level heights. Thus, the oscillation may be real, but its cause is not definitively known. Savage and Plafker (1991) suggested a tectonic, rather than oceanographic, basis. Larsen *et al.* (2003) concurred, but neither group of authors offered a mechanism for the behavior. If such an oscillation existed in the years following the earthquake then the leveling results along Turnagain Arm, which lies between Anchorage and Seward, might include this unaccounted for motion.

Savage and Plafker (1991) used the tide gauge data that was available through 1988. Later, Cohen and Freymueller (2001) re-examined the tide gauge data making use of observations extending through another decade, i.e., until the end of 1998. The longer set of observations was critical for recognizing time-dependent changes in the vertical motion at some of tide gauge sites. Even after the annual sea-level heights were corrected for the apparent oceanographic effects, the interannual noise was still quite large and a long set of observations was required in order to extract anything other than a linear trend from the data. Cohen and Freymueller (2001) found that there has been a significant change in the uplift rate near the city of Kodiak. The mean postseismic uplift rate through the end of 1998 was  $16.5 \pm 0.7$  mm/yr,

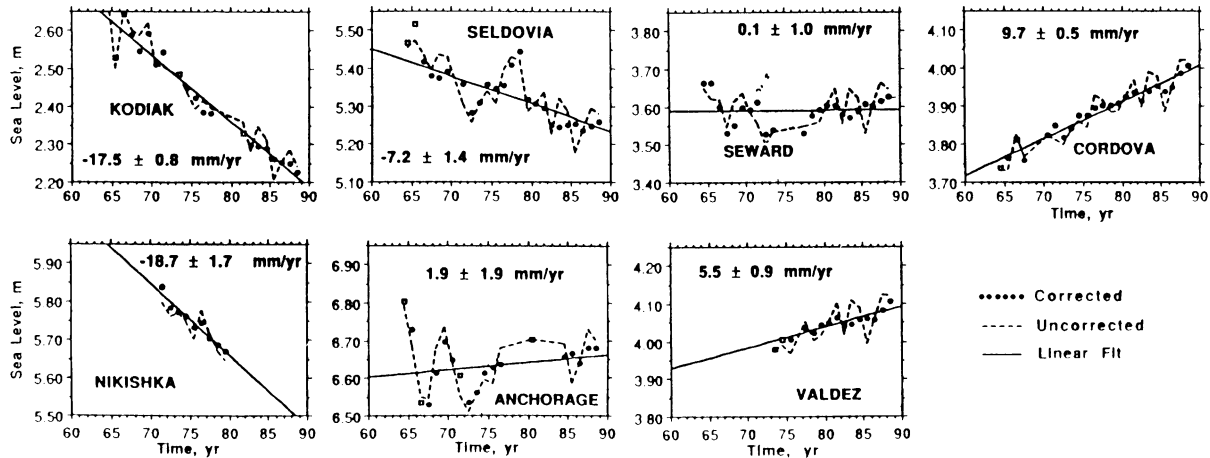


FIG. 14. Apparent sea level heights deduced from southcentral Alaska tide gauges. The data corrected for short-period fluctuations in sea level are shown as solid points. The solid lines show the least squares fit to the corrected data and the dashed lines connect the uncorrected data. The rates deduced from the least squares analysis are also shown. From Savage and Plafker (1991).

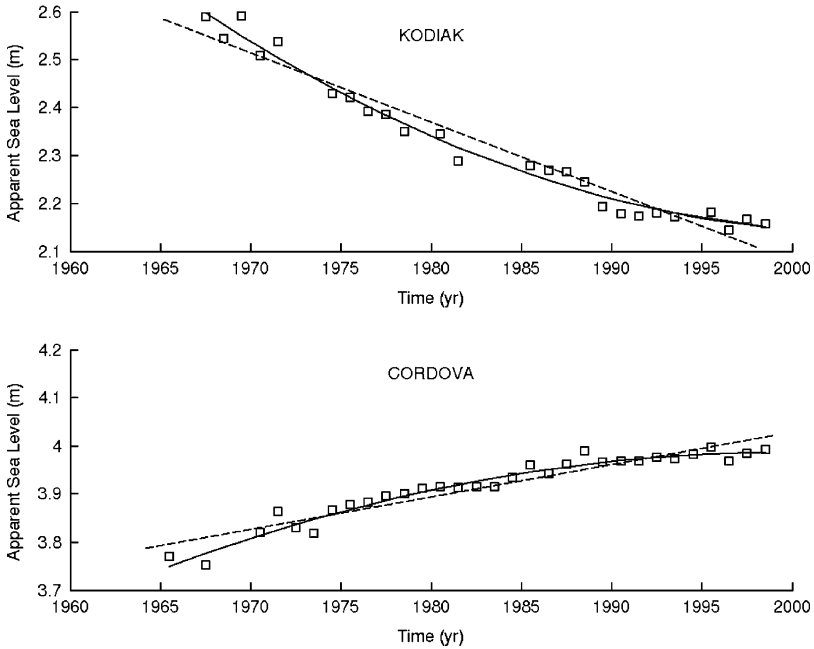


FIG. 15. Apparent sea level heights for the Kodiak and Cordova tide gauge sites. The corrected annual mean data are shown as open squares, the best-fitting straight line by dashes and the best-fitting quadratic polynomial by the solid line. From Cohen and Freymueller (2001).

but the rate changed by  $-0.67 \pm 0.11 \text{ mm/yr}^2$  over the time span of the data (Fig. 15). When taken into account, this rate change of nearly 7 mm/yr per decade brings other observed uplift rates on Kodiak in line with the tide gauge observations. These other observations include VLBI measurements from the late 1980s and early 1990s, recent GPS observations, and a combined analysis of daily tide gauge and Topex-Poseidon sea height observations (S. Nerem, private communication, 2001).

Cohen and Freymueller (2001) used the Kodiak tide gauge data to derive a time constant of about 12 yr for a 50% reduction in the uplift rate from its initial postseismic peak. There is one complicating event in the Kodiak tide gauge history. The measurement site was changed from St Paul Harbor to Women's Bay, a short distance away, in 1984. The repositioning of the tide gauge opens up the possibility that the apparent deceleration in the uplift rate was an artifact of the location change, but this appears not to be the case. The two sites were connected by a leveling survey and the tide gauges were run at the two sites

simultaneously for a couple months to verify that the height record was not distorted by the change. Thus, the change in the time-averaged uplift rate from  $23.1 \pm 1.4$  mm/yr at St Paul Harbor (between 1967 and 1981) to half that,  $10.1 \pm 1.1$  mm/yr, at Women's Bay (1985–1998), appears to reflect a change in the postseismic uplift rate, not a change in measurement location.

Cohen and Freymueller (2001) found that the subsidence rate has decreased at Cordova since the earthquake. The mean vertical displacement rate through 1998 was  $-4.7 \pm 0.4$  mm/yr, while the rate change was  $0.76 \pm 0.14$  mm/yr<sup>2</sup>. About 17 years was required for a 50% reduction in the subsidence rate from its peak value. The qualitative confidence in the reality of the rate change at Cordova is less than for Kodiak because the rate change at Cordova is more dependent on the end points of the time series. In addition, there is corroborating data from sources other than the tide gauge at Kodiak, but not at Cordova. However, the rate change estimate for Cordova did pass statistical testing, namely the *F*-ratio test at 99% probability for a formally meaningful improvement over the constant rate estimate. A rate change may also have occurred at Valdez. The time series at Valdez is shorter than at Kodiak and Cordova, so the results are even less definitive; however, the aforementioned analysis by Larsen *et al.* (2003) also finds a time dependence in the uplift rates at Kodiak, Cordova, and Valdez, but not at Nikiski or Seldovia.

The uplift rate derived by Cohen and Freymueller (2001) for Seldovia was a rather rapid  $11.3 \pm 0.8$  mm/yr, a result consistent with that of Savage and Plafker (1991). While there was no indication of time dependence in this uplift rate, it is unlikely that a rate of about a centimeter per year can be sustained throughout the entire several-hundred-year recurrence period for a great earthquake. For example, with a recurrence period of 750 yr and an uplift rate of 1 cm/yr; the expected coseismic vertical displacement would be about 7.5 m, much larger than the observed coseismic uplift. Thus we speculate, as did Savage and Plafker (1991), that there may be a long term time relaxation of the tide gauge signal at some, if not all, of the tide gauge sites.

The uplift rate at Nikiski as deduced by Cohen and Freymueller (2001),  $11.9 \pm 0.8$  mm/yr, was about half that derived by Savage and Plafker (1991). The Nikiski data used by Savage and Plafker (1991) extended only into the early 1980s, whereas Cohen and Freymueller (2001) also considered data from 1997 and 1998, so the more recently derived rate is probably more reliable as a long-term average.

It is intriguing to note that uplift-rate decay times of a few years were seen in the leveling data collected along Turnagain Arm, i.e., down-dip of the region of large slip. Longer decay times were found from the tide gauges (Cordova and Kodiak) that are located near regions of modest slip at the edges of the coseismic

rupture zone. No rate decay has been observed at Seldovia, a region of small coseismic moment release. The speculation that the decay time might be inversely related to the coseismic stress drop is qualitatively consistent with nonlinear rheological properties of rocks.

Before leaving the discussion of tide gauge data, we should mention that most of the analyses have accounted for the effects of global sea-level rise and post-glacial rebound in only rudimentary fashion. Fortunately, these two signals produce not more than a few mm/yr of relative vertical motion, so detailed models have not been essential. Larsen *et al.* (2003) derived a simple model for vertical motions in Alaska based on data for past and present ice unloading (using, for the most part, data from Arendt *et al.* (2002)). Their model suggests that the uplift from ice melting near the Kenai Peninsula is small. However, for some Earth models, uplift rates of up to several mm/yr occur on the Kenai Peninsula. These result mainly from the large ice unloading in southeast Alaska. This unloading could produce a broad-scale uplift feature across the Kenai Peninsula; however, Larsen *et al.* (2003) find that the tide gauge data are too sparse to improve the Earth model.

### 3.4. Multidecadal Postseismic Uplift Deduced from Comparisons of GPS and Leveling Observations

Some of the geodetic data sets collected in the aftermath of the earthquake have not been used in any studies of crustal motion and others have been used only recently. The leveling profile from Matanuska to Glennallen, for example, has not been systematically resurveyed since immediately after the earthquake. Indeed, many of the survey markers from this profile may not have survived to the present. On the Kenai Peninsula the situation is better. A detailed leveling survey was conducted along the major roads of the Kenai Peninsula shortly after the earthquake. While this leveling survey was tied to that done along Turnagain Arm, no subsequent systematic releveing was performed on the peninsula. In recent years, however, extensive GPS surveys have been conducted in this region. Some of the GPS observations have been made at the surviving leveling marks, while others have been made at sites better suited for GPS techniques. These modern surveys began in 1993 and the survey data have been analyzed jointly with GPS data from along Turnagain Arm and near Anchorage. Additional GPS data have been collected at locations across Cook Inlet from the Kenai Peninsula, on Kodiak Island, and near Valdez, although few, if any, of these observations are tied to historic leveling measurements. It should be noted, however, that even on the Kenai Peninsula, the majority of the historic survey markers are no longer

present or cannot be found, having disappeared due to road construction or other causes.

Usually, the comparison of heights obtained from leveling and GPS is difficult because the two heights are determined in fundamentally different coordinate systems: the orthometric or sea-level height system for leveling and the geometric coordinate system for GPS. However, these two height systems can be connected well enough to determine relative height changes if a high quality, local geoid height model is available (n.b., global geoid height models do not have the spatial resolution necessary to make the transformation). In the Kenai region, gravity observations were made concurrent with the 1964 height observations. In addition, ship surveys in the nearby waters provided additional gravity information. These gravity data were used by the US National Geodetic Survey (Smith and Milbert, 1999) to derive a detailed local geoid height model for Alaska as part of an overall effort to develop a precision geoid height model for the entire United States. The geoid height model has been used to determine relative height changes from a comparison of the recent GPS observations with the 1964 leveling data. In performing such an analysis, one assumes that the time-dependent changes in the relative geoid height are small compared to the crustal movements. The largest source of error in the determination of height changes from this analysis is the uncertainty in the relative geoid height. This uncertainty increases with distance from the local reference. Cohen *et al.* (1995) and Cohen and Freymueller (1997) found that the maximum height change on the Kenai Peninsula from 1964 to the early to mid 1990s, relative to Seward, was approximately 1 m. Seward is an appropriate reference location since, as we reviewed earlier, the tide gauge data indicate that it has only slow vertical movement. Figure 16 shows that the cumulative uplift since 1964 reaches a maximum of around 1 m in the center of the Kenai Peninsula and drops somewhat as one progresses inland to the northwest. Figure 16 is a revision of a figure presented in Cohen and Freymueller (1997) with the figure shown here being based on an updated geoid height model, GEOID99 (Smith and Roman, 2001), and additional data that were not in the older version. The updated model results in a greater consistency in the uplift of the western Kenai Peninsula sites. In addition to showing the uplift at leveling/GPS sites, the figure also shows the uplifts determined at several of the tide gauges discussed earlier. There is excellent agreement between the uplifts estimated from tide gauge data and those deduced from the differenced GPS-leveling observations at Nikiski in the northwest portion of the peninsula. The uplift derived from the tide gauge record at Seldovia appears to be somewhat less than that derived at the GPS-leveling sites observed just to the northeast, but the difference is not great and is consistent with the expected fall-off in uplift with decreasing distance to the trench.

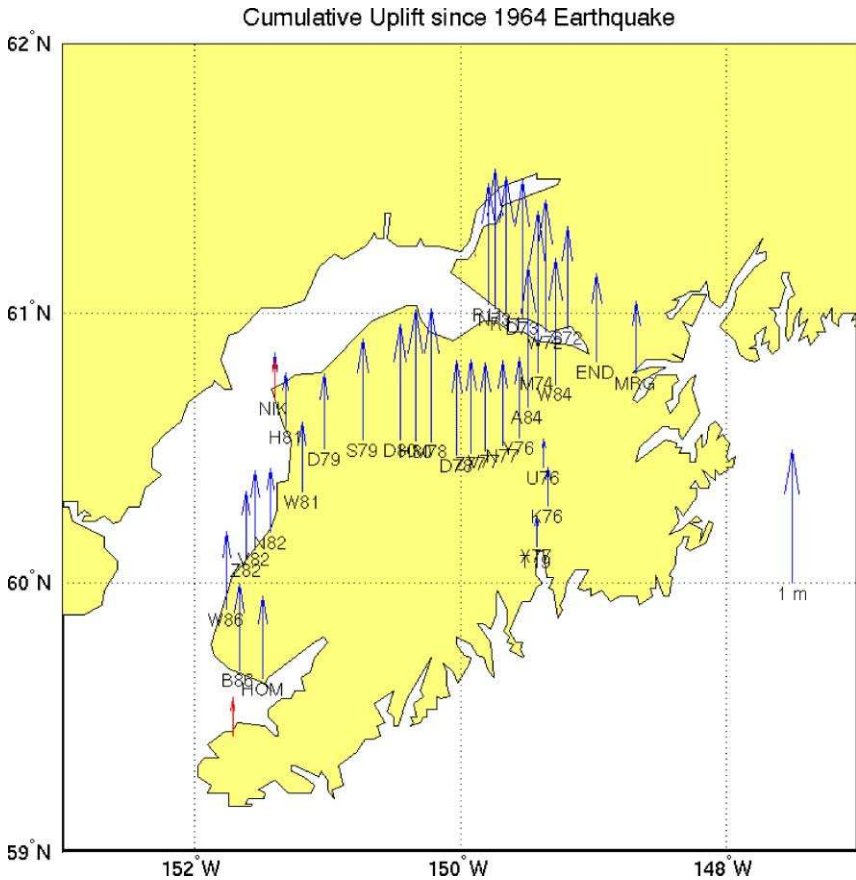


FIG. 16. Uplift since 1964 on Kenai Peninsula and adjacent areas. The uplift is plotted relative to tide gauge station T19 at Seward ( $60^{\circ}07'43''\text{N}$ ,  $149^{\circ}25'43''\text{W}$ ). The red arrows show the uplift as determined from tide gauge observations, the blue arrows show the uplift determined by comparing post-earthquake leveling height observations to contemporary GPS vertical position determinations (using relative geoid heights from the GEOID99 model to transform between the orthometric and geometric coordinate systems). Although there are both random and systematic measurement errors in both the leveling and the GPS measurements, the uncertainty in the deduced uplift is dominated by the poorly known baseline-length-dependent error in the relative geoid height. Thus, the uplift of sites close to Seward are better constrained than those farther away.

Along Turnagain Arm the uplift exceeds 1 m at several locations. Although the greater-than-1 m uplift deduced along Turnagain Arm is consistent with the uplift derived on the Kenai Peninsula, the uplift would have to decrease steeply to the northwest to be consistent with the nearly zero uplift at the Anchorage tide gauge location. The uplifts along Turnagain Arm are derived, in part, by connecting leveling lines observed in 1964 on the Kenai Peninsula and along Turnagain Arm with the connection done at a site observed in both surveys. Specifically, the height derived for the common site from the least squares adjustment of the Kenai data was held fixed in the adjustment of the Turnagain Arm profile. Therefore, we cannot exclude the possibility that there is a significant bias in the uplift profile along the Turnagain Arm. More work is needed to determine whether the bias exists and, if it does, whether it is associated with an error in the geoid height model. Also the cumulative uplifts derived by comparing relatively recent observations with ones made shortly after the earthquake could be affected by oscillatory motions such as those observed at the Seward and Anchorage tide gauges if those oscillations were due to crustal movement. However, the peak cumulative uplift amplitudes well exceed any oscillation seen in the tide gauge signal.

VLBI observations conducted in the mid-late 1980s were the first systematic measurements of horizontal motion in southcentral Alaska made using space-geodetic techniques. Ma *et al.* (1990) deduced that the motion of the VLBI site on Kodiak Island, near the city of Kodiak, was  $11.7 \pm 1.0$  mm/yr at an azimuth of  $315 \pm 5^\circ$  in a North America-fixed reference frame. They also deduced that Sourdough, a site located at  $63^\circ 40'N$ ,  $146^\circ 29'W$  or somewhat less than 300 km north-northwest of Valdez, was moving not more than  $\sim 5$  mm/yr relative to the interior of North America.

### 3.5. Contemporary GPS Observations of Crustal Motion: Spatial and Temporal Variability

The advent of GPS technology has resulted in an extensive set of geodetic observations made through the 1990s and into the 2000s. Freymueller *et al.* (2000) reported on GPS observations made at the aforementioned leveling locations on the Kenai Peninsula and at a number of the newer sites better suited to GPS measurements. Their observations have been combined with those of Savage *et al.* (1998) who examined a profile that extended further toward the trench and further inland than the Kenai network, but had less range along-strike. The pattern of horizontal crustal deformation is shown in Fig. 17. The figure shows an intriguing along-strike variation in the crustal deformation, specifically,

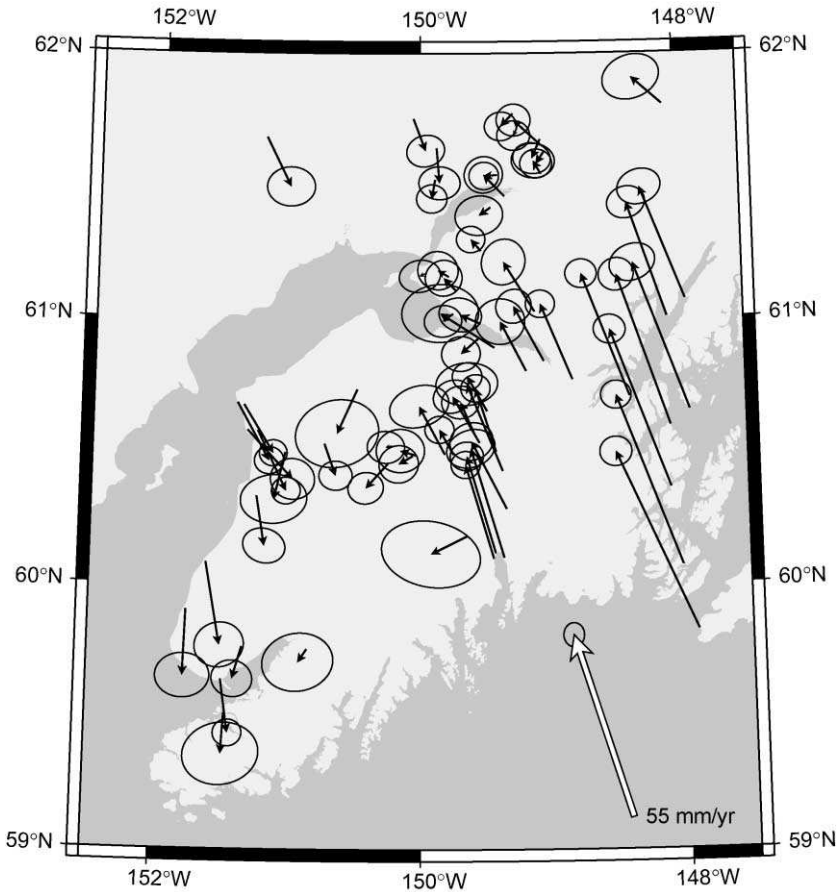


FIG. 17. Horizontal crustal velocities as deduced from GPS observations made in the middle and late 1990s on the Kenai Peninsula and surrounding areas (The figure is based on Zweck *et al.* (2002) and includes data from several research groups).

a difference between the direction of motion on the eastern and western sides of the Kenai Peninsula. The velocities on the eastern side were consistent with strain accumulation along a shallow locked plate interface. The velocities were oriented north–northwest in accord with the N17°W direction of the Pacific Plate relative to North America in this region (Zweck *et al.*, 2002). The velocities decreased with distance from the trench. The maximum velocity observed was  $\sim 57$  mm/yr at site MOTG, located  $\sim 150$  km from the trench. The velocity decreased to

~32 mm/yr near Seward and to ~10 mm/yr at ~300 km from the trench. The exception to the general trend was a relatively low horizontal velocity of about 30 mm/yr at Middleton Island (MIDD). This site is located about 90 km from the trench, presumably over a region where the subducting Pacific Plate is very shallow and not strongly coupled to the overriding North America Plate (MIDD also displayed an atypically large vertical velocity of ~20 mm/yr possibly due to continuous slip on a local fault branching upward from the megathrust). Surprisingly the velocities of sites located on the western side of the Kenai Peninsula were oriented in almost the opposite direction to those of the eastern side, indicating trenchward movement relative to stable North America. The magnitudes were large, exceeding 20 mm/yr at several locations. The trenchward velocities of the western Kenai sites are not compatible with a model of a locked shallow plate boundary. This finding suggests that the coupling between the overriding North America Plate and subducting Pacific Plate is small in the western Kenai Peninsula, a contrast to strong coupling nearer to PWS. However, the observed velocity variations are empirical facts, whereas the inferences about coupling depend somewhat on the model.

The contrasting behavior between the eastern and western Kenai Peninsula velocities mirrors in some ways the differences in the coseismic moment release seen along the up-dip extensions of the eastern and western Kenai Peninsula regions. Large coseismic displacements occurred on the eastern Kenai Peninsula as part of the rupture of the PWS asperity, as previously mentioned. When we discuss the details of deformation modeling later in this article, we will say more about the interpretation of the contemporary crustal movements observed in the vicinity of the Kenai Peninsula.

The contemporary crustal deformation across the Aleutian subduction zone near Kodiak has been studied by Savage *et al.* (1999) using GPS techniques. At distances of about 106 km to about 250 km from the trench, observed velocities decrease with distance from the trench (see also Zweck *et al.*, 2002). The magnitudes, relative to stable North America, decrease from about 35 mm/yr for a site on Chirikof Island, southwest of Kodiak Island (see also Fletcher *et al.*, 2001) to about 7 mm/yr for site KARL on the western side of Kodiak Island (Fig. 18). Savage *et al.* (1999) showed that these data fit an elastic dislocation model if the displacements are considered relative to Kodiak city. The more recent Zweck *et al.* (2002) model considers the velocities relative to the North America plate and includes some additional features. For example, sites located 250–375 km from the trench on the Alaska Peninsula move trenchward, a behavior that is once again inconsistent with the model of a locked plate interface. In addition, there is an along-strike variation in velocities of sites on the Pacific coast of Kodiak Island. Neither the Savage *et al.* (1999) nor Zweck *et al.* (2002) model allows

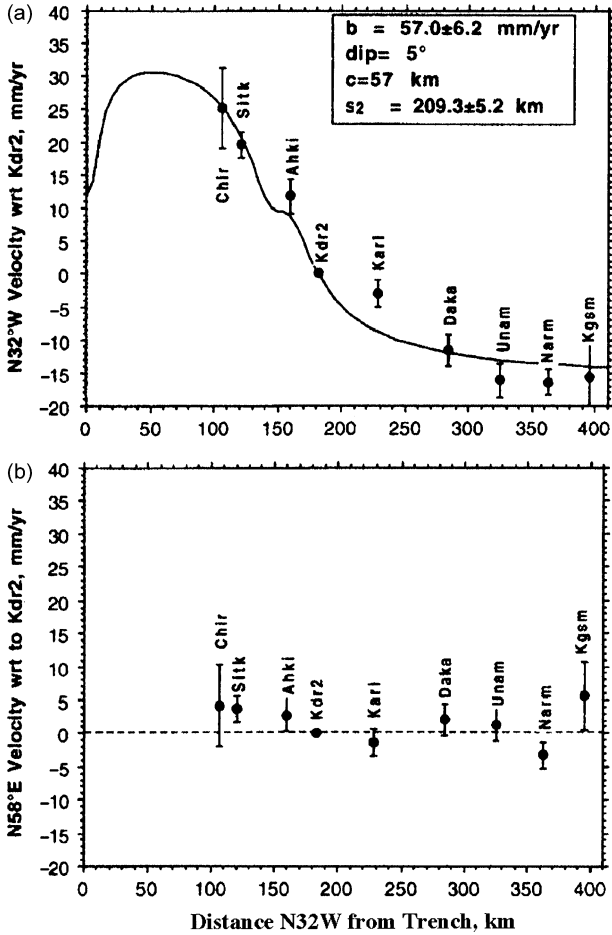


FIG. 18. Velocity profiles in the Katmai–Kodiak Island region relative to site Kdr2 (on Kodiak Island) as a function of the distance N32°W from the trench. The error bars are two standard deviations. The upper panel shows the trench normal velocities (i.e., in the N32°W direction), while the lower panel shows the trench parallel velocities. The curve in the upper panel is the computed relative displacement using elastic dislocation theory with the following parameters: relative plate velocity,  $b = 57$  mm/yr, dip angle =  $5^\circ$ , horizontal distance from the trench to the point above the up-dip end of the locked plate interface,  $c = 57$  km, length of locked plate interface,  $s_2$ , 209.3 km. Although the sites are shown as a function of distance from the trench there are considerable along-strike variations in their locations as well. Chir is on Chirikof Island, well southwest of Kodiak Island (KI), Sitk is on Sitkinak Island, slightly southwest of KI, Ahkl and Kdr2 are near the trenchward shore of KI, Karl is on the far shore of KI, and Daka, Unam, Narm, and Kgs m are on the Alaska Peninsula, across Shelikof Strait from KI. From Savage *et al.* (1999).

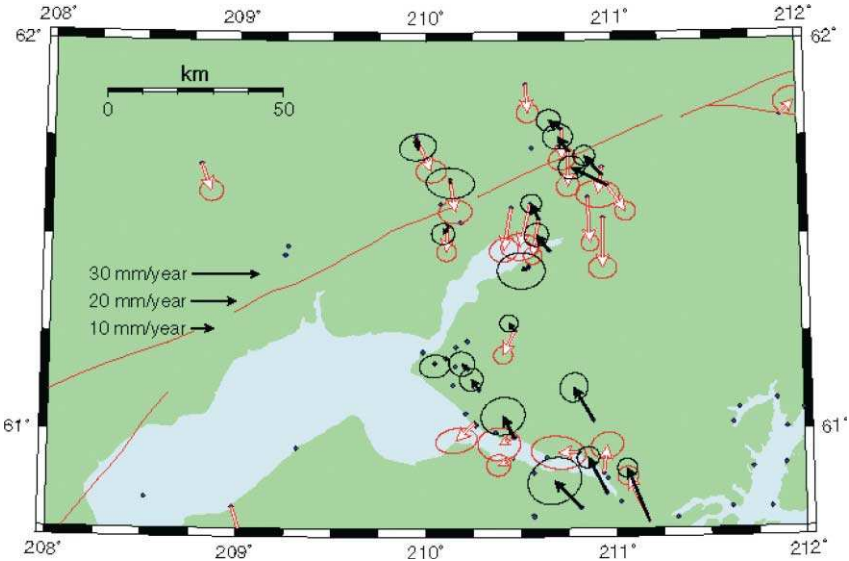


FIG. 19. Change in velocities near Anchorage as reported by Freymueller *et al.* (2001). The solid black vectors show GPS-derived velocities, relative to North America before 1998; the open red vectors show velocities from 1998 to 2001.

the deformation rates on Kodiak Island to vary with time, although such a possibility is indicated by the aforementioned tide gauge observations.

Recent observations of crustal movement north of Anchorage have revealed another large-amplitude, transient phenomenon (Fig. 19) several decades after the earthquake. From about 1995 to late 1997 or early 1998, the crustal velocities near Anchorage were consistent with velocities on the eastern Kenai Peninsula as determined from GPS observations (Freymueller *et al.*, 2001). They were oriented in a north to north–northwest direction relative to interior Alaska with magnitudes reflecting the decrease in crustal velocity with distance from the trench. However, the velocities derived from data collected between 1998 and 2001 were in the opposite direction and resembled those on the western Kenai Peninsula. The change in surface velocities had magnitudes as large as 25 mm/yr and were apparently due to slip on the plate interface at a depth of  $\sim 35$  km. Freymueller *et al.* (2001) have called this phenomenon “The Great Alaska ‘Earthquake’ of 1998–2001” because the rate and duration of the fault slip appears to be greater than that geodetically observed in similar aseismic slip events elsewhere. This event lasted longer than other

recently observed subduction zone transients. It also differs in that it represents an acceleration of slip on a portion of the plate interface that was already slipping prior to the event.

Some words of caution are needed about comparing velocity plots provided by different workers. In the several velocity plots shown above there are ambiguities in the site locations relative to the trench. These ambiguities are associated with interpreting the location and strike of the trench. For example, Savage *et al.* (1998) plot the aforementioned MOTG site at 145–150 km from the trench, whereas Freymueller *et al.* (2000) plot the same site at about 170 km from the trench. When we compare data to model predictions another ambiguity arises. The model parameterization often involves adopting a constant value for the dip angle of the subducting slab over a considerable range of distances from the trench. Of course, the actual dip angle varies with location, albeit slowly in the shallow portions of the subduction zone. Thus, there is an uncertainty in the location of model distances relative to actual distance from the trench.

In addition to the uncertainty in the location of various points relative to the trench and to model origins, there are also some systematic differences in the data analysis, particularly for vertical motion. Freymueller *et al.* (2000) found consistently greater uplift rates than did Savage *et al.* (1998). The differences approach 10 mm/yr in some cases. For the most part these differences are due to reference frame issues and seem to have been largely resolved by careful consideration of these coordinate system matters. Recent work on vertical GPS velocities (Chris Larsen, private communication) show that Freymueller *et al.* (2000) overestimated vertical velocities because they tied their reference frame to North America through site FAIR in Fairbanks rather than defining North America motion through an ensemble of International Terrestrial Reference Frame velocities. There is far better consistency from analyst-to-analyst in the horizontal velocities than the vertical ones, as is typically the case.

#### 4. MODELS OF SOUTHCENTRAL ALASKA PRESEISMIC AND POSTSEISMIC CRUSTAL DEFORMATION

In the preceding sections we have focused on the geodetic measurements themselves and direct inferences from those measurements that do not depend strongly on specific model assumptions. This is not to say that model assumptions have not entered either implicitly or explicitly into the results we reviewed. Indeed, a variety of geophysical models are often required in order to reduce the raw observations of geodetic data. Many of these models are needed to convert the actual measurement observables, such as the time a signal is received from a

GPS satellite or the height observed on a measuring rod, into geodetic quantities such as 3-D positions. Such models include those for solid earth tides, atmospheric and ionospheric propagation, relativistic effects, and various forcings on the orbits of the GPS satellites. Other models are needed to infer geophysically significant parameters from the geodetic quantities. For example, estimating coseismic slip requires a model of the subduction zone geometry. This geometry is often constrained by seismic inferences that depend on other model assumptions.

In the present section our focus is on models used in interpreting geodetic observations rather than performing data reduction. For example, models of the coseismic motion led to the idea that shallow thrust, subduction zone earthquakes are a key component of plate tectonics, as we have already noted. Here we consider the postseismic and interseismic motion as well. Elastic rebound theory has helped explain several aspects of the deformation cycle and attempts have been made (with not entirely satisfactory results) to combine elastic rebound theory with plate bending theory as in Rosenbaum (1974). An important point to remember when considering both the models of crustal deformation and the data they seek to explain is that coseismic and interseismic displacements are often oppositely directed and of nearly equal magnitude when considered over several, or even a single earthquake, cycle. Since long-term geologic deformation is the cumulative result of these and other motions (such as glacial rebound), it usually develops at a much slower rate than short-term indicators would suggest.

In modeling strain accumulation, the most commonly employed model is that of a locked fault plane embedded in either an elastic half-space or layered elastic–viscoelastic half-space. A conventional method for modeling the accumulation of strain is to conceptually decompose the driving motion into two terms, each associated with slip along the plate interface (Savage and Prescott, 1978; Savage, 1983). The first term is due to steady-state, i.e., constant velocity, fault-slip, rigid block translation, and no stress or strain accumulation. The second term is cyclic and consists of two parts: the response to virtual backward slip along the locked portion of the megathrust between earthquakes and the response to forward slip (usually along the same segment of the megathrust) during the earthquake. This cyclic term drives the crustal deformation. Although this conceptual decomposition has been applied to both elastic and viscoelastic models, it is particularly simple in the former case because there are analytical solutions for different types of dislocations embedded in an elastic half-space. The simple model is often made more sophisticated by considering complexities in the fault geometry, the finite thickness of the subducting and overriding plates, and strain accumulation and/or slip on subsidiary faults. Another method employed in modeling strain

accumulation between earthquakes is to mathematically lock the shallow portions of the plate interface together but allow for free slip below the locked patch. The strain accumulation is driven by imposing velocity constraints on the sides of the model, along the plate–asthenosphere interfaces, and/or along the bottom of the model. Although this approach incorporates a realistic representation of the kinematics of plate boundary deformation, in practice it is not always the easiest model to implement. In addition, there is a variety of questions about the best choices for lithospheric basal boundary conditions. Elastic dislocation calculations that are based on closed-form analytical solutions are usually based on the backslip model, but finite element calculations can employ either approach.

For calculating transient postseismic deformation, two competing models are often investigated. One invokes deep fault creep as the driver of postseismic surface motion and the other invokes viscoelastic flow at depth. The differences between the physics of these two models are discussed in considerable detail in Cohen (1999). Here, we just summarize a few salient features. When an earthquake ruptures through a finite portion of the lithosphere, there is a sudden change in the stress field in the surrounding medium. The release of stress in the upper layers of the crust and mantle is accompanied by an increase in stress below. There are several possible responses of the Earth to this stress redistribution. One response is for a portion of the fault plane lying down-dip of the coseismic rupture to slip aseismically in order to relieve the stress imposed across it. Typically, the surface deformation due to this process is computed by considering slip on a buried fault in an elastic half-space, although the half-space need not have spatially uniform elastic properties. Another response is for ductile flow to occur in portions of the lower crust and/or mantle, with the depth of this flow depending on temperature, pressure, and rock type. The ductile flow couples back to the overlying elastic layer, causing both surface and subsurface deformation. In postseismic rebound studies the ductile flow is usually modeled as a viscoelastic process with the strain rate proportional to stress (linear viscoelastic flow) or a power of stress (non-linear, power law flow). The viscous properties are temperature-dependent and, therefore, can vary greatly with depth, although the majority of the models considered so far use a single value for the viscosity. Creep-at-depth and viscoelastic flow are not the only processes that can produce significant postseismic deformation. Some other candidates include surface aftercreep and poroelasticity. In addition, the complex fault rheology implied by state-dependent friction laws can produce both stable and unstable slip responses to stressing.

In trying to interpret the uplift observed along the Turnagain Arm, Brown *et al.* (1977) considered several physical mechanisms: creep on a buried fault,

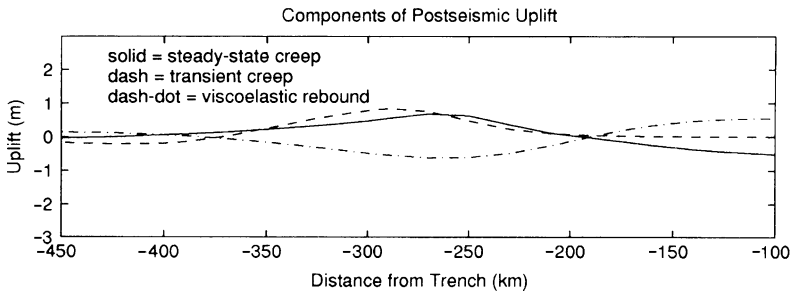
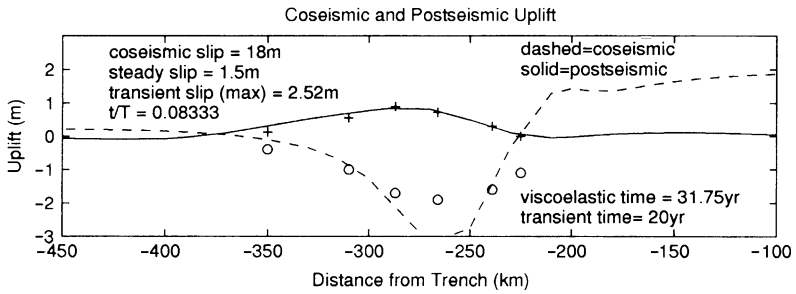
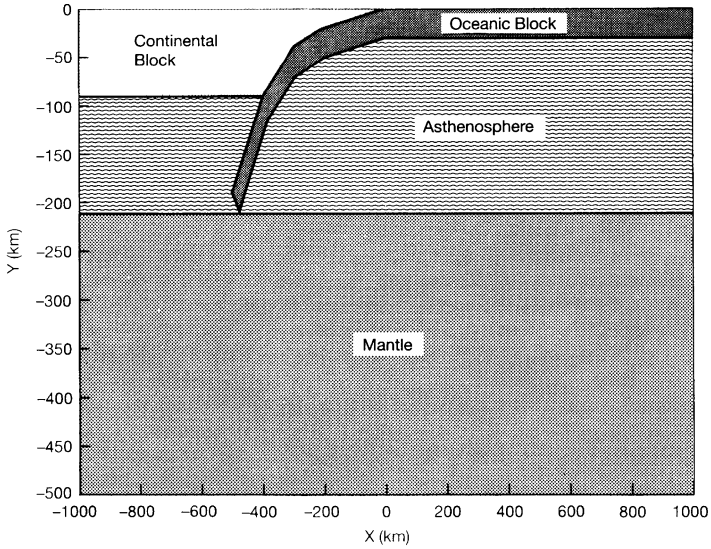
viscoelastic flow, strain accumulation on the megathrust due to the continuing convergence between the North America and Pacific Plates, strain accumulation on a subsidiary fault, subsurface magmatic activity, and dilatancy effects. They concluded that the latter two mechanisms did not offer a viable explanation for the observed uplift, but that buried slip, viscoelastic rebound, and strain accumulation on the megathrust were realistic possibilities. Given the rate of plate convergence, they argued that strain accumulation, by itself, could not explain the bulk of the postseismic uplift; it certainly cannot explain the time dependence of the uplift. However, Brown *et al.* (1977) found that down-dip creep on the megathrust, amounting to a couple meters slip between 1964 and 1975, offers a satisfactory explanation for the observed uplift. At least part of the deep slip region might be on that portion of the plate interface that did not rupture during the earthquake, but lies above the aforementioned thermally allowed down-dip limit to the locking depth. Viscoelastic flow could not be entirely excluded as an alternative explanation. However, this mechanism was less satisfactory to Brown *et al.* (1977) because they could not find seismic wave attenuation evidence for a viscosity consistent with the  $\sim 5$  yr relaxation time observed in the uplift rates.

In contrast to Brown *et al.* (1977), Wahr and Wyss (1980) argued that a viscoelastic model did provide a good explanation for the uplift observed after three Alaska-Aleutian earthquakes (the 1964 PWS earthquake, an event in the central Aleutians in 1957 and another in the western Aleutians in 1965). They chose a Maxwell relaxation time,  $\tau = \eta/\mu = 1$  yr, where  $\eta$  is the viscosity of the viscoelastic material and  $\mu$  the material's rigidity. The novel aspect of their model is that the viscoelastic material was placed in a rectangular inclusion in the overthrust block adjacent to an unlocked portion of the plate interface rather than in a horizontal layer, the asthenosphere. In the case of the 1964 earthquake, the inclusion was taken to be 40 km wide and 60 km high, extending from 20 to 80 km depth. The required inclusion appears to be more than 400 km from the trench and would lie about 25 km north of Anchorage. One objection to this model is that the location of the inclusion does not coincide with existing volcanic features, the most likely sites for viscoelastic flow. A somewhat lesser difficulty is that a Maxwell time of 1 yr implies a very low viscosity of about  $10^{18}$  Pa s. Such a low value seems unlikely but could, perhaps, be reconciled with rock mechanics if the effects of a power law rheology and the large stress change associated with an earthquake are considered or flow is governed by the transient response of a composite viscous material in the lower crust (Ivins, 1996). Cohen (1996) considered both elastic afterslip, viscoelastic rebound in a low-viscosity layer, and a combination of the two processes as a mechanism for the observed uplift on the Kenai Peninsula. The simplest model that was consistent with the

data was a pure afterslip model. By contrast, a purely viscoelastic model was not very successful because the predicted behavior either: (1) failed to fit the contemporary observations or (2) gave unrealistically large uplifts later in the earthquake cycle. A combined model involving both afterslip and viscoelastic flow did provide an adequate explanation for the data. The required afterslip was greater than that required in the purely elastic model because the slip had to be sufficient both to compensate for the subsidence produced by viscoelastic flow and to produce the observed vertical upward motion (Fig. 20).

Lundgren *et al.* (1995) published a finite element, elastic, spherical shell model of crustal deformation in Alaska. The boundary conditions and constraints they imposed on the model were selected fault orientations and slip rates and baseline rates of change derived from VLBI observations at Nome, Fairbanks (Gilcreek), Sourdough, Alaska and Whitehorse, Canada. Many of the parameters of their model would probably be revised if the analysis were to be repeated today since contemporary geodetic observations (Fletcher and Freymueller, 1999; Fletcher, 2002; Fletcher and Freymueller, 2003), as well as new geological information, have provided a wealth of constraints not available to the earlier workers. In particular, the new geodetic observations show that the motion of the Yakutat block is significantly different from that of the Pacific plate. Lundgren *et al.* (1995) assumed that the Yakutat block moved with the Pacific plate, which caused their model to predict substantial contraction across the strike-slip Fairweather fault and inboard of it. However, the study was noteworthy as one of the earlier attempts to integrate space geodetic data and geologic data into a mutually consistent model of crustal deformation in Alaska.

Piersanti *et al.* (1997) considered the effects of viscoelastic rebound to the 1964 earthquake on VLBI measurements between a site near Fairbanks in central Alaska and Whitehorse in northwestern Canada as well as with several other sites in Alaska, specifically Nome on the west coast, Kodiak Island, Sand Point, in the central Aleutians west of the rupture, Yakataga, in southcentral Alaska, east of the rupture zone, and at Sourdough, also in the interior of Alaska. Their model employed a spherical Earth geometry and a 200 km-thick, low-viscosity channel with viscosities in the range  $10^{19}$ – $10^{20}$  Pa s. The computed rates of change in the lengths and transverse components of the relative position vectors, for the mid-to-late 1980 time frame, ranged from 0.1 to as much as 9 mm/yr. The observed velocities were generally of the same magnitude, but overall the agreement between the predicted and observed velocities was not particularly good. The model calculations assumed an overly steep dip angle of  $20^\circ$  for the coseismic rupture plane. This model also placed the fault at much greater depths than indicated by the most reliable studies of the PWS earthquake. Other model



parameters are also somewhat questionable in view of what is now known both about the geometry of the interface and the parameters of the earthquake.

The contemporary horizontal crustal velocities observed in the vicinity of the Kenai Peninsula and Kodiak Island have been discussed in the previous section. The northwesterly oriented crustal velocities on the eastern portions of the Kenai Peninsula and in the Kodiak-Katmai region have been analyzed using conventional elastic dislocation models of strain accumulation on the shallow locked portion of the plate interface. For example, Freymueller *et al.* (2000) experimented with several different models. In the first, the locked plate interface was represented by a single plane. In this model the dip angle was set to  $3^\circ$ , a value derived from seismological observations. The adjusted parameters of the model are the down-dip end of the locked interface and the back-slip velocity. In the second model, the dip-angle was also adjusted. In the third model, postseismic creep was permitted on a deep segment of the interface. The parameters of the three models are given in Table 2 and the comparison between observed and computed velocities for the models is shown in Fig. 21. Taken as a whole, the models provide a satisfactory fit to the horizontal velocity data, but are less successful in explaining the vertical data.

Savage *et al.* (1998) also used an elastic dislocation model to explain the northwestward motion of the sites observed across the central portion of the 1964 rupture zone (Fig. 22). They used a back-slip velocity of 65 mm/yr instead of the plate convergence rate of about 55 mm/yr in an attempt to account for a long-term transient response to the earthquake. It is not clear to what extent the higher-than-plate-velocity convergence rate would be required in a fully 3-D model that also took into account the very shallow dip angle of the plate interface at shallow depths.

As mentioned earlier, the trenchward motion of sites on the western Kenai Peninsula cannot be explained by any simple model of strain accumulation along a locked plate interface. Freymueller *et al.* (2000) suggested that the difference between the north–northwest motion of the eastern side of the Kenai Peninsula

---

FIG. 20. (Top panel): a schematic representation of a viscoelastic model used in finite element calculations of crustal deformation. The subducting and overthrust plates are elastic; the asthenosphere is viscoelastic. For the calculations in this figure, the asthenosphere extends to great depth, but in other calculations it is underlain by an elastic or higher viscosity mantle. (Middle panel): cumulative postseismic uplift (solid line) on the Kenai Peninsula from 1964 to 1993 predicted by a combined deep transient creep-viscoelastic rebound model. The dashed line shows the predicted coseismic subsidence while the plus signs and circles give the measured uplift reported in Cohen *et al.* (1995) and the coseismic subsidence from the model of Holdahl and Sauber (1994), respectively. (Bottom panel): contributions to the predicted postseismic uplift from steady plate convergence, viscoelastic rebound, and transient creep. From Cohen (1996).

TABLE 2. Parameters for the Eastern Kenai Deformation Models of Freymueller *et al.* (2000)

Model	Dip <sub>1</sub> (deg)	Width <sub>1</sub> (km)	$\alpha_1$	Ext (km)	Dip <sub>2</sub> (deg)	Width <sub>2</sub> (km)	$\alpha_2$	$\chi_v^2$
1 locked interface plane with dip angle fixed	3.5	297.07	-1.0					2.919
1 locked interface plane with dip angle estimated	1.998	272.46	-1.0					2.318
1 locked interface plane and 1 post-seismic slip plane with rake estimated	5.518	273.67	-0.972	43.36	44.94	399.80	1.21ds, 0.19ss	1.978

The parameter, dip<sub>1</sub>, is the dip angle of the locked plate interface, width<sub>1</sub> is the along-dip width of the locked portion of the plate interface, ext is the width of the gap between the locked plate interface and a postseismically creeping portion of the plate interface, dip<sub>2</sub> is the dip angle of the postseismic creep plane, and  $\chi_v^2$  is the reduced chi-squared fit between the model and observation velocities. In the third model, ds indicates the dip-slip component and ss, the strike-slip component. The  $\alpha$  parameters are multiplicative factors for the plate velocity that describe the inferred steady-state slip. Negative values indicate back-slip, a proxy for a fully ( $\alpha = 1$  or partially ( $-1 < \alpha < 0$ ) locked plate interface. A value of  $\alpha = 0$  indicates no slip, or an uncoupled plate boundary, and a positive value for  $\alpha$  indicates forward slip due, for example, to postseismic creep or episodic aseismic slip. The subscripts on  $\alpha$  are analogous to that for dip and width.

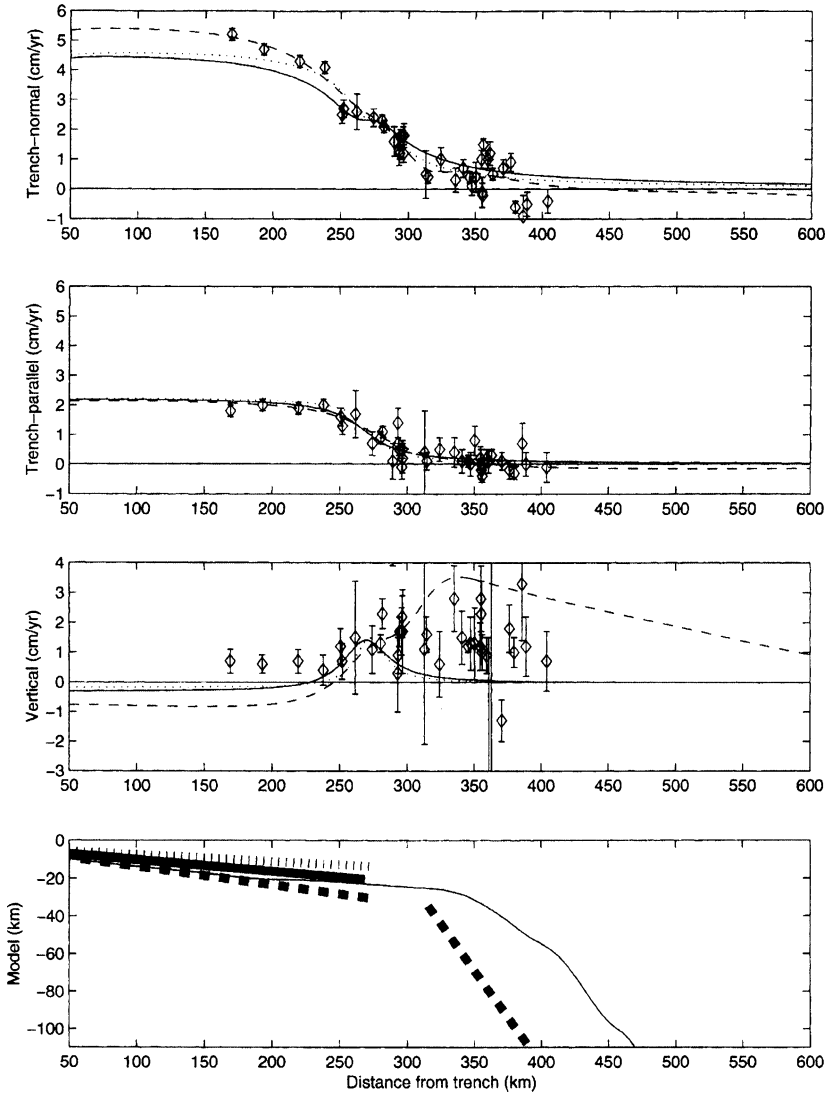


FIG. 21. Elastic dislocation models for eastern Kenai Peninsula. The solid curve is the best fitting model with dip constrained to match the inferred slab position, the dotted curve is the best fitting model with the dip angle estimated, and the dashed model is the best fitting model that includes both strain accumulation and postseismic creep-at-depth. For the latter model, the dip angle of the shallow plane was fixed. The parameters for these three models are shown in Table 2. From Freymueller *et al.* (2000).

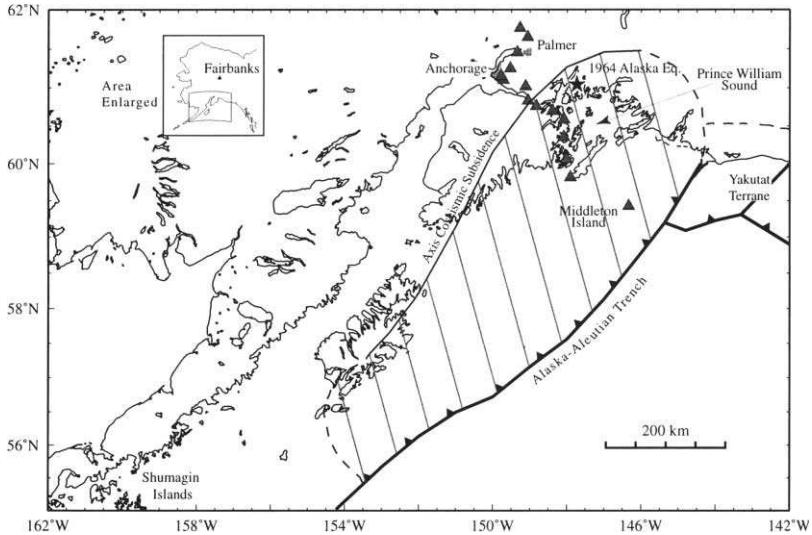


FIG. 22. The top panel shows a network of campaign GPS sites in southcentral Alaska. The horizontal and vertical velocities derived from observations at these sites are shown in the middle panels while the bottom panel shows a schematic sketch of the plate interface geometry used in an elastic dislocation calculation (whose results are shown as solid lines in the data panels). From Savage *et al.* (1998).

and the southwest motion on the west (relative to North America) reflects short wavelength variability in plate coupling with strong coupling in the east and weak coupling in the west. An intriguing possibility is that the coupling varies not only spatially, but also temporally, reflecting a diffusive or propagating phenomenon at depth.

Zweck *et al.* (2002) extended the previous 2-D inversion analysis of the GPS data to three dimensions and included a larger GPS data set. They estimated the spatial distribution of the coupling coefficient between the Pacific and North America plate by inverting crustal velocities for over 200 GPS sites in southcentral Alaska, with most of them being located on or near the Kenai Peninsula, PWS, Kodiak Island and portions of the Alaska Peninsula. They found the plates to be strongly coupled at the PWS and Kodiak asperities (Fig. 23) and weakly coupled in between, in agreement with the previous paragraph. They also suggested that ongoing reverse slip at a rate of 80–100 mm/yr at depths of 30–40 km is responsible for the observed trenchward motion on the western side of the Kenai Peninsula. The same mechanism may also be responsible for trenchward velocities on the Alaska Peninsula near Kodiak Island. In their analysis of the Kodiak data discussed in the previous section, Savage *et al.* (1999)

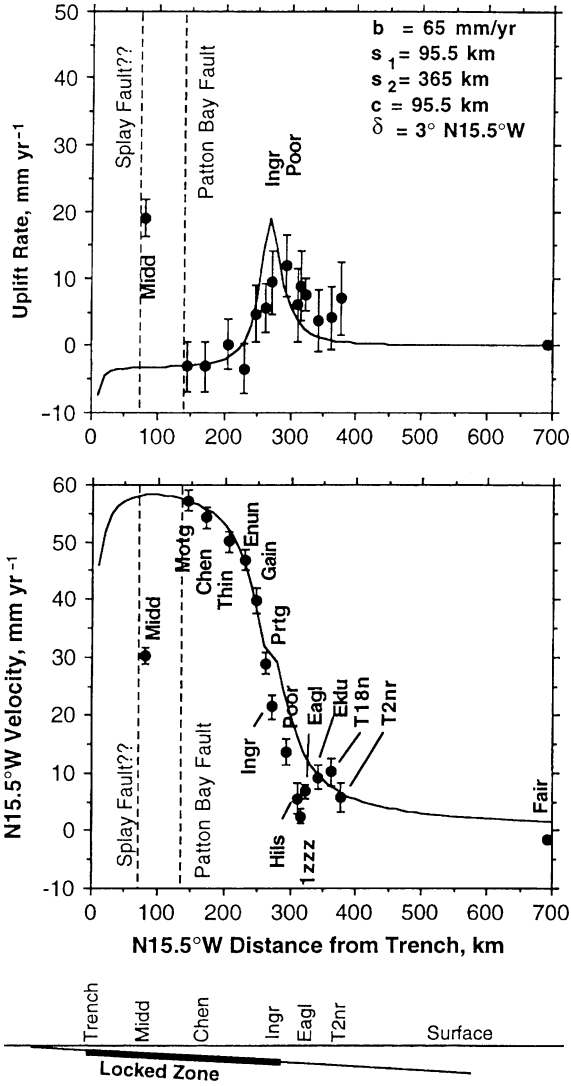


FIG. 22. Continued.

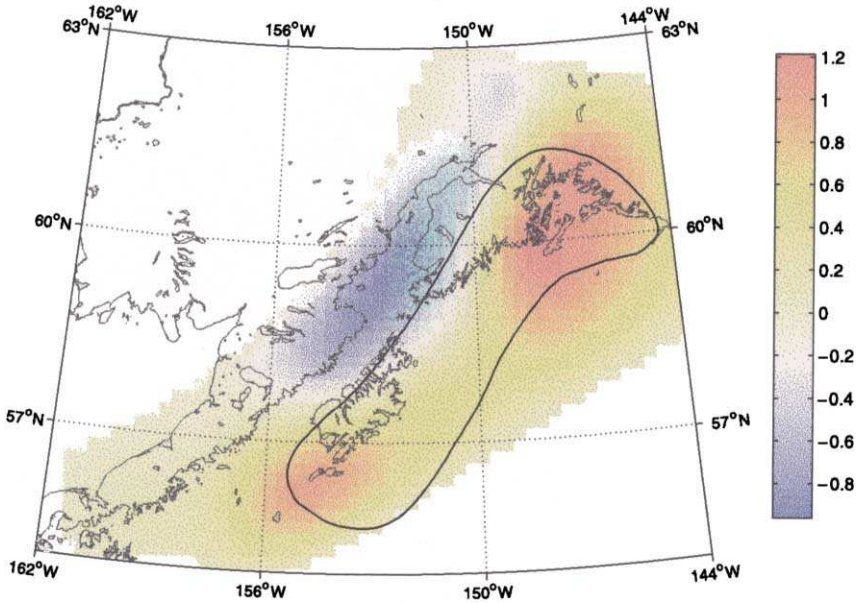


FIG. 23. Spatial variation in plate coupling as derived from inversion of an elastic model. The color coded parameter,  $a$ , is defined by setting the slip on the plate interface to be  $(1 - a)V$  where  $V$  is the relative plate velocity. Thus  $a$  is defined somewhat differently than  $\alpha$  in Table 2. When  $a = 1$ , there is full coupling; when  $a = 0$ , the plates are uncoupled; and when  $a$  is negative, the surface velocities are trenchward. From Zweck *et al.* (2002).

inferred that the shallow plate interface beneath and offshore of southwestern Kodiak Island is strongly coupled. However, Zweck *et al.* (2002) attributed the trenchward motion of sites arcward of the city of Kodiak, and the along-strike variations in deformation to continuing postseismic deformation following the 1964 earthquake.

Bird (1996) developed a 2-D finite element model of the Alaska-Bering Sea region that included variable crust and lithospheric thickness, heat flow, and many plate boundary and interior faults. He studied 46 variants of the model to investigate the effects of shear traction on the megathrust, fault friction, internal friction of lithospheric blocks and mantle creep strength. He concluded that both fault friction and driving traction on the Aleutian megathrust are low. He also concluded that the present neotectonic regime is a transient response to Plio-Pleistocene glacial mass redistribution and differs from typical tectonic flow in the Tertiary. The model predictions cannot be tested against southcentral Alaska

geodetic observations because only long term, not cyclic deformations are considered.

## 5. SUMMARY

The crustal deformation in southcentral Alaska is remarkable in several ways. In the 1964 earthquake there was  $\sim 25$  m of horizontal coseismic motion, in the year after the earthquake there was  $\sim 150$  mm/yr relative uplift, in the four decades following the earthquake there was over 1 m cumulative uplift. Progressing from east to west across the Kenai Peninsula, one finds  $\sim 180^\circ$  rotations in the contemporary velocity vectors. There were temporal reversals in the velocity vector orientations near Anchorage in the late 1990s. Thus, the theme that emerges from studies of crustal deformation for the PWS earthquake zone is one of temporal and spatial variability. Although there is much still to be learned about the mechanisms responsible for the time-dependent crustal deformation signals, it seems likely that a variety of processes interact to produce the complex signal that is observed. These processes may include fault-centered stable and unstable sliding phenomena, as governed by state- and rate-dependent friction laws (Tse and Rice, 1986), and bulk phenomena such as viscoelastic flow. As geodetic observations in southcentral Alaska span only a few decades, it is quite remarkable that a myriad of deformation styles have already been observed. However, the Alaska seismic zone is not unique in revealing a complexity in the temporal-spatial distribution of crustal deformation. For example, silent earthquakes and aseismic slip events have been recently observed at subduction zones in Cascadia (Dragert *et al.*, 2001), Japan (Ozawa *et al.*, 2002), Mexico (Kostoglodov *et al.*, 2003), and elsewhere. Although the deformations that have been observed thus far in southcentral Alaska are due primarily to plate tectonic and seismic processes, it is likely that the more subtle effects of glacial rebound and long-term, long-wavelength relaxation processes will have to be considered in future studies. Models of increasing sophistication that can account both for earthquake-cycle and permanent deformation will be required to explain the seismotectonics and geological evolution of the subduction zone.

## ACKNOWLEDGEMENTS

The authors have worked with many colleagues who have shared their insights and observations on Alaska seismotectonics. We express our appreciation, in particular, for the many contributions of Chris Larsen, Hilary Fletcher, Sandy Holdahl, Jeanne Sauber, Max Wyss, and Chris Zweck. Renata Dmowska and Kurt Feigl provided valuable reviews on both the scientific and pedagogical aspects of the initial version of this chapter.

## REFERENCES

- Arendt, A. A., Echelmeyer, K. A., Harrison, W. D., Lingle, C. S., and Valentine, V. B. (2002). Rapid wastage of Alaska glaciers and their contribution to rising sea level. *Science* **297**, 382–386.
- Atwater, T., and Severinghouse, J. (1989). Tectonic maps of the northeast Pacific. In “The Eastern Pacific Ocean and Hawaii” (E. L. Winterer, D. M. Hussong, and R. W. Decker, eds.), *The Geology of North America*, Geological Society of America, Boulder, pp. 15–20.
- Bartsch-Winkler, S., and Schmoll, H. R. (1992). Utility of radiocarbon-dated stratigraphy in determining late Holocene earthquake recurrence intervals, upper Cook Inlet region, Alaska. *Geol. Soc. Am. Bull.* **104**, 684–694.
- Beckman, H.M. (1980). Geologic map of Alaska, U.S. Geological Survey Special Map.
- Bird, P. (1996). Computer simulations of Alaskan neotectonics. *Tectonics* **15**, 225–236.
- Brocher, T. M., Fuis, G. S., Fisher, M. A., Plafker, G., Moses, M. J., Taber, J. J., and Christensen, N. I. (1994). Mapping the megathrust beneath the northern Gulf of Alaska using wide-angle seismic data. *J. Geophys. Res.* **99**, 11663–11685.
- Brown, L. D., Reilinger, R. E., Holdahl, S. R., and Balazs, E. I. (1977). Postseismic crustal uplift near Anchorage, Alaska. *J. Geophys. Res.* **92**, 3369–3377.
- Carver, G. A., and McCalpin, J. P. (1996). Paleoseismology of compressional tectonic environments. In “Paleoseismology” (J. McCalpin, ed.). Academic Press, San Diego, pp. 183–270.
- Christensen, D. H., and Beck, S. L. (1994). The rupture process and tectonic implications of the great 1964 Prince William Sound earthquake. *Pure Appl. Geophys.* **142**, 9–53.
- Cohen, S. C. (1996). Time-dependent uplift of the Kenai Peninsula and adjacent areas of south central Alaska since the 1964 Prince William Sound earthquake. *J. Geophys. Res.* **101**, 8595–8604.
- Cohen, S. C. (1998). On the rapid postseismic uplift along Turnagain Arm, Alaska following the 1964 Prince William Sound earthquake. *Geophys. Res. Lett.* **28**, 1213–1215.
- Cohen, S. C. (1999). Numerical models of crustal deformation in seismic zones. In “Advances in Geophysics 41” (R. Dmowska, and B. Saltzman, eds.). Academic Press, San Diego, pp. 133–232.
- Cohen, S. C., and Freymueller, J. T. (1997). Deformation on the Kenai Peninsula, Alaska. *J. Geophys. Res.* **102**, 20479–20487.
- Cohen, S. C., and Freymueller, J. T. (2001). Crustal uplift in the south central Alaska subduction zone: new analysis and interpretation of tide gauge observations. *J. Geophys. Res.* **106**, 11259–11270.
- Cohen, S. C., Holdahl, S., Caprette, D., Hilla, S., Safford, R., and Schultz, D. (1995). Uplift of the Kenai Peninsula, Alaska, since the 1964 Prince William Sound earthquake. *J. Geophys. Res.* **100**, 2031–2038.
- Combellick, R. A. (1991). Paleoseismicity of the Cook Inlet Region, Alaska: evidence from peat stratigraphy in Turnagain and Knik Arms. Professional Report 112. State of Alaska, Division of Geological and Geophysical Surveys, Fairbanks.
- Combellick, R. A. (1992). The penultimate great earthquake in southcentral Alaska: evidence from a buried forest near Girdwood. Public Data File 92-12. State of Alaska, Division of Geological and Geophysical Surveys, Fairbanks.
- Combellick, R. A. (1993). Investigation of peat stratigraphy in tidal marshes along Cook Inlet, Alaska to determine the frequency of 1964-style great earthquakes in the Anchorage region. Public Data File 93-84. State of Alaska, Division of Geological and Geophysical Survey, Fairbanks.

- DeMets, C., and Dixon, T. H. (1999). New kinematic models for Pacific-North America motion from 3 MA to present, 1: evidence for steady motion and biases in the NUVEL-1A model. *Geophys. Res. Lett.* **26**, 1921–1924.
- DeMets, C., Gordon, R. G., Argus, D. F., and Stein, S. (1990). Current plate motions. *Geophys. J. Int.* **101**, 425–478.
- DeMets, C., Gordon, R. G., Argus, D. F., and Stein, S. (1994). Effects of recent revisions to the geomagnetic reversal time scale on estimates of current plate motions. *Geophys. Res. Lett.* **21**, 2191–2194.
- Doser, D. I., Veileux, A. M., and Velasquez, M. (1999). Seismicity of the Prince William Sound region for over thirty years following the 1964 great Alaska earthquake. *Pure Appl. Geophys.* **154**, 593–632.
- Dragert, H., Wang, K., and James, T. S. (2001). A silent slip event of the deeper Cascadia subduction interface. *Science* **292**, 1525–1528.
- Eberhart-Phillips, D., Haeussler, P. J., Freymueller, J. T., Frankel, A. D., Rubin, C. M., Craw, P., Ratchkovski, N. A., Anderson, G., Carver, G. A., Crone, A. J., Dawson, T. E., Fletcher, H., Hansen, R., Harp, E. L., Harris, R. A., Hill, D. P., Hreinsdóttir, S., Jibson, R. W., Jones, L. M., Kayen, R., Keefer, D. K., Larsen, C. F., Moran, S. C., Personius, S. F., Plafker, G., Sherrod, B., Sieh, K., Sitar, N., and Wallace, W. K. (2003). The 2002 Denali Fault Earthquake, Alaska: a large magnitude, slip-partitioned event. *Science* **300**, 113–119.
- Estabrook, C. H., and Jacob, K. H. (1991). Stress indicators in Alaska. In “Neotectonics of North America, Decade Map Volume 1, Chapter 21.” (D. B. Slemmons, D. B. Engdahl, M. D. Zoback, and D. D. Blackwell, eds.). Geological Society of America, Boulder.
- Estabrook, C. H., Jacob, K. H., and Sykes, L. R. (1994). Body wave and surface wave analysis of large and great earthquake along the Eastern Aleutian Arc, 1923–1993: implications for future events. *J. Geophys. Res.* **99**, 11643–11662.
- Ferris, A., Abers, G. A., Christensen, D. H., and Veenstra, E. (2003). High resolution image of the subducted Pacific (?) plate beneath central Alaska, 50–150 km depth. *Earth. Planet. Sci. Lett.* **214**, 575–588.
- Fitch, T. J. (1972). Plate convergence, transcurrent faults, and internal deformation adjacent to Southeast Asia and western Pacific. *J. Geophys. Res.* **77**, 4432–4460.
- Fletcher, H. J. (2002). “Crustal Deformation in Alaska Measured Using the Global Positioning System” (Ph.D. dissertation), University of Alaska Fairbanks, 135pp.
- Fletcher, H. J., and Freymueller, J. (1999). GPS constraints on the motion of the Yakutat Block. *Geophys. Res. Lett.* **26**, 3029–3032.
- Fletcher, H. J., and Freymueller, J. (2002). Tectonics of interior Alaska, a study using GPS measurements. American Association for the Advancement of Science (abstract).
- Fletcher, H. J., and Freymueller, J. T. (2003). New constraints on the motion of the Fairweather fault, Alaska, from GPS observations. *Geophys. Res. Lett.* **30(3)**, 1139, doi: 10.1029/2002GL016476.
- Fletcher, H. J., Beavan, J., Freymueller, J., and Gilbert, L. (2001). High interseismic coupling of the Alaska subduction zone SW of Kodiak island inferred from GPS data. *Geophys. Res. Lett.* **28**, 443–446.
- Freymueller, J. T., Cohen, S. C., and Fletcher, H. (2000). Variations in present day deformation, Kenai Peninsula, Alaska, and their implications. *J. Geophys. Res.* **105**, 8079–8102.
- Freymueller, J. T., Zweck, C., Fletcher, H., Hreinsdóttir, S., Cohen, S. C., and Wyss, W. (2001). The great Alaska “earthquake” of 1998–2001. *Eos, Trans. Am. Geophys. U.* **82(47)**, Fall Meet. Suppl. Abstract.

- Harding, S. T., and Algermissen, S. T. (1972). The focal mechanism of this and related earthquakes. In "The Great Alaska Earthquake of 1964, Seismology and Geodesy." National Academy of Sciences, Washington, DC, pp. 197–233.
- Hastie, L. M., and Savage, J. C. (1970). A dislocation model for the 1964 Alaska earthquake. *Bull. Seismol. Soc. Am.* **60**, 1389–1392.
- Holdahl, S. R., and Sauber, J. (1994). Coseismic slip in the 1964 Prince Williams Sound earthquake: a new geodetic inversion. *Pure Appl. Geophys.* **142**, 55–82.
- Hreinsdóttir, S., Freymueller, J. T., Fletcher, H. J., Larsen, C. F., and Bürgmann, R. (2003). Coseismic slip distribution of the 2002 MW 7.9 Denali fault earthquake, Alaska, determined from GPS measurements. *Geophys. Res. Lett.* **30**, 1670, doi: 10.1029/2003GL017447.
- Ivins, E. R. (1996). Transient creep of a composite lower crust 2. A polyminerale basis for rapidly evolving postseismic deformation modes. *J. Geophys. Res.* **101**, 28005–28028.
- Johnson, J. M. (1999). Heterogeneous coupling along the Alaska-Aleutians as inferred from Tsunami, seismic, and geodetic inversions (R. Dmowska, and B. Saltzman, eds.), *Advances in Geophysics*, Vol. 39. Academic Press, San Diego, pp. 1–116.
- Johnson, J. M., Satake, K., Holdahl, S. R., and Sauber, J. (1996). The 1964 Prince William Sound Earthquake: joint inversion of tsunami and geodetic data. *J. Geophys. Res.* **101**, 522–532.
- Kanamori, H. (1970). The Alaska earthquake of 1964: radiation of long-period surface waves and source mechanisms. *J. Geophys. Res.* **75**, 5029–5040.
- Kikuchi, M., and Fukao, Y. (1987). Inversion of long-period P waves from great earthquakes along subduction zones. *Tectonophysics* **144**, 231–247.
- Kostoglodov, V., Lowry, A., Singh, S., Larson, K., Santiago, J., Franco, S., and Bilham, R. (2003). A large silent earthquake and the future rupture of the Guerrero seismic gap, Mexico. *Geophys. Res. Abstr.* **5**, 10411.
- Lahr, J. C., and Plafker, G. (1980). Holocene Pacific-North American Plate interaction in southern Alaska; implications for the Yakataga seismic gap. *Geology* **8**, 483–486.
- Larsen, C. F., Motyka, R., Freymueller, J., and Echelmeyer, K. A. (2003). Tide gauge records of uplift along the northern Pacific–North America plate boundary, 1937 to 2001. *J. Geophys. Res.* **108**, doi: 10.1029.2001JB001685.
- Lay, T., and Wallace, T. C. (1995). "Modern Global Seismology." Academic Press, San Diego, p. 7.
- Little, T. A., and Naeser, C. W. (1989). Tertiary tectonics of the Border Ranges Fault System, Chugach Mountains, Alaska: deformation and uplift in a forearc setting. *J. Geophys. Res.* **94**, 4333–4359.
- Lundgren, P., Saucier, F., Palmer, R., and Langon, M. (1995). Alaska crustal deformation: finite element modeling constrained by geological and very long baseline interferometry data. *J. Geophys. Res.* **100**, 22033–22045.
- Ma, C., Sauber, J. M., Bell, L. J., Clark, T. A., Gordon, D., Himwich, E., and Ryan, J. W. (1990). Measurement of horizontal motions in Alaska using very long baseline interferometry. *J. Geophys. Res.* **95**, 21991–22011.
- McCaffrey, R. (1992). Oblique plate convergence, slip vectors, and forearc deformation. *J. Geophys. Res.* **97**, 8905–8915.
- Miyashita, K., and Matsu'ura, M. (1978). Inversion analysis of static displacement data associated with the Alaska earthquake of 1964. *J. Phys. Earth* **26**, 333–349.
- Moore, J. C., Diebold, J., Fisher, M. A., Sample, J., Brocher, T., von Huene, R., Rowe, C., Stone, D., Stevens, C., and Sawyer, D. (1991). EDGE deep seismic reflections transect of the eastern Aleutian arc-trench layered lower crust reveals underplating and continental growth. *Geology* **19**, 420–425.

- Nishenko, S. P., and Jacob, K. H. (1990). Seismic potential of the Queen Charlotte-Alaska-Aleutian seismic zone. *J. Geophys. Res.* **95**, 2511–2532.
- Oldow, J. S., Bally, A. W., Ave' Lallemand, H. G., and Leeman, W. P. (1989). Phanerozoic evolution of the North American cordillera; United States and Canada. In "Geology of North America—An Overview" (A. W. Bally, and R. A. Palmer, eds.). Geological Society of America, Boulder, pp. 139–232.
- Oleskevich, D. A., Hyndman, R. D., and Wang, K. (1999). The updip and downdip limits to great subduction earthquakes: thermal and structural models of Cascadia, south Alaska, SW Japan, and Chile. *J. Geophys. Res.* **104**, 14965–14991.
- Ozawa, S., Murakami, M., Kaidzu, M., Tada, T., Sagiya, T., Hatanaka, Y., Yarai, H., and Nishimura, T. (2002). Detection and monitoring of ongoing aseismic slip in the Toka region, central Japan. *Science* **298**, 1009–1012.
- Page, R. A., Biswas, N. N., Lahr, J. C., and Puplan, H. (1991). Seismicity of continental Alaska. The Geology of North America, Decade Map, Vol. 1, The Geological Society of America, Boulder, pp. 47–68.
- Parkin, E. J. (1972). Horizontal crustal movements. In "The Great Alaska Earthquake of 1964, Seismology and Geodesy." National Academy of Sciences, Washington, DC, pp. 419–434.
- Pavlis, T. L., and Crouse, G. W. (1989). Late Mesozoic strike slip movement on the Border Ranges Fault System in the Eastern Chugach Mountains, Southern Alaska. *J. Geophys. Res.* **94**, 4321–4332.
- Perez, O. J., and Jacob, K. H. (1980). Tectonic model and seismic potential of the eastern Gulf of Alaska and Yakataga seismic gap. *J. Geophys. Res.* **85**, 7132–7150.
- Piersanti, A., Spada, G., and Sabadini, R. (1997). Global postseismic rebound of a viscoelastic Earth: theory for finite faults and application to the 1964 Alaska earthquakes. *J. Geophys. Res.* **102**, 477–492.
- Plafker, G. (1965). Tectonic deformation associated with the 1964 Alaskan earthquake. *Science* **148**, 1675–1687.
- Plafker, G. (1972). Tectonics. In "The Great Alaska Earthquake of 1964, Seismology and Geodesy." National Academy of Sciences, Washington, DC, pp. 113–188.
- Plafker, G., Lajoie, K. R., and Rubin, M. (1992). Determining recurrence intervals of great subduction zone earthquakes in southern Alaska by radiocarbon dating. In "Radiocarbon After Four Decades: An Interdisciplinary Perspective" (R. E. Taylor, A. Long, and R. S. Kra, eds.). Springer, New York, pp. 436–453.
- Plafker, G., Moore, J. C., and Winkler, G. R. (1994). Geology of the southern Alaska margin. In "The Geology of North America, Vol. G-1, the Geology of Alaska." The Geological Society of America, Boulder, pp. 389–449.
- Ponko, S. C., and Peacock, S. M. (1995). Thermal modeling of the southern Alaska subduction zone: insight into the petrology of the subducting slab and overlying mantle wedge. *J. Geophys. Res.* **128**, 22117–22128.
- Pope, A. J. (1972). Strain analysis of horizontal crustal movements in Alaska based on triangulation surveys before and after the Earthquake. In "The Great Alaska Earthquake of 1964, Seismology and Geodesy." National Academy of Sciences, Washington, DC, pp. 435–448.
- Prescott, W. H., and Lisowski, M. (1977). Deformation at Middleton Island, Alaska during the decade after the Alaska earthquake of 1964. *Bull. Seismol. Soc. Am.* **67**, 579–586.
- Prescott, W. H., and Lisowski, M. (1980). Deformation at Middleton Island, Alaska. *Bull. Seismol. Soc. Am.* **70**, 1887–1892.
- Press, F. (1965). Displacements, strains, and tilts at teleseismic distance. *J. Geophys. Res.* **70**, 2395–2412.

- Press, F., and Jackson, D. J. (1965). Vertical extent of faulting and elastic strain energy release. *Science* **147**, 867–868.
- Pulpan, H., and Frohlich, C. (1985). Geometry of the subducted plate near Kodiak Island and lower Cook Inlet, Alaska, determined from relocated earthquake hypocenters. *Bull. Seismol. Soc. Am.* **75**, 791–810.
- Ratchkovski, N. A., and Hansen, R. A. (2002). New constraints on tectonics of interior Alaska: earthquake locations, source uncertainties, and stress regime. *Bull. Seismol. Soc. Am.* **92**, 998–1014.
- Rosenbaum, J. G. (1974). Theory of warping of southern Alaska before Alaska earthquake, 1964. *J. Geophys. Res.* **79**, 3294–3301.
- Ruff, L., and Kanamori, H. (1983). The rupture process and asperity distribution of three great earthquakes from long-period diffracted P-waves. *Phys. Earth Planet. Int.* **31**, 202–229.
- Rundle, J. B., Turcotte, D. L., and Klein, W. (2000). Introduction in geocomplexity and the physics of earthquakes. American Geophysical Union Geophysical Monograph 120, Washington, DC.
- Savage, J. C. (1983). A dislocation model of strain accumulation and release at a subduction zone. *J. Geophys. Res.* **88**, 4984–4996.
- Savage, J. C., and Lisowski, M. (1991). Strain accumulation along the Denali Fault at the Nenana River and Delta River Crossings, Alaska. *J. Geophys. Res.* **96**, 14481–14492.
- Savage, J. C., and Plafker, G. (1991). Tide gage measurements of uplift along the south coast of Alaska. *J. Geophys. Res.* **96**, 4325–4335.
- Savage, J. C., and Prescott, W. H. (1978). Asthenospheric readjustment and the earthquake cycle. *J. Geophys. Res.* **83**, 3369–3376.
- Savage, J. C., Svarc, J. L., Prescott, W. H., and Gross, W. K. (1998). Deformation across the rupture zone of the 1964 Alaska earthquake, 1993–1997. *J. Geophys. Res.* **103**, 21275–21283.
- Savage, J. C., Svarc, J. L., and Prescott, W. H. (1999). Deformation across the Alaska-Aleutian subduction zone near Kodiak. *Geophys. Res. Lett.* **26**, 2117–2120.
- Sella, G. F., Dixon, T. H., and Mao, A. (2002). REVEL: a model for recent plate velocities from space geodesy. *J. Geophys. Res.* **107**, 10.1029/2000JB000033.
- Shennan, I. A., Scott, D. B., Rutherford, M., and Zong, V. (1999). Microfossil analysis of sediments representing the 1964 earthquake, exposed at Girdwood Flats, Alaska, USA. *Quaternary Int.* **60**, 55–73.
- Sherburne, R. W., Algermissen, S. T., and Harding, S. T. (1972). Hypocenter, origin time, and Magnitude. In “The Great Alaska Earthquake of 1964, Seismology and Geodesy.” National Academy of Sciences, Washington, DC, pp. 29–49.
- Small, J. B., and Wharton, L. C. (1972). Vertical displacements. In “The Great Alaska Earthquake of 1964, Seismology and Geodesy.” National Academy of Sciences, Washington, DC, pp. 449–461.
- Smith, D. A., and Milbert, D. G. (1999). The GEOID96 high resolution geoid height model for the United States. *J. Geod.* **73**, 219–236.
- Smith, D. A., and Roman, D. R. (2001). GEOID99 and G99SSS: 1-arc-minute geoid models for the United States. *J. Geod.* **75**, 469–490.
- Stauder, W. (1972). Introduction (to I: parameters of the main shock). In “The Great Alaska Earthquake of 1964, Seismology and Geodesy.” National Academy of Sciences, Washington, DC, pp. 23–28.
- Stauder, W., and Bollinger, G. A. (1966). The focal mechanism of the Alaska earthquake of March 28, 1964 and of its aftershock sequence. *J. Geophys. Res.* **71**, 5283–5295.
- Stephens, C. D., Page, R. A., and Lahr, J. C. (1990). Reflected and mode-converted seismic waves within the shallow Aleutian subduction zone, southern Kenai Peninsula, Alaska. *J. Geophys. Res.* **95**, 6883–6897.

- Suito, H., Freymueller, J. T., and Cohen, S. C. (2003). 3-D viscoelastic FEM modeling of postseismic deformation caused by the 1964 Alaska earthquake, southern Alaska. IUGG General Assembly, Sapporo, Japan (poster).
- Thatcher, W. (1995). Microplate versus continuum descriptions of active tectonic deformation. *J. Geophys. Res.* **100**, 3885–3894.
- Tichelaar, B. W., and Ruff, L. J. (1993). Depth of seismic coupling along subduction zones. *J. Geophys. Res.* **98**, 2017–2037.
- Tocher, D. (1972). General introduction: tectonics and seismic effects of the Alaska earthquake and the seismicity of Alaska. In “The Great Alaska Earthquake of 1964, Seismology and Geodesy.” National Academy of Sciences, Washington, DC, pp. 1–7.
- Tse, S. T., and Rice, J. R. (1986). Crustal earthquake instability in relation to depth variation of frictional properties. *J. Geophys. Res.* **91**, 9452–9472.
- Urdike, R. G., and Schmoll, H. R. (1985). A brief resume of the geology of Anchorage and vicinity. Public-data File 85-2. Alaska Division of Geological and Geophysical Surveys, Fairbanks.
- Vine, F. J., and Mathews, D. H. (1963). Magnetic anomalies over oceanic ridges. *Nature* **199**, 947–949.
- Von Huene, R., Fisher, M. A., and Bruns, T. R. (1987). Geology and evolution of the Kodiak margin, Gulf of Alaska. In “Geology and Resource Potential of the Continental Margin of Western North America and Adjacent Ocean Basins—Beaufort Sea to Baja California” (D. W. Scholl, A. Grantz, and Vedder, eds.). Texas Circum-Pacific Council for Energy and Mineral Resources, Houston, pp. 191–212.
- Von Huene, R., Klaeschen, D., and Fruehn, J. (1999). Relation between the subducting plate and seismicity associated with the great 1964 Alaska earthquake. *Pure Appl. Geophys.* **154**, 575–591.
- Wahr, J., and Wyss, M. (1980). Interpretation of postseismic deformation with a viscoelastic relaxation model. *J. Geophys. Res.* **85**, 6471–6477.
- Whitten, C. A. (1972). Introduction: an evaluation of the geodetic and photogrammetric surveys. In “The Great Alaska Earthquake of 1964, Seismology and Geodesy.” National Academy of Sciences, Washington, DC, pp. 415–417.
- Williams, C. A., McCaffrey, R., and Qamar, A. (2001). Inversions of geodetic data for rotation pole and deformation mechanism at subduction zones: applications to Cascadia, Sumatra, and Alaska. *EOS Trans. AUG* **82**.
- Wolf, L. W. and Davies, J. N. (1986). A comparison of acceleration values derived from recent seismic hazard studies of the Anchorage area, Alaska: Part I. Public-data File 86-85. Alaska Division of Geological and Geophysical Surveys, Fairbanks.
- Wolf, L. W., Stone, D. B., and Davies, J. N. (1991). Crustal structure of the active margin, south central Alaska: an interpretation of seismic refraction data from the Trans-Alaska crustal Transect. *J. Geophys. Res.* **96**, 16455–16469.
- Wyss, M., and Brune, J. N. (1972). A complex multiple rupture. In “The Great Alaska Earthquake of 1964, Seismology and Geodesy.” National Academy of Sciences, Washington, DC, pp. 60–64.
- Yeats, R. S., Sieh, K., and Allen, C. R. (1996). Chapter 8, strike-slip faults. In “The Geology of Earthquakes.” Oxford University Press, New York.
- Zhao, D., Christensen, D., and Puzan, H. (1995). Tomographic imaging of the Alaska subduction zone. *J. Geophys. Res.* **100**, 6487–6504.
- Zweck, C., Freymueller, J. T., and Cohen, S. C. (2002). Three dimensional elastic dislocation modeling of the postseismic response to the 1964 Alaska Earthquake. *J. Geophys. Res.* **107**, 10.129/2001JB000409.

**This page is intentionally left blank**

## RELATING FAULT MECHANICS TO FAULT ZONE STRUCTURE

RONALD L. BIEGEL AND CHARLES G. SAMMIS

*Department of Earth Sciences, University of Southern California,  
Los Angeles, CA 90089-0740, USA*

### ABSTRACT

The fault zone of a mature large-displacement fault may be idealized as a nested hierarchical structure consisting of a core of extremely fine grained material surrounded by coarser granulated gouge and breccia which is in turn bordered by fracture-damaged wall rock in which the fracture density decreases with distance to a regional background level. While there are significant variations in the symmetry of this structure, virtually all fault zones have a core of deformed granular rock within which most of the displacement appears to have occurred, often on an extremely narrow prominent slip surface. In many faults, the gouge and breccia layer is missing from one or both sides of the fault zone. For strike-slip faults, this appears to be associated with variations in the lithology of the wall rock. For dip-slip faults it is most likely a consequence of the exhumation of only one wall by the fault motion. In normal faults, the layered structure appears on the footwall while the hanging wall shows almost no damage. For reverse faults it is the hanging wall which contains the layered structure. Mechanisms proposed to explain the formation of these fault zone structures are reviewed with an eye toward whether they shed any light on the earthquake process.

Conversely, mechanical models for earthquake nucleation, propagation, and arrest are reviewed to see how fault zone structure might affect these processes. A key parameter in these models is the characteristic displacement  $D_c$  required to reduce friction from its static to its dynamic value. In nucleation,  $D_c$  determines the size of the smallest earthquake. The observation of magnitude zero earthquakes, implies  $D_c$  is on the order of microns, comparable to values measured in the laboratory. For propagation,  $D_c$  is closely related to the fracture energy, which is the integrated value of stress times displacement from zero to  $D_c$ . Dynamic models of large earthquakes find fracture energies on the order of  $1 \text{ MJ/m}^2$  and  $D_c$  on the order of centimeters. The implication is either that only large earthquakes nucleate on large faults, or that the  $D_c$  which controls nucleation is different from that which controls propagation because they reflect different processes. Two such processes that might produce a larger  $D_c$  for propagation are the frictional heating of pore fluid and off-fault damage.

Finally, models for earthquake arrest based on barriers requiring large values of fracture energy also yield fracture energies on the order of MJ/m<sup>2</sup>.

## 1. INTRODUCTION

An earthquake is commonly modeled as a stick-slip friction instability on a fault plane nucleated by a drop in frictional resistance from the static value to a dynamic one. This reduction in friction requires a characteristic sliding displacement  $D_c$  and is usually described by either a displacement weakening or velocity weakening rheology (Dieterich, 1978b, 1979a,b, 1986; Tullis and Weeks, 1986; Marone, 1998). The fracture energy  $G$  required to reduce friction to its dynamic value is the area under the stress–displacement curve during the weakening process (Rice, 1980; Rice *et al.*, 2004).

The observation that values of  $D_c$  and  $G$  measured in the laboratory are usually orders of magnitude smaller than those inferred from seismic measurements has raised the question of how these parameters scale from lab experiments to natural fault zones (Kanimori and Heaton, 2000; Andrews, 2002, 2004; Abercrombie and Rice, 2004). In fact, it is not obvious that the asperity mechanism observed to operate in the laboratory (Dieterich and Kilgore, 1994, 1996) is the controlling mechanism in the field. Even laboratory experiments that include a layer of simulated fault gouge (Biegel *et al.*, 1989; Marone and Scholz, 1989) do not come close to approximating the structural complexity of natural fault zones, which have a complex layered structure comprised of a narrow core of extremely fine particles surrounded by thicker layers of coarser gouge and breccia that are, in turn, bordered by fracture-damaged wall rock.

We begin this review by summarizing field studies of the deep structure of fault zones that have been exhumed by regional uplift and erosion. Although many faults are exposed at the surface, there are surprisingly few that have been exhumed from seismogenic depth and are suitable for detailed structural analysis (Faulkner *et al.*, 2003). We have also included several examples of active faults that have been drilled and cored. Although examples are sparse, we are able to identify structural elements that tend to be common to all fault zones as well as significant variations between the fault zones for different modes of faulting (strike-slip, normal, and reverse) and even along the strike and dip of a single fault.

We ask two related sets of questions. First, how does a fault zone form? What produces variation along a single fault and between faults with different modes of faulting? Is information about the mechanics of faulting encoded in the structure (Cowan, 1999; Evans *et al.*, 2000)? Second, how does fault zone structure affect earthquake mechanics? Specifically, what controls  $D_c$  and  $G$ ? Here we focus

separately on the nucleation, propagation, and arrest of earthquake ruptures. Finally, we explore the roles of off-fault damage and water in the granulated layers.

A thorough review of both the structure and evolution of faults and earthquake mechanics is beyond the scope of this paper. Rather we attempt a tight focus on the area of overlap between structure and mechanics.

## 2. FAULT ZONE ROCKS

In many locations tectonic uplift and erosion have exposed fault zones to depths that were once seismogenically active. Although exhumed fault zone rocks have been described, and their origin debated, since the time of Lapworth (1885), the first attempt at organization into a coherent model of an active fault zone was by Sibson (1977, 1982, 1986a,b, 1989). A slightly modified form of his proposed fault rock classification scheme, given in Fig. 1, is widely used today (Scholz, 2002). Sibson recognized that brittle deformation mechanisms (crack growth and grain size reduction) are active only in the top 10 km of the earth's crust (the "elastico-frictional" regime), while plastic-ductile mechanisms (mainly thermally activated creep) operate at the higher temperatures in the lower part of the crust ("plastiductile" regime). Sibson (1977) proposed the conceptual model for a fault zone, shown in Fig. 2, in which the fault zone structure depends mainly on depth.

## 3. THE STRUCTURE OF MATURE, LARGE DISPLACEMENT STRIKE-SLIP FAULTS

While many strike-slip fault zones are exposed at the surface, they generally offset shallow sedimentary layers and are not suitable for structural studies that bear on earthquake mechanics. While such exposures offer an opportunity to date past events, they do not expose evidence of processes in the deeper seismogenic zone between about 2 and 15 km. The best exposures for studying earthquake mechanics are of faults that have been exhumed from several kilometers and that were inactive during exhumation. For faults that remain active during their exhumation, structures formed at shallow depth are superimposed on structures formed at seismogenic depths, making their identification and interpretation more difficult.

### 3.1. The Punchbowl and San Gabriel Faults in Southern California

The San Gabriel and Punchbowl faults in southern California are examples of strike-slip faults that were not active during most of their exhumation, so there is

**Textural Classification of Fault Rock**

Incohesive	Random fabric		Foliated				
	Fault breccia (visible fragments >30% of rock mass)						
	Fault gouge (visible fragments <30% of rock mass)		Foliated gouge				
Cohesive	Nature of matrix	Glass/devitrified glass	Pseudotachylite				
			Tectonic reduction in grain size dominates grain growth by recrystallization and neomineralization	Crush breccia (fragments > 0.5 cm) Fine crush breccia (0.1 < fragments <0.5 cm) Crush microbreccia (fragments <0.1 cm)		0-10	Percent of matrix
	Cataclasite series	Protocataclasite		Protomylonite		10-50	
		Cataclasite		Mylonite series	Mylonite	Phyllonite series	
	Ultracataclasite	Ultramylonite	90-100				
Grain growth pronounced			Blastomylonite				

FIG. 1. Textural classification of fault rock proposed by Sibson (1977) as modified by Scholz (2002).

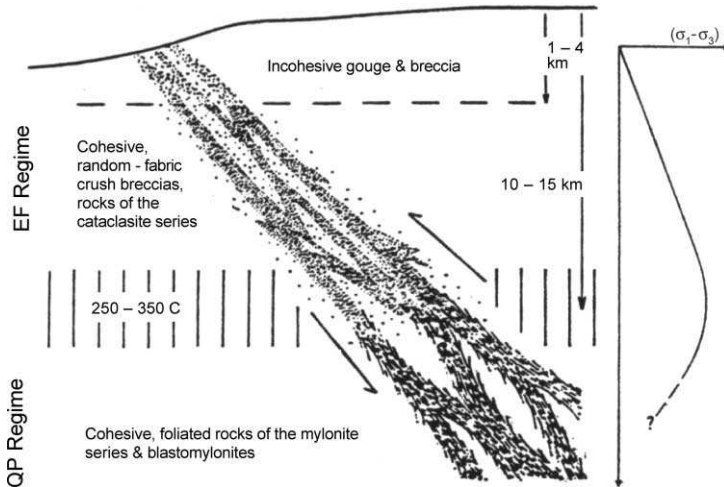


FIG. 2. Sibson's (1977) model of a fault zone. EF denotes the elasto-frictional regime where brittle deformation mechanisms dominate. QP denotes the quasi-plastic regime where ductile deformation prevails, beginning around the 250°C geothermal.

minimal overprinting of shallow activity during their uplift. They became inactive when the primary strike-slip plate boundary motion jumped to the current San Andreas fault north of the mountains, and were subsequently exhumed by thrust faulting on the frontal fault system responsible for uplift of the San Gabriel Mountains.

Detailed studies of the Punchbowl and San Gabriel faults in southern California (see map in Fig. 3) were initiated in the 1980s. Anderson *et al.* (1983) proposed that the exposed structure of the San Gabriel fault zone may be representative of the modern San Andreas fault zone at depth. They analyzed the mineralogy and size distribution of the fault gouge (Sammis *et al.*, 1986) and concluded that the San Gabriel fault zone, and by analogy the modern San Andreas fault zone, narrows with depth to the brittle-ductile transition, about 5–10 km. From there it widens again as ductile deformation mechanisms increasingly dominate with depth (see Fig. 4).

The Punchbowl fault is a right-lateral strike-slip fault once considered the main trace of the San Andreas system. The exposed fault zone has been exhumed from a depth of about 2 to 4 km by the uplift of the San Gabriel Mountains. The section of the fault studied by Chester and Logan (1986) is bounded to the northeast by the Punchbowl formation, mainly comprised of sandstone and conglomerate rocks, while the southwest side of the fault contacts an igneous and metamorphic



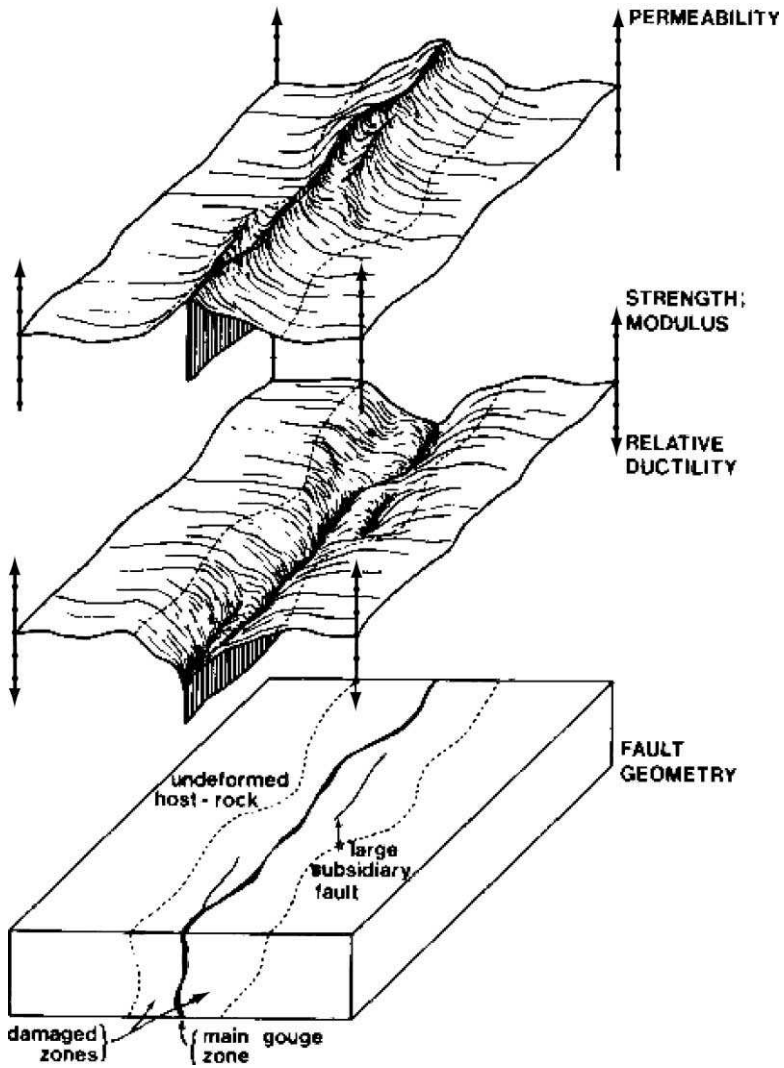


FIG. 5. Fault structure and mechanical properties of the Punchbowl fault according to Chester and Logan (1986). The surfaces indicate variation in properties along and across the fault zone.

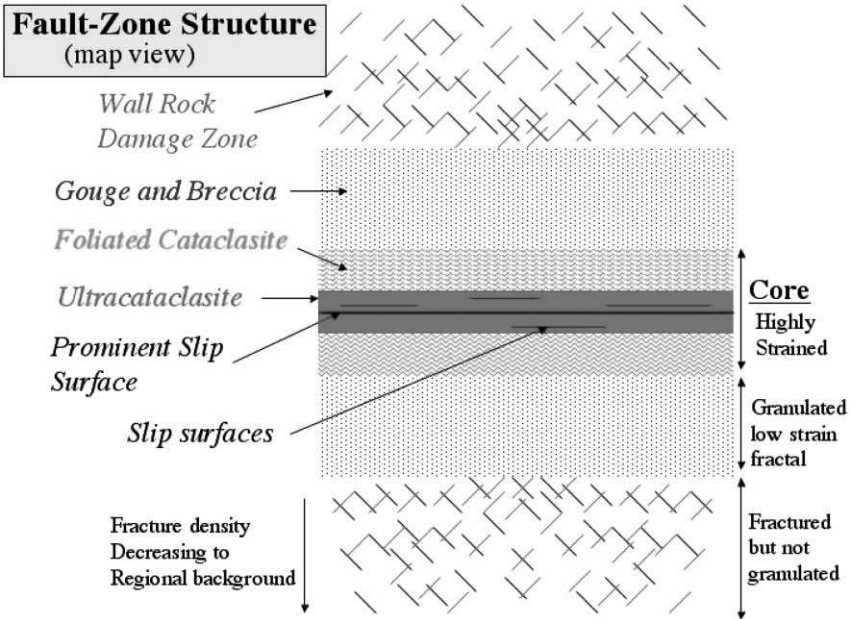


FIG. 6. The Punchbowl model fault zone structure in map view. The Punchbowl fault is a mature large displacement strike-slip fault.

elements are used to represent the architecture of most strike-slip faults (Chester *et al.*, 2004).

### 3.2. The Idealized Punchbowl Model

We consider the Punchbowl fault an ideal fault for our review. It is relatively symmetric and has nearly all the elements you might find in any other fault. Chester and Logan (1986) described the Punchbowl fault as an inner *gouge* layer bounded by a *damage zone* on both sides. Chester *et al.* (1993) revised the structure. His layer of gouge became the *fault core* comprised of an inner layer of *ultracataclasite* bounded by an outer layer of *foliated cataclasite*.

The 1993 Punchbowl model has a *damage zone* which includes layers of gouge and breccia as well as fractured wall rock. Since gouge and breccia are granular materials, we refer to these zones as *gouge* and *breccia* layers to distinguish them from fractured, but not granulated, wall rock shown in Fig. 6. Beginning at the center and working outwards, the layers of the Punchbowl model are as follows.

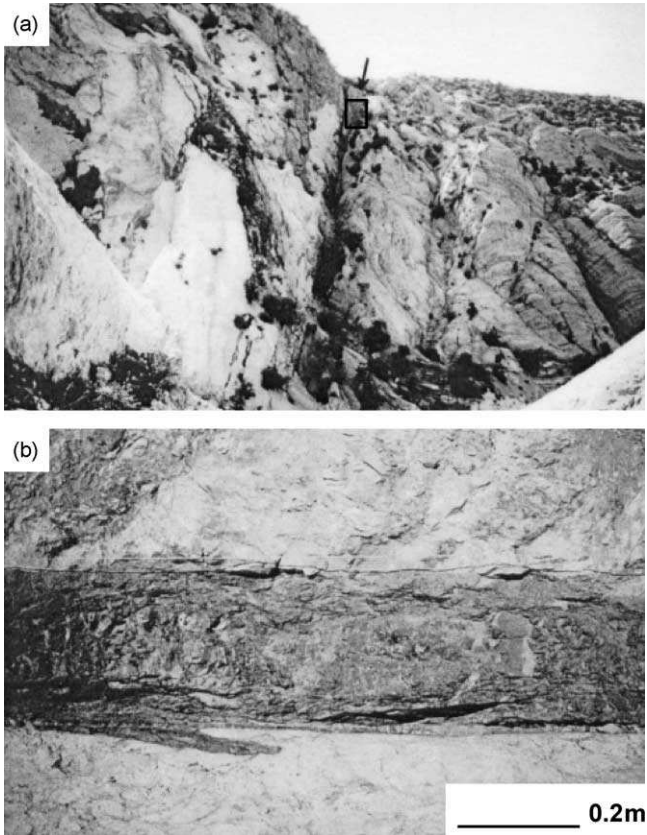


FIG. 7. A photo (top, (a)) looking northwest at the Punchbowl fault from Devils Chair. The Punchbowl fault cuts through the center from top to bottom. The bottom photo (b) shows the *ultracataclasite* layer at horizontal-center with *foliated cataclasites* above and below (from Chester and Chester, 1998).

1. *The fault core:* At the center of the Punchbowl model is the fault core (see Fig. 7a,b) that accommodates virtually all of the slip during earthquakes. It is comprised of an *ultracataclasite layer* sandwiched between two layers of *foliated cataclasite*.

(a) *The ultracataclasite layer:* At the center of the fault core is a layer of cohesive ultracataclasite, usually only centimeters to decimeters thick (Chester *et al.*, 1993). This layer consists primarily of angular particles less than 10  $\mu\text{m}$  in diameter (see Fig. 8a) and products of chemical alteration

(see Fig. 8b) such as cross-cutting calcite veins that indicate a pervasive presence of water. The layer contains numerous fracture surfaces, subparallel to fault strike, none of which are more than a few meters in length except for one which Chester and Chester (1998) dubbed the “prominent fracture surface” (PFS) (see Fig. 9a,b). The PFS is present and continuous in all exposures of the ultracataclasite. This, and the fact that it has a low roughness in the slip parallel direction, makes it a prime candidate for a velocity weakening surface (Chester and Chester, 1998). Due to the cohesive nature of the layer and the extremely small size of the particles, Chester and Logan (1986) inferred that it lacks significant porosity and is highly impermeable.

- (b) *The foliated cataclasite layer*: The ultracataclasite layer is bounded by foliated cataclasites (see Fig. 7b) that extend several meters from the ultracataclasite boundary (Chester *et al.*, 1993). Foliated cataclasites are cohesive fault rocks considered a product of intense shearing due to strain localization near the ultracataclasite layer. The intense shearing of the foliated cataclasites caused Chester *et al.* (1993) to distinguish it from other granular fault rock, such as gouge and breccia. Together, the ultracataclasite and foliated cataclasite layers comprise the fault core.

2. *The gouge and breccia zone*: The fault core is bordered by layers of gouge and breccia (Sibson, 1977). Chester *et al.* (1993) included these rocks in the damage zone because they lacked extensive shearing. We choose to retain a separate classification, which we call the gouge and breccia zone, to distinguish it from the fracture-damaged, but not granulated wall rock. It is not clear whether the boundary between the gouge and breccia zone and the wall rock-damage zone is sharp or gradational.

Chester *et al.* (1993) examined the particle-size distributions of three samples from the gouge and breccia layer in the San Gabriel fault. Two of the samples, SG13H and SG13K in Fig. 10, were taken from within the gouge–breccia zone and a third sample, SG13A, was taken adjacent to the fault core. Thin sections of SG13H and SG13K showed a texture consisting of non-cohesive grains. The size distributions are shown in Fig. 10. Samples SG13H and SG13K both showed fractal distributions remarkably similar to those reported by Sammis *et al.* (1987) and interpreted as evidence that “constrained comminution” was active in the gouge–breccia layer. If so, then most comminution in these two layers had ended and they are relict structures (Ben-Zion and Sammis, 2003). By contrast, SG13A displayed a non-fractal distribution peaked at small grain size, which may indicate that additional fragmentation has occurred in the gouge near the ultracataclasite layer. Similar peak distributions have been observed in the gouge layer adjacent to the core of the San Andreas fault in southern California (An and Sammis, 1994;

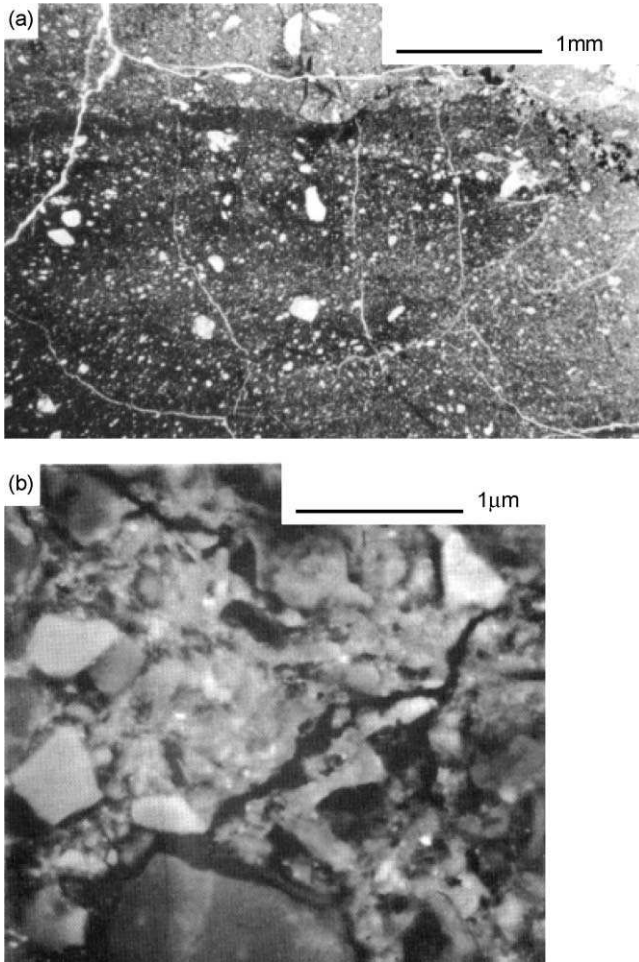


FIG. 8. Photomicrographs of ultracataclasite from the San Gabriel fault. (a) Sample showing veins penetrating the ultracataclasite matrix. Scale bar is 1 mm. Note that very few particles are larger than 10  $\mu\text{m}$  in diameter. (b) Ultracataclasite under scanning electron microscopy. Scale bar is 10  $\mu\text{m}$ . Note the angular surfaces of the particles suggesting fragmentation in tension (from Chester *et al.*, 1993).

Reches and Dewers, 2004) and may indicate additional fragmentation following shear localization in the fault core.

3. *The wall rock damage zone:* Beyond the gouge and breccia zone is the *wall rock damage zone* characterized by a fracture density above regional background.

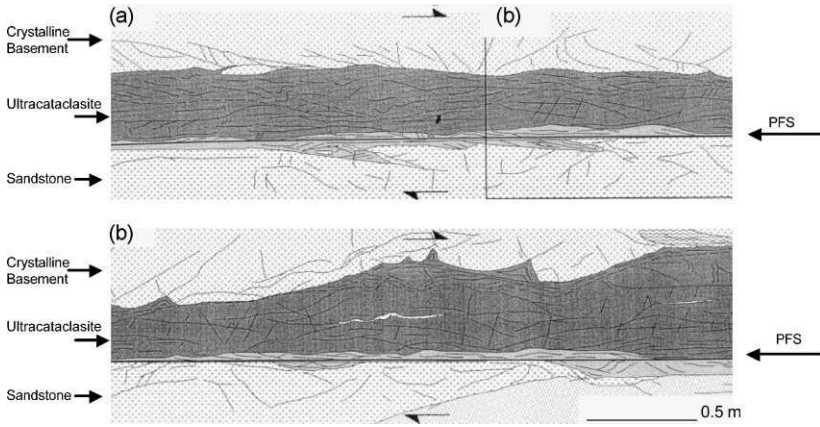


FIG. 9. The Punchbowl fault drawn in cross-section. In the top drawing (a), the ultracataclasite is the dark horizontal-central layer. It is bounded by on both sides by foliated cataclasites. The bottom drawing is a close up of the top layer showing localization of slip along the PFS. Arrows show the primary fracture surface (from Chester and Chester, 1998).

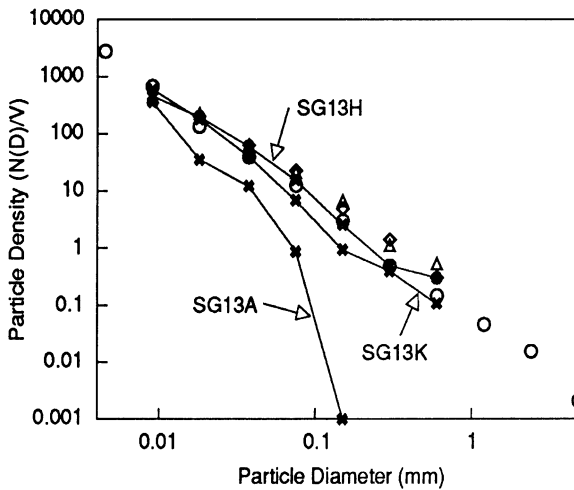


FIG. 10. Particle size distributions for San Gabriel fault samples. SG13H and SG13K were samples taken from within the gouge and breccia zone. SG13A was a sample taken from the fault zone adjacent the ultracataclasite/foliated cataclasite boundary. Open circles are from Sammis *et al.* (1987), diamonds are from Biegel *et al.* (1989), and triangles are from Marone and Scholz (1989).

This zone differs from the gouge and breccia zone by being non-granular. Although high, the fracture density is not sufficient to produce distinct particles. Included within the damage zone are subsidiary faults tens of meters in length and oriented subparallel to the fault (Chester and Logan, 1986; Chester *et al.*, 1993, 2003; Wilson *et al.*, 2003). Although our discussion is limited to faults with large displacements, the damage zones of small displacement faults have been recently reviewed by Kim *et al.* (2004).

The width of the damage zone is determined by where the crack density falls to a background level of the host rock, usually meters to kilometers from the fault core (Schulz and Evans, 1998, 2000; Wilson *et al.*, 2003). The exact extent of damage around any fault is difficult to determine. Chester and Logan (1986) made a rough count of mesoscopic damage elements while traversing the fault. Figure 11 shows a damage peak within the gouge–breccia layer, adjacent to the fault core, declining to near background levels about 10–20 m from the core.

To more accurately measure the extent of the damage zone around the Punchbowl fault, Wilson *et al.* (2003) made thin sections from samples of the damage zone and analyzed the crack damage. Figure 12 is a log-linear plot of

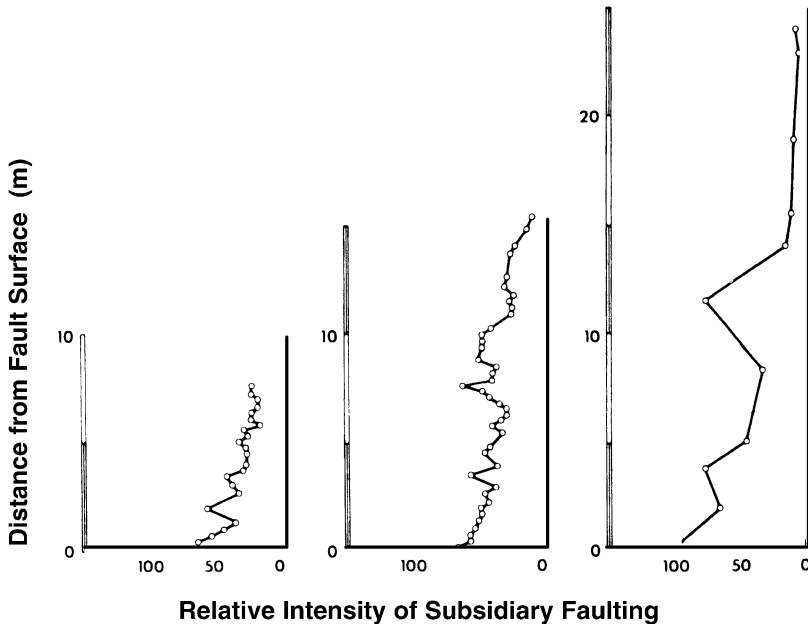


FIG. 11. Mesoscopic damage with distance from the Punchbowl fault. Damage includes subsidiary faults and cracks measured while in the field (from Chester and Logan, 1986).

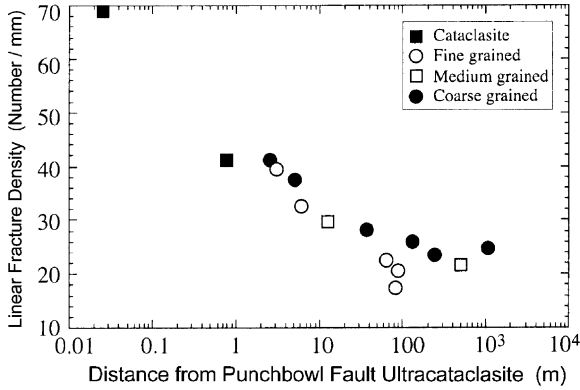


FIG. 12. Microscopic damage with distance from the Punchbowl fault. The damage continues decreasing for  $\sim 100$  m from the fault (from Wilson *et al.*, 2003).

their results showing that the damage zone can be detected up to 100 m from the core of the Punchbowl fault.

### 3.3. The Nojima Fault, Japan

The Nojima fault, a NE–SW striking right-lateral fault, is a branch of the Median Tectonic Line (MTL) which ruptured near Osaka Bay on January 17, 1995, in a magnitude 7.2 earthquake. Within 12 months the Geological Survey of Japan drilled a borehole that penetrated the fault core and retrieved samples from across the fault (Ito *et al.*, 2000). Figure 13 is a diagram of the fault zone and GSI borehole.

The Nojima fault zone structure mirrors the Punchbowl model in most respects. Core samples from the borehole showed the protolith was an equigranular Nojima granodiorite (Tanaka *et al.*, 2000). From petrographic analysis of the fault rock, Tanaka *et al.* (2000) concluded that the borehole entered the fault zone at 426 m depth and yielded four kinds of fault rock: weakly deformed and altered granodiorite, fault breccia, fault gouge and cataclasite (see Fig. 14). Within the fault zone, Tanaka *et al.* (2000) observed seven zones of highly sheared rock, concluding that cataclasis was diffused during initial stages of faulting but gradually localized with slip accumulation. The main shear zone, corresponding to the ultracataclasite layer in the Punchbowl model, was located at  $\sim 623$  m depth and was the thickest shear

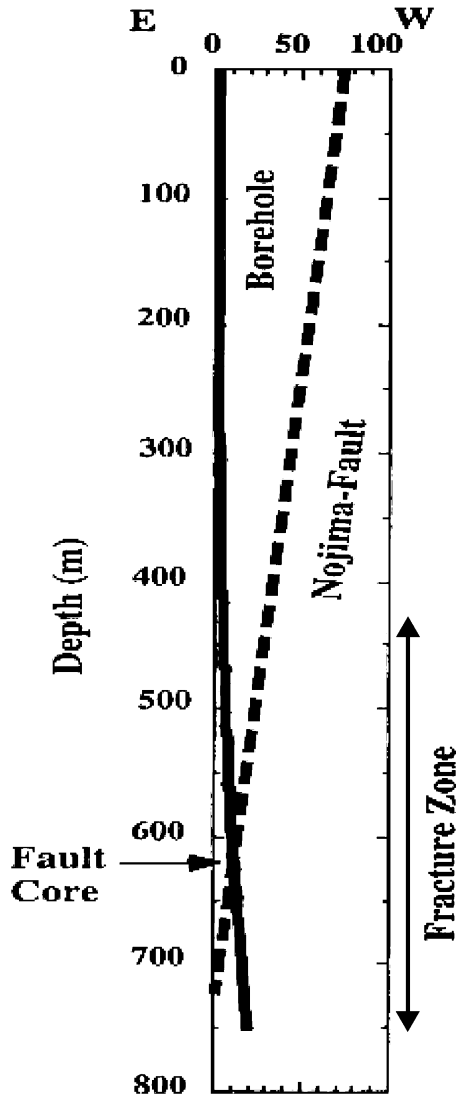


FIG. 13. Diagram of the Geological Survey of Japan borehole and the Nojima fault, Japan (from Ito *et al.*, 2000).

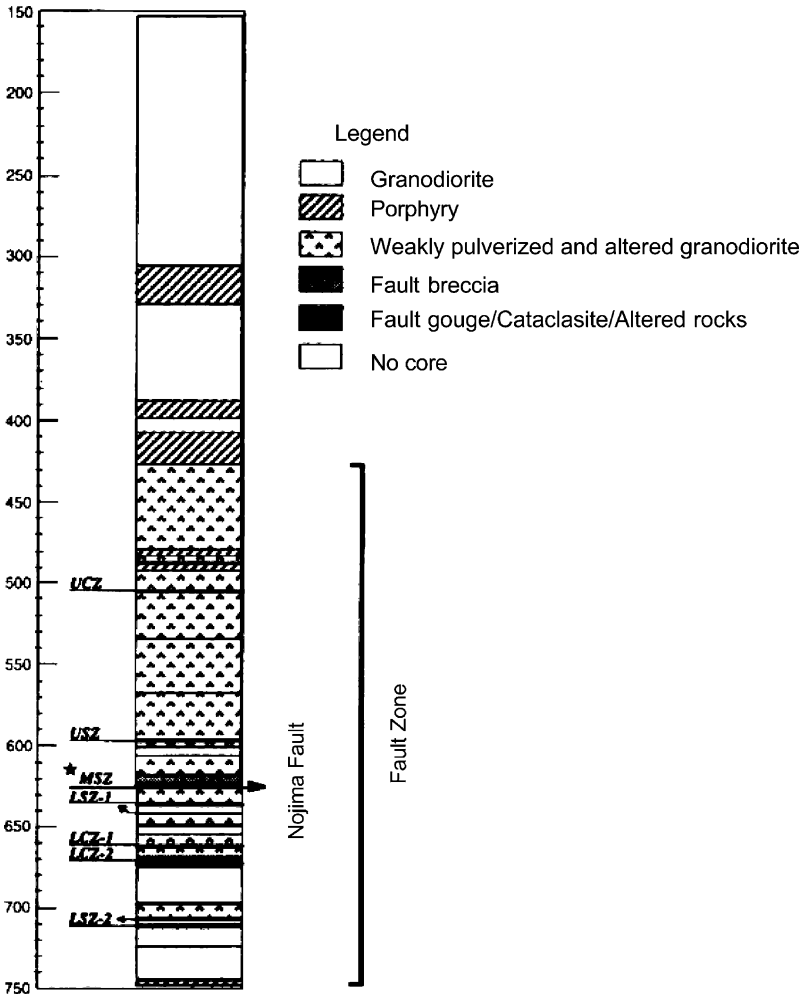


FIG. 14. Schematic diagram of the Nojima fault rock as observed in core samples retrieved from the GSJ borehole. UCZ, USZ, MSZ, LSZ-1, LSZ-2, LCZ-1, and LCZ-2 denote each of the seven cataclasite layers observed by Tanaka *et al.* (2000). Note that MSZ is the main shear zone and the fault surface was located at the bottom of this layer.

zone at  $\sim 30$  cm, almost identical to the Punchbowl. Tanaka *et al.* (2000) conclude from a number of geophysical measurements that the main fault surface of the 1995 earthquake appeared at the bottom of the main shear zone along a principal slip surface.

Fujimoto *et al.* (2000) found evidence that the history of the faults uplift was encoded in the fault gouge. They found three types of gouges in the main shear zone and theorized that the differences were a consequence of the depth at which each layer of gouge formed. The oldest gouge probably formed deeper than 7 km depth and has since been uplifted. It was very fine grained and contained cryptocrystalline materials, possibly pseudotachylite. An intermediate depth gouge was formed at 4–7 km depth and possessed fine grains and foliations. The most recently formed gouge possessed random fabric and coarse grains, characteristics of shallow depth cataclasis.

Samples from the fault core were observed to have unusually low strength and permeability (Lockner *et al.*, 2000). Low strength measurements support the Punchbowl model of a fault which has a weak core that enhances strain localization. Low permeability measurements support the theory that the fault core acts as an impermeable barrier to fluid flow. Outside the fault core but within the gouge and breccia zone, permeability increased sharply but then decreased with increasing distance from the fault core (see Fig. 15). This supports the model of gouge and breccia zones as conduits to fluid flow on either side of an impermeable fault core (Tsutsumi *et al.*, 2004). As expected, the strength of the gouge and breccia samples was observed to increase with distance from the fault core.

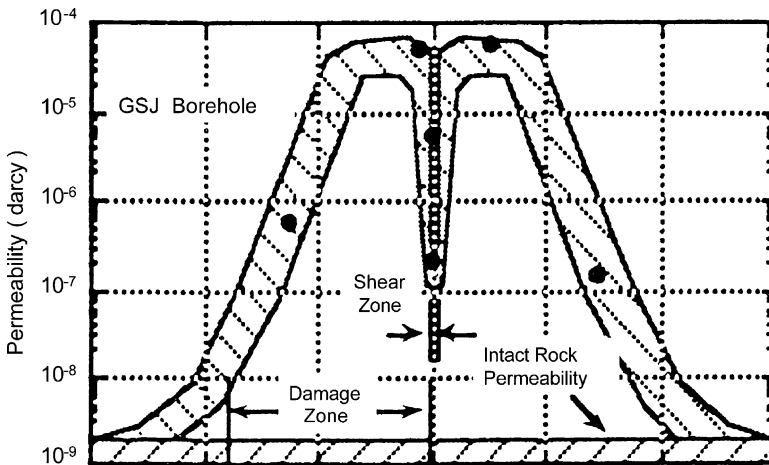


FIG. 15. Nojima fault core permeability at 50 MPa pressure. The central shear zone is marked by low permeability and bounded on both sides by high permeability damage zones (from Lockner *et al.*, 2000).

### 3.4. The Median Tectonic Line, Japan

The MTL is a right-lateral strike-slip fault dipping about  $65^\circ$  to the north and located in the Mie prefecture. With a length of nearly 1000 km, it is the most prominent onshore fault in Japan. Ichikawa (1980) estimated that the MTL has been active since the Cretaceous and has a poorly constrained displacement between 200 and 1000 km.

When Wibberley and Shimamoto (2003) examined the fault zone structure and measured the permeability of borehole samples, they found asymmetrical structures and suggested the reason had to do with the different lithologies on either side of the fault: Ryoke mylonite on the north side and Sambagawa schist on the south.

While examining thin sections of the Ryoke mylonite, Takagi (1986) saw evidence of significant grain size reduction and mylonization in samples taken up to 1500 m from the fault core. This mylonization was overprinted by cataclasis, leading him to conclude that at one time the Ryoke formation underwent mylonitic deformation, but was later uplifted to the brittle field where it experienced additional cataclasis. The Sambagawa schist also has evidence of cataclasis, but no evidence of grain size reduction or mylonization. Takagi suggests that the two very different strain histories of the Ryoke and Sambagawa formations are somehow responsible for the asymmetric fault structures of the MTL.

Wibberley and Shimamoto (2003) describe the fault zone as follows: a 10-cm-wide ultracataclasite layer is bounded to the north by a 4-m-wide layer of foliated cataclasites, bounded in turn by gouge, breccia, and damage zones that extend 300 m into the Ryoke mylonite wall rock. To the south, the ultracataclasite layer is bounded by a 15-m-wide layer of foliated cataclasite, which borders directly on the Sambagawa schist wall rock. There is no gouge and breccia layer, or damage zone, to the south of the MTL.

From core sample measurements, Wibberley *et al.* found that the ultracataclasite and foliated cataclasite layers were almost impermeable. Samples to the north of the MTL, in the 300-m-wide gouge and breccia layer, and damage zone, had high permeabilities. Only low permeability zones could be found south of the MTL.

### 3.5. The Carboneras Fault, Southeastern Spain

The Carboneras fault is a major left lateral fault, part of the Trans-Alboran Shear Zone that cuts across the southeastern margin of the Iberian Peninsula (Rutter *et al.*, 1986; Keller *et al.*, 1995; Bell *et al.*, 1997; Faulkner *et al.*, 2003). Estimates of the amount of lateral displacement vary from 18 km to 35 to 40 km

(Keller *et al.*, 1995). Bell *et al.* (1997) concluded from observations and radiometric dating of offset streams that lateral slip on the fault ended 100 ka. Afterward it was uplifted and eroded about 1.5–4 km (Rutter *et al.*, 1986).

Faulkner *et al.* (2003) reported that the Carboneras fault was one of the few faults they knew that did not fit into the Punchbowl model. The fault is about 1 km in width having alternating layers of foliated cataclasite and ultracataclasite, each on average  $\sim 100$  m thick, separated by lenses of shattered country rock. They argue that the differences between the Carboneras and Punchbowl faults result from the different country rock of the two faults. The Punchbowl protolith is quartzofeldspathic rock, known to be strain weakening which facilitates localization into a single core. The Carboneras fault cuts through phyllosilicate rich country rock. Phyllosilicates are known to strain harden contributing to make an ultracataclasite layer that strain hardens and delocalizes strain (Logan *et al.*, 1992). Faulkner *et al.* (2003) hypothesize that with increasing displacement, different layers of the ultracataclasite lock up which causes additional blocks of the country rock to break off and incorporate into the fault.

In contrast, Keller *et al.* (1995) view the Carboneras fault as a *system* comprised of a plurality of faults zones, each zone separated from the other by shear lens which they consider the main architectural units of the fault system. Each fault zone has most of the structure of the Punchbowl fault, including gouge and cataclasite zones (foliated and ultracataclasite layers) tens of meters thick and lengths of hundreds of meters to kilometers. They conclude that tectonic shear is distributed over the different faults according to the dominant stress field at the time.

#### 4. THE STRUCTURE OF MATURE, LARGE DISPLACEMENT DIP-SLIP FAULTS

In general, the structure of dip-slip fault zones is asymmetric. In normal faults, the footwall shows the Punchbowl structures and the hanging wall is usually undamaged. In reverse faults, the hanging wall shows the Punchbowl structures and the footwall is undamaged (Cooper and Norris, 1994). This is probably a consequence of the exhumation of the upward moving wall while the opposing wall has remained at shallow depth (Cowan *et al.*, 2003).

##### 4.1. The Badwater Turtleback Normal Faults, Death Valley, CA

Cowan *et al.* (2003) described four low-angle normal faults located in the Black Mountains, southern California (see Fig. 16). Due to normal slip, the

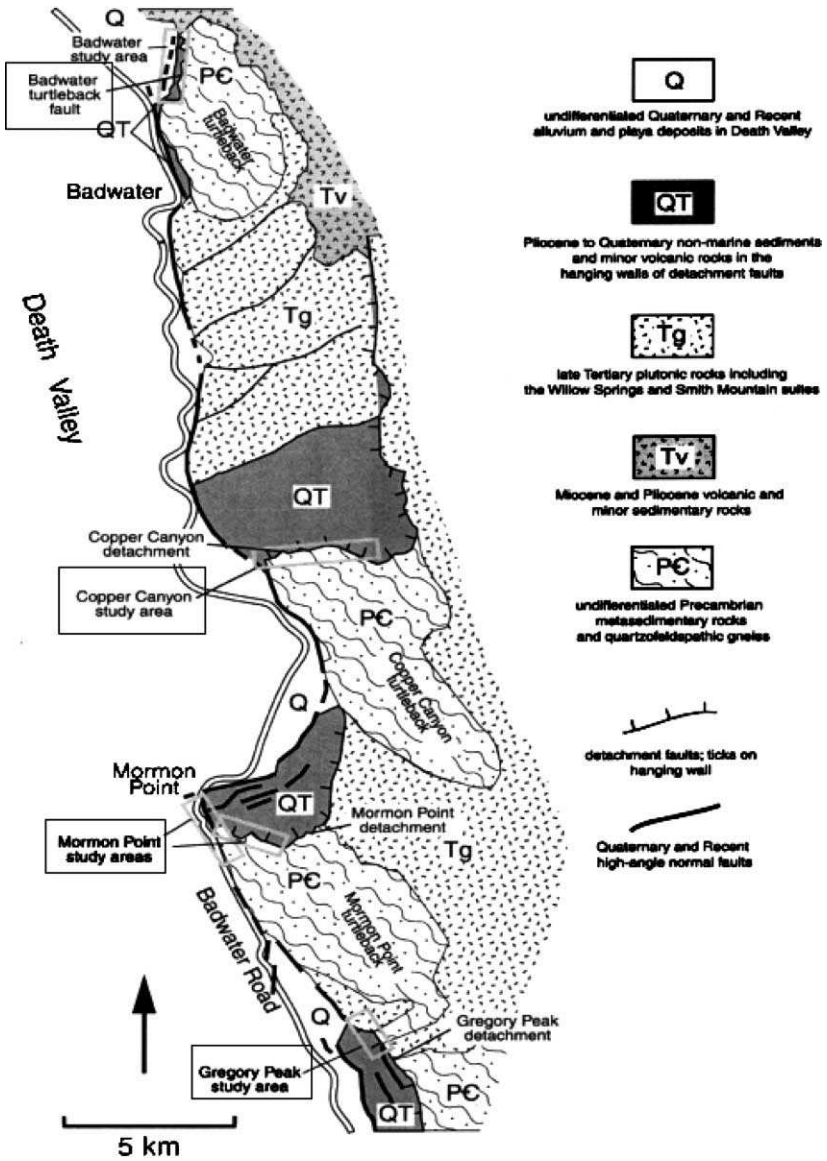


FIG. 16. Geologic map of the western flank of the Black Mountains, southern California. The four normal faults studied by Cowan *et al.* (2003) are shown in boxes.

footwall was exhumed from depths estimated at 10–12 km. The total throw on the fault was 4.5–7 km minimum and 10–15 km maximum. Figure 17a,b shows the structure of the Badwater Turtleback fault zone. Cowan *et al.* (2003) conclude that all four fault zones in this study had similar structures that could be characterized as follows:

1. The hanging wall shows none of the damage usually associated with wall rock, such as microfractures and subsidiary faults. Instead, it contains numerous planar, listric normal faults, often with injections of fault gouge from the fault core. Cowan *et al.* suggest these injections of ultracataclasite are evidence of generalized gouge mobility which we discuss in more detail below.
2. A PFS (which Cowan calls a principal slip surface) forms the lower bound of the hanging wall.
3. The fault core contains two zones:
  - Zone 1:* an upper zone of fault rock that corresponds to the ultracataclasite layer in the Punchbowl model with thickness of  $\sim 10\text{--}20$  cm.
  - Zone 2:* a lower zone of mostly foliated breccia on average  $\sim 40$  cm thick. This probably corresponds to the foliated cataclasite zone in the Punchbowl model since it appears to have accommodated significant shear and should be included in the fault core.
4. A footwall with spatially variable damage extending about 10 m or less below the PSS. This corresponds to the damage zone in the Punchbowl model. It is interesting that the low strain gouge and breccia zones in the Punchbowl model appear to be missing in these normal faults.

The authors attribute this fault asymmetry to progressive upward transport of the footwall. They suggest that at one time, when both sides of the fault were at depth, the fault may have been symmetric and both walls may have contained similar deformation structures. As the footwall was progressively transported upward, the highly damaged footwall and gouge zone came to be juxtaposed against essentially undamaged hanging wall rock which was only recently buried.

#### 4.2. The Chelungpu Fault, Taiwan

The Chelungpu fault is a major reverse fault in Taiwan (Meng, 1963; Chang, 1971), one of three major east-dipping faults in that region, with an age of about 700 ka (Chen *et al.*, 2000). In the north, it follows the bedding of the Pliocene age Chinshui shale, dipping steeply to the east 45–80°, while in the south it dips only 20–40° east, crossing the Chinshui bedding planes at an angle.

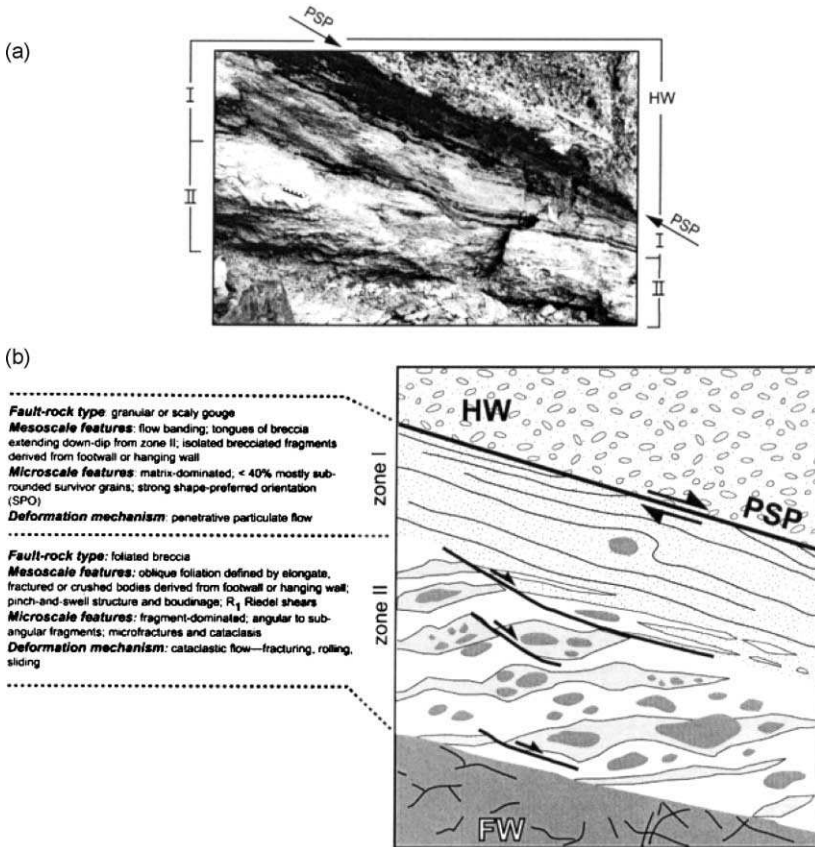


FIG. 17. (a) Photograph of the Badwater fault zone. HW, hanging wall of quaternary fanglomerate; PSP, principle slip plane; I, fault rocks in Zone I; II, fault rocks in Zone II; FW, footwall. (b) Generalized cross-section of a detachment fault in the Black Mountains. Fault rock thickness in Zones I and II typically range from  $\sim 10$  cm to 1 m (from Cowan *et al.*, 2003).

The Chelungpu fault in Taiwan ruptured on September 21, 1999, in the  $M_W$  7.6 Chi-Chi earthquake (Shin and Teng, 2001). Both seismic and GPS data recorded significant differences in propagation between the southern and the northern sections of the fault. Lee *et al.* (2002) reported that GPS measurements showed a northward increase in horizontal displacement, trending from 2 to 3 m in the south to 7 to 8 m in the north, with vertical offsets from 2 m in the south to 4 m in the north to about 8 m along the northern-most part of the fault (Chen *et al.*, 2001). The average slip velocity on the southern part of the fault was about 40 cm/s

while the northern section experienced more than 2 m/s (Huang *et al.*, 2001; Ma *et al.*, 2003). Rise times and stress drops also differed markedly (Huang *et al.*, 2001).

Following the Chi-Chi event, several boreholes were drilled into the northern and southern sections of the fault plane. Heermance *et al.* (2003) observed that the northern cores showed a very thin, localized ultracataclasite layer about 1–20 cm thick. Extremely narrow (50–300  $\mu\text{m}$  thick) clay layers were also seen that probably originated with previous ruptures. In addition, the cores had an elevated fracture density extending 30–50 m into the hanging wall above the fault. The fracture density dropped off abruptly in the footwall (see Fig. 18). Here it is the exhumation of the hanging wall from depth that probably explains this asymmetry (Cowan *et al.*, 2003).

Core samples from the southern borehole differed from those in the north. They possessed a 20–70 m wide zone of diffuse sheared clay gouge subparallel to the bedding planes of the Chinshui shale.

Heermance *et al.* (2003) suggest that the different structure found in the northern and southern core samples indicates different degrees of localization occurring in the two sections. The northern fault plane is parallel to the bedding of the Chinshui shale, which enhances localization. In the south, the fault plane crosses the bedding, so localization is less developed.

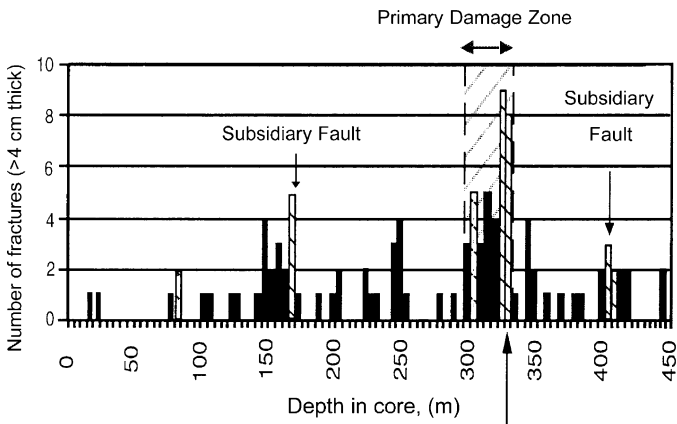


FIG. 18. Number of fractures in core samples taken at different depths in Chelungpu borehole. Only fractures greater than 4 cm in length were counted. Note the increase in fracture density at about 300 m and an abrupt drop in fractures at about 326 m (from Heermance *et al.*, 2003).

At least three different mechanisms have been proposed to explain the complex fault rupture observed in the Chi-Chi earthquake, and each of these depends upon the structure of the Chelungpu fault. Heermance *et al.* (2003) propose that the different degrees of localization observed in the northern and southern sections may explain the different styles of rupture. The high degree of localization in the north facilitated a high slip velocity, large displacement and the absence of high frequency ground motion. The opposite was observed to the south where localization is less developed.

In contrast, Ma *et al.* (2003) propose that fault lubrication in the northern section of the fault explains the differences in rupture behavior (Brodsky and Kanamori, 2001). Fault lubrication is most likely to occur when the fault walls are close together due to extreme localization. Under those conditions a wave develops in front of the rupture and relieves the normal load so the rupture quickly and smoothly propagates. Finally, Oglesby and Day (2001) argue that fault geometry alone can explain the rupture differences observed in the Chi-Chi earthquake.

## 5. FORMATION OF FAULT ZONE STRUCTURE

Having reviewed field observations of exhumed zones, we turn our attention to the question of how these structures are formed, and whether they might contain useful information about the earthquake process. We begin with the formation of shear zones in low porosity crystalline rock containing preexisting tensile fractures, then turn our attention to shear zone formation in high porosity rock.

### 5.1. Fault Zone Formation in Low Porosity Jointed Rock

Segall and Pollard (1983a,b) studied fault formation in granodiorite exposures of the Sierra Nevada Mountains near Bear creek, CA. They began by distinguishing between joints and small faults. *Joints* were tensile fractures in rock with no apparent shear offset while *small faults* had notable shear displacement. They hypothesized that the small faults were formed by reactivation of preexisting joints, which is energetically more favorable than creating new fracture surface. They added that whenever a suitable number of preexisting joints are present, the preexisting structures will have a strong influence on the nucleation and growth of subsequent faults.

Martel *et al.* (1988) continued Segall and Pollard's (1983a,b) work at Bear creek by grouping fractures into "domains" with approximately the same

orientation. Under shear loading, all cracks within a domain form small faults. As shear strain increases, oblique fractures (called “splay fractures”) propagate from the ends of the faults to link with other small faults within the domain (Segall and Pollard, 1980; Vermilye and Scholz, 1998; Paschell and Evans, 2002). As the density of splay fractures increases, the rock between the small faults is broken into blocks. Each domain forms two parallel fractures on opposite sides, which Martel *et al.* called “boundary fractures”. These act as the edges of a developing through-going fault. With increasing shear strain, the blocks between the boundary fractures are crushed, thus forming a through-going fault shown in Fig. 19a,b. Martel *et al.* suggested these crushed blocks are the origin of fault zone rock (Shipton *et al.*, 2001; Shipton and Evans, 2003). According to Sammis *et al.* (1987) subsequent shearing of this zone creates a fractal particle distribution leading to shear localization and the formation of the fault core.

Other workers have extended the fault forming process to other rock types. These same mechanisms have been shown to work in carbonates (Willemse *et al.*, 1997; Kelly *et al.*, 1998), shales (Engelder *et al.*, 2001), and low porosity sandstones (Cruikshank *et al.*, 1991; Zhao and Johnson, 1992; Myers, 1999; Flodin *et al.*, 2003; Myers and Aydin, 2004).

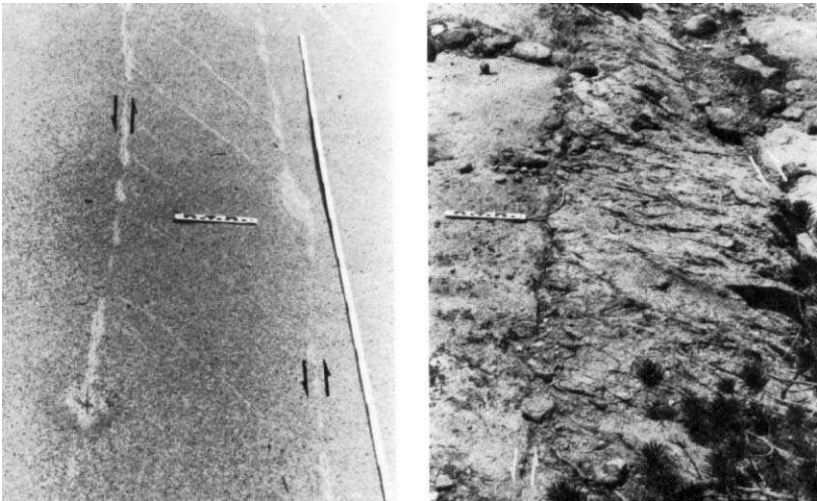


FIG. 19. Simple shear fault zones in different stages of development. *Left*, fault zone in early stage of formation. Double arrows mark the boundary faults. *Right*, fault zone in mature stage of development. Note the contrast in fractures between the two faults. The ruler is 15 cm for scale.

## 5.2. Fault Zone Formation in High Porosity Sandstones

Aydin (1978) and Aydin and Johnson (1978) studied fault formation in the Entrada and Navajo Sandstones of the San Rafael Desert, Utah. In that region, structures called *deformation bands* are commonly found. Often associated with porous ( $> 15\%$ ) sandstone, Aydin (1978) suggested that deformation bands are a strain hardening mechanism. A band can only accommodate a limited amount of strain before it is abandoned and a new adjacent band forms. As deformation bands accumulate, they form *zones* shown in Fig. 20a,b. Eventually one band within the zone becomes a *slip surface* and all future strain becomes localized onto that surface. Thus, fault formation in porous sandstone involves three successive strain mechanisms; deformation bands, deformation zones, and localized slip surfaces. These processes were examined experimentally by Mair *et al.* (2000, 2002) and their results supported the assumptions of Aydin. See also Davatzes and Aydin (2003) and Flodin and Aydin (2004a,b).

Shipton *et al.* (1997), Cowie and Shipton (1998), and Shipton and Cowie (2001, 2003) studied the evolution of these slip surfaces to large displacements in

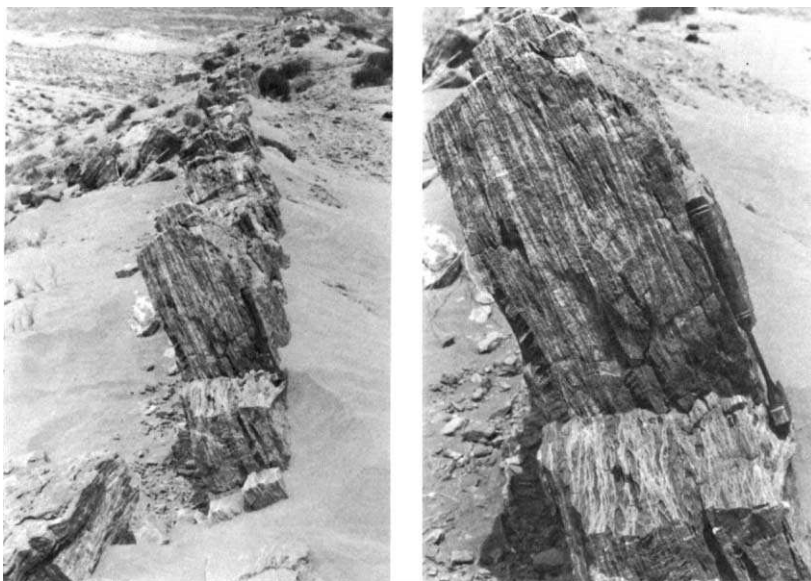


FIG. 20. Zone of deformation bands at Horse Seep Creek in the San Rafael Desert, Utah. *Left*, a row of deformation bands standing as a tilted wall 1 m high. Note the book for scale along the right side of the first zone. *Right*, close-up view of a zone showing parallel and subparallel bands in vertical section.

the Big Hole and Blueberry faults, Navaho Sandstone, Utah. Both normal faults have large numbers of deformation bands and slip surfaces which form part of the damage zones around these two faults. They found that increasing displacement along the slip surfaces leads to splay fractures which begin to link the slip surfaces. Eventually, the surfaces coalesce into a dominant slip surface which forms a through-going fault. The blocks of rock between the linked slip surfaces are crushed to form the fault zone rocks for the new fault, as in the crystalline rock discussed above (Schultz and Balasko, 2003).

### 5.3. Fractal Fragmentation and Shear Localization

The fault formation theories we have reviewed thus far explain the existence of shear fractures with a layer of crushed rock sandwiched between them. They do not explain the complex layered structure of the Punchbowl model in Fig. 3, which requires mechanisms to do the following: (1) form a low strain gouge–breccia layer, (2) localize deformation to a core where additional fragmentation produces the foliated cataclasite and ultracataclasite layers within which the mean grain size has been reduced to 1  $\mu\text{m}$  or less, and (3) create a damage zone with fracture density decreasing outward into the host rock.

Sammis *et al.* (1987) proposed that the low strain gouge and breccia layer were formed by a mechanism they dubbed “constrained comminution”. In normal comminution processes, such as grinding or milling, the particles are free to move relative to one another. The fracture probability of a particle is controlled by its size, with larger particles being weaker because they contain larger flaws. When a particle breaks, the size distribution of the fragments is controlled by the Poissonian distribution of these flaws, and the resultant observed “Rosin-Ramler” particle distribution is an exponential function (Sammis *et al.*, 1986). In constrained comminution, the high confining pressure in the faulting environment prevents grains from changing neighbors. In this environment, a grain’s fracture probability is controlled primarily by the loading geometry of its neighbors and secondarily by its size. The grains most likely to fail are those with nearest neighbors of the same size, since they are under uniaxial compressive point loads and fail in tension. Largest particles with same size neighbors are fragmented first since they are the weakest. Isolated large particles survive since they are “cushioned” by being surrounded by smaller particles that more evenly distribute the load. Comminution proceeds by eliminating progressively smaller particles with same-sized neighbors ultimately producing a gouge having no neighbors of the same size at any scale. This is the geometry of the Sierpinski gasket, which had a fractal dimension of 1.58 in 2-D and 2.58 in 3-D, and is the dimension

measure by Sammis *et al.* (1987) in the Lopez Canyon fault gouge and by Chester *et al.* (1993) in the San Gabriel fault.

Biegel *et al.* (1989) simulated constrained comminution in a double-shear friction apparatus that transformed an initially uniform grain size distribution into a fractal distribution with dimension 2.6 following a shear strain of about three. They found that the evolution of the fractal structure was associated with an observed transition from velocity strengthening (stable) friction to velocity weakening (potentially unstable) friction. The mechanical explanation for this transition was that the evolution of a fractal structure suppresses fragmentation, which is inherently velocity strengthening, and promotes shear localization and slip between particles, which is inherently velocity weakening (Sammis and Steacy, 1994). This was the reason Ben-Zion and Sammis (2003) considered the fractal gouge and breccia layer to be a relict structure left over from early fault formation.

#### 5.4. Fragmentation and Off-Fault Damage in the Process Zone of Large Earthquakes

Sammis *et al.* (1987) and Biegel *et al.* (1989) suggested that a lower limit exists to constrained comminution, probably at the scale of 1  $\mu\text{m}$ . In the engineering literature, this is known as the “grinding limit” at which grains run out of starter flaws and deform plastically (Prasher, 1987). Yet, electron photographs show that the ultracataclasis layer contains submicron size grains, as does gouge in the San Andreas fault zone (Reches and Dewers, 2004). Moreover, these grains have sharp angular edges suggesting tensile fracture. A mechanism different from constrained comminution must be working inside the ultracataclasis layer, one capable of fragmenting grains to submicron size. Four possible fragmentation mechanisms are as follows.

##### 5.4.1. *Dynamical Loading by a Propagating Slip-Pulse*

One mechanism for additional tensile fragmentation is high-speed dynamic loading in the crack-tip process zone of an earthquake rupture (Scholz *et al.*, 1993). Rice *et al.* (2004) have shown that a propagating slip pulse generates stresses within the process zone that are strong enough to fragment rock to distances on the order of meters and to nucleate slip on off fault fractures to hundreds of meters thus continuing the fragmentation process close in and generating the damage zone in the wall rock that decreases with distance from the core.

#### 5.4.2. Normal Stress Reduction by a Passing Wrinkle-Pulse

Andrews and Ben-Zion (1997) and Ben-Zion and Andrews (1998) demonstrated that a reduction of the normal stress can result from a contrast in material properties across the fault plane. This material contrast also tends to favor propagation in one direction (the direction of motion of the weaker wall). Such unidirectional propagation of many ruptures is a potential source of asymmetry in the fault zone, because more damage will accumulate on the tensile side of the crack tip. Brune *et al.* (1993) and Brune (2001) argued that such dynamic unloading of the normal stress during passage of an earthquake rupture is capable of fragmenting particles in the ultracataclasis layer.

#### 5.4.3. Failed Branching as a Fragmentation Mechanism

An additional potentially important dynamic fragmentation mechanism involves *branching*. Dynamical branching of shear rupture onto intersecting or adjacent faults was investigated by Dmowska *et al.* (2000, 2002). Their studies demonstrated that under the right conditions, dynamical branching will indeed take place. But while conditions near the crack tip will often favor such branching, the more distant stress field may not. Poliakov *et al.* (2002) and Kame *et al.* (2003) found that a dynamic stress field near the tip of a propagating rupture may favor out-of-plane crack branching at small distances, which is then suppressed by the dynamic field at greater distances. In this case, many small failed branches form near the tip of an earthquake rupture. The result is an array of “failed branches” which further fragment the fault zone core.

#### 5.4.4. Tensile Cracks Produced During Intersonic Shear Crack Experiments

A related fragmentation mechanism is suggested by laboratory studies of intersonic shear crack propagation. Samudrala *et al.* (2002) observed a myriad of short tensile cracks emanating at high angles to the main path of the intersonic shear crack (see Fig. 21).

### 5.5. Wear

Power *et al.* (1988) and Power and Tullis (1991) measured the roughness of fault surfaces, finding self-similarity over a range of scale lengths from microns to meters. They argued that since surface irregularities were present at all scales,

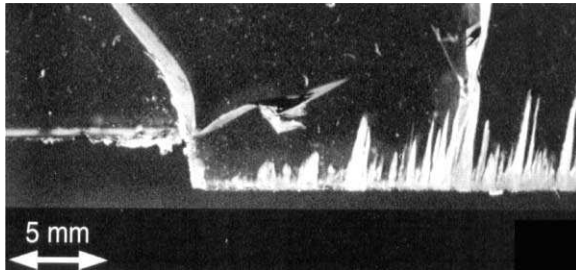


FIG. 21. Secondary tensile cracks formed in the tensile half of a specimen during intersonic shear crack growth experiments (from Samudrala *et al.*, 2002). The opposing surface was sheared left to right against the specimen shown in the photograph.

wear from opposing surfaces should occur at all scales. At small slip, the mismatch of opposing fault surfaces leads to wear of the high frequency irregularities. With more slip, the lower frequency surface features contribute to the wear.

Wang and Scholz (1994) modeled fault wear as the sum of a transient and a steady state process. The original contact and sliding of the surfaces produces transient wear that decays exponentially with sliding distance. This type of wear favors the elimination of the high frequency irregularities. Steady state wear is a linear process that increases with fault slip. This wear eliminates the low frequency irregularities at a rate that is linearly proportional to slip distance.

Wear experiments using a rotary shear apparatus failed to produce enough gouge to explain observations in natural faults (Wang and Scholz, 1994). Wang suggested this was because wear is mainly an abrasion process while fault zones are governed by different mechanisms, or mechanisms in addition to abrasion (Wang and Scholz, 1994). Our review of fault zone formation in an earlier section supports this conclusion. However, Chester *et al.* (2004) have suggested that the extremely fine particles in the ultracataclasite layer of the core may be produced by wear during frictional sliding on the prominent fracture surface.

## 5.6. Pseudotachylytes

Pseudotachylytes (also spelled, pseudotachylites) are somewhat rare melted fault rocks found within inactive, exhumed fault zones (McKenzie and Brune, 1972; Sibson, 1973, 1975, 2003). Shand (1916) coined the term to distinguish his newly discovered fault rock from similar looking, already well known glassy, basalts called tachylytes (Magloughlin and Spray, 1992). Pseudotachylytes have

been described in numerous fault zones (Wenk, 1978; Magloughlin, 1989, 1992), including the Nojima fault (Boullier *et al.*, 2000; Ildefonse *et al.*, 2000).

The exact mechanism for generating pseudotachylytes is not known but there is good agreement that most are products of frictional melting of cataclasites during seismic events in the brittle regime. Heat generated along a fault per unit area is

$$Q = \tau u \text{ (J/mm}^2\text{)} \quad (1)$$

where  $u$  is slip distance and  $\tau$  is the shear strength. When enough localization has occurred to sufficiently reduce the thickness of a slip zone, temperatures can reach the melting point of rock, about 1000°C (Sibson, 2003).

Nevertheless, some pseudotachylytes show clear evidence of originating in the ductile regime (Wenk and Weiss, 1982) but these are thought to form when seismic ruptures from the brittle regime propagate to the lower reaches of the crust (Magloughlin and Spray, 1992).

In contrast to the melting hypothesis, Wenk (1978) suggests that pseudotachylytes are not products of frictional heating, but rather a product of dynamic shock deformation. He argues that the high strain rates present during earthquakes are sufficient to convert highly comminuted cataclasite into a glass. This solves the problem of the heat flow paradox.

Theoretically, frictional heating on fault planes should make pseudotachylytes common. Nevertheless, none have been found at the Punchbowl or San Gabriel faults and overall pseudotachylytes are rarely found in most fault zones. Sibson (2003) argues that one possible explanation for the absence of widespread frictional melting is the presence of fluid saturated fault zones. When the temperature reaches 100°C the fluid pressure increases to near lithostatic levels. This relieves the normal stress and prevents further frictional heating for the remainder of the slip event. We return to this mechanism, called “thermal pressurization”, later in the paper.

Another possible mechanism that could explain the absence of frictional heating and melting is dynamic stress changes during an earthquake. Brune (2001) argues that dynamic reduction of normal stress across a fault occurs during propagation of a “wrinkle pulse”. Any reduction of normal stress diminishes the shear strength,  $\tau$ , thereby reducing the generated heat.

## 6. EFFECTS OF FAULT ZONE STRUCTURE ON DYNAMIC RUPTURE

Having reviewed field observations of fault zone structure and ideas as to how it might have formed, we now ask how this structure might affect rupture

dynamics during an earthquake. We consider separately the effect of structure on the nucleation of a rupture, its propagation, and its arrest.

### 6.1. Effects of Fault Zone Structure on the Nucleation of an Earthquake

It is generally accepted that an earthquake nucleates as a stick-slip friction instability on a fault plane (Dieterich, 1972, 1974; Rice, 1980; Lapusta and Rice, 2003). This instability is caused by a decrease of frictional strength from a static value  $f_s$  to a lower dynamic one  $f_d$ , which occurs over a characteristic displacement  $D_c$  (Dieterich, 1978a,b, 1979a,b; Ruina, 1983). The corresponding drop in shear resistance  $\Delta\tau = \sigma_n(f_s - f_d)$  at normal stress  $\sigma_n$  can be used to define a ‘‘rheological stiffness’’,  $k_r$ , as

$$k_r = \frac{\Delta\tau}{D_c}. \quad (2)$$

A stick-slip instability is possible only if this rheological stiffness is greater than the stiffness  $k_1$  of the loading system. In this case, as displacement increases, the force resisting slip falls faster than does the force driving it, and slip accelerates.

The question here is, what physically determines the characteristic displacement  $D_c$  on a natural fault? Direct observations of slip between two surfaces in the laboratory have shown that  $D_c$  is directly related to the size of contacting asperities (Dieterich and Kilgore, 1994, 1996). If an earthquake nucleates on the prominent slip surface within the core, then rock-on-rock laboratory experiments may be directly relevant to natural faults. However, if the entire core is involved in nucleation, then it may be a granular phenomenon controlled by a characteristic strain (Marone and Kilgore, 1993). In this case  $D_c$  will be larger for thicker fault cores, and may be considerably larger in natural faults than in laboratory experiments.

Observational constraints can be placed on  $D_c$  for natural faults since it controls the minimum size of an earthquake. Dieterich (1986, 1992) demonstrated that the stability condition  $k_r > k_1$  can be used to estimate the minimum radius of an unstable slipping patch. The stiffness of a slipping patch can be estimated using the displacement at its center in a remote shear stress field  $\tau$

$$k_1 = \frac{\tau}{u} = \frac{7\pi\mu}{24r}. \quad (3)$$

The condition  $k_r > k_l$  then yields the radius of a minimum unstable slip patch as

$$r_c = \frac{7\pi\mu D_c}{24\Delta\tau}. \quad (4)$$

An earthquake is only possible on slip patches having  $r > r_c$ .

Richardson and Jordan (2002) present evidence from small events in deep South African mines that the minimum event that nucleates as a stick-slip friction instability has a magnitude near 0.5. By using this to find an equivalent minimum patch radius, they estimated a characteristic displacement on the order of 100  $\mu\text{m}$ , on the same order as laboratory measurements.

This  $D_c$  is much smaller than values estimated from the propagation and arrest of large earthquakes, which are typically on the order of cm to tens of cm (Gatterri and Spudich, 2000). The implication is either that the  $D_c$  for large events really is larger, in which case large faults do not produce small events, or that the  $D_c$  estimated from the propagation and arrest of large events is controlled by different mechanisms than those responsible for nucleation (Kanamori and Heaton, 2000). The first possibility is not supported by data, although it is always possible that the small events, which appear to nucleate on large faults, are actually nucleated on small subparallel faults. We now explore the second possibility that the larger  $D_c$  inferred from seismic data represents a different mechanism.

## 6.2. Effect of Fault Zone Structure on the Propagation of an Earthquake Rupture

Once an earthquake rupture has nucleated, its propagation is controlled by the flow of elastic energy to the stress concentration at its tip (Freund, 1972, 1979; Ida, 1972, 1973; Ida and Aki, 1972; Hussein *et al.*, 1975, 1976; Rice, 1980; Dmowska and Rice, 1986; Aki and Richards, 2002). We illustrate the physics of propagation using the analytical solution for a propagating shear pulse from Rice *et al.* (2004) shown in Fig. 22. This model was motivated by Heaton's (1990) observation that slip during many large earthquakes occurs as a propagating dislocation with finite width  $L$  as illustrated in Fig. 23. In the model, a slipping patch of length  $L$  propagates on a fault plane at constant velocity  $v_r$ . Concentration at the leading crack tip increases the regional stress from its initial value of  $\tau_0$  to a peak value  $\tau_{\text{peak}}$ , which is determined by the coefficient of static friction  $f_s$  such that  $\tau_{\text{peak}} = f_s \sigma_n$ . When slip begins, shear stress on the fault plane falls to a residual dynamic value  $\tau_{\text{res}} = f_d \sigma_n$ , where  $f_d$  is the coefficient of dynamic friction. This decrease in fault strength occurs over a distance  $R$  and

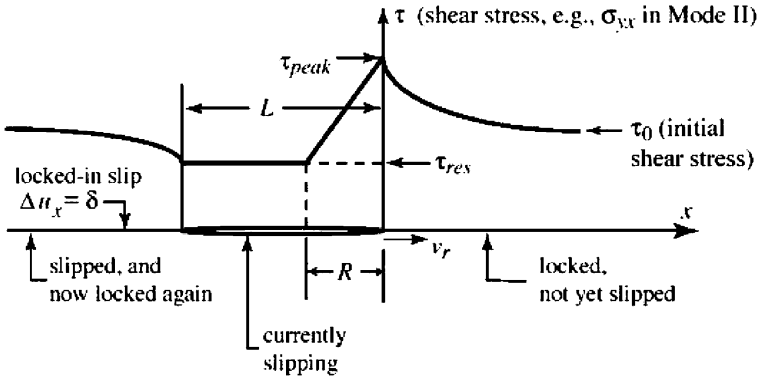


FIG. 22. Stress field around a slip pulse during rupture propagation. This plot is shear stress against distance.  $R$  is the slip weakening distance.  $L$  is the length of the pulse. Note the pulse is locked at the left (from Rice, 2003).

requires a characteristic displacement  $D_c$  (which Rice *et al.* (2004), call  $\delta_1$ ). The total locked-in slip produced by the slip patch is  $\delta$ .

The fracture energy in this model is the area under the slip-weakening curve as illustrated in Fig. 24. It may be written

$$G \equiv \int_{x=0}^{x=-R} [\tau(\Delta u_x) - \tau_{res}] d\Delta u_x = \frac{\mu \delta^2}{\pi L} F_1\left(\frac{R}{L}\right) F_2\left(\frac{v_r}{c_s}\right). \quad (5)$$

Functions  $F_1$  and  $F_2$  are defined in Rice *et al.* (2004). Observed values for  $L$ ,  $v_r$ , and  $\delta$  for the seven earthquakes in Heaton (1990), were used in Eq. (4) to estimate  $G$ . The function  $F_1$  varies by a factor of two as  $R/L$  varies from  $0^+$  to 1.

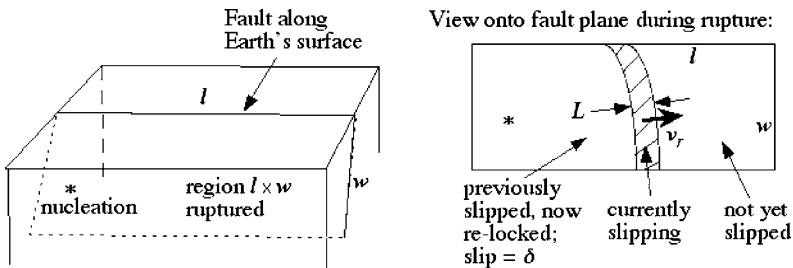


FIG. 23. *Left*, drawing of fault plane on which rupture will propagate. *Right*, shows the slip pulse propagating across fault plane at length,  $L$ , from the source, denoted by asterisk. Note the pulse is not slipping to the front of the pulse, and locks up after the pulse passes (from Rice, 2003).

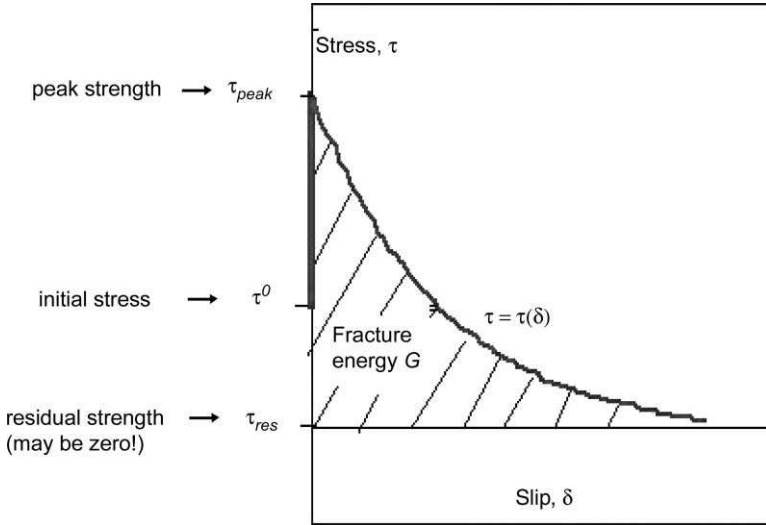


FIG. 24. Relation of fracture energy to slip weakening. The fracture energy is defined as the area under the graph of shear stress vs. slip distance.

Since we have no way of knowing  $R/L$ , this introduces a factor of two uncertainty into the estimates which varied from 0.1 to 9 MJ/m<sup>2</sup> (including the factor), averaging 2–4 MJ/m<sup>2</sup>.

The fracture energy inferred by Rice *et al.* (2004) was observed to increase with displacement (event size) consistent with observations by Abercrombie and Rice (2004). This is also consistent with earlier results from Scholz *et al.* (1993), who used the post-yield fracture mechanics model of Cowie and Scholz (1992) to argue that fracture energy should increase linearly with fault length.

The characteristic displacement was estimated from the fracture energy

$$D_c = \frac{G}{(\tau_{peak} - \tau_{res})} \quad (6)$$

by assuming that  $\tau_{peak} \gg \tau_{res}$ ,  $(\tau_{peak} - \tau_{res}) \approx \tau_{peak} = f_s \bar{\sigma}_n$ . These estimates of  $D_c$  are obviously uncertain by the same factor of two inherent in  $G$ , and range from 0.3 to 10 cm (including the factor), averaging 2–4 cm. There is also a slight increase in  $D_c$  with event size.

The stress drop was also estimated from the fracture energy

$$(\tau^0 - \tau_{\text{res}}) = \frac{G}{\delta}. \quad (7)$$

Including the factor of two uncertainty in  $G$ , these values ranged from 0.3 to 6.6 MPa with an average of 2–4 MPa. There was no apparent trend in stress drop with event size.

The stress concentration near the crack tip for this model is shown in Fig. 25 where all distances are scaled by  $R_0^*$ , the value of  $R$  in the low rupture velocity, low stress drop limit which is proportional to  $G/(\text{strength drop})^2$ . At high rupture speeds, secondary faulting and damage should extend to distances from the prominent slip surface on the order of  $1-2 R_0^*$  which is on the order of 1–80 m for a 100 MPa strength drop.

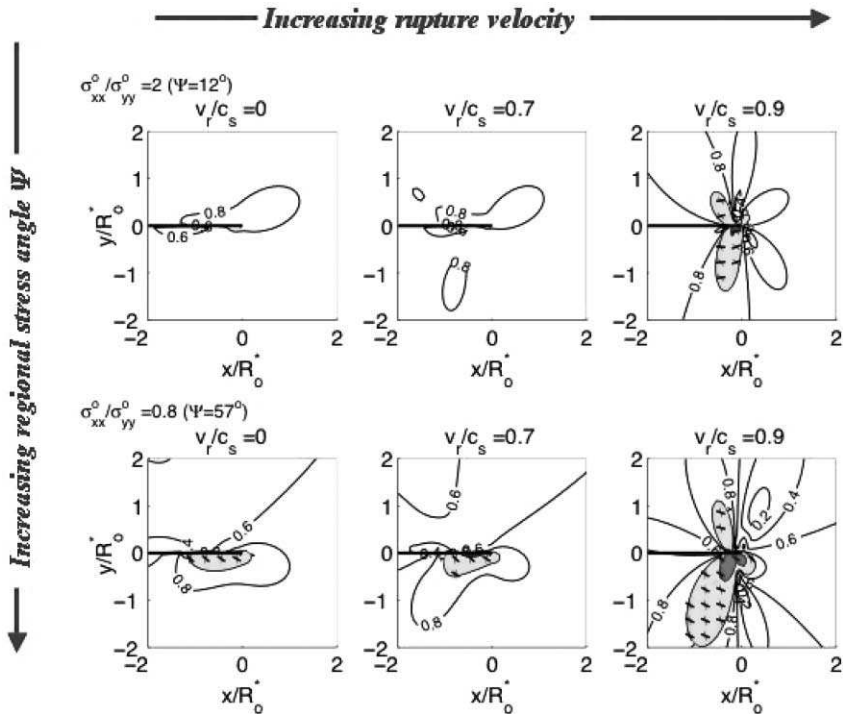


FIG. 25. Contour plot of shear stress normalized by the Coulomb criterion as a function of position surrounding the tip of a slip pulse. Within shaded areas this number is  $>1$ , meaning slip on preexisting fractures is possible (from Rice, 2003).

How this off-fault damage affects the fracture energy of an earthquake is an open question. Andrews (2004) has proposed a dynamic model which explains off-fault damage as a by-product of propagating rupture energy that transforms the elasticity of fault zone material to a pseudo-elastic medium. This reduces the energy flow to the tip of subsequent ruptures and effectively increases  $D_c$  and  $G$ .

Burgmann and Pollard (1994) examined slip profiles from the Superstition Hills earthquake and observed that the profiles were not elliptical as predicted by fracture mechanics. They used numerical modeling to study parameters controlling the evolution of mature faults and proposed lateral heterogeneities in elasticity of the rock as a possible cause for the non-elliptical profiles.

Manighetti *et al.* (2001) presented field evidence that off-fault damage may play an important role in earthquake mechanics. They measured slip profiles of about 300 normal faults in the Afar region of NE Africa with lengths from 100 m to 60 km and vertical displacements ranging from 1 to 1000 m. Although the maximum slip,  $d_{\max}$ , was proportional to the fault length,  $L$  ( $d_{\max} = 0.015L$ ), they found that only about 15% had the elliptical slip profiles predicted by elastic dislocation theory. The remaining 85% had triangular slip profiles. Figure 26 shows a slip profile for one normal fault.

Manighetti *et al.* (2004a) demonstrated that the relaxation of the crack tip stress concentration by off-fault fracture damage leads to a triangular slip profile. This relaxation of stress at the crack tip also reduces the stress intensity factor and suppresses crack growth. Manighetti *et al.* (2004a) argue that such faults grow mainly by linking with other faults producing the observed hierarchical

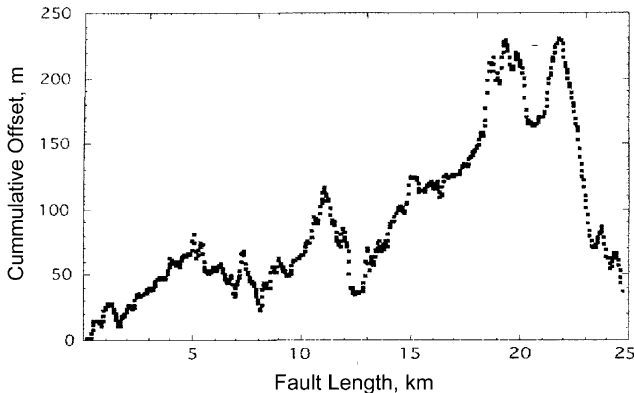


FIG. 26. A multi-segment normal fault slip profile taken from Manighetti *et al.*, 2001. The profile suggests the fault is actually comprised of three subsegments, each with its own triangular slip profile (from Manighetti *et al.*, 2004a,b).

substructure in which the triangular slip profile is composed of smaller triangles. Manighetti *et al.* (2004b) have extended this work to show that cumulative slip profiles for strike-slip faults tend to be triangular as do the slip profiles of individual large earthquakes.

The central question in relating fault zone structure to dynamic propagation is: what physical mechanism of weakening operates during slip? Andrews (2002) and Rice (2003) argue that the thermal pressurization of pore fluid may be a primary mechanism. Rice (2003) shows that either the shearing of a thin layer of saturated gouge or slip on a prominent slip surface in contact with saturated cataclastic layers can yield values of  $G$  and  $D_c$  comparable to those inferred by Abercrombie and Rice (2004) and Rice *et al.* (2004). The thermal pressurization model even yields the slight increase in  $G$  with slip (event size) inferred in these papers, and by Scholz *et al.* (1993). Although the water temperature rises a few hundred degrees C, melting does not occur at shallow to moderate depths. In this model, the porosity and permeability of the fault core are important parameters. The characteristic displacement in this model is the slip required to frictionally heat the pore fluid, and bears no relation to the asperity-based  $D_c$  thought to control nucleation. This may explain why the two values appear to be so different.

### 6.3. Effect of Fault Zone Structure on the Arrest of an Earthquake Rupture

What stops an earthquake rupture once it begins to propagate? Two possibilities are: (1) it encounters a fault patch requiring a large fracture energy  $G$  (Papageorgiou, 2003) or (2) it encounters a region of low shear stress. In either case the flow of elastic energy to the crack tip is not sufficient to provide the fracture energy and propagation stops. For example, Aki (1979) calculated the fracture energy of a barrier required to stop the Parkfield earthquake. Assuming a stress drop of 5 MPa and a fracture radius of 3 km, Aki estimated that a patch having  $G = 0.8 \text{ MJ/m}^2$  would stop the event. For the 1857 Fort Tejon, a barrier with  $G = 100 \text{ MJ/m}^2$  was required to halt propagation. These and other estimates are summarized by Li (1987). One interesting question is whether such barriers can be recognized by studying exhumed faults in the field. Do areas of increase in fracture energy correspond to geometrical asperities on the fault plane, such as bends and jogs of the fault plane, or do they reflect variation in the fault zone rocks along the strike? It is well known that the thickness of the gouge and breccia layers vary significantly along strike. Is it possible that these variations record the arrest of rupture?

## 7. DISCUSSION

This review has focused on the overlap between fault zone structure and fault mechanics. We asked how earthquakes modify fault zone structure and how structure of fault zones might affect earthquake mechanics. We found that fault zone structure is mostly the result of two processes: fault growth and dynamic stress concentrations in the process zone of large earthquakes. During growth, faults develop a zone of crushed rock as smaller faults are linked and geometrical barriers are removed in an evolution toward geometrical simplicity. Latter stages involve fractal fragmentation and shear localization. (For a complimentary review of these processes, see Ben-Zion and Sammis, 2003.) However, this crushed zone is further modified by the dynamic stresses at the fronts of propagating earthquake ruptures. These stresses are capable of granulating rock to distances of meters from the fault plane and producing fresh fractures to distances on the order of hundreds of meters (Rice *et al.*, 2004).

The effect of fault zone structure on earthquake mechanics was discussed in the context of the nucleation, propagation and arrest of rupture. The question of whether nucleation is a surface phenomenon occurring on the prominent slip surface or a granular phenomenon including the entire fault core is still an open question. The observation that values of  $D_c$  and  $G$  found for the smallest earthquakes in South African mines are in agreement with those observed in the laboratory (Richardson and Jordan, 2002) suggests that  $D_c$  and  $G$  can be treated as material properties when considering earthquake nucleation.

The effect of structure on propagation is more subtle, usually involving models that include the effects of water within the fault core. Some have suggested that the impermeable fault core acts as a seal that holds fluids within it and frictional heating produces thermal pressurization and weakening. Sibson (2003) argues that the lack of evidence for frictional melting along faults strongly suggests thermal pressurization is an active mechanism during earthquakes. Abercrombie and Rice (2004) have suggested that thermal pressurization could lengthen the characteristic displacement,  $D_c$ , because the energy used by the earthquake to raise fluid temperatures also reduces the amount of available energy needed to continue propagating the rupture. This delay in the stress drop has the effect of increasing the fracture energy,  $G$ . Andrews (2004) has suggested off-fault damage may likewise reduce the strain energy available for propagating the rupture. If this is true, it explains why  $D_c$  and  $G$  measured in the laboratory are orders of magnitude smaller than values measured for earthquakes. It also implies that during the propagation phase of an earthquake  $D_c$  and  $G$  are not physical constants derived from ordinary linear elastic fracture mechanics, but rather properties of the fault zone structure.

The effect of structure on arrest of earthquakes is usually discussed in the context of heterogeneities either in the fault zone or in the stress field. The heterogeneity can take two forms: either a high stress barrier, such as an asperity which can resist the propagating rupture front, or a region of stress relaxation near a recently slipped fault which reduces the strain energy available to continue rupture propagation. Manighetti *et al.* (2001, 2004a,b) argue that these heterogeneities can be observed through their control on the shape of slip profiles.

The number of exhumed fault zones that have been characterized is small and many questions remain. What produces fault zone asymmetry observed in some strike-slip faults? Is it lithology or dynamic propagation effects? How does fault zone structure change with depth? No single exhumed fault has been studied over a significant range of seismogenic depths. What is the wavelength and amplitude of along-fault variations in structure for a single fault, and what is its source? The answers to these and other questions as to the relation between the structure and mechanics of faults will require many more field studies of suitable exhumed fault zones.

#### ACKNOWLEDGEMENTS

We would like to thank Frederick Chester for helpful discussions regarding the Punchbowl and San Gabriel faults. We would also like to thank Geoffrey King and two anonymous reviewers for their many helpful suggestions for improving this paper.

#### REFERENCES

- Abercrombie, R., and Rice, J. (2004). Can observations of earthquake scaling constrain slip weakening? *Geophys. J. Int.* submitted.
- Aki, K. (1979). Characterization of barriers on an earthquake fault. *J. Geophys. Res.* **84**, 6140–6148.
- Aki, K., and Richards, P. (2002). “Quantitative Seismology.” 2nd ed. University Science Books, Sausalito, CA.
- An, L., and Sammis, C. G. (1994). Particle-size distribution of cataclastic fault materials from Southern California—A 3-D study. *Pure Appl. Geophys.* **143**, 203–227.
- Anderson, J. L., Osborne, R. H., and Palmer, D. F. (1983). Cataclastic rocks of the San Gabriel fault—an expression of deformation at deeper crustal levels in the San Andreas fault zone. *Tectonophysics* **98**, 209–251.
- Andrews, D. J. (2002). A fault constitutive relation accounting for thermal pressurization of pore fluids. *J. Geophys. Res.* **107**(B12), ESE 15-1–15-8.
- Andrews, D. J. (2004). Rupture dynamics with energy loss outside the slip zone. *J. Geophys. Res.* submitted for publication.
- Andrews, D. J., and Ben-Zion, Y. (1997). Wrinkle-like slip pulse on a fault between different materials. *J. Geophys. Res.* **102**, 553–571.
- Aydin, A. (1978). Small faults formed as deformation bands in sandstone. *Pure Appl. Geophys.* **116**, 913–930.

- Aydin, A., and Johnson, A. (1978). Development of faults as zones of deformation bands and as slip surfaces in sandstone. *Pure Appl. Geophys.* **116**, 931–942.
- Bell, J. W., Amelung, F., and King, G. (1997). Preliminary late quaternary slip history of the Carboneras fault, southeastern Spain. *J. Geodyn.* **24**, 51–66.
- Ben-Zion, Y., and Andrews, D. J. (1998). Properties and implications of dynamic rupture along a material interface. *Bull. Seismol. Soc. Am.* **88**, 1085–1094.
- Ben-Zion, Y., and Sammis, C. G. (2003). Characterization of fault zones. *Pure Appl. Geophys.* **160**, 677–715.
- Biegel, R., Sammis, C. G., and Dieterich, J. (1989). The frictional properties of a simulated gouge having a fractal particle distribution. *J. Struct. Geol.* **11**, 827–846.
- Boullier, A. M., Ohtani, T., Fujimoto, K., Ito, H., Dubois, M., and Ildefonse, B. (2000). Fluid inclusions in pseudotachylites from the Nojima fault (Japan): implications for seismic processes. *EOS, Trans. Am. Geophys. Union* **81(48)**, 1101.
- Brodsky, E. E., and Kanamori, H. (2001). Elastohydrodynamic lubrication of faults. *J. Geophys. Res.* **106**, 16357–16374.
- Brune, J. N. (2001). Fault-normal dynamic unloading and loading: an explanation for “non-gouge” rock powder and lack of fault-parallel shear bands along the San Andreas fault. *EOS, Trans. AGU* **82(47)**, Fall Meet. Suppl., Abstract S22B-0655.
- Brune, J., Brown, S., and Johnson, P. (1993). Rupture mechanism and interface separation in foam rubber models of earthquakes: and possible solution to the heat flow paradox and the paradox of large overthrust. *Tectonophysics* **218**, 59–67.
- Burgmann, R., and Pollard, D. (1994). Slip distributions on faults: effects of stress gradients, inelastic deformation, heterogeneous host-rock stiffness, and fault interaction. *J. Struct. Geol.* **16**, 1675–1690.
- Chang, S. L. (1971). Subsurface geologic study of the Taichung Basin, Taiwan. *Petrol. Geol. Taiwan* **8**, 21–45.
- Chen, C. H., Ho, H. C., Shea, K. S., Lo, W., Lin, W. H., Chang, H. C., Huang, C. S., Lin, C. W., Chen, G. H., Yang, C. N., and Lee, Y. H. (2000). “Geologic map of Taiwan.” Central Geologic Survey, Ministry of Economic Affairs, ROC, scale 1:500,000.
- Chen, Y. G., Chen, W. S., Lee, J. C., Lee, Y. H., Lee, C. T., Chang, H. C., and Lo, C. H. (2001). Surface rupture of 1999 Chi-Chi earthquake yields insights on active tectonics of central Taiwan. *Bull. Seismol. Soc. Am.* **91**, 977–985.
- Chester, F., and Chester, J. (1998). Ultracataclasite structure and friction processes of the Punchbowl fault, San Andreas system, California. *Tectonophysics* **295**, 199–221.
- Chester, F. M., and Logan, J. M. (1986). Implications for mechanical properties of brittle faults from observations of the Punchbowl fault zone, California. *Pure Appl. Geophys.* **124**, 79–106.
- Chester, F. M., Evans, J. P., and Biegel, R. L. (1993). Internal structure and weakening mechanisms of the San Andreas fault. *J. Geophys. Res.* **98**, 771–786.
- Chester, J. S., Kronenberg, A. K., Chester, F. M., and Guillemette, R. N. (2003). Characterization of natural slip surfaces relevant to earthquake mechanics. *EOS, Trans. AGU* **84(46)**, Fall Meet. Suppl., Abstract S42C-0185.
- Chester, F. M., Chester, J. S., Kirschner, D. L., Schulz, S. E., and Evans, J. P. (2004). Structure of large-displacement strike-slip fault zones in the brittle continental crust. In “Rheology and Deformation in the Lithosphere at Continental Margins” (G. Karne, B. Taylor, N. Driscoll, and D. Kohlstedt, eds.). Columbia University Press, New York.
- Cooper, A., and Norris, R. (1994). Anatomy, structural evolution, and slip rate of a plate-boundary thrust: the Alpine fault at gaunt Creek, Westland, New Zealand. *Geol. Soc. Am. Bull.* **106**, 627–633.

- Cowan, D. (1999). Do faults preserve a record of seismic slip? A field geologist's opinion. *J. Struct. Geol.* **21**, 995–1001.
- Cowan, D., Cladouhos, T., and Morgan, J. (2003). Structural geology and kinematic history of rocks formed along low-angle normal faults, Death Valley, California. *Geol. Soc. Am. Bull.* **115**, 1230–1248.
- Cowie, P. A., and Scholz, C. H. (1992). Physical explanation for the displacement–length relationship of faults using a post-yield fracture mechanics model. *J. Struct. Geol.* **14**, 1133–1148.
- Cowie, P., and Shipton, Z. (1998). Fault tip displacement gradients and process zone dimensions. *J. Struct. Geol.* **20**, 983–997.
- Cruikshank, K., Zhao, G., and Johnson, A. (1991). Analysis of minor fractures associated with joints and faulted joints. *J. Struct. Geol.* **13**, 865–886.
- Davatzes, N., and Aydin, A. (2003). Overprinting faulting mechanisms in high porosity sandstones of SE Utah. *J. Struct. Geol.* **25**, 1795–1813.
- Dibblee, T. W. (1968). Displacements on the San Andreas fault system in the San Gabriel, San Bernardino, and San Jacinto Mountains, Southern California. (W. R. Dickinson, and A. Grantz, eds.), Proceedings of Conference on Geologic Problems, San Andreas Fault System, Vol. XI, Stanford University Publications in Geological Sciences, Palo Alto, CA, pp. 260–268.
- Dibblee, T. W. (1987). Geology of the Devil's Punchbowl, Los Angeles County, California. In "Geological Society of America Centennial Field Guide—Cordilleran Section" (M. L. Hill, ed.).
- Dieterich, J. (1972). Time-dependent friction in rocks. *J. Geophys. Res.* **77**, 3690–3697.
- Dieterich, J. (1974). Earthquake mechanisms and modeling. *Annu. Rev. Earth Planet. Sci.* **2**, 275–301.
- Dieterich, J. (1978a). Preseismic fault slip and earthquake prediction. *J. Geophys. Res.* **83**, 3940–3947.
- Dieterich, J. (1978b). Time-dependent friction and the mechanics of stick-slip. *Pure Appl. Geophys.* **116**, 790–806.
- Dieterich, J. (1979a). Modeling of rock friction, 1. Experimental results and constitutive equations. *J. Geophys. Res.* **84(B5)**, 2161–2168.
- Dieterich, J. (1979b). Modeling of rock friction, 2. Simulation of pre-seismic slip. *J. Geophys. Res.* **84(B5)**, 2169–2175.
- Dieterich, J. (1986). A model for the nucleation of earthquake slip. In "Earthquake Source Mechanics" (S. Das, J. Boatwright, and C. H. Scholz, eds.), Geophysical Monograph Series 37, Vol. 6. AGU, Washington, DC, pp. 37–47.
- Dieterich, J. (1992). Earthquake nucleation on faults with rate- and state-dependent strength. *Tectonophysics* **211**, 115–134.
- Dieterich, J., and Kilgore, B. (1994). Direct observation of frictional contacts: new insights for state-dependent properties. *Pure Appl. Geophys.* **143**, 283–302.
- Dieterich, J., and Kilgore, B. (1996). Imaging surface contacts: power law contact distributions and contact stresses in quartz, calcite, glass and acrylic plastic. *Tectonophysics* **256**, 219–239.
- Dmowska, R., and Rice, J. R. (1986). Fracture theory and its seismological application. In "Continuum Theories in Solid Earth Physics" (R. Teisseyre, ed.), Physics and Evolution of the Earth's Interior, Vol. 3, Elsevier, Amsterdam, pp. 187–255.
- Dmowska, R., Becker, T. W., and Rice, J. R. (2000). Barrier jumping and going astray on a bend: which faults do it better? *EOS, Trans. Am. Geophys. Union* **81**, 1085.
- Dmowska, R., Rice, J. R., and Kame, N. (2002). Fault branching and rupture directivity. *EOS, Trans. Am. Geophys. Union* Fall Meet. Suppl., Abstract NG21B-0939.
- Engelder, T., Haith, B. F., and Younes, A. (2001). Horizontal slip along Alleghanian joints of the Appalachian plateau: evidence showing that mild penetrative strain does little to change the pristine appearance of early joints. *Tectonophysics* **336**, 31–41.

- Evans, J. P., Shipton, Z. K., Pachell, M. A., Lim, S. J., and Robeson, K. (2000). The structure and composition of exhumed faults, and their implications for seismic processes. In "Proceedings of the 3rd Conference on Tectonic Problems of the San Andreas Fault System" (G. Bokelmann, and R. Kovach, eds.). Stanford University, Palo Alto, CA.
- Faulkner, D. R., Lewis, A. C., and Rutter, E. H. (2003). On the internal structure and mechanics of large strike-slip fault zones: field observations of the Carboneras fault in southeastern Spain. *Tectonophysics* **367**, 235–251.
- Flodin, E., and Aydin, A. (2004a). Evolution of a strike-slip fault network, Valley of Fire State Park, southern Nevada. *Geol. Soc. Am. Bull.* **116**, 42–59.
- Flodin, E., and Aydin, A. (2004b). Faults with asymmetric damage zones in sandstone, Valley of Fire State Park, southern Nevada. *J. Struct. Geol.* **26**, 983–988.
- Flodin, E., Prasad, M., and Aydin, A. (2003). Petrophysical constrains on deformation styles in Aztec sandstone. *Pure Appl. Geophys.* **160**, 1589–1610.
- Freund, L. B. (1972). Energy flux into the tip of an extending crack in an elastic solid. *J. Elastic.* **2**, 341–349.
- Freund, L. B. (1979). The mechanics of dynamic shear crack propagation. *J. Geophys. Res.* **84**, 2199–2209.
- Fujimoto, K., Tanaka, H., Tomida, N., Ohtani, T., and Ito., H. (2000). Characterization of fault gouge from GSJ Hirabayashi core samples and implications for the activity of the Nojima fault, *Proceedings of the International Workshop on the Nojima Fault Core and Borehole Data Analysis*, USGS Open File Report 00-129, pp. 81–102.
- Guatteri, M., and Spudich, P. (2000). What can strong-motion data tell us about slip-weakening fault-friction laws? *Bull. Seismol. Soc. Am.* **90**, 98–116.
- Heaton, T. H. (1990). Evidence for and implications of self-healing pulses of slip in earthquake rupture. *Phys. Earth Planet. Inter.* **64**, 1–20.
- Heermance, R., Shipton, Z., and Evans, J. (2003). Fault structure control on fault slip and ground motion during the 1999 rupture of the Chelungpu fault, Taiwan. *Bull. Seismol. Soc. Am.* **93**, 1034–1050.
- Huang, W. G., Wang, J. H., Huang, B. S., Chen, K. C., Chang, T. M., Hwang, R. D., Chiu, H. C., and Tsai, C. C. P. (2001). Estimates of source parameters for the 1999 Chi-Chi, Taiwan, earthquake based on Brune's source model. *Bull. Seismol. Soc. Am.* **91**, 1190–1198.
- Husseini, M., Jovanovich, D., Randall, M., and Freund, L. (1975). The fracture energy of earthquakes. *Geophys. J. R. Astron. Soc.* **43**, 367–385.
- Husseini, M., Jovanovich, D., and Randall, M. (1976). Fracture energy and aftershocks. *Geophys. J. R. Astron. Soc.* **45**, 393–406.
- Ichikawa, K. (1980). Geohistory of the median tectonic line of southwest Japan. *Mem. Geol. Soc. Jpn* **18**, 187–212.
- Ida, Y. (1972). Cohesive force across the tip of a longitudinal-shear crack and Griffith's specific surface energy. *J. Geophys. Res.* **77**, 3796–3805.
- Ida, Y. (1973). The maximum acceleration of seismic ground motion. *Bull. Seismol. Soc. Am.* **63**, 959–968.
- Ida, Y., and Aki, K. (1972). Seismic source time function of propagating longitudinal-shear cracks. *J. Geophys. Res.* **77**, 2034–2044.
- Ildefonse, B., Pezard, P. A., Ito, H., Zamora, M., and Boullier, A. M. (2000). Physical properties of the Nojima fault from shallow drilling at Hirabayasi, Japan, after the 1995 Kobe earthquake ( $M = 7.2$ ). *EOS, Trans. Am. Geophys. Union* **81(48)**, 1100.

- Ito, H., Kuwahara, Y., Tsutomu, K., Fujimoto, K., and Ohtani, T. (2000). Outline of the Nojima fault drilling by GSI: structure, physical properties and permeability structure from borehole measurements crossing the Nojima fault, Japan, *Proceedings of the International Workshop on the Nojima Fault Core and Borehole Data Analysis*, USGS Open File Report 00-129, pp. 71–80.
- Jahns, R. H., ed. (1954). California division of mines bulletin 170. In “Geology of Southern California.” California Division of Mines, San Francisco.
- Kame, N., Rice, J., and Dmowska, R. (2003). Effects of pre-state and rupture velocity on dynamic fault branching. *J. Geophys. Res.* **108**, ESE 13-1–13-21.
- Kanamori, H., and Heaton, T. (2000). Microscopic and macroscopic physics of earthquakes. In “GeoComplexity and the Physics of Earthquakes” (J. Rundle, D. Turcotte, and W. Klein, eds.), Geophysical Monograph Series, Vol. 120. AGU, Washington, DC, pp. 147–163.
- Keller, J. V., Hall, S. H., Dart, C. J., and McClay, K. R. (1995). The geometry and evolution of a transpressional strike-slip system: the Carboneras fault, SE Spain. *J. Geol. Soc. Lond.* **152**, 339–351.
- Kelly, P., Sanderson, D., and Peacock, D. (1998). Linkage and evolution of conjugate strike-slip fault zones in limestones of Somerset, Northumbria. *J. Struct. Geol.* **20**, 1477–1493.
- Kim, Y. S., Peacock, D. C., and Sanderson, D. J. (2004). Fault damage zones. *J. Struct. Geol.* **26**, 503–517.
- Lapusta, N., and Rice, J. (2003). Nucleation and early seismic propagation of small and large events in a crustal earthquake model. *J. Geophys. Res.* **108(B4)**, ESE 8-1–8-5.
- Lapworth, C. (1885). The Highland controversy in British geology; its causes, course and consequence. *Nature* **32**, 558–559.
- Lee, J. C., Chu, H. T., Angelier, J., Chan, Y. C., Hu, J. C., Lu, C. Y., and Rau, J. (2002). Geometry and structure of northern surface ruptures of the 1999  $M_w = 7.6$  Chi-Chi, Taiwan earthquake: influence from inherited fold belt structures. *J. Struct. Geol.* **24**, 173–192.
- Li, V. C. (1987). Mechanics of shear rupture applied to earthquake zones. In “Fracture Mechanics of Rock” (B. K. Atkinson, ed.). Academic Press, New York, pp. 351–428.
- Lockner, D., Naka, H., Ito, H., and Ikeda, R. (2000). Permeability and strength of core samples from the Nojima fault of the 1995 Kobe earthquake, *Proceedings of the International Workshop on the Nojima Fault Core and Borehole Data Analysis*, USGS Open File Report 00-129, pp. 147–152.
- Logan, J. M., Dengo, C. A., Higgs, N. G., and Wang, Z. Z. (1992). Fabrics of experimental fault zones; their development and relationship to mechanical behavior. In “Fault Mechanics and Transport Properties of Rocks” (B. Evans, and T.-F. Wong, eds.). Academic Press, New York, pp. 33–69.
- Ma, K. F., Brodsky, E. E., Mori, J., Song, T. R. A., and Kanamori, H. (2003). Evidence for fault lubrication during the 1999 Chi-Chi, Taiwan, earthquake ( $M_w$  7.6). *Geophys. Res. Lett.* **30(5)**, 48-1–48-4.
- Magloughlin, J. F. (1989). Nature and significance of pseudotachylite from the Nason Terrane, North Cascade Mountains, Washington. *J. Struct. Geol.* **11**, 907–917.
- Magloughlin, J. F. (1992). Microstructural and chemical changes associated with cataclasis and friction melting at shallow crustal levels: the cataclasite–pseudotachylite connection. *Tectonophysics* **204(3/4)**, 243–260.
- Magloughlin, J. F., and Spray, J. G. (1992). Frictional melting processes and products in geological materials: introduction and discussion. *Tectonophysics* **204(3/4)**, 197–204.
- Mair, K., Main, I., and Elphick, S. (2000). Sequential growth of deformation bands in the laboratory. *J. Struct. Geol.* **22**, 25–42.

- Mair, K., Elphick, S., and Main, I. (2002). Influence of confining pressure on the mechanical and structural evolution of laboratory deformation bands. *Geophys. Res. Lett.* **29**(10), 49-1–49-4.
- Manighetti, I., King, G., Gaudemer, Y., Scholz, C. H., and Doubre, C. (2001). Slip accumulation and lateral propagation of active normal faults in Afar. *J. Geophys. Res.* **106**, 13667–13696.
- Manighetti, I., King, G., and Sammis, C. G. (2004a). The role of off-fault damage in the evolution of normal faults. *Earth Planet. Sci. Lett.* **217**, 399–408.
- Manighetti, I., Campillo, M., Sammis, C. G., Mai, P. M., and King, G. (2004b). Evidence for self-similar, triangular slip distributions on earthquakes; implication for earthquake and fault mechanics. *J. Geophys. Res.* submitted for publication.
- Marone, C. (1998). Laboratory-derived friction laws and their application to seismic faulting. *Annu. Rev. Earth Planet. Sci.* **26**, 643–696.
- Marone, C., and Kilgore, B. (1993). Scaling of the critical slip distance for seismic faulting with shear strain in fault zones. *Nature* **362**, 618–621.
- Marone, C., and Scholz, C. (1989). Particle-size distribution and microstructures within simulated fault gouge. *J. Struct. Geol.* **11**, 799–814.
- Martel, S., Pollard, D., and Segall, P. (1988). Development of simple strike-slip fault zones, Mount Abbot quadrangle, Sierra Nevada, California. *Geol. Soc. Am. Bull.* **100**, 1451–1465.
- McKenzie, D., and Brune, J. N. (1972). Melting on fault planes during large earthquakes. *Geophys. J. R. Astron. Soc.* **29**, 65–78.
- Meng, C. Y. (1963). San-I overthrust. *Petrol. Geol. Taiwan* **2**, 1–20.
- Myers, R. (1999). “Structure and Hydraulics of Brittle Faults in Sandstone” (Ph.D. thesis), Stanford University, Stanford, CA, p. 176.
- Myers, R., and Aydın, A. (2004). The evolution of faults formed by shearing across joint zones in sandstone. *J. Struct. Geol.* **26**, 947–966.
- Noble, L.F. (1954). Geology of the Valyermo (7 1/2') quadrangle and vicinity, California. US Geological Survey Map GQ-50, scale 1:24,000.
- Oglesby, D. D., and Day, S. (2001). Fault geometry and the dynamics of the 1999 Chi-Chi (Taiwan) earthquake. *Bull. Seismol. Soc. Am.* **91**(5), 1099–1111.
- Papageorgiou, A. (2003). The barrier model and strong ground motion. *Pure Appl. Geophys.* **160**, 603–634.
- Paschell, M., and Evans, J. (2002). Growth, linkage, and termination processes of a 10-km-long strike-slip fault in jointed granite: the Gemini fault zone, Sierra Nevada, California. *J. Struct. Geol.* **24**, 1903–1924.
- Poliakov, A., Dmowska, R., and Rice, J. (2002). Dynamic shear rupture interactions with fault bends and off-axis secondary faulting. *J. Geophys. Res.* **107**(B11), ESE 6-1–6-18.
- Power, W., and Tullis, T. (1991). Euclidian and fractal models for the description of rock surface roughness. *J. Geophys. Res.* **96**(B1), 415–424.
- Power, W., Tullis, T., and Weeks, J. (1988). Roughness and wear during brittle faulting. *J. Geophys. Res.* **93**(B12), 15268–15278.
- Prasher, C. (1987). “Crushing and Grinding Process Handbook.” Wiley, New York, 474 pp.
- Reches, Z., and Dewers, T. (2004). Gouge formation by dynamic pulverization during earthquakes. *Earth Planet. Sci. Lett.* submitted for publication.
- Rice, J. R. (1980). The mechanics of earthquake rupture. In “Physics of the Earth’s Interior” (A. Dziewonski, and E. Boschi, eds.). North-Holland, Amsterdam.
- Rice, J. R. (2003). Earthquake fracture energies and weakening of faults by thermal pressurization of pore fluid. *EOS, Trans. AGU* **84**(46), Fall Meet. Suppl., Abstract S41G-01.

- Rice, J., Sammis, C. G., and Parsons, R. (2004). Off-fault secondary failure induced by a dynamic slip-pulse. *Bull. Seismol. Soc. Am.* in press.
- Richardson, E., and Jordan, T. (2002). Seismicity in deep gold mines of South Africa: implications for tectonic earthquakes. *Bull. Seismol. Soc. Am.* **92**, 1766–1782.
- Ruina, A. (1983). Slip instability and state variable friction laws. *J. Geophys. Res.* **88(B12)**, 10359–10370.
- Rutter, E. H., Maddock, R. H., Hall, S. H., and White, S. H. (1986). Comparative microstructures of natural and experimentally produced clay-bearing fault gouges. *Pure Appl. Geophys.* **124**, 3–30.
- Sammis, C. G., and Steacy, S. (1994). The micromechanics of friction in a granular layer. *Pure Appl. Geophys.* **142**, 778–794.
- Sammis, C. G., Osborne, R., Anderson, J., Banerdt, M., and White, P. (1986). Self-similar cataclasis in the formation of fault gouge. *Pure Appl. Geophys.* **124**, 54–78.
- Sammis, C. G., King, G., and Biegel, R. (1987). The kinematics of gouge deformation. *Pure Appl. Geophys.* **125**, 777–812.
- Samudrala, O., Huang, Y., and Rosakis, A. J. (2002). Subsonic and intersonic shear rupture of weak planes with a velocity weakening cohesive zone. *J. Geophys. Res.* **107(B8)**, ESE 7-1–7-32.
- Scholz, C. H. (2002). “The Mechanics of Earthquakes and Faulting.” 2nd ed. Cambridge University Press, Cambridge.
- Scholz, C. H., Dawers, N. H., Yu, J. Z., Anders, M. H., and Cowie, P. A. (1993). Fault growth and fault scaling laws—preliminary results. *J. Geophys. Res.* **98**, 21951–21961.
- Schultz, R., and Balasko, C. (2003). Growth of deformation bands into echelon and ladder geometries. *Geophys. Res. Lett.* **30**, SDE 5-1–5-4.
- Schulz, S. E., and Evans, J. (1998). Spatial variability in microscopic deformation and composition of the Punchbowl fault, southern California: implications for mechanisms, fluid–rock interaction, and fault morphology. *Tectonophysics* **295**, 223–244.
- Schulz, S. E., and Evans, J. (2000). Mesoscopic structure of the Punchbowl fault, southern California and the geologic and geophysical structure of active strike-slip faults. *J. Struct. Geol.* **22**, 913–930.
- Segall, P., and Pollard, D. (1980). Mechanics of discontinuous faults. *J. Geophys. Res.* **85**, 4337–4350.
- Segall, P., and Pollard, D. (1983a). Joint formation in granitic rock of the Sierra Nevada. *Geol. Soc. Am. Bull.* **94**, 563–575.
- Segall, P., and Pollard, D. (1983b). Nucleation and growth of strike slip faults in granite. *J. Geophys. Res.* **88**, 555–568.
- Shand, S. J. (1916). The pseudotachylite of Parijs (Orange Free State). *Q. J. Geol. Soc. Lond.* **72**, 198–221.
- Shin, T., and Teng, T. (2001). An overview of the 1999 Chi-Chi, Taiwan, earthquake. *Bull. Seismol. Soc. Am.* **91**, 895–913.
- Shipton, Z., and Cowie, P. (2001). Damage zone and slip-surface evolution over  $\mu\text{m}$  to km scales in high-porosity Navajo sandstone, Utah. *J. Struct. Geol.* **23**, 1825–1844.
- Shipton, Z., and Cowie, P. (2003). A conceptual model for the origin of fault damage zone structures in high-porosity sandstone. *J. Struct. Geol.* **25**, 333–344.
- Shipton, Z. K., and Evans, J. P. (2003). Slip localization on narrow surfaces within exhumed fault zones: implications for earthquake rupture processes and seismic energy budgets. *EOS, Trans. AGU* **84(46)**, Fall Meet. Suppl., Abstract S41G-02.
- Shipton, Z., Cowie, P., and Vermilye, J. (1997). Fault displacement profiles and off-fault damage: interpreting the record of fault growth. *Abstr. Programs—Geol. Soc. Am.* **29**, 199.

- Shipton, Z., Evans, J., Lim, S., Pachell, M. and Robeson, K. (2001). Structure and geochemistry of fault zones exhumed from seismogenic depths, Sierra Nevada, California; implications for earthquake nucleation and propagation, *Earth System Processes: Programmes with Abstracts*, **37**, Geological Society of America and Geological Society of London, International.
- Sibson, R. (1973). Interaction between temperature and pore-fluid pressure during earthquake faulting and a mechanism for partial or total stress relief. *Nat. Phys. Sci.* **243**, 66–68.
- Sibson, R. (1975). Generation of pseudotachylite by ancient seismic faulting. *Geophys. J. R. Astron. Soc.* **43**, 775–794.
- Sibson, R. (1977). Fault rocks and fault mechanisms. *J. Geol. Soc. Lond.* **133**, 191–213.
- Sibson, R. (1982). Fault zone models, heat flow, and the depth distribution of earthquakes in the continental crust of the United States. *Bull. Seismol. Soc. Am.* **72**, 151–163.
- Sibson, R. (1986a). Brecciation processes in fault zones: inferences from earthquake rupturing. *Pure Appl. Geophys.* **124**, 159–175.
- Sibson, R. (1986b). Earthquakes and rock deformation in crustal fault zones. *Annu. Rev. Earth Planet. Sci.* **14**, 149–175.
- Sibson, R. (1989). Earthquake faulting as a structural process. *J. Struct. Geol.* **11**, 1–14.
- Sibson, R. (2003). Thickness of the seismic slip zone. *Bull. Seismol. Soc. Am.* **93**, 1169–1178.
- Takagi, H. (1986). Implications of mylonitic microstructures for the geotectonic evolution of the Median Tectonic Line, central Japan. *J. Struct. Geol.* **8**, 3–14.
- Tanaka, H., Tomida, N., Sekiya, N., Tsukiyama, Y., Fujimoto, K., Ohtani, T., and Ito, H. (2000). Distribution, deformation and alteration of fault rocks along the GSJ core penetrating the Nojima Fault, Awaji Island, Southwest Japan. *Proceedings of the International Workshop on the Nojima Fault Core and Borehole Data Analysis*, USGS Open File Report, 00-129, pp. 81–101.
- Tsutsumi, A., Nishino, S., Miziguchi, K., Hirose, T., Uehara, S., Sato, K., Tanikawa, W., and Shimamoto, T. (2004). Principal fault zone width and permeability of the active Neodani fault, Nobi fault system, southwest Japan. *Tectonophysics* **379**, 93–108.
- Tullis, T. E., and Weeks, J. D. (1986). Constitutive behavior and stability of frictional sliding of granite. *Pure Appl. Geophys.* **124**, 10–42.
- Vermilye, J., and Scholz, C. (1998). The process zone: a microstructural view of fault growth. *J. Geophys. Res.* **103(B6)**, 12223–12238.
- Wang, W., and Scholz, C. (1994). Wear processes during frictional sliding of rock: a theoretical and experimental study. *J. Geophys. Res.* **99(B4)**, 6789–6800.
- Wenk, H. R. (1978). Are pseudotachylites products of fracture or fusion? *Geology* **6**, 507–511.
- Wenk, H. R., and Weiss, L. E. (1982). Al-rich calcic pyroxene in pseudotachylite: an indicator of high pressure and high temperature? *Tectonophysics* **84**, 329–341.
- Wibberley, C., and Shimamoto, T. (2003). Internal structure and permeability of major strike-slip fault zones: the median tectonic line in Mie prefecture, southwest Japan. *J. Struct. Geol.* **25**, 59–78.
- Willemsse, E., Peacock, D., and Aydin, A. (1997). Nucleation and growth of strike-slip faults in limestones from Somerset, UK. *J. Struct. Geol.* **19**, 1461–1477.
- Wilson, J. E., Chester, J. S., and Chester, F. M. (2003). Microfracture analysis of fault growth and wear processes, Punchbowl fault, San Andreas system, California. *J. Struct. Geol.* **25**, 1855–1873.
- Zhao, G., and Johnson, A. (1992). Sequence of deformations recorded in joints and faults, Arches National Park, Utah. *J. Struct. Geol.* **14**, 225–236.

**This page is intentionally left blank**

# PAST SURFACE TEMPERATURE CHANGES AS DERIVED FROM CONTINENTAL TEMPERATURE LOGS—CANADIAN AND SOME GLOBAL EXAMPLES OF APPLICATION OF A NEW TOOL IN CLIMATE CHANGE STUDIES

JACEK MAJOROWICZ,<sup>a,b</sup> JAN SAFANDA<sup>c</sup> AND WALTER SKINNER<sup>d</sup>

<sup>a</sup>*NGC, 105 Carlson Close, Edmonton, Alta., Canada T6R 2J8*

<sup>b</sup>*Northern Plains Climate Research Center, University of North Dakota, Grand Forks, ND 58202-8358, USA*

<sup>c</sup>*Geophysical Institute, Czech Academy of Sciences, Bocni II, Sporilov, Czech Republic*

<sup>d</sup>*Climate Research Branch, Environment Canada, Downsview, Ont., Canada M3H 5T4*

## ABSTRACT

The application of well temperature profiles in the context of the recent global warming debate has been in use only for the last 18 years [Science 234 (1986) 689], but the influence of surface temperature variations due to climatic changes of all time scales on subsurface temperatures and heat flow variation with depth has been recognized for much longer [Bull. Geol. Soc. Am. 34 (1923) 703]. The borehole climate method is unique as it is based on the direct physical link between the measured temperature–depth profile and the reconstructed parameter of the past climate, the ground surface temperature (GST). It is unlike most of the other approximate methods of the past climate reconstruction. It has proved to be quite successful in reconstructing two robust signals: (a) the amplitude of the last glacial/interglacial temperature difference and (b) the surface temperature trend of the last 100–150 years and eventually, when combined with the surface air temperature series, in estimating their pre-observational means (POMs). A reconstruction of less robust signals of the little ice age, medieval climatic optimum, Boreal, Atlantic and possibly some other climatic periods of the Holocene fails even in most cases of purely conductive subsurface thermal regime.

Borehole temperature profiles are not proxy for surface temperature, but a direct measure of the energy balance at the Earth's continental surface. The signal underground is, however, attenuated considerably through heat diffusion. The degradation of the signal imposes a physical limit on the information potentially retrieved from the observed subsurface temperature anomalies.

We describe the basic features and problems of the method of reconstruction of GST history from the temperature–depth profiles measured in boreholes which is illustrated by Canadian and other continental examples.

## 1. INTRODUCTION

Evidence of climate warming is apparent especially in the higher latitude regions of the globe. The weather records and proxy indicators of the climate variability and change in some regions of the globe and especially in the relatively recently (this century) settled areas or vast empty regions of the Arctic are limited. These are critical for the verification of the simulations of climatic changes by modeling (AOGCM simulations, IPCC, 2001). These models project that land areas will warm more rapidly than the global average and that such warming will be particularly strong at higher latitudes.

As temperatures become higher and air remains warmer for longer periods, many physical and biological changes occur. Glaciers melt, sea ice and ice sheets degrade, permafrost thaws, sea levels rise, large areas become deserts and the ecosystem responds to these threshold changes in the physical environment (IPCC, 2001). This vulnerability of the land and sea areas to a climate change requires intensive study of the recent climatic history and of the past climatic variations. Short observational records in high latitude Arctic regions, and in recently settled regions, require the use of proxy climate methods to reconstruct past climate variations. These involve studies of isotopes in ice cores ( $^{13}\text{C}$ ), isotopic chemistry of annual growth increments in corals, tree ring width and density structure, percent summer melts, fossil foraminifera studies or inversions of temperature with depth signals from stabilized wells (Pollack and Huang, 2000).

The application of well temperature profiles in the context of the recent global warming debate has been in use only for the last 17 years (Lachenbruch and Marshall, 1986; an extended list of references can be found, e.g., in Pollack and Huang, 2000; Pollack *et al.*, 2000), but the influence of surface temperature variations due to climatic changes of all time scales on subsurface temperatures and heat flow variation with depth has been recognized for much longer (Lane, 1923; Birch, 1948). The influence of the surface temperature time-varying boundary condition upon the upper 100–1000 m has been modeled using forward model approach and corrections to heat flow with depth have been applied. This model has been referring to Pleistocene ice age. This technique is widely used in heat flow studies (Beck, 1977; Clauser, 1984; Kukkonen, 1987; Jessop, 1990b; Clow, 1992; Primenov *et al.*, 1996; Mareschal *et al.*, 1999; Safanda *et al.*, 2004). The concept of climatic perturbation upon heat flow variation with depth has been recognized in the interpretation of temperature profiles and heat flow variations with depth from deep drillings like KTB (Clauser *et al.*, 1997) and Kola deep well (Kukkonen and Clauser, 1994) and it was accepted as a probable cause of heat flow variations with depth through Europe (Kukkonen and Joeleht, 2003).

The first direct use of the heat flow variation with depth from well temperature profiles in the estimation of the surface temperature histories was developed in studies of wells in the Canadian Shield (Beck and Judge, 1969; Cermak, 1971). These studies concentrated mainly on climatic change during the Holocene period. Cermak (1971) was the first to reconstruct Holocene temperature variations from well temperature profiles in the Kapuskasing area of the Canadian Shield. Lachenbruch and Marshall (1986) reminded us that climatic information contained in temperature–depth profiles could be used in the context of the recent climatic change debate on industrial age warming and its relation to preceding pre-observational surface temperature levels (long-term mean temperature; Lachenbruch *et al.*, 1988a). Lachenbruch and Marshall (1986) provided examples of temperature logs from permafrost areas of Northern Alaska showing substantial disturbance to the upper 100–150 m of measured profiles due to surface climatic warming. These recent climatic warming effects visible in temperature logs were shown also to be present to the south of Alaska in most Canadian well temperature profiles (Jessop, 1990a,b; Guillou-Frottier *et al.*, 1998; Majorowicz *et al.*, 1999a) and elsewhere (see Huang and Pollack, 1998; Pollack and Huang, 2000 for the global database information).

Over the past two or three decades the geothermal method has been used to examine recent global warming, and the contribution from borehole temperature reconstructions of past climatic variations has been significant. The method is based on the physical principle that the past changes in the Earth's surface energy balance propagate into the subsurface and appear as perturbations of the subsurface thermal regime. The main assumption of this method is that climate changes are accompanied by long-term temperature changes of the Earth's surface, which propagate downwards and can be reconstructed as ground surface temperature (GST) histories. Due to the low thermal diffusivity of rocks, GST changes propagate downward slowly and are recorded as transient perturbations to the steady-state temperature field. For typical values of the thermal diffusivity of rocks, i.e., about  $10^{-6} \text{ m}^2 \text{ s}^{-1}$ , excursions in GST for 10, 1000 and 30,000 years ago produce maximum temperature anomalies at depths of 25, 250 and 1370 m in the present subsurface temperature field, respectively. Therefore, the temperature profile measured in a borehole a few hundred meters deep may contain information about GST changes in the last millennium and boreholes 1500–2000 m deep may yield GST histories for the end of the last ice age.

Surface temperature reconstruction must be posed as an inverse problem. The approach begins with detailed temperature measurements in a borehole from which surface temperature changes are inferred, as well as heat flux changes and their error back in time. Reconstruction of surface heat flux histories and GST

histories from the analyses of heat flux and temperature anomalies detected in the shallow subsurface have yielded important paleoclimatic information regarding the thermal state of about 30% of the Earth's surface and its temporal variability (Huang *et al.*, 2000; Pollack and Huang, 2000). These data have recently allowed calculation of net heat absorbed, for regional analyses (Majorowicz and Skinner, 1997; Beltrami *et al.*, 2000; Beltrami, 2002) and for all continental areas over the past 50 years (Beltrami *et al.*, 2002). Estimates of oceanic, atmospheric, and cryogenic heat gain over the same time period have shown that the present warming has a global character.

Borehole temperature profiles are not proxy for surface temperature, but a direct measure of the energy balance at the Earth's continental surface. The signal underground is, however, attenuated considerably through heat diffusion. The degradation of the signal imposes a physical limit on the information potentially retrieved from the observed subsurface temperature anomalies. Proxy records like most popular tree rings method, on the other hand, have higher resolution but their interpretation as a climatic indicator is not always straightforward.

In this paper the basic features and problems of the method of reconstruction of GST history from the temperature–depth profiles measured in boreholes are outlined and illustrated.

## 2. BASIC FEATURES OF GROUND SURFACE TEMPERATURE RECONSTRUCTION

The reconstruction of the GST history for time interval  $[t_0, t_1]$  from the subsurface temperature profile  $T(z, t_1)$ , measured between the surface and depth  $z_b$  at time  $t_1$ , implicitly requires that the perturbations in  $T(z, t)$  caused by the GST variation before time  $t_0$  cannot be distinguished from the steady-state field within the depth interval  $[0, z_b]$  at time  $t_1$ . This requirement can be satisfied by considering  $t_0$  sufficiently far away from  $t_1$ .

The GST change will produce a disturbance to a linear portion of the well temperature profile assuming constant conductivity  $K$  and diffusivity  $\alpha$ . The linear portion of the well temperature profile represents steady flow of heat  $Q$  from the Earth's interior according to Fourier relation:

$$Q = K\Gamma_0 \quad (1)$$

where  $K$  is the thermal conductivity and  $\Gamma_0$  is the thermal gradient.

Extrapolation of the linear portion of thermal profile controlled by deep heat flow  $Q$  and thermal conductivity  $K$  to the surface  $z_0$  yields the intercept

temperature  $T(z_0)$ . The deviation of the measured temperature profile  $T(z)$  from the extrapolated linear profile results in temperature anomaly  $\Delta T(z)$  (Fig. 1) which in the simplest interpretation represents the response of the ground to recent rise of the mean annual surface temperature from a previous long-term

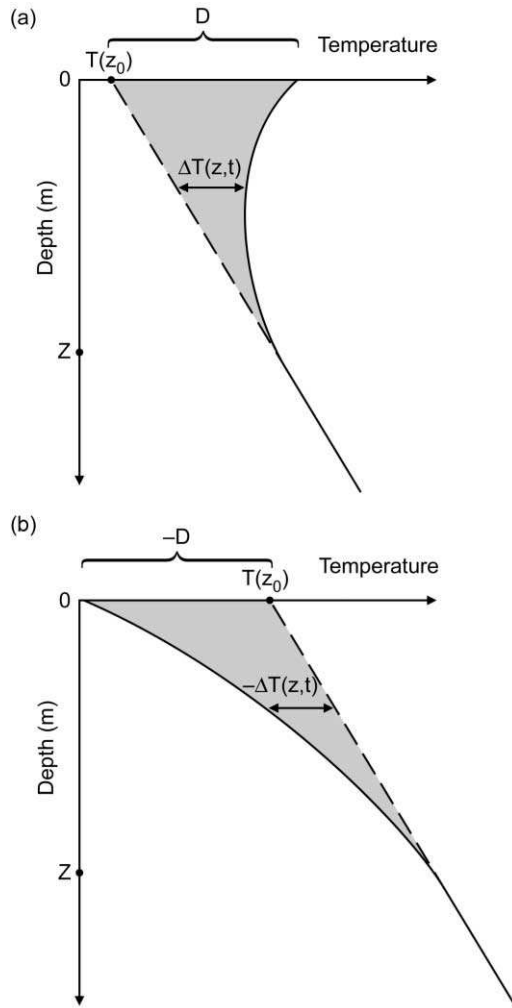


FIG. 1. Schematic representation of the effect of the surface temperature on the geotherm due to a step increase of surface temperature (a) and step decrease of the surface temperature (b).

value  $T(z_0)$  (positive anomaly values) or recent cooling (in case of negative anomaly). The combination of subsequent warming and cooling events complicates the disturbing signal with depth as illustrated in Fig. 2 for simple models.

Inhomogeneities in rock properties and three-dimensional effects limit the resolution of the details of  $T(z, t)$ , where  $t$  is the time; however, a one-dimensional model is capable of resolving the general magnitude of recent temperature changes and timing of its onset. In the simple one-dimensional transient model of

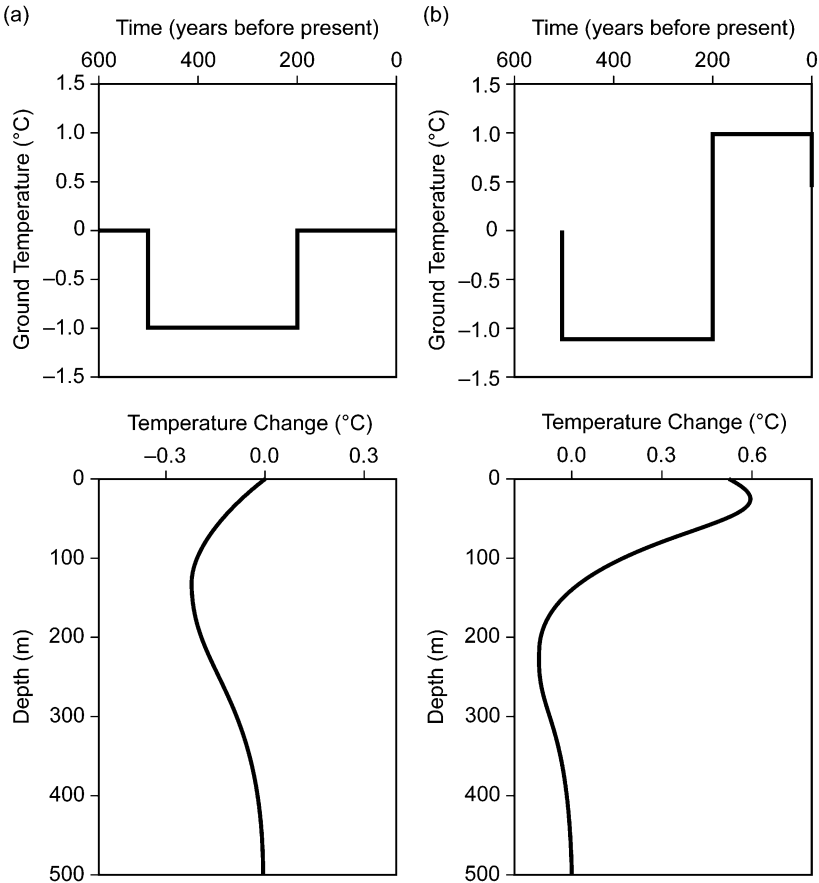


FIG. 2. Hypothetical three-step ground temperature history and its thermal diffusive response underground.

the effects of surface GST change upon temperature–depth, the assumption of homogenous subsurface media is a simplification. Temperature change with depth and time can be written as

$$T(z, t) = T(z_0) + \Gamma_0 z + \Delta T(z, t) \quad (2)$$

where  $t$  is the time and  $\Delta T(z, t)$  represents the response of the ground to recent mean annual warming or cooling of the surface from the previous long-term value  $T(z_0)$ , and  $\Delta T(z, t)$  is governed by the differential equation:

$$d^2 \Delta T(z, t) / dz^2 = (1/\alpha) dT/dt \quad (3)$$

where  $\alpha = K/\rho c$  is the thermal diffusivity,  $\rho$  is the density and  $c$  is the heat capacity.

Surface temperature variation with time in simple models can be described by a three-parameter law:

$$\Delta T(0, t) = D(t/t^*)^{n/2} \quad \text{for } 0 < t < t^*, \quad n = 0, 1, 2, \dots \quad (4)$$

which forms the surface boundary condition for the solution of Eq. (3).

The initial condition is

$$\Delta T(z, t) = 0 \quad (5)$$

The solution of Eqs. (3)–(5) for  $t = t^*$  is according to Lachenbruch *et al.* (1988a):

$$\Delta T(z) = D 2^n \gamma(0.5^n + 1) i^n \operatorname{erfc}(z/(4\alpha t^*)^{-0.5}) \quad (6)$$

where  $i^n \operatorname{erfc}(B)$  is the  $n$ th integral of the error function of  $B$  and  $\gamma(B)$  is the gamma function of  $B$  and  $D$  is the surface temperature increase.

The above solution gives the ground temperature after the warming event of duration  $t^*$  with surface temperature change  $D$ . The model can be changed with an adjustment of  $n$ . These functions control the model of GST change as follows: a step increase for  $n = 0$ , parabolic increase for  $n = 1$ , linear change for  $n = 2$ , exponential for  $n = 4$ , etc.

It is difficult to extract the mean annual surface temperature value for the last 1–2 years prior to logging because of the annual oscillations of the temperature in the uppermost 10–20 m. In addition, the temperature profile usually starts at least a few meters below the surface for different technical reasons.

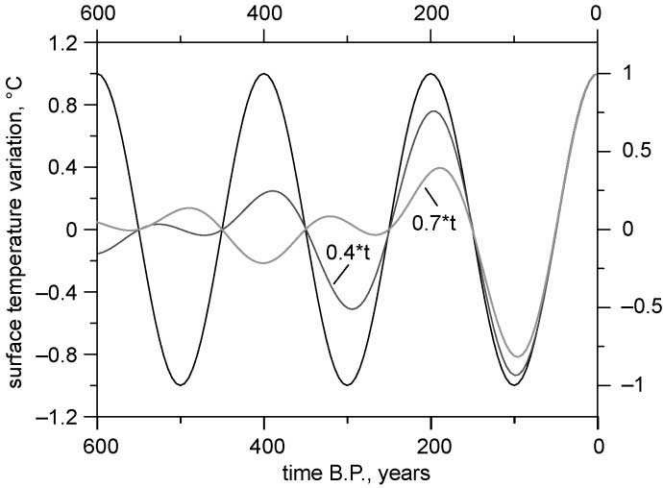


FIG. 3. The distortion of the periodic surface temperature history due to averaging. Synthetic example of a distortion of the periodic surface temperature history due to the averaging of  $0.4t$  and of  $0.7t$  is given, respectively.

For more complicated surface temperature histories where inversion techniques are used, the GST value reconstructed for time  $t = \tau$  before logging represents an average over the time interval, the width of which is proportional to  $\tau$  (Clow, 1992). This is due to the diffusive character of the heat conduction. The rate at which the averaging interval increases with  $\tau$  depends strongly on the level of noise inevitably present in each temperature log and on the density of the temperature sampling. For a typical log with depth step 5–10 m and level of noise of the order of hundredths of kelvin (0.01 K), GST is estimated as an average over about  $0.5\tau$  (Fig. 3).

### 3. HEAT GAIN BY THE EARTH DUE TO CLIMATIC WARMING

Climatic warming causes downward flow of heat into the ground, which is related to an unbalanced climatic flux  $C(z, t)$  due to climatic warming (Fig. 4).

$C(z, t)$  can be estimated by the conventional gradient method:

$$C(z, t) = -K dT(z)/dz \tag{7}$$

For a typical temperature versus depth profile in the area of Barrow, AK characterized by recent warming of 5 K, Lachenbruch *et al.* (1988a,b) estimated

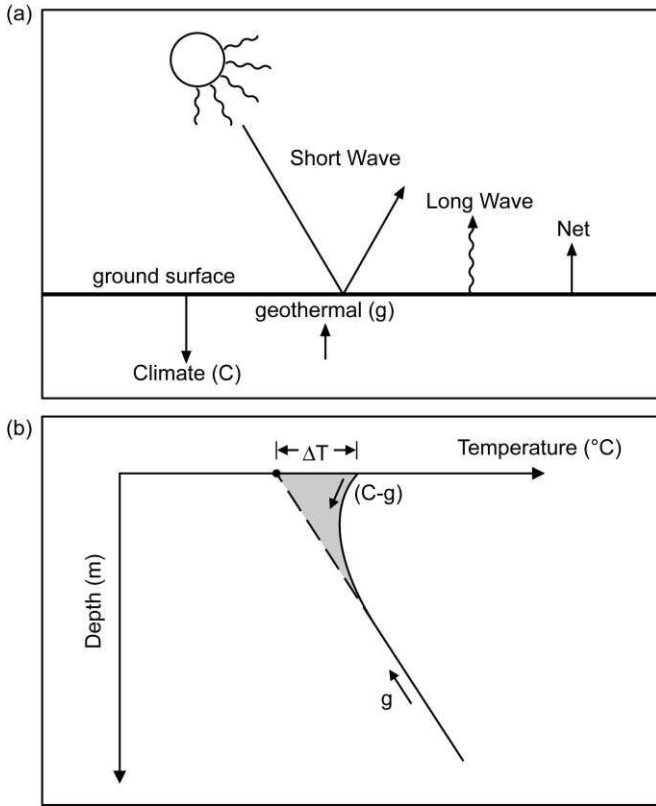


FIG. 4. Comparison of typical unbalanced climate flux  $C$ , with geothermal flux  $g$  and other fluxes of Earth's surface (a) and the role of climate flux in the geothermal regime (b) (modified from Lachenbruch, 1994).

a large heat flux of  $0.1 \text{ W m}^{-2}$ . Beltrami *et al.* (2000) estimated from eastern Canadian wells that the downward average surface heat flux over the last 100 years is approximately  $0.07 \text{ W m}^{-2}$  which is comparable with average upward deep Earth's heat flow. Recent ground warming effects upon the thermal regime will dominate the upper 100–200 m only as the Earth is a poor conductor and the heat will not flow much deeper in such a short period.

The amount of energy stored in the ground due to surface temperature warming can be calculated by integration of the area  $A$  of the anomaly  $T(z)$  shown by shading in Fig. 4.

The total heat absorbed per unit surface area is

$$H = A\rho c \quad (8)$$

where  $\rho$  is the density ( $\text{kg m}^{-3}$ ) and  $c$  is the heat capacity ( $\text{J kg}^{-1} \text{ }^\circ\text{C}^{-1}$ ).  $H$  is expressed in  $\text{J m}^{-3}$ .

The total energy for the surface area  $S$  is

$$E = HS \quad (9)$$

The energy absorbed in the upper 150 m of the ground due to warming related to landscape changes (land clearing) in this century alone is estimated to be  $30 \times 10^{18}$  J in Alberta farming areas (Majorowicz and Skinner, 1997). The heat gain by the crust in Canadian regions where evidence of a large magnitude ground surface warming in the last century exists ( $1\text{--}5^\circ\text{C}$ ) has been estimated to be approximately  $10^{21}$  J (Majorowicz and Skinner, 1997).

Regional heat flux history can be calculated from weighted average of the time history (Beltrami *et al.*, 2000). The heat flux (positive into the ground)  $C(z, t)$  can be expressed in terms of

$$\begin{aligned} Q(z, t) &= K \, dT(z, t)/dz = K(1/\alpha^{1/2})d^{1/2}(T(z, t) - T_0)/dt^{1/2} \\ &= (Kc/\pi)^{-1/2}(d/dt) \int_0^t (T(z, s)ds/(t - s)^{1/2}) \end{aligned} \quad (10)$$

where  $s$  is the integration time variable.

The above equation allows the estimation of ground heat flux from GST history. The global heat flux estimate (Beltrami *et al.*, 2002) indicates that the average global land surface ground temperature increase of  $0.45^\circ\text{C}$  is related to an increase in the heat flux of  $0.018 \text{ W m}^{-2}$  over the last 200 years. Estimates of heat flux using Eq. (10) show that over the past 50 years (1950–2000) average heat flux is  $0.039 \pm 0.0035 \text{ W m}^{-2}$ . This flux deposited  $9.1 \pm 0.8 \times 10^{21}$  J of heat into the continental crust (Beltrami *et al.*, 2002). For a comparison, heat gained by ocean, atmosphere and cryosphere is  $18.2 \times 10^{22}$  and  $6.6 \times 10^{21}$  J, respectively, over the past half a century. While the land surface boundary represents only 29% of the Earth's surface, it gains approximately 50% of the heat of the ocean. Assessment of that heat gain is important as it influences radiatively important biogeochemical cycles.

#### 4. TEMPERATURE PROFILES WITH DEPTH

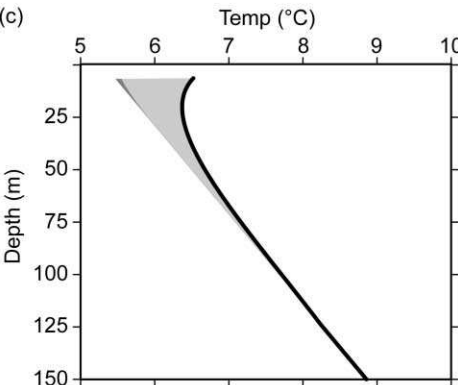
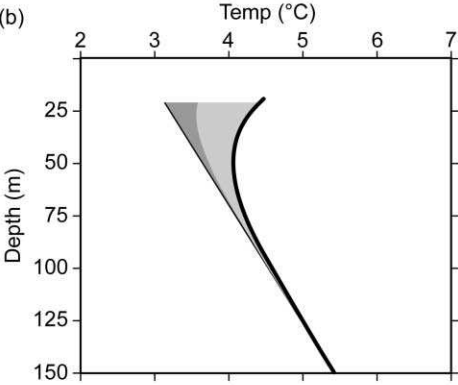
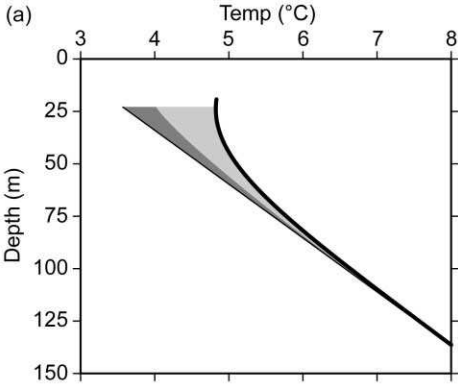
The basic data used to reconstruct surface temperature history are equilibrium temperature profiles usually taken several months to years after the drilling disturbance in water-filled wells. The accuracy of this information is critical in any type of GST reconstruction.

Temperature logs are made using portable logging equipment with a thermistor probe or a probe with platinum sensor calibrated to approximately 1–3 mK for thermistor of 10 k $\Omega$ . The description of the equipment used for the temperature logs done in Canada is given in Jessop (1990b). Higher relative accuracy of 0.001°C (temperature resolution) can be achieved with frequency tools if so designed (Blackwell, 1999; Blackwell *et al.*, 1999).

The wells are normally diamond or rotary drilled with water or drilling mud circulated through the well. That is a cause for a disturbance of the thermal equilibrium conditions. Return to equilibrium temperature, in first approximation, follows an exponential decay of disturbance with time. Therefore, wells need to be left undisturbed by any drilling operations for at least several months to achieve near equilibrium state. In practical terms, the disturbance should be equal or less than the accuracy of the measurement. The time period a well requires to rest depends on the time of drilling is relatively short (days, month) for wells hundreds of meters deep and very long for deep wells of several thousand meters depth (month to years). For climate studies, measurements of temperature with depth are usually made in the upper few hundred meters. The tendency for the wells to slant relative to the vertical is common for deep wells but is not a frequent problem in the shallower well data used in climate studies. In the other case, corrections are applied (Jessop, 1990b).

Temperature logs for which there is evidence of disturbance by water flow in the well or immediately outside the casing or in the porous rock media surrounding it are rejected. Examples of ideal logs with little evidence of water disturbance or rapid changes of conductivity with depth are shown in Fig. 5. The logs shown were done to a depth of 150 m in three wells in the Canadian Sedimentary Basin. Portable equipment consisting of surface measuring registering device (the Wheatstone bridge), cable and thermistor probe are usually used. The temperature–depth profiles were based on point measurements taken at 2 m intervals in the water-filled wells. All temperature profiles show characteristic inversion of temperature with depth in the upper several tens of meters of the profile—a result of a surface temperature increase in the last several decades.

Some wells can be influenced by water disturbance, such as the flow of water outside the casing or into the well itself. Water disturbance is usually



readily apparent (see examples shown in Jessop, 1990b) and is rejected from further analysis. Abrupt changes in the geothermal gradient are usually due to an input of water behind the casing. A different style of disturbance can be caused by water seepage through porous and permeable rock (either upward or downward) and is less apparent. This can also cause heat flow disturbance. The effect upon the vertical component of heat flow is only significant in case of large differences in topography and related hydraulic head changes combined with abundance of water and good rock permeability. Such examples are well recognized and described by Jessop (1990b). The influence of water circulation in the sedimentary basin has been recently re-analyzed based on new data on permeability and crossformational water seepage velocity (Blackwell, 1999; Majorowicz *et al.*, 1999b). Clastic sediments with a large fraction of clays and shales that are characteristic for the depths in which temperature logs are made in most sedimentary basins to a depth of few hundred meters show very low permeability leading to very low water velocities of less than  $10^{-2}$  m/year, for water moving along the bedding of the formations. The vertical component of such flow is 10–1000 times lower. Dimensional analysis provides a measure of the strength of convective versus conductive heat transfer through the examination of the Peclet number for heat transfer in porous media  $Pe_h$ , defined as

$$Pe_h = \rho_f c_f I q / K_m \quad (11)$$

where  $I$  is a characteristic dimension in the main direction of the fluid flow,  $\rho$  is the density,  $c$  is the specific heat,  $K$  is the thermal conductivity and the subscripts f and s refer to fluid and solid.

In most cases known to us the Peclet number is usually very small ( $1.2 \times 10^{-2}$ ) which shows that the transport of heat by fluid movement is negligible and the main mechanism for heat transfer is conduction.

Permeability in the crystalline rocks is even less though water movements along fractures can be a problem (Jessop, 1990b). It is therefore estimated that

---

FIG. 5. Examples of typical near surface deviations of temperature in function of depth—a result of the surface temperature increase this century. Temperature logs (shown by darker thick lines) are from three characteristic well sites in Western Canada Sedimentary Basin. (a) Sion, (b) Cold Lake, (c) Sounding Creek (see Majorowicz and Skinner, 1997 for the location). First and second well (a and b) are in the areas where, respectively, land clearing or local deforestation took place. The third well (c) is in the grassland area. Dark shaded areas show possible effects of 1°C surface warming 50 years ago (a) and 20 years ago (b). Light shaded areas show possible effects of the climatic forcing due to air surface warming. It is obvious that the surface change is more than 1°C in all three cases.

the change in heat flow is smaller than the errors due to temperature gradient accuracy which depend on well thermal equilibrium and accuracy of temperature measurement. Current consensus, based on new data and modeling, is that the effects of water circulation upon heat transfer in sedimentary basins have been overestimated (Blackwell, 1999).

Many cases of heat flow variation with depth can now be explained by thermal conductivity variations. A better knowledge of the thermal conductivity of clastics showed low conductivity of shales ( $1.05\text{--}1.45\text{ W m}^{-1}\text{ K}^{-1}$  according to Blackwell *et al.*, 1999). Conductivity of shales measured using the divided bar method applied to cells with mix of rock chips and water has been overestimated in the past (Blackwell *et al.*, 1999). It is only in regions of high topographic relief with a high density of vertical conduits (i.e., the Rocky Mountain foothills) where the effect can be a consideration (Majorowicz *et al.*, 1999b). Wells from sedimentary basins are located mostly in the flat areas like those of the Prairies of western Canada or in the mid-west of USA (the Dakotas, etc.) and the lowlands of Northern Europe. Repeated measurements in wells at different times and measurements in wells in close proximity that are open to different aquifers at numerous sites in the Prairies of western Canada (Majorowicz and Skinner, 1997) clearly show a conductive character of the heat flow transfer. Also, the small diameter of the wells relative to their length disallows any convection in the well bore, significant enough to disturb the thermal regime (Jessop, 1990b). Repeated logs after the last disturbance in the well is a good way to confirm a conduction thermal regime in the wells.

In Canada, well sites are located in a wide variety of surface environments, such as the boreal forest, grasslands, deserts, permafrost regions, etc. In the majority of cases, temperature versus depth profiles are the result of a single log in one well over a depth range from the static water level to the bottom of the well. At some sites, the temperature profile is a stacked set of measurements with different water levels and depths from several wells at one site (usually wells located within a 100 m radius of each other).

In ice-bearing northern regions, the process of return of wells to thermal equilibrium (equilibrium between the fluid filling the well and the surrounding rock/ice media) can be as long as one to several years. In such cases equilibrium geotherm is calculated from several logs taken in different times over a period of days, month, years (Lachenbruch *et al.*, 1988b). As a rough approximation the recovery to equilibrium state is completed within the accuracy of measurement of temperature in a period that is 10–20 times greater than the time of drilling. It is possible to estimate equilibrium temperature from a series of measurements using extrapolation. Such extrapolation is usually achieved by plotting the observed temperature  $T$  against logarithmic function of the time elapsed since the end of

drilling  $t_e$  and the time duration of drilling  $t_d$ . The time function is given by

$$F_d = \ln((t_e + t_d)/t_e) \quad (12)$$

The function  $F_d$  becomes zero when the time elapsed is very large, and thus the temperature extrapolated to the axis gives equilibrium temperature of the well as well as the surrounding rock.

Other corrections are: correction for nearby bodies of water, correction for the inclination of the borehole, correction for topographic relief (usually needed in mountainous terrains), correction for plane slopes (when relief occurs close to well site or when the collar of the borehole is within the inclined area) (Jessop, 1990b).

## 5. THERMAL CONDUCTIVITY AND DIFFUSIVITY

Thermal conductivity  $K$  controls geothermal gradient variations at the steady deep geothermal heat flow  $Q$ . It is therefore important to know variations of thermal conductivity with depth in order to estimate change in heat flow related to surface temperature history. According to the theory of heat conduction, downward propagation of thermal waves is attenuated so the amplitude of these waves diminishes exponentially with depth. The shorter waves are filtered out at shallower depths and long wave variations at deeper depths. The pace of wave propagation is a diffusive process controlled by the diffusivity  $\alpha = K/\rho c$ .

The thermal conductivity of rocks is much lower than, for example, that of metals. The rocks of the Earth's crust acts as an insulator. Rock conductivity is in the range  $1.5-6 \text{ W m}^{-1} \text{ K}^{-1}$  depending on rock type. The conductivity of water-filling pores or cracks is rather small (about  $0.6 \text{ W m}^{-1} \text{ K}^{-1}$ ). Errors in conductivity determination at depth can be the limiting factor in distinguishing the climatic signal. The surface wave temperature signal is attenuated in a short depth-distance because of the low diffusivity of the rock.

Conductivity is normally measured in the laboratory. Rock samples are extracted during drilling as cores. Conductivity in water-saturated cores or in a mix of rock chips and water in small cells is usually measured by the divided bar method. The sample is placed in a column through which heat is conducted and conductivity is obtained by comparison with other parts of the column (Jessop, 1990b). Other methods involve the use of optical scanning with no contact with the rock sample (Popov, 1997). The use of these methods depends on the availability of core samples. In many wells, rock cores are not available

as rotary drilling process brings only rock chips with upward circulating well mud. In such cases estimates of thermal conductivity variations with depth use net rock analysis (fractions of rock types and pore filling fluid) and the assignment of known regional averages of rock thermal conductivity. The fraction of rock types and pore space can be determined using wire well logs like acoustic, resistivity, radioactive, etc. (Blackwell *et al.*, 1999). The effective thermal conductivity of the rock formation ( $n$ th interval) is calculated from Jaeger (1965) by the equation:

$$K_{\text{eff}}(n) = \frac{\sum l_i}{\sum (l_i/K_i)} \quad (13)$$

where  $K_i$  is the conductivity assigned to the  $i$ th rock type and  $l_i$  is the thickness.

The large uncertainty in  $K$  determination (commonly 5–15%) is the limiting factor especially for extracting an attenuated climatic signal at larger depth (>100 m). At a common continental geothermal gradient of  $30 \text{ mK m}^{-1}$  and thermal conductivity of  $2.5 \text{ W m}^{-1} \text{ K}^{-1}$ , heat flow will be  $75 \text{ mW m}^{-2}$ . In such case, 10% uncertainty in conductivity ( $0.25 \text{ W m}^{-1} \text{ K}^{-1}$ ) and 10% in geothermal gradient uncertainty will result in heat flow uncertainty of  $15 \text{ mW m}^{-2}$ . At 100 m uncertainty of temperature determination 0.3 K is large when comparing with common anomaly due to surface warming to be in decimals of a degree.

Thermal diffusivity  $\alpha = K/\rho c$  governs transient-state heat conduction. It is an important parameter in the calculation of ground surface history from temperature–depth data. The value commonly used for model calculations is  $10^{-6} \text{ m}^2 \text{ s}^{-1}$  but the time diffusivity of rocks may be much lower for some near surface water-filled clastic rocks ( $0.6 \times 10^{-6} \text{ m}^2 \text{ s}^{-1}$ ) or higher for the crystalline rocks of the shield ( $1.2 \times 10^{-6} \text{ m}^2 \text{ s}^{-1}$ ).

Diffusivity depends directly on conductivity. It is strongly influenced by water in cracks and pores because water has both low conductivity and high volumetric heat capacity ( $\rho c$ ). The combined density and specific heat give the volumetric heat capacity which in case of water/rock combination may be directly added:

$$\rho c = \phi \rho_w c_w + (1 - \phi) \rho_s c_s \quad (14)$$

where  $\phi$  is the porosity and the subscripts w and s refer to water and solid. With an increase in porosity of rock saturated with water, a decrease in diffusivity is apparent from Eq. (13).

## 6. INVERSIONS

GST reconstruction from subsurface temperature profiles presents an inverse problem. Due to its complexity, all existing techniques for “systematic” inversion assume that heat transfer is by conduction only through a one-dimensional heterogeneous medium. This assumption excludes the advective component of heat transfer due to subsurface fluids or convective disturbances within the fluid-filled borehole, as well as lateral heterogeneity in thermophysical parameters of rocks, uneven surface relief or space variations of the surface temperature from the account as they may bias the reconstruction (Shen *et al.*, 1995). These effects and processes can be considered in “non-systematic” or random inversion approaches like the Monte Carlo method.

At present, the most frequently used systematic inversion methods are functional space inversion (FSI) technique (Shen and Beck, 1992) and the singular value decomposition (SVD) (Mareschal and Beltrami, 1992). In both methods, the mathematical representation of the physical processes relating the GST changes and the subsurface temperatures is reduced to the one-dimensional heat conduction problem. Different comparisons have shown similar results in most of the cases considered (Beck *et al.*, 1992; Wang, 1992). The basic features of the problem of the GST history reconstruction will be demonstrated here using the FSI algorithm.

The FSI method is basically the generalized least-squares inversion method. It uses the so-called Bayesian approach, when both the measured temperature profile, the parameters of the physical model and the sought history of the surface temperature are treated as random quantities in the probabilistic model defined by *a priori* estimates of these quantities and their standard deviations (SDs). The *a priori* values are modified during the inversion in order to reach the *a posteriori* configuration with maximum probability.

The inversion scheme is usually framed very conservatively in terms of a null hypothesis, i.e., with an *a priori* assumption that there is no climate signal present in the inverted borehole temperature profiles. It renders the analysis independent of any other proxy interpretations. *A priori* SD of GST variations, usually 0.5–2 K, permits a deviation from the null hypothesis if the data push in that direction. This approach can be combined with the known GST history, for instance, from the meteorological observations, as an *a priori* estimate for the recent part of the reconstructed period. A further statistical property of the sought GST history, which must be fixed prior to the inversion, is the characteristic time of correlation of the GST variations. In order to stabilize the solution in accordance with the decreasing resolution of the method for the more remote variations, Shen and Beck (1991, 1992) recommend a linear decrease of the

characteristic time from the most remote to the most recent period considered in the inversion. For instance, in reconstructing the last millennium it is 500–100 years, in reconstructing the last 50,000 years it is about 10,000–100 years.

The thermophysical parameters, whose *a priori* values and SDs must be defined at the beginning of the inversion, are: thermal conductivity, heat sources and specific heat of rocks encountered within the borehole together with an estimate of the surface temperature  $T_0$  at time  $t_0$  and the heat flow  $C_b$  at the bottom at depth  $z_b$ . It stems from the character of the problem that *a posteriori* values of  $T_0$  and  $C_b$  are well resolved and are close to the correct values even when their *a priori* estimates are incorrect, provided their SDs are big enough to render the inversion a freedom to push the estimates in the proper direction. On the other hand, values of specific heat and heat production are practically unresolved by the data, but because of their small influence on the subsurface temperature field a qualified *a priori* estimate of their mean values is sufficient. A very important parameter of the inversion is the thermal conductivity. It controls the temperature gradient and hence its variations with depth and determines the shape of the steady-state part of the measured temperature profile. If the conductivity depth profile of the inverted borehole is not known, all variations of the positive temperature gradient can be theoretically explained as a consequence of the depth variations of the thermal conductivity. Uncertainty in this parameter, expressed by its *a priori* SD, plays a critical role in the inversion. As will be shown later, choices of *a priori* SDs of conductivity and/or measured temperature data provide also a method for suppressing undesired effects of noise in the input data on the resulting GST history.

The measured temperature profile is an *a priori* estimate of the random quantity, which can be changed during the inversion within a frame given by the probabilistic model based on *a priori* SDs. In the course of inversion, the  $T-z$  profile is decomposed into *a posteriori* steady-state and transient components. As a rule, the short-wave variations of the temperature gradient are compensated for by variations in the conductivity profile and thus incorporated into the steady-state component of the temperature.

Because the amplitude of the GST changes propagating downward attenuates exponentially, the magnitude of the present subsurface response to variations over the last millennium is, with the exception of the quite recent changes, of the order of hundredths of degrees. Many factors can produce non-climatic vertical variations of temperature of a similar magnitude to climatic factors. The typical source of these variations is unrecognized vertical and/or lateral variations of thermal conductivity. Vertical variations, if recognized, may be considered in the inversion. Lateral variations cannot be taken into account due to one-dimensional representation of the problem.  $T-z$  profiles, when inverted

with typical values of *a priori* SDs of conductivity observed in lithologically uniform units, about few tenths of  $\text{W m}^{-1} \text{K}^{-1}$ , and of temperature measurements, first hundredths of kelvin, produce spurious GST history based on the amplification of this kind of noise (Shen *et al.*, 1995). As numerical experiments have shown (Shen *et al.*, 1995), suppression of the noise can be achieved by increasing the SD of the *a priori* thermal conductivity model and of the measured temperatures to values about  $1\text{--}2 \text{ W m}^{-1} \text{K}^{-1}$  and  $0.05\text{--}0.2 \text{ K}$ . Larger *a priori* SDs of the conductivity and the temperature data mean that an increasing relative weight is given on the *a priori* GST history, whereas *a priori* conductivity and temperature data can be adjusted in the course of the inversion. Consequently, *a posteriori* GST histories for larger SDs are closer to *a priori* GST hypothesis and the risk of interpreting the noise as the climatic signal is attenuated. Such a kind of inversion is referred to as “loose” inversion in contrast to “tight” inversion carried out with smaller *a priori* SDs. The potential disadvantage of the loose inversion—the loss of the GST history resolution in case of high quality data with a real climatic signal—is evident.

The above-described method’s assumption excludes the advective component of heat transfer due to subsurface fluids or convective disturbances within the fluid-filled borehole, as well as lateral heterogeneity in thermophysical parameters of rocks, uneven surface relief or space variations of the surface temperature from the account. These effects and processes can be considered in “non-systematic” or random inversion approach, referred generally to as the Monte Carlo method, which requires basically only solution of the direct problem. The present techniques of solution of the direct problem enable us to consider a broad spectrum of processes. Probably, the first use of the Monte Carlo method for the GST reconstruction from the borehole temperature profiles was reported by Cermak (1971). Recently, Dahl-Jensen *et al.* (1998) used the Monte Carlo method for reconstruction of the surface temperature history from the 3000 m deep temperature profile measured through the Greenland Ice Core Project borehole. Besides the heat conduction, they also considered the convective transport of heat caused by the ice shield accumulation and spreading. The main features of the Monte Carlo method can be well demonstrated on their approach. Their model parameters to be determined by inversion were mean surface temperatures in the 125 time intervals of progressively increasing length from 10 years at present to 25 ka at 450 ka ago, and the geothermal heat flow density. All other parameters like thermal conductivity and diffusivity of ice sheet and basement rocks, as well as the rate of snow and ice accumulation and the ice-flow velocity, were estimated independently before the start of the inversion. The Monte Carlo method was used to test randomly selected combinations of surface temperature histories and

geothermal heat flow densities by using them as input to the coupled heat- and ice-flow model. Of the  $3.3 \times 10^6$  models tested during the random walk about  $1 \times 10^6$  have resulted in the temperature–depth profile which differed from the observed one by less than the observation variance, and have been accepted. Of these  $1 \times 10^6$  accepted models every 500 was only considered. The waiting time of 500 has been chosen to exceed the maximum correlation length of the output model parameters. This was a necessary condition for the remaining 2000 models to be uncorrelated. This formulation of the Monte Carlo method enabled to estimate the likelihood of possible temperature histories and geothermal heat flow densities. The histograms of 2000 acceptable surface temperature values for each of the 125 time intervals considered and one histogram for the geothermal heat flow density were fitted by soft curves, the maxima and shapes of which define the most likely model values and their SDs, respectively.

## 7. JOINT INVERSIONS

The joint inversion of several profiles (Beltrami and Mareschal, 1992; Pollack *et al.*, 1996) can be used in an attempt to suppress the noise and extract the common climatic signal. This procedure is based on the assumption that in a region with similar climatic history, the joint processing suppresses the randomly distributed noise and what remains is a common climatic signal. For example, with respect to topography, it is assumed that some boreholes are located in valleys and some others are situated at higher elevations. Joint inversion is conceptually different from simple averaging. A simultaneous inversion searches for the common transient component of the ground surface history from an assemblage of the temperature logs in a chosen region. According to Pollack *et al.* (1996) simultaneous inversion can be quite effective in suppressing the effects of observational and representational noise. While averaging of the individual inversions from temperature–depth data from different boreholes can always be accomplished, a simultaneous inversion from the same set of data may not be possible as the inversion scheme will not result in convergence of the solution. In such cases the usual practice is to reject some wells for which common inversion does not work, an indication of various non-climatic perturbations and local terrain-related microclimatic effects. The advantages of simultaneous inversion include the representation of a regional GST history consistent with the site histories at individual borehole locations. Averaging of single inversions is another approach used in characterization of the regional surface temperature change (Pollack *et al.*, 1996).

## 8. ALTERNATIVE APPROACH—DETERMINING THE PRE-OBSERVATIONAL MEAN LEVEL

When the surface air temperature (SAT) has been measured within the same climatic region as the borehole and the borehole is deep enough to relate to some interval of climatic history prior to the beginning of the instrumental observations, an alternative approach (Lachenbruch *et al.*, 1988a; Chapman *et al.*, 1992; Harris and Chapman, 1995) to the temperature profile inversion can be used. In this procedure the borehole temperature profile is used only to extend the observed SAT series before the beginning of the instrumental period by estimating the long-term POM surface temperature. The POM is chosen as a value that generates, together with the SAT series, the transient component of the synthetic profile that best fits the shape of the transient component of the log. This is usually determined as the difference between the log and regression line fitted to the lowermost portion of the temperature log, the so-called reduced temperature. The general concept of combining the climate and geothermal records was demonstrated by Lachenbruch *et al.* (1988a). They concluded that 100 years of weather records are insufficient to answer the question about the magnitude of recent warming. They proposed that the additional assumption must be made for the GST levels at the pre-industrial record time.

This method requires the assumption that the GST change model is the same as the SAT changes for the observational portion of the record. While this assumption is valid in many areas, it may not be valid in others. Tracking surface temperature changes in the ground is a very complicated process in which variations in moisture, albedo, length of freezing period, snow cover, land clearing and other factors can obstruct the correlation relationships.

## 9. METHOD LIMITATIONS

The main methodological problem is the one-dimensional, purely conductive representation of the subsurface temperature field used by all existing systematic inversion algorithms. This ignores lateral inhomogeneities of the thermophysical parameters of rocks, the effects of topography and space variations of the surface temperature as well as any departures from the conductive mode of the subsurface heat transfer. The main practical problem is the presence of noise in the temperature logs which contributes, together with the diffusive character of the downward propagation of the surface changes, to the rapid loss of resolution of the more remote surface temperature history. The reconstructed GST histories

represent temporal changes of the ground temperature at the upper boundary of the heat conduction domain, which usually begins within a few meters below the surface. The GST variations are assumed to track the long-term air temperature changes. Validity of the above assumption is a key issue in interpreting the results in terms of the long-term climatic variability.

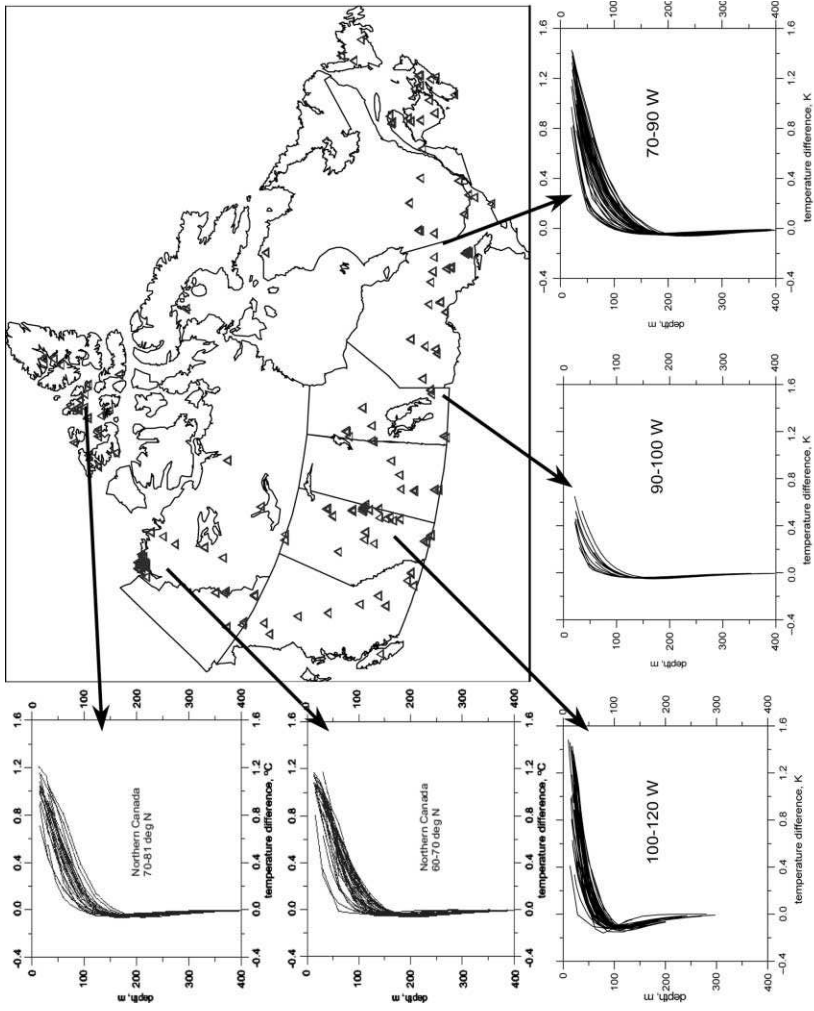
## 10. CASE STUDIES DEMONSTRATING THE BASIC FEATURES OF THE INVERSION METHOD

The case study presented here will illustrate the capability of the inversion method to infer information about recent climatic changes from well temperature profiles. Recent warming is clearly evident in the subsurface temperature profiles in northern North America (Canada and Alaska, USA). Anomalies of temperature with depth  $\Delta T(z)$  for Canada (Fig. 6) show the effects of high recent ground surface warming. The majority of upper 100–200 m below the ground surface has warmed. Preceding cooling is also evident in some cases. In Fig. 7 we show the last 1000 years of the GST history obtained by simultaneous inversions of large sets of borehole profiles (more than 10 in each group) across Canada (south of 60°N) (Majorowicz *et al.*, 2002). It is evident that the most robust signal present in the data is that of the recent surface temperature warming, which started approximately 100–200 years ago. Only this signal is seen by the loose simultaneous inversions with *a priori* SDs  $2 \text{ W m}^{-1} \text{ K}^{-1}$  for conductivity and 0.1 K for temperature data (Fig. 7a). The GST histories yielded by the tight simultaneous inversions with SDs  $0.5 \text{ W m}^{-1} \text{ K}^{-1}$  and 0.05 K (Fig. 7b) suggest greater amplitudes of the warming and slightly different times of its onset in the various geographic regions.

The recent warming observed in the North America was preceded by the cold period with lowest temperatures attained in the 18th and 19th centuries. This minimum is seen in western and eastern temperature profiles as well as in northern data. Reconstructions of the GST history from borehole temperature profiles reproduce the warming, but the data of the preceding minimum are rather scattered. By inverting a synthetic temperature–depth profile, calculated as a response to a model consisting of linear 1.5 K increase of the surface temperature in 1850–2000 AD and preceded by a constant temperature, it was found that

---

FIG. 6. Well site locations in Canada. *A posteriori* transient components for Arctic (60–70°N and 70–81°N) and three southern Canadian regions (south of 60°N) calculated during the simultaneous inversion of temperature profiles in wells.



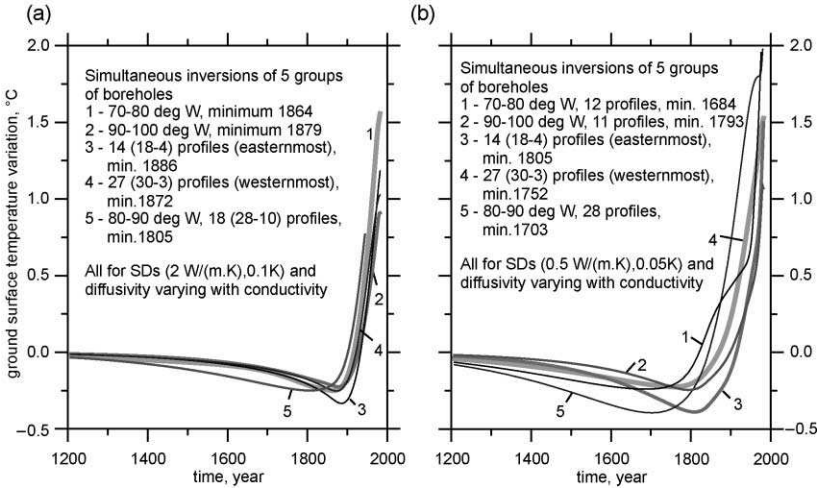


FIG. 7. GST histories obtained by simultaneous inversions of profiles from five geographical zones in Canada. Panel (a) shows the results obtained by the loose simultaneous inversions with *a priori* SDs  $2 \text{ W m}^{-1} \text{ K}^{-1}$  for conductivity and  $0.1 \text{ K}$  for temperature data. Panel (b) shows the results yielded by the tight simultaneous inversions with SDs  $0.5 \text{ W m}^{-1} \text{ K}^{-1}$  and  $0.05 \text{ K}$ .

a spurious minimum can appear in this synthetic case (Fig. 8). Results are shown for two different values of the rock diffusivity  $0.6 \times 10^{-6} \text{ m}^2 \text{ s}^{-1}$  (Fig. 8a) and  $1.0 \times 10^{-6} \text{ m}^2 \text{ s}^{-1}$  (Fig. 8b), typical for the unconsolidated sediments and for crystalline rocks, respectively. The minimum is very shallow for profile lengths greater than 150 m (diffusivity  $0.6 \times 10^{-6} \text{ m}^2 \text{ s}^{-1}$ ) or 200 m (diffusivity  $1.0 \times 10^{-6} \text{ m}^2 \text{ s}^{-1}$ ), but becomes more pronounced for shorter profiles. Its position on the time scale moves toward present with the shortening of the profile. The depth 150 m (diffusivity  $0.6 \times 10^{-6} \text{ m}^2 \text{ s}^{-1}$ ) or 200 m (diffusivity  $1.0 \times 10^{-6} \text{ m}^2 \text{ s}^{-1}$ ) is also the minimum required for true reproduction of the long-term mean temperature before the onset of the warming trend in the middle of the 19th century.

Good example of such spurious minimum showing up on the GST history from FSIs of temperature profile of length  $<150 \text{ m}$  versus deeper temperature profile ( $>400 \text{ m}$ ) is shown for the example of south-western Polish wells in the area of Sudetian Mountains and its foreland (Majorowicz *et al.*, 2004a). GST history based on the upper parts of the profiles above the abrupt thermal gradient changes for the upper 95 m in Długopole well bore, 115 m in Janików, 189 m in Lubrza, 115 m in Pełczyn, 200 m in Ptakowice, 115 m in Oleśnica, 290 m in Waliszów, 75 m in Wołczyn, and 135 m in Wybłyszczów showed  $1^\circ\text{C}$

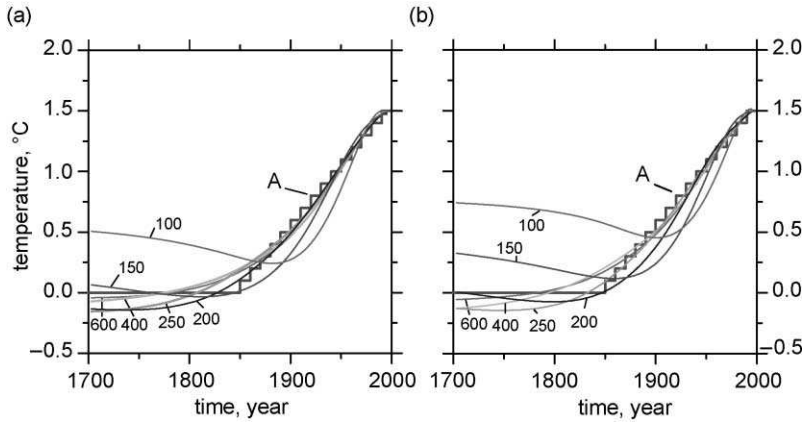
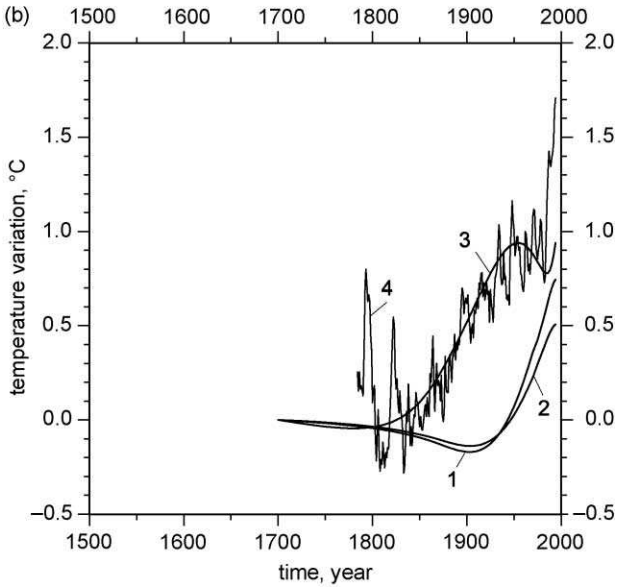
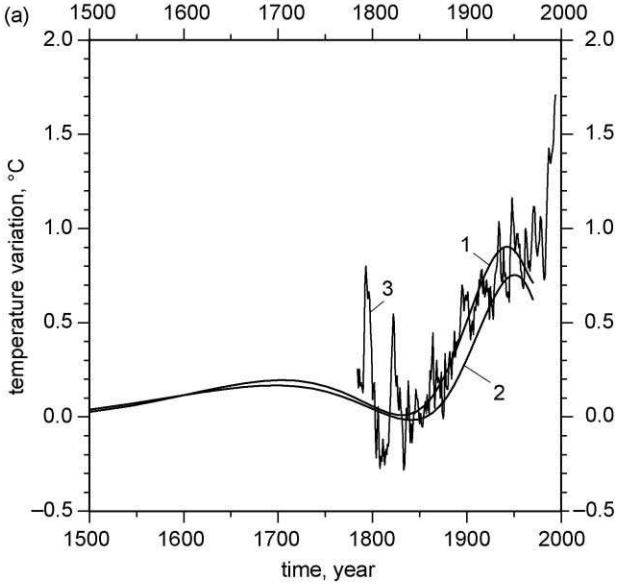


FIG. 8. FSI's GST histories of the synthetic profile based on the assumed GST history (line A) and truncated to various depths. Both noise-free and noisy ( $SD = 0.02^{\circ}\text{C}$ ) data are shown. Labels mark depth of the inverted profile. (a) Diffusivity  $1.0 \times 10^{-6} \text{ m}^2 \text{ s}^{-1}$  (typical for crystalline crust terrains) and (b) diffusivity  $0.6 \times 10^{-6} \text{ m}^2 \text{ s}^{-1}$  (typical for sedimentary basin).

warming in the 20th century (see Majorowicz *et al.*, 2004a for the well logs) (Fig. 9a). The misfit of these GST histories with the homogeneous surface temperature time series shown in Fig. 9a can be due to very short sections of the high precision profiles used in the inversion. GST histories based on the simultaneous FSIs of deep ( $>450 \text{ m}$ ) temperature profiles obtained from deep continuous logs are shown in Fig. 9b. We also show the inversion of the deepest high precision well temperature profile in Grodziec borehole from the point measurements with depth (Fig. 9a). Results show much higher warming signal than the short logs and very good ( $>0.8$ ) statistical correlation with the homogenized SAT time series. The magnitude of warming for the 19th–20th century is  $0.9 \pm 0.1^{\circ}\text{C}$ . This warming period is preceded by a colder period. The last number could be a minimal warming as higher warming magnitude was calculated using a simple model based on surface temperature for the observational period (homogenized Warsaw series, Lorenc, 2000) and POM (method of Harris and Chapman, 1995) of  $-1.53^{\circ}\text{C}$  below the 1951–1980 mean temperature level.

For better understanding of differences between the SAT series and the GST histories reconstructed from borehole profiles, it is useful to look at the inversion of the synthetic temperature–depth profile calculated using the surface SAT forcing. To do this, an inversion of the synthetic subsurface temperature profile generated by SAT series is used as a forcing function at the Earth's surface (Clauser and Mareschal, 1995). The method is illustrated by the use of the SAT



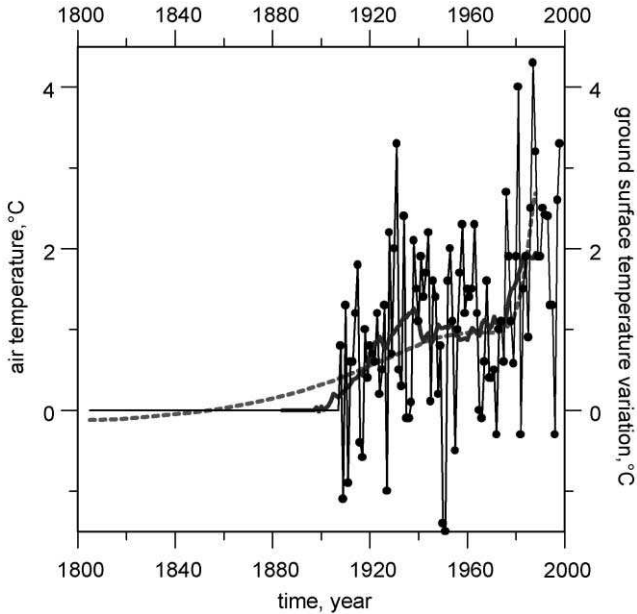


FIG. 10. Comparison of SAT time series (circles) for 1908–1998 for Waseca SAT station in western Canada ( $53^{\circ}08'N$ ,  $109^{\circ}24'W$ ) with GST history (dashed line) reconstructed by FSI from the synthetic profile based on the SAT series and the shown pre-observational mean. The thick line denotes the 21-year running average.

series recorded by Environment Canada in the typical meteorological network station at Waseca (Western Canadian Plains) during the period 1908–1998 (Majorowicz *et al.*, 2002). The data represent a typical meteorological series recorded in north-western parts of the North American continent which are rather short observational records in comparison with Europe or even eastern parts of the North American continent. Figure 10 shows the SAT time series from Waseca

---

FIG. 9. Reconstruction of ground surface temperature history in Poland. (a) Derived from the continuous temperature profiles from wells deeper than 450 m. Curve 1—reconstruction from the continuous temperature logs which indicate large ground surface temperature warming; curve 2—average based on all wells; curve 3—homogeneous air temperature series from Warsaw (11-year running average) (Lorenc, 2000). (b) Curves 1 and 2—reconstructions based on the upper portions of precision temperature profiles above the region of abrupt thermal gradient changes for the high and low assumed error of the *a priori* conductivity model; curve 3—reconstruction based on the entire depth of temperature profile in well Grodziec; curve 4—homogeneous air temperature series from Warsaw (11-year running average) (Lorenc, 2000) (modified from Majorowicz *et al.*, 2004a).

meteorological station in western Canada ( $53^{\circ}08'N$ ,  $109^{\circ}24'W$ ) for the period 1908–1998 with a 21-year running average filter. Also shown is the GST history inverted from the noise-free synthetic profile corresponding to the observed series (used as surface forcing). The “logging” time of the synthetic profile was 1993, which means that the younger SAT series (1993–1998) was not considered. The POM used in calculating the synthetic profile was  $0.5^{\circ}C$  lower than the mean SAT of the 1910–1919 decade. It is observed that the reconstructed GST history of the last 50 years is close to the SAT running average, and the warming rate of the first 30 years of the observations is appreciably larger than the warming rate indicated for this period by inversion. The inversion results depend on the chosen value of the POM. It is therefore difficult to place the SAT data in the perspective of the long-term change because of the short record time.

A reconstruction of less robust signals of the little ice age, medieval climatic optimum, Boreal, Atlantic and possibly some other climatic periods of the Holocene fails even in most cases of purely conductive subsurface thermal regime for several reasons. We have poor knowledge of the thermal conductivity variations in the borehole preventing proper separation of steady-state and transient components of the temperature profile. This can be improved by detailed sampling of the drill-core for conductivity measurements, followed by calculation of representative averages of conductivity in the individual depth intervals, which can be considered in the inversion algorithm. We also have little information about lateral conductivity variations, which can produce spurious signals and which can be neither recognized from the drill-core nor taken into account in the present one-dimensional inversion software. The other problem is possible time variability of the air versus GST offset, which can interfere with the air temperature changes. On the other hand, large amplitude of glacial–post-glacial surface and subsurface temperature changes can be detected from most of the logs in Europe (Kukkonen, 1987).

Numerical simulations indicate that the late Pleistocene climate variations should have a considerable effect on the subsurface temperature field in those parts of central and north-eastern Europe, which were not covered by the Fennoscandian ice sheet and where the glacial–interglacial surface temperature amplitude assessed by different proxy methods is of the order of  $10^{\circ}C$  (Zoth and Haenel, 1988). The depth extent of the temperature perturbation, distinguishable from the background noise, is estimated at 2–3 km. The predicted effect of an increase of the vertical temperature gradient with depth is actually observed in deep boreholes in this part of Europe and the first attempts to use it as an independent estimate have yielded the surface temperature amplitudes of 5– $15^{\circ}C$  (Clauser *et al.*, 1997; Rajver *et al.*, 1998; Safanda and Rajver, 2001; Kukkonen and Joleht, 2003).

One excellent example of the influence of post-glacial surface temperature change, permafrost melting and recent climatic warming on the temperature–depth curve and timing of its recovery in post-glacial environment can be illustrated by a model for the north-eastern Poland affected by Pleistocene glaciation (Safanda *et al.*, 2004). Typical temperature–depth curvature was observed in the low heat flow area above the norite–anorthosite intrusive characterized by a very low heat generation  $0.1 \mu\text{W m}^{-3}$  (Fig. 11). The effect of the temperature gradient increase with depth is especially strongly pronounced in the European Lowland including Polish territory exposed to a harsh periglacial climate in the forefront of the Fennoscandian ice sheet during the last (Weichselian) glacial. The deep temperature profiles used in estimating the last

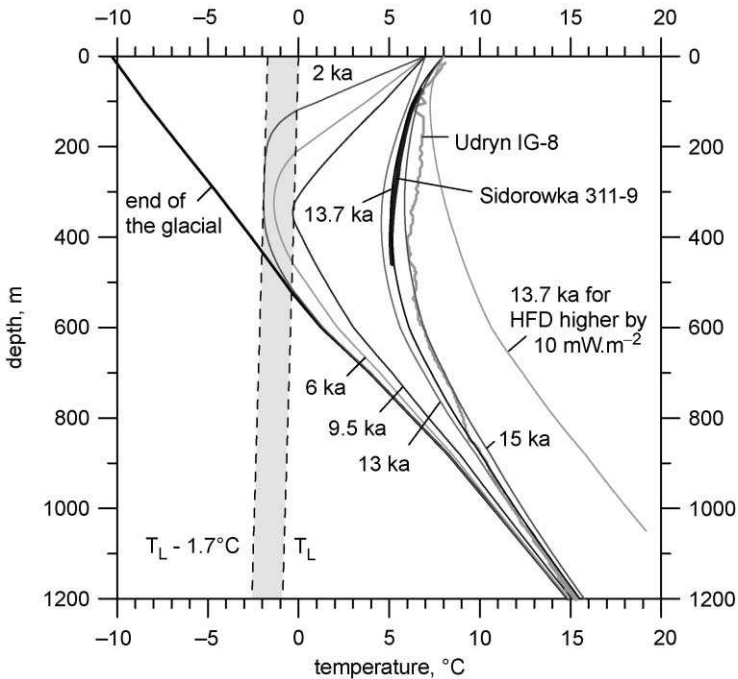


FIG. 11. Numerical simulation of subsurface temperature time changes in Udryn (NE Poland) during Holocene. The assumed initial temperature–depth profile at the end of the glacial (time 0) is in equilibrium with surface temperature of  $-10.3^{\circ}\text{C}$  extrapolated from the lowermost part of profile Udryn IG-8 below 2 km (not shown) and the geothermal model of the site. The most right-hand profile demonstrates the effect of the higher heat flow assumed for areas outside the anorthosite massif. Curve  $T_L$  is the depth-dependent thawing (liquidus) temperature. Curves  $T_L - 1.7^{\circ}\text{C}$  and  $T_L$  delineate the thawing range of the interstitial ice (modified from Safanda *et al.*, 2004).

glacial temperatures revealed low, but positive temperature gradients gradually increasing with depth to the values undisturbed by the glacial cycles (Clauser *et al.*, 1997; Safanda and Rajver, 2001; Safanda *et al.*, 2002; Szewczyk, 2002; Kukkonen and Joeleht, 2003). A qualitatively different picture is provided by an extensive set of temperature logs measured in NE Poland (54°N, 23°E, 100–200 m a.s.l.) in the 1960s–1970s. They revealed a negative temperature gradient in the uppermost 400 m with a minimum temperature at this depth. A typical example is the 2.3 km deep profile measured in borehole Udryn IG-8, the upper part of which is shown in Fig. 11. The logs from the Krzemianka–Udryn area show inversion of temperature with depth resulting in a temperature minimum around 400 m. These observations made by Majorowicz (1976) led him to believe that a shape of the temperature–depth profiles is a result of glaciations which have existed in this area of Poland in the past. The only available borehole, in which the previous results could have been verified, is 482 m deep hole Sidorowka 311-9. The hole was drilled in 1974 in a distance of 4 km from deep bore hole Udryn IG-8 in practically identical geological conditions. It had been standing for more than 11 months when the precise temperature logging was done in it in July 2003. The logging reached a depth of 458 m and confirmed the existence of the temperature minimum 5.1°C at a depth of 406 m. Below this point the temperature starts to increase with depth again (Fig. 11). This phenomenon cannot be explained neither by downward water motion nor by a thermal conductivity variation with depth. There is no realistic alternative to the climatic explanation. Similar subsurface temperature conditions occur at present, in higher latitudes north of 62°N, for instance, in the West Siberian Platform, where even a relic permafrost is observed hidden below the thawed subsurface layer in the depth range of 100–300 m (Duchkov and Devyatkin, 1992).

Simulated time changes of the subsurface temperature since the end of the last glacial by solving numerically the transient heat conduction equation in a geothermal model of the Udryn area were done (Safanda *et al.*, 2004). It was assumed, in agreement with the previous calculations, that the subsurface temperature was close to an equilibrium with the mean glacial surface temperature at the end of the glacial some 14–15 ka ago (Hartmann, 1994) and that the surface warming had not reached the depth of 2 km since that time to present. The climatically undisturbed lowermost part of the Udryn IG-8 profile (below 2 km depth) was then extrapolated to the surface and yielded the mean glacial temperature of  $-10.3^{\circ}\text{C}$  and the permafrost thickness of 520 m. In simulating the downward propagation of the warming from  $-10.3$  to  $+7^{\circ}\text{C}$  at the end of the glacial (identical with time 0 of the simulation) and to  $+8^{\circ}\text{C}$  in the last 150 years, we have taken into account the dependence of the thermal conductivity and the specific heat of the encountered rocks on the porosity and a content of the

interstitial water and ice (Galushkin, 1997). Accounting for the effect of the latent heat necessary for thawing the interstitial ice in the 520-m-thick permafrost layer has turned out to be crucial for matching the calculated and observed profiles in realistic times (Galushkin, 1997). In the absence of this heat sink, the subsurface warming would have proceeded much faster and the negative temperature gradient would have disappeared by many thousands of years earlier. The best coincidence between the Sidorowka profile and the synthetic curves was achieved for a time of simulation 13.7 ka, which agrees quite well with the time since the end of the last glacial. One of the sensitive parameters of the model is a fraction of the interstitial water, which stays liquid at subzero temperatures (Nixon, 1986; Galushkin, 1997). A consideration of the additional warming from  $+7$  to  $+8^{\circ}\text{C}$  in the last 150 years, which has improved the fit in the uppermost 200 m, is based on the FSI reconstruction of the recent GST history from the Sidorowka profile (Fig. 12) and is compatible with the general trend observed in Poland (Majorowicz *et al.*, 2004a).

The existence of more than 500 m deep permafrost in NE Poland was a result of a very low mean surface temperature during the glacial, which seems to have been by  $18^{\circ}\text{C}$  lower than the present one and low undisturbed subsurface

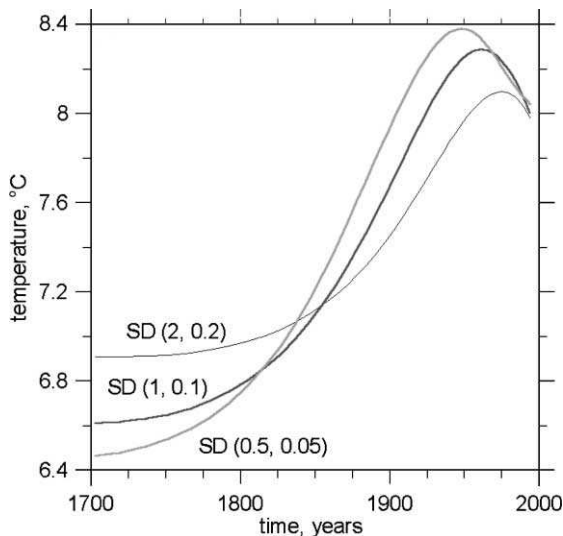


FIG. 12. Recent ground surface warming inferred from the upper part of the temperature–depth profile of Sidorowka 311-9 in north-eastern Poland. The most conservative history corresponding to the largest *a priori* SDs ( $2 \text{ W m}^{-1} \text{ K}^{-1}$ ,  $0.2 \text{ K}$ ) of the thermal conductivity model and the measured temperatures was used in the subsurface temperature simulation.

temperature gradient conditioned by a low heat flow, about  $40 \text{ mW m}^{-2}$ . The low heat flow can be explained by a very low heat production of anorthosites ( $0.2 \mu\text{W m}^{-3}$ ) calculated from measured U, Th and K isotope content in core samples from wells in the area of the intrusion (Majorowicz, 1984).

#### 11. CASE STUDIES DEMONSTRATING THE BASIC FEATURES OF THE "POM" APPROACH

Lachenbruch *et al.* (1988a), Harris and Chapman (1995, 2001) and Harris and Gosnold (1999) have shown that the method combining in the model SAT record and variable POM can be used in studies of climatic histories for local and large regional scales. It was found that some of the observed temperature–depth profiles from mid-west US (Harris and Chapman, 1995; Harris and Gosnold, 1999) and western Canada (Manitoba and Saskatchewan; Majorowicz *et al.*, 1999a) can be fitted to a SAT–POM model in which part of the model is based on the available instrumental record (SAT) and part (before the time of instrumental record) on the assumed POM level. Harris and Gosnold (1999) and Majorowicz *et al.* (1999a) used temperature logs from North Dakota in the USA and Saskatchewan in Canada. They found that the discrepancy in warming reflected in SAT time series and GST histories based on FSI of the temperature–depth signal could be spurious and can be attributed to our lack of knowledge of GST prior to the beginning of the SAT record (lower POM levels than the inversion method gives).

A European example of usefulness of the SAT–POM modeling approach has been illustrated recently by Safanda *et al.* (2002). They used long SAT series from Lisbon and a nearly 200 m deep borehole located 100 km to the east of Lisbon for a practical demonstration of the POM concept as described above (Correia and Safanda, 2001). It was assumed that the transient component of the present subsurface temperature at the borehole site represents a response to SAT variations similar to those observed in the Lisbon. Among the transient components of the synthetic profiles, curve corresponding to  $\text{POM} = 15.65^\circ\text{C}$  was found to be the best fit to the shape of the reduced temperature calculated as a difference between the measured  $T-z$  profile and the linear fit to its lowermost (140–180 m) portion. The mean of the SAT series in the period 1856–1900 was found to be  $15.6^\circ\text{C}$ . This result is consistent with the FSI results (Correia and Safanda, 2001).

The GST history generated by the Regina (Saskatchewan, Canada) SAT series and preceding models of surface temperature change were used by Majorowicz *et al.* (1999a) and compared to FSI solution for the temperature–depth

profiles in the Riverhurst wells located nearby (within several kilometers) in the region (51°N, 107°W). Here we show a detailed analysis of the FSIs for different *a priori* constraints and a variety of SAT–POM models.

Calculated misfit between the measured and synthetic transient profiles (calculated using root-mean-square method) enables us to determine the best POM for the SAT data used as a forcing function and to calculate the parameters POM anomaly. We test this procedure using Riverhurst 9c temperature profile measured in 1997 (Majorowicz *et al.*, 1999a). Harris and Chapman (1995) approach has been followed, i.e., the use of the *a posteriori* transient component resulting from the application of FSI to the profile. Majorowicz *et al.* (1999a) used SAT-boxcar model (boxcar model for the pre-observational time). Here we discuss the dependence of the transient anomaly of temperature obtained in this way on the inversion parameters, namely, on *a priori* SDs of conductivity and measured temperature to illustrate and compare the POM approach versus FSI method (Figs. 13–16). In order to find out how strong the dependence is, we use the transients corresponding to the two most common SDs:  $1.0 \text{ W m}^{-1} \text{ K}^{-1}$  and 0.10 K (the loose inversion) and  $0.5 \text{ W m}^{-1} \text{ K}^{-1}$  and 0.05 K (the tight inversion). These transients were compared with the synthetic temperature–depth profiles calculated analytically from the SAT series from Regina station as surface forcing. Regina is one of the stations in the region of southern Saskatchewan (Figs. 17 and 18). The best fit for the “loose” transient was achieved for  $\text{POM} = -0.78 \text{ K}$  (relative to the 1951–1970 average) and for the “tight” inversion for  $\text{POM} = -0.74$ . The profiles are shown in Figs. 13 and 14. The synthetic profiles for the two SDs versions differ very little. The sources of the difference are the different POMs ( $-0.78$  versus  $-0.74 \text{ K}$ ) and also the slightly different *a posteriori* thermal conductivity-versus-depth distribution, which is considered in the solution of the heat conduction equation.

Differences between the transient based FSI and the best POM synthetic profile are shown in Figs. 15 and 16. The maximum of the difference is at 100.1 m (loose inversion) and 94.2 m (tight inversion). The depth of the maximum is used in calculation of the average time of the “boxcar” low surface temperature event (sudden drop of surface temperature followed by a period of zero temperature increase followed by a sudden temperature rise). For the diffusivity considered in processing the Riverhurst profile 9c,  $0.625 \text{ mm s}^{-1}$ , the average times are 254 years (loose inversion) and 225 years (tight inversion). When we consider that the boxcar event (lower temperature for the time period) ended just at the beginning of the SAT observations at the Regina station in 1898, the “boxcar” low level periods are then 1588–1898 and 1646–1898, respectively. The surface temperature decrease relative to the best POM is 0.33 and 0.49 K for the two SDs versions, respectively. The corresponding temperature profiles and their

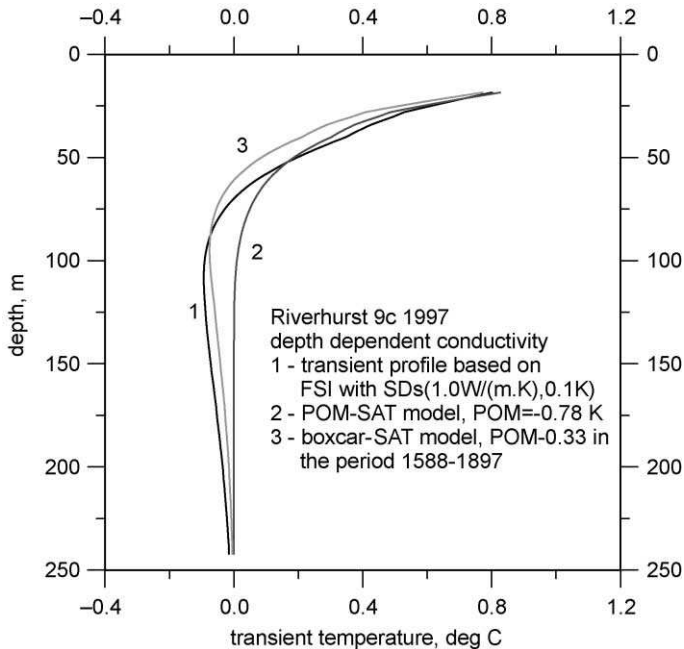


FIG. 13. Comparison of transient components of temperature–depth profile (Riverhurst 9c) for the case of depth-dependent conductivity and FSIs with *a priori* parameters ( $1.0 \text{ W m}^{-1} \text{ K}^{-1}$ ,  $0.01 \text{ K}$ )—loose inversion case (a).

differences with transients are shown in Figs. 13 and 14 and Figs. 15 and 16, respectively.

Although the root-mean-square misfit has decreased, it can be seen from the figures that the introduction of the boxcar event improves the coincidence between the transients and the synthetic profiles below the depth of about 75 m only. Above 70 m the coincidence deteriorates as the synthetic profiles are cooler in the upper 70 m.

Because there is a freedom in duration of the boxcar event given by the time span between its average time and the beginning of the observations, we shortened, as a second iteration, its duration by 100 years (50 years at each end). As a result, the amplitude of the surface temperature decrease increases from 0.33 to 0.48 K and from 0.49 to 0.81 K in the two SDs versions. A very slight improvement of the misfit can be seen in Figs. 15 and 16, where the corresponding profiles are shown by the dotted lines. A large portion of the misfit stems from the differences in the upper 70 m.

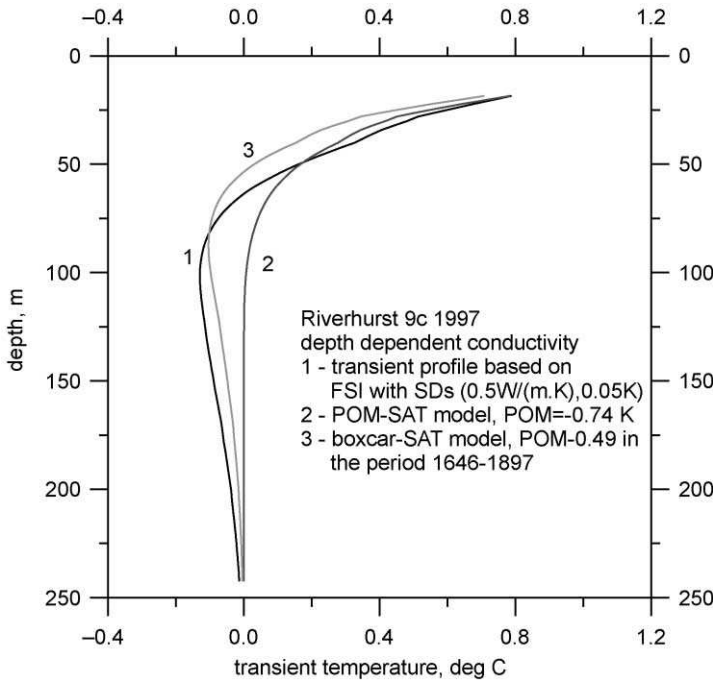


FIG. 14. Comparison of transient components of temperature–depth profile Riverhurst 9c for the case of depth-dependent conductivity and FSI with *a priori* parameters ( $0.5 \text{ W m}^{-1} \text{ K}^{-1}$ ,  $0.05 \text{ K}$ )—tight inversion case (b).

The above example shows that the transient component of the measured temperature profile can be explained by the surface temperature history observed at the meteorological station (Regina station). There was a very good coincidence for the uppermost 60 m, when the SAT data were combined with the best POM. When we try to improve it by introducing the boxcar event, the coincidence below 60 m depth deteriorates. The differences stem from the surface temperature variations prior to the observational period. If the boxcar event is real, then the observed SAT does not explain the shape of the measured transient in the first 60 m of the borehole. On the contrary, the GST history obtained by FSI reproduces the log within the  $\pm 0.03 \text{ K}$ , as can be seen from Figs. 17 and 18, where curve 4 represents the difference between *a posteriori* and *a priori* profiles for the corresponding SDs versions of the FSI method. In this case, the FSI approach seems to give better coincidence of the GST history model with the observed SAT series.

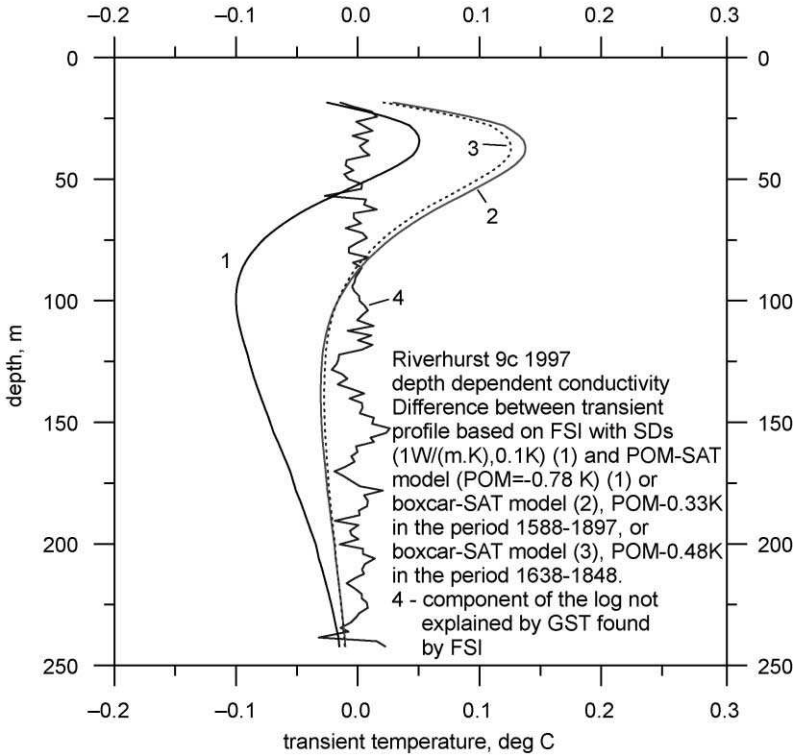


FIG. 15. Comparison of differences between transient components of temperature–depth profile for loose inversion case (c).

## 12. HEMISPHERIC AND CONTINENTAL RECONSTRUCTIONS OF GST FROM WELL TEMPERATURES

A global data set now exists containing now close to 1000 well temperature profiles (Huang and Pollack, 1998; Huang *et al.*, 2000) and can be used for estimates of global (continental) GST history. Pollack *et al.* (2000) stacked continental GST histories obtained from specially parameterized FSI of 358 well temperature profiles from North America, Europe, Africa and Australia. Wells with temperature profiles 200–500 m deep were selected. Borehole temperature reconstructions use ensemble averaging (“stacking”) as an important filter for removing non-climatic site-specific effects. The number and geographic distribution of the boreholes are insufficient to determine a

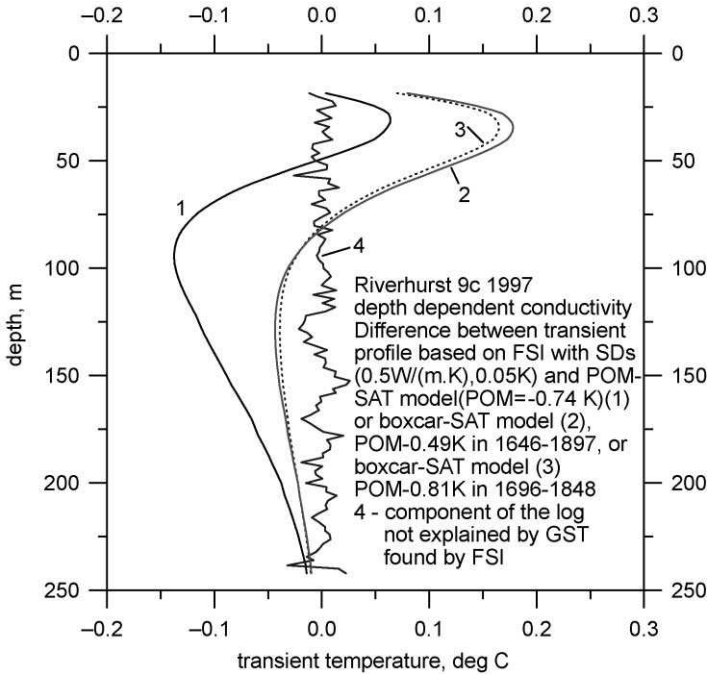


Fig. 16. Same as that for the tight inversion case (d).

robust average for small areas ( $5^\circ \times 5^\circ$ ) used for SAT observations or multi-proxy data geographical representation (Mann *et al.*, 2003). This averaging procedure allowed Pollack *et al.* (2000) to reconstruct GST history for the past five centuries 1500–1998 AD. The subsurface temperatures indicate surface temperatures have increased by about 1.0 K over the past five centuries and 0.5 K in the 20th century alone. This result offers an independent confirmation of the unusual nature of the 20th century warming that has emerged from other multi-proxy analyses (see Mann *et al.*, 2003 for the latest review of the literature).

Subsequent work of Huang *et al.* (2000), Pollack and Huang (2000), Pollack *et al.* (2000) and Pollack and Smerdon (2003) based on the large global data set (Fig. 19a) confirmed their previous result. The above works also demonstrated that the hemispheric continental reconstructions are very similar to the instrumentally determined SAT trend (Fig. 19b). It also showed that while borehole temperature profiles on continents imply a warming of Earth's solid

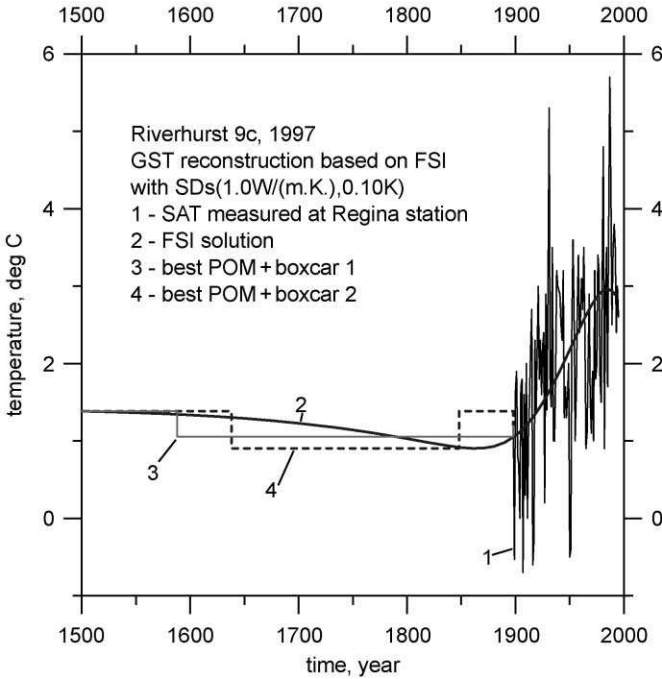


FIG. 17. FSI solution, SAT–POM and boxcar-SAT models for loose inversion case (e).

surface of about 1 K over the past five centuries, multi-proxy (mostly tree-ring-based) reconstructions estimate only about 0.5 K temperature change over the same time interval. This discrepancy is well illustrated in Fig. 19c for the northern hemisphere where the data are most abundant. Independent study of the global data set (826 temperature profiles) with the use of different inversion scheme (SVD) showed that the ground surface has warmed up by 0.9 K over the last five centuries (Beltrami, 2002). This result confirmed large surface warming increase showed by previous work of the Pollack group (Huang *et al.*, 2000; Pollack and Huang, 2000; Pollack *et al.*, 2000; Pollack and Smerdon, 2003).

The third independent confirmation of high surface warming from inversions of geothermal profiles comes from Harris and Chapman (2001) who analyzed the northern hemisphere data set. They used the model combining SAT and POM to fit northern hemisphere transients of temperature–depth profiles. Their work showed that POM level is some 0.7 K lower than the reference temperature level for the recent decades and that the five-century change exceeds 1 K (Fig. 20).

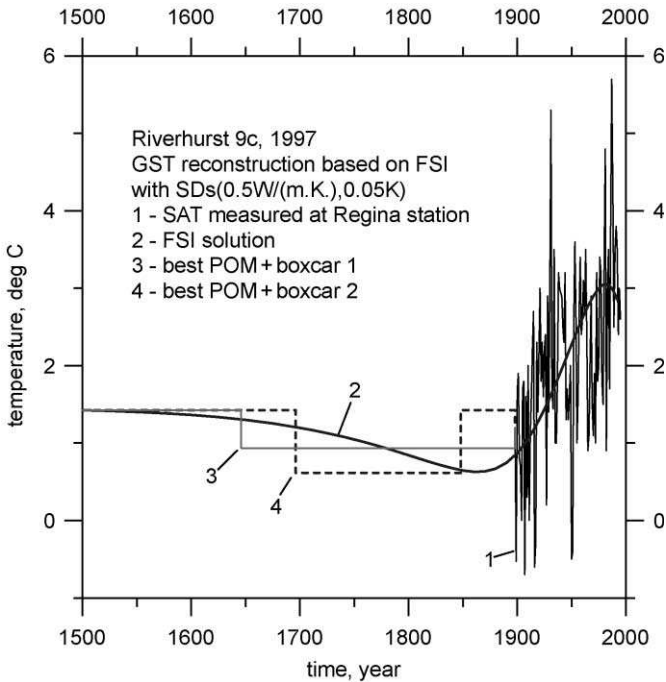


FIG. 18. Same as that for the tight inversion case.

The model of GST reconstruction assumes that the northern hemisphere SAT observations parallel GST change for the same recent time period of more than a century and it searches (by the use of the formalized numerical procedure) for the pre-observational log term mean, POM.

Recently, Pollack and Smerdon (2003) have re-examined the mean hemispheric warming using a variety of grid sizes and occupancy weighting schemes, and have found that the five-century warming falls in the range 0.89–1.07 K, a range that includes all published results from three different geothermal groups (see above) that have analyzed the primary temperature versus depth data.

### 13. CANADIAN EXAMPLES

To analyze regional GST histories in Canada, we have performed both FSI individual inversions with subsequent averaging and simultaneous inversions of

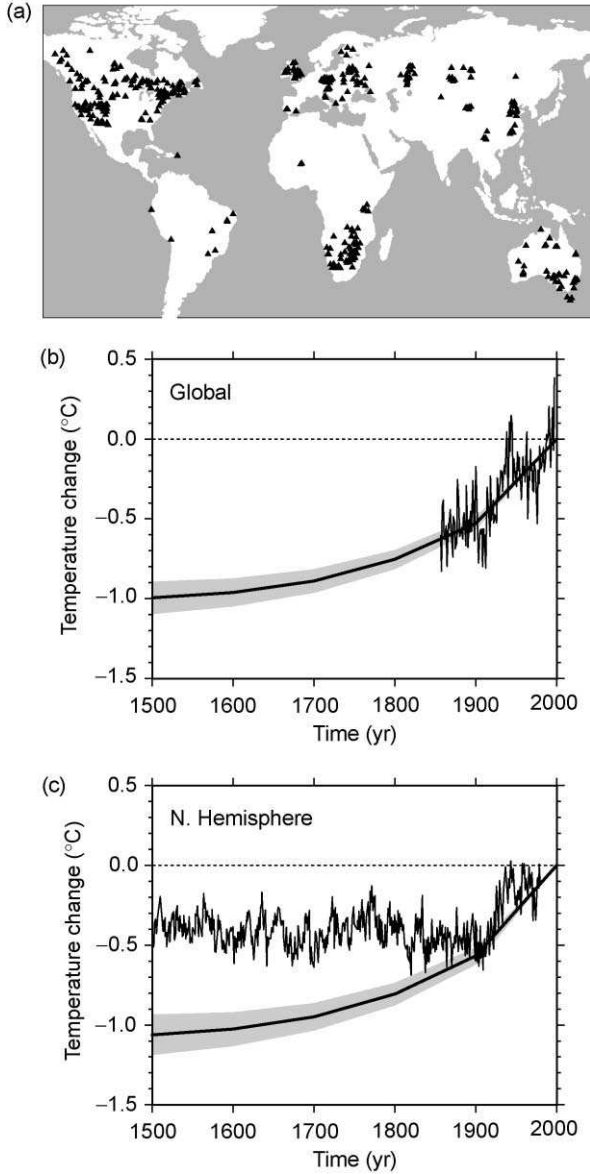


FIG. 19. Global and northern hemispheric GST histories derived from well temperature continental data (a) compared to SAT time series based mean annual history (b) and multi-proxy for the northern hemisphere according to Mann *et al.* (1998) and (c) according to Huang *et al.* (2000) (modified).

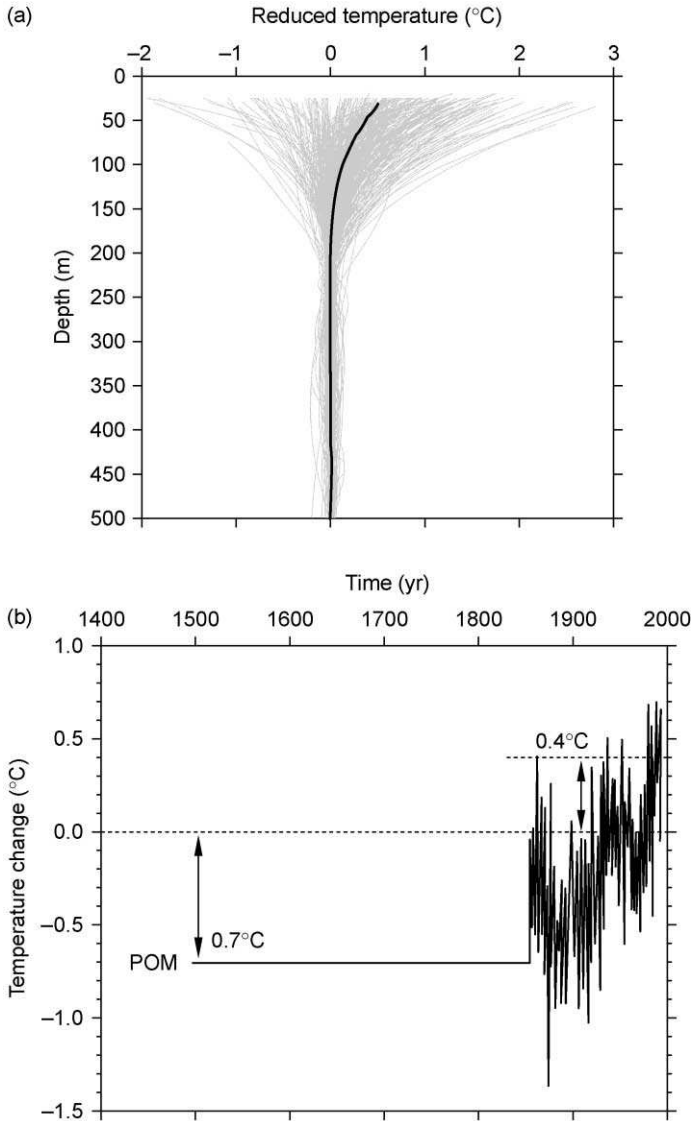


FIG. 20. Model of surface temperature change with time composed from observational time series and the pre-observational mean ( $-0.7^{\circ}\text{C}$ ) (b) consistent with averaged transient temperature–depth component based on numerous well temperature logs for the northern hemisphere (a) (modified from Harris and Chapman, 2001).

the temperature versus depth logs for three ensembles of wells. The calculated transient components of temperature–depth profiles from Canada all show evidence of warming in the upper 200 m (Fig. 6). The transient components of temperature versus depth profiles from central (Fig. 6) and western Canada (Fig. 6) show evidence of near surface (100 m) climatic disturbance. Data from all of the deep logs, as well as data from shallower logs (less than 150 m but not used in this study for GST history reconstruction because the shallow depth is insufficient to resolve signals before 19th century), also show evidence of extensive ground temperature warming in the 20th century. It is observed that the onset of warming at depth is deeper in east-central Canadian wells.

Figure 21 shows an example of GSTH variability for one specific region in Canada (eastern Canada east of  $70^{\circ}\text{W}$ ). It compares individual inversions, simultaneous inversions, and averaged GST histories for 18 selected eastern Canadian wells all located east of  $70^{\circ}\text{W}$ . All individual GST histories show warming over the past century. It shows that individual GST histories are quite variable when compared from site to site and averaging or simultaneous inversion of these is needed. The stacking of GST results from individual wells, or the simultaneous inversion of several logs used for regional, continental or global GST history curves, ignores well-to-well variability, some of which is the result of varying local surface and climatic conditions. These can be also due to a real site-to-site variability in the climatic warming as such variability has been observed from the SAT data for Canada.

Inversion of 141 logs using one inversion scheme, which used measured and estimated conductivity values for each well, allowed calculation of rates of GST change ( $^{\circ}\text{C}/100$  years) across Canada for the 19th and 20th centuries (Figs. 22 and 23) by fitting a ramp function to the continuous GST history obtained with FSI. In order to identify major spatial patterns, warming events (positive rates of temperature change) and the cooling events (negative rates of temperature change) were examined. Analysis of 141 individual temperature well logs across Canada (south of  $60^{\circ}\text{N}$ ) shows that in 95% of cases there is a significant warming in the previous century (Fig. 23). There are some cases of cooling in the proximity of the Pacific and Atlantic Oceans. It could be asked if these well-to-well variations in GST history are a result of data noise or if there is information about regional/local scale variability across Canada.

A westward retardation of the onset of warming is identified. It is apparent from these general patterns that there are large regional differences in the timing of major warming events across Canada. While large areas of east-central Canada were warming in the 19th century, there were large areas of western Canada that had no change and even cooled.

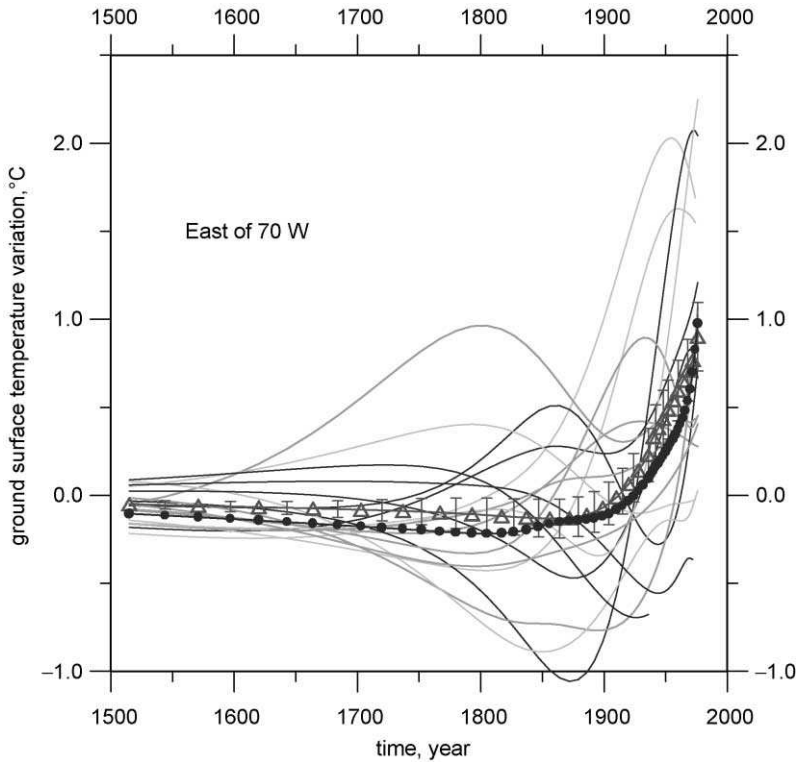


FIG. 21. GST histories yielded by individual FSIs of each of the 18 temperature logs available from eastern Canada (east of 70°W). Despite the appreciable scatter of the individual histories, their average (triangles with  $\pm 1$  standard error bars) is close to the simultaneous inversion (circles) (modified from Majorowicz *et al.*, 2002).

The spatial variation in warming and cooling over the instrumental record around the northern hemisphere and globally (IPCC, 2001) and across Canada (Gullett and Skinner, 1992; Zhang *et al.*, 2000) is also evident in pre-instrumental times, as identified from inversions of temperature logs from all continents (Huang *et al.*, 2000; Pollack and Huang, 2000) and across Canada (Majorowicz *et al.*, 2002). The onset of earlier warming in east-central Canada precedes that of the “industrial age” by a century or more.

Some suggestions explaining such differences can be made. The greater warming of the continental interiors in the past is confirmed here by the GST history for the central-western Canadian Plains (east of the Cordillera) and also

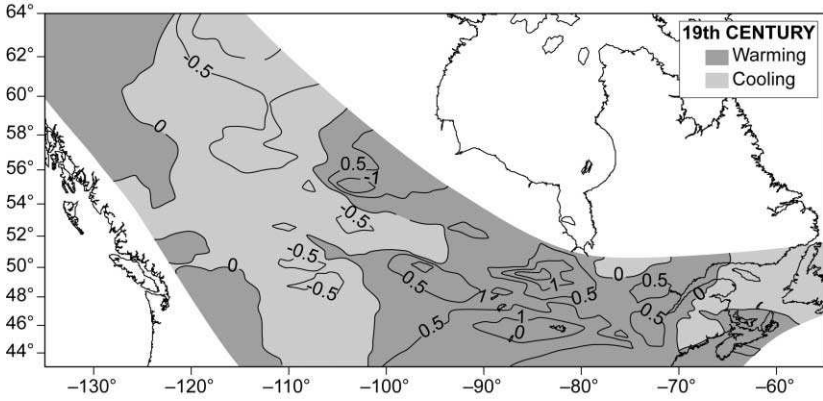


FIG. 22. Patterns of GST warming and cooling (in °C) across central-southern Canada based on the FSIs of individual wells across Canada for the 19th century.

by the Ontario and western Quebec data. This may be due both to the moderating effect of the oceans on the coastal margins and to positive feedback related to the hydrologic cycle, including the timing of freezing and melting, and changes in the area distribution of ice and snow on land. In Canada, the greatest warming in the last half of the 20th century occurred in winter and spring, the times of year

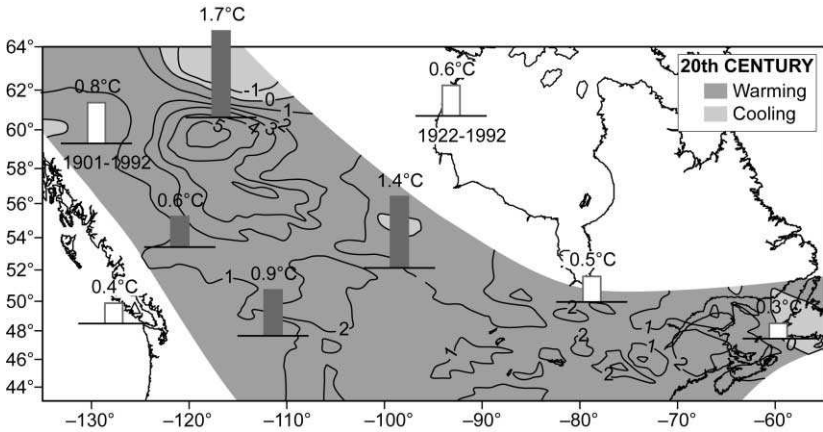


FIG. 23. Patterns of GST warming and cooling (in °C) across central-southern Canada based on the FSIs of individual wells across Canada for the 20th century. The bars show SAT warming in 20th Century.

when reductions in surface snow and ice amounts can greatly affect regional climate. Canada is located entirely in mid to high latitudes where inter-annual and longer-term variations in atmospheric circulation patterns can have a considerable effect on regional climate. A persistent change in the normal jet stream track will affect temperatures differently in various regions of the country by changing the relative frequency of their exposure to warm and cold air masses. An additional factor contributing to the observed differences can be anthropogenic related to land use change. Settlement and land clearing began in western Canada in the early 20th century and progressed northward throughout the century. Settlement in eastern Canada was much earlier, in the mid to late 19th century. It is unlikely that this effect alone could explain east–west differences. The main forcing is likely due to climatic warming (Skinner and Majorowicz, 1999), however, land cover changes due to deforestation and conversion of grassland to agricultural land can dramatically alter surface temperature and the subsurface temperature field. This influence in western and northern Canada is limited to last decades of the 20th century (Majorowicz and Skinner, 1997; Lewis, 1998; Skinner and Majorowicz, 1999) and to more than a century in eastern Canada (Lewis, 1998).

The western Canadian region was the last to warm, beginning in the late 19th century. However, the western Canadian region has experienced the largest warming magnitudes in Canada since that time. This is confirmed both by the instrumental SAT records and by the FSI reconstruction of GST history from well temperature data. It is important to note that in eastern Canada, the warming began about 100 years before the beginning of the industrial age. In western Canada, the onset of the latest warming began with the industrial age.

Northern Canadian wells are of special importance. We have performed (Majorowicz *et al.*, 2004b) individual inversions with subsequent averaging, as well as simultaneous inversions of the temperature versus depth logs for two ensembles of wells for a total of 61. The transient components of temperature–depth profiles were calculated for two regions in Arctic Canada—(a) Arctic Islands at latitude 74–81°N and (b) Canadian Beaufort–Mackenzie plain at latitude 63–70°N (Fig. 24). Some single logs are also available for Labrador and these are included in the analysis of the combined data for 60–81°N. There is evidence of warming in the upper 200 m (Fig. 6). This is comparable with other regions in Canada south of 60°N (also shown in Fig. 6). In the two northern regions, the increase of many transient components towards the surface is reduced in the uppermost 30–50 m. This cooling feature is not present in the temperature/depth profiles south of 60°N (Majorowicz *et al.*, 2002).

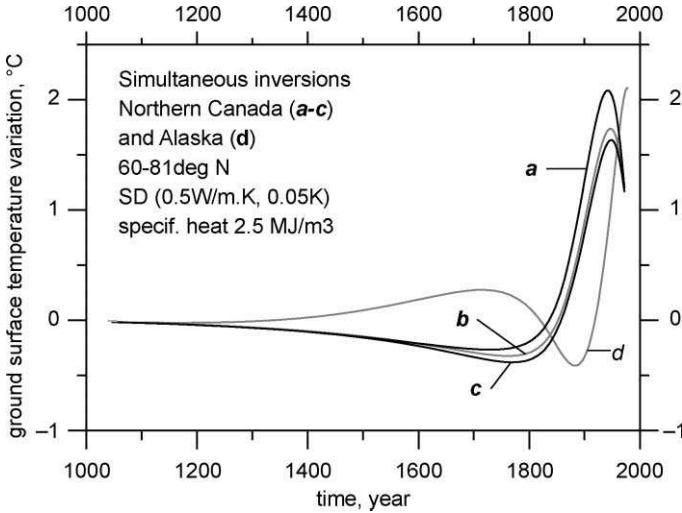


FIG. 24. Comparison of the GST histories based on the simultaneous inversion of all deep  $T-z$ . Curve a—24 profiles of the northern group (see Fig. 6 for location); curve b—all profiles for Arctic Canada (60–81°N, see Fig. 6 for locations); curve c—37 profiles of the southern group (see Fig. 6 for location); curve d—Alaska Coastal Plain equilibrium well temperature logs shown in Lachenbruch *et al.* (1988a) (modified from Majorowicz *et al.*, 2004c).

Figure 24 shows the GST histories obtained by simultaneous inversions of 37 profiles of the southern group (Beaufort–Mackenzie area) and 24 profiles of the northern group (Arctic Islands), all 61 profiles from all of the area between 60–81°N in Canada and in Alaska (based on equilibrium temperature well logs for the coastal plain, Lachenbruch *et al.*, 1988b). *A priori* SDs are  $0.5 \text{ W m}^{-1} \text{ K}^{-1}$ , 0.05 K, and the diffusivity was proportional to the thermal conductivity because the specific heat of  $2.5 \text{ MJ m}^{-3}$  was constant. Differences in GST histories between the southern and northern groups are minor. Minimum temperature occurs in the late 18th century and maximum temperature occurs in the 20th century. The amplitude between the minimum and the maximum is approximately 2°C. Alaska GSTH show later onset of recent warming as suggested previously by Lachenbruch and Marshall (1986).

The GST history curves obtained by the simultaneous inversion of all the logs in the Canadian Arctic and also by the averaging technique are shown in Fig. 25a and b. There is a considerable difference between the GST history obtained by the simultaneous inversion of 61 northern Canada profiles and the GST

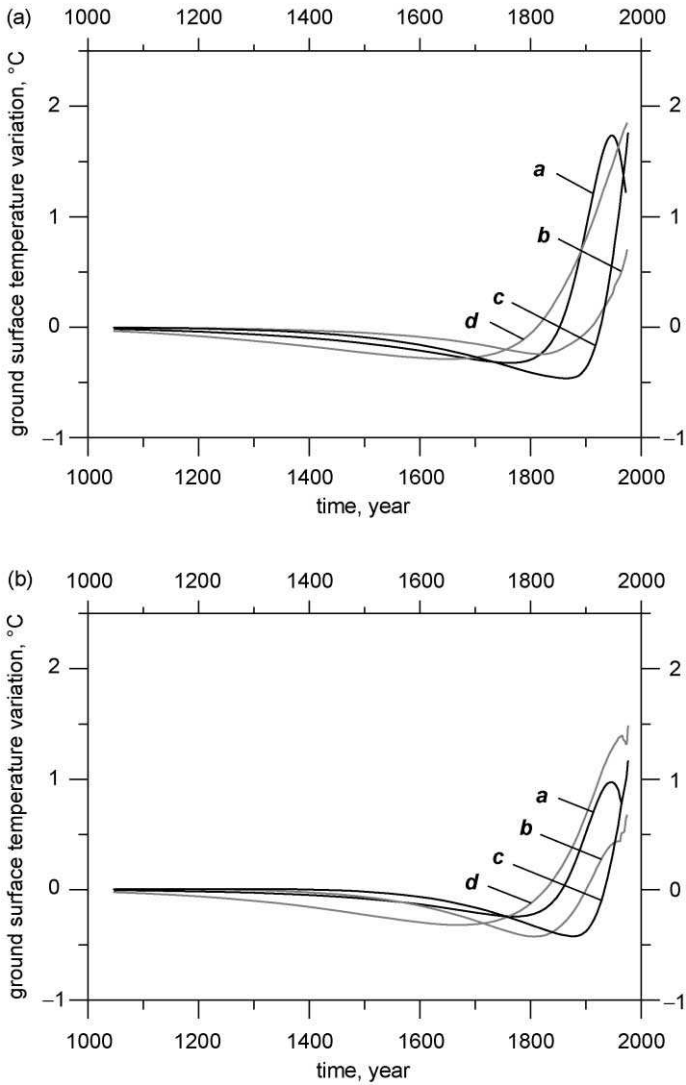


FIG. 25. (a) Comparison of the GST histories from simultaneous FSIs for the Arctic Canada (60–81°N) (curve a) with those in southern Canada south of 60°N: curve b—central and eastern Canada 70–90°W; curve c—central Canada between 90–100°W; curve d—western Canada east of the Rocky Mountains between 100–120°W. (b) Same as above for the averages of the individual FSIs (modified from Lachenbruch, 1994).

history calculated as an average of the individual inversions. The amplitude between the late 18th century minimum and the late 20th century maximum is much lower ( $1.3^{\circ}\text{C}$ ) than that from simultaneous inversions. This may be caused by the influence on the average of a small number of profiles with strong cooling after initial warming. In the probabilistic model of the simultaneous inversion, however, the shape of these profiles is probably ascribed to unnoticed thermal conductivity variations with depth.

The northern Canada GST histories end in 1976 because for many profiles the younger GST history is not resolved due to early time of logging, or the greater depth of the first temperature measurement. The time of logging varied between the 1970s to the early 1980s. The assumed parameters of all inversions were the same as previously given. The results of these two conceptually different procedures are susceptible to the random effects of noise. It is apparent from the simultaneous inversion of all 61 temperature logs that the warming in northern Canada in the 19th century, and throughout the 20th century, is high (about  $2^{\circ}\text{C}$ ). Warming began as early as the late 18th century. The estimated uncertainty in timing of this event is  $\pm 50$  years and is mainly related to our uncertainty in diffusivity. The time interval of averaging of GST variations increases with movement away from the present. Temperature logs considered in this paper allow fair resolution of last warming event and preceding GST level for at least the last 500 years.

The above simultaneous and averaged FSIs of well temperatures for the northern regions show small differences in the magnitude of recent warming from the northern region to the southern region (Fig. 25a and b). A comparison with GST histories in southern Canada (Majorowicz *et al.*, 2002) shows that GST history for the northern Canada wells is very similar to that for central and eastern Canada. Most of the Canadian wells show warming in the last 200 years.

#### 14. CIRCUMPOLAR WARMING

The Northern Canadian well temperature data shown above are from high latitudes. The Canadian Arctic Island data are the highest latitude location compared to well temperature data from the IHFC (International Heat Flow Commission) database (Pollack *et al.*, 2000). They show one of the largest GST warming in the circumpolar regions of the northern hemisphere. Figure 26 shows that Canadian Arctic warming magnitude is significantly higher than that for the whole of the northern hemisphere. We note, however, that northern

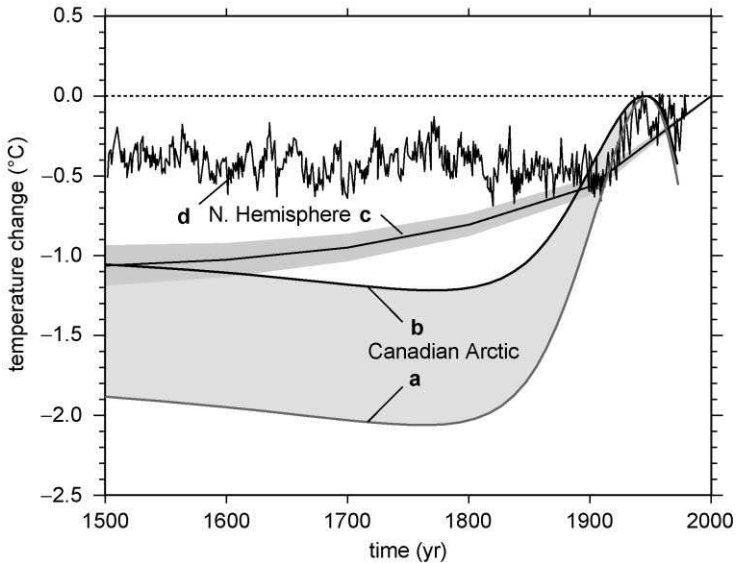


FIG. 26. Comparison of the northern (north of 60°N) Canada GST history derived from the simultaneous inversion of well temperature profiles with northern hemisphere proxy surface temperature histories from various sources (Mann *et al.*, 1998) and well temperature based GST history (Huang *et al.*, 2000) (modified from Majorowicz *et al.*, 2004b).

hemisphere reconstructions are mainly from the areas to the south of the Canadian Arctic.

There is a considerable difference between the GST history obtained by the simultaneous inversion of all 61 profiles and the GST history calculated as an average of the individual inversions (Fig. 26). The amplitude between the late 18th century minimum and the late 20th century maximum is much lower (1.3°C) than that from simultaneous inversions. However, in both cases (simultaneous inversion and averaging of individual inversions) Canadian Arctic warming is significantly higher than that of the northern hemisphere.

Large GST warming (>1°C; usually 1–2°C) is also present in other circumpolar locations in the northern hemisphere (Fig. 27). However, northward trend of higher warming is not proven by the available data. There has been no strong south-to-north gradient in warming magnitude when northern data are compared with data south of 60°N which also show warming close to 1–2°C (Majorowicz *et al.*, 2002).

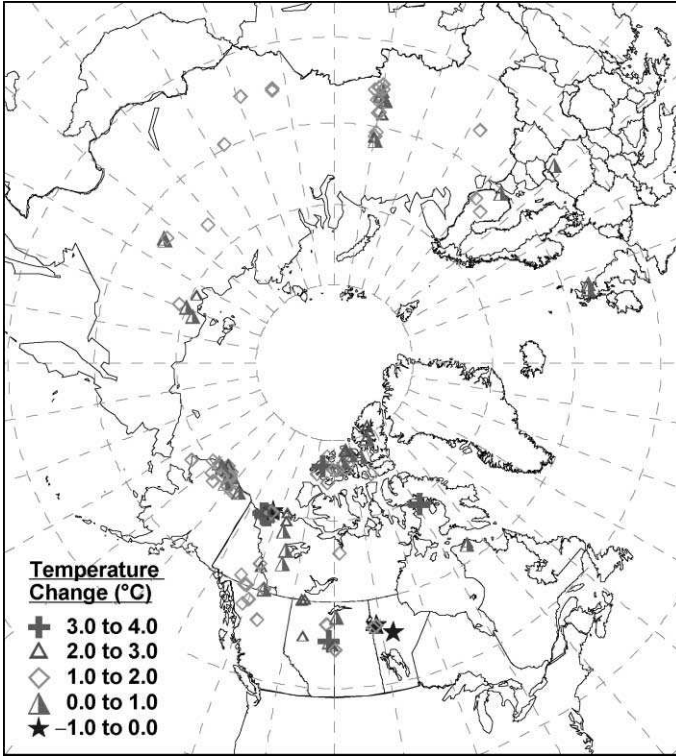


FIG. 27. Circumpolar well temperature locations and warming amplitude derived from well temperature profiles (according to data from Huang *et al.*, 2000; Pollack *et al.*, 2000; Majorowicz *et al.*, 2004b).

### 15. OBSCURING FACTORS

The GST history derived from temperature profiles in wells is an independent estimate of long-term warming magnitude, which can be compared with surface temperature time series and proxy reconstructions, of which growing season variability as deduced from tree rings is most common. The geothermal method provides a direct physical measure of temperature change. The main problem is the ideal situation in which the temperature changes with time at the surface are tracked by the underground temperature changes is not always met. The assumption of heat transfer by conduction only is well justified in areas with negligible vertical movement of underground water. It is usually the case in

terrains with flat or subdued topography and is typical for the regions of plains and deserts. Heat conduction is not the only heat transfer mechanism in soil (Kane *et al.*, 2001). The reconstructed GST histories are therefore temporal changes of the GST on the upper boundary of the heat conduction domain, which begins only few meters below the surface. The long-term relationship between the ground surface and SATs is therefore the key issue in interpreting the GST histories in terms of long-term climatic variability. The general belief is that, on the long-temporal scale, mean annual GSTs track the mean annual SATs taken at screen height (1.5 m above the surface of the ground). The results of recent studies (Putnam and Chapman, 1996; Beltrami, 2001; Schmidt *et al.*, 2001) indicate that the dominating mechanism of heat transfer in the soil is heat conduction. These studies are corroborated by earlier studies of long-term observations (Baker and Ruschy, 1993) which demonstrated a close correlation of subsurface mean annual soil temperatures at a meteorological station with SATs at the same location in north-central USA for 1963–1990 AD. However, the magnitude of the difference between the mean annual ground surface and SATs at a given site varies according to the number of days with snow cover or the content of soil moisture at the beginning of the freezing season. The difference, however, is relatively insensitive to the depth of the snow layer (Schmidt *et al.*, 2001). If these parameters change randomly from year to year and their mean values do not change on the time scale of the GST history reconstruction, then the present interpretation of the GST history as a first-order estimate of the air temperature history is correct. This problem has been studied in experimental air–ground climate stations located in different climatological settings (Putnam and Chapman, 1996; Cermak *et al.*, 2000; Schmidt *et al.*, 2001).

Factors like deforestation or forest fires can significantly change surface temperature and influence underground temperature regime (Majorowicz and Skinner, 1997; Lewis, 1998; Skinner and Majorowicz, 1999). Such changes observed by well temperature profiles in wells usually in remote regions may not be recorded by a meteorological station far from well location or tree ring growth research location (mainly located in far north or tree line extremes of the mountainous regions for the best temperature sensitivity conditions). SAT observations are mostly located in a fenced grassed areas, and in many cases unlike the surrounding landscape, and record mainly atmospheric-related temperature changes, and possibly the feedback effect in the regional context (Skinner and Majorowicz, 1999).

The deforestation/land clearing/land use factor can significantly skew generally normal statistical distribution of GST changes towards high values in some areas. GST changes as high as 3–5 K observed in some areas of mid-west of the North American continent, Cuba, Cordillera of British Columbia or

Western Canada Sedimentary basin (Cermak *et al.*, 1992; Majorowicz and Skinner, 1997; Lewis, 1998; Skinner and Majorowicz, 1999, respectively) can be a result of the effects of land clearing and resulting in a net effect of higher ground surface warming. This relates to land drying and loss of natural cooling mechanism given by respiring trees. Lewis (1998) and Skinner and Majorowicz (1999) determined that the transpiration component of the heat budget for Vancouver Island biomass and for the Alberta/Saskatchewan boreal forest biomass, respectively, can be responsible for 0.5–2 K change in specific areas. These include mainly recently deforested areas. A more complicated situation is presented by naturally burned boreal forest areas in which depletion of biomass by fire results in initial ground surface warming followed by cooling due to natural or induced regrowth of the forest (Majorowicz and Skinner, 1997).

While an offset between GST and SAT series is possible due to reasons listed above, long-term changes in soil moisture accompany long-term changes in GST (such as soil desiccation associated with long-term warming). It is likely that trends of air and GST may slowly diverge because the latent heat effects in the soil play a diminished role over time (Majorowicz and Skinner, 1997). This may explain why GST and SAT time series parallel each other over decades as observed in many locations (Baker and Ruschy, 1993; Majorowicz and Skinner, 1997).

#### 16. COMPARISON OF WELL TEMPERATURE DERIVED GST HISTORIES WITH OBSERVATIONS AND OTHER PROXY CLIMATE INFORMATION

It is difficult to compare the GST histories and patterns of GST warming through time with the SAT records because of the relatively short duration of the SAT records especially in quite recently settled regions of North America (ca. 100 years) and especially in the Arctic (ca. 50 years). In many cases, this precludes proper comparison with “filtered” long-term GST histories derived from well temperature logs as shown above (Fig. 10).

A comparison of the GST histories derived from inversion well temperature profiles with multi-proxy reconstructions (mostly tree-ring-based climatic reconstructions) is complicated, as the temporal frequency of each is quite different (high for tree ring or isotope-based reconstructions and low for the geothermal method). To reconcile both series, one needs to filter the high frequency proxy data for comparison with the GST histories. An example shown here is that of tree-ring-based annual, spring/summer weighted surface temperature history (Archambault and Bergeron, 1992) and the GST history derived from well temperature profile in Quebec (Canada) using SVT inversion scheme (Beltrami *et al.*, 1995) (Fig. 28a–d). Reconstruction of high-resolution

ground temperature histories can be achieved by combining the dendrochronological and geothermal data together. However, it often occurs that changes shown by tree ring indexing in first decades/century of tree growth can be quite different from those of GSTH, especially in the first part of the tree ring reconstruction as illustrated in Fig. 28a–d (compare Fig. 28b and c).

Long-term differences between GSTH from well temperature profiles and multi-proxy climatic histories are quite obvious when comparing the Huang *et al.* (2000) reconstruction for the northern hemisphere with that of Mann *et al.* (1998), respectively (Fig. 19). Multi-proxy reconstructions give typical estimates of a net warming of about 0.5 K while the geothermal-based GST net change is approximately 1 K. According to Huang *et al.* (2000) and Pollack *et al.* (2000) the difference may be accounted for by one aspect of tree ring data analysis. Tree ring width must be standardized to account for the long-term growth trends related to age. These standardization techniques use filters that may make long-term climatic trends susceptible to removal by the same filter (Pollack and Huang, 2000). Some reconciliation of differences between well temperature data and other multi-proxy reconstructions of the SAT history has been recently attempted by Mann *et al.* (2003), who dismiss the 20th century similarity between GSTH from geothermal data and SAT time series from meteorological stations. They argue that the borehole data trend is biased as it reflects very little of the spatial structure of SAT over the hemisphere. This comparison of areally weighted  $5^{\circ} \times 5^{\circ}$  grid averages of SAT trend to the borehole-determined 20th century temperature trend for the same grid elements is questioned by Pollack and Smerdon (2003). They argue that the number and geographical distribution of the boreholes is insufficient to determine robust averages for these areas. Pollack and Smerdon (2003) used a variety of grid sizes and occupancy weighting schemes and found that the five-century GST warming from well temperatures is 0.87–1.07 K, i.e., higher than most of multi-proxy-based temperature increases over the last five centuries (0.5 K), which confirms the major finding of their previous work. Mann *et al.* (2003) argue that their application of optimal signal estimation yields a hemispheric borehole SAT reconstruction that is largely consistent with instrumental data available in the past centuries, and is indistinguishable in its major features from several published long-term temperature estimates based on both climate proxy data and model simulations.

The above global and hemispheric comparisons between multi-proxy and well temperature surface temperature histories over the last 5–10 centuries suffer from incompatibility of different data sets and their spatial representation. Well temperature data in the northern hemisphere, for which most comparisons were made, are mainly limited to the mid-latitudes (Huang *et al.*, 2000), and a variety

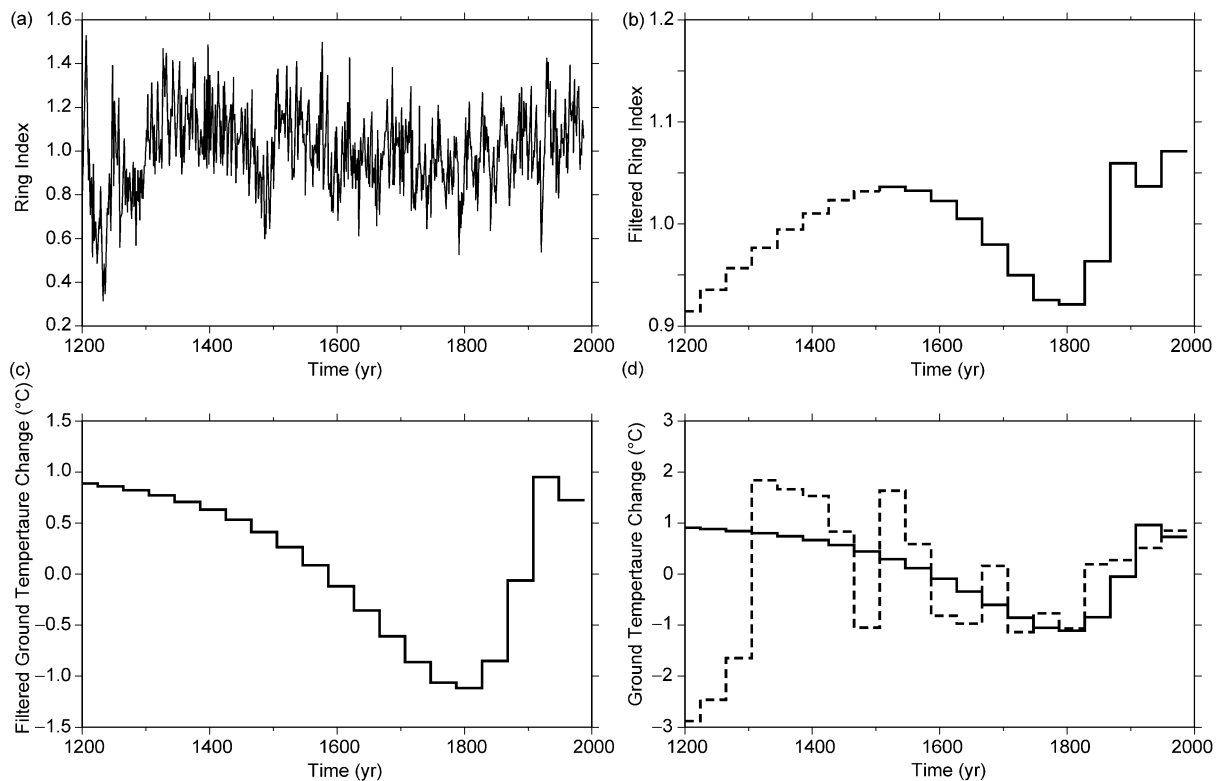


FIG. 28. Comparison of tree ring (a, b), well temperature based reconstruction (c) and combined well temperature—tree ring history (d) (modified from Beltrami *et al.*, 1995).

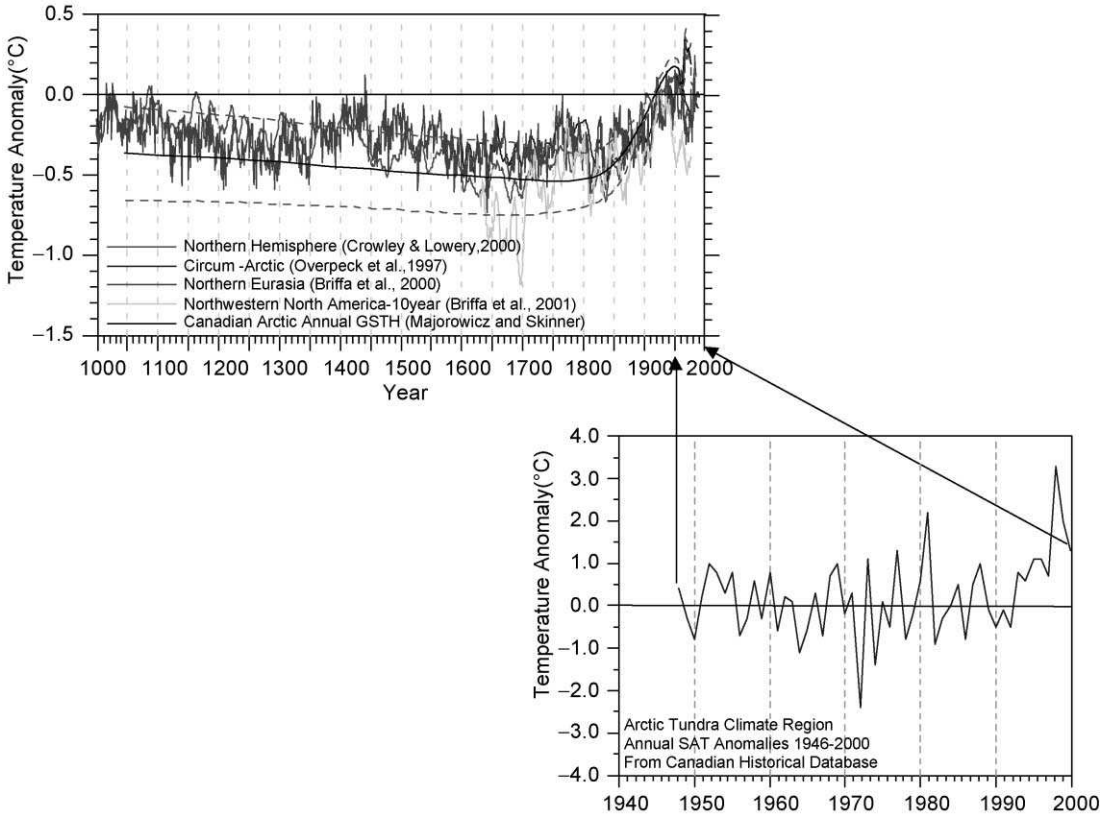


FIG. 29. Comparison of northern Canada GST history with other multi-proxy surface temperature reconstructions.

of landscapes including large open plains depleted of forest cover due to land development over the past few centuries. Multi-proxy data are mainly based on samples from forested regions where temperature-sensitive tree growth dominates (latitudinal and altitudinal tree line).

Comparisons for smaller regions are a valuable alternative to “global” or “hemispheric” studies as a way to check reconstructions of both methods: geothermal and multi-proxy in similar environment. Figure 29 shows a comparison of the Arctic Canada GSTH from FSI of temperature logs with northern/polar multi-proxy reconstructions from Overpeck *et al.* (1997) recalibrated by Osborn and Briffa (2002) and north-western North America curve of Briffa *et al.* (2001). Other multi-proxy reconstructions like northern hemisphere surface temperature history (Crowley and Lowery, 2000) and Northern Eurasia are also shown. The northwestern North America history of Briffa *et al.* (2001) compares very well with Canadian Arctic annual average GSTH from well temperature profiles. Arctic well temperature logs are from sites well outside the influence of man-made terrain changes, unlike the regions to the south where some data may be coming from deforested or surface altered terrains.

## 17. CONCLUSIONS

The borehole climate method is unique as it is based on the direct physical link between the measured temperature–depth profile and the reconstructed parameter of the past climate, the GST. It is unlike most of the other approximate methods of the past climate reconstruction. It has proved to be quite successful in reconstructing two robust signals: (a) the amplitude of the last glacial/interglacial temperature difference and (b) the surface temperature trend of the last 100–150 years and eventually, when combined with the SAT series, in estimating their POMs. A reconstruction of less robust signals of the little ice age, medieval climatic optimum, Boreal, Atlantic and possibly some other climatic periods of the Holocene fails even in most cases of purely conductive subsurface thermal regime for the following reasons.

1. Poor knowledge of the thermal conductivity variations in the borehole prevents proper separation of steady-state and transient components of the temperature profile. This can be improved by detailed sampling of the drill-core for conductivity measurements, followed by calculation of representative averages of conductivity in the individual depth intervals, which can be considered in the inversion algorithm.

2. Little information about lateral conductivity variations, which can produce spurious signals and which can be neither recognized from the drill-core nor taken into account in the present one-dimensional inversion software.
3. A possible time variability of the air versus GST offset, which can interfere with the air temperature changes. More profound insight into different aspects of this problem can be expected from data which are being collected in a few borehole climate observatories in the North America and Europe.

Despite these problems, the geothermal method provides a robust estimate of the long-term warming amplitude and gives good information about temperature levels in the period preceding warming. In carefully chosen areas with limited surface disturbances the geothermal method proves to give remarkably good results which compare well with observations and selected multi-proxy reconstructions. The result of this method gives an independent (from other multi-proxy) constraint for the global climatic warming.

One of the most important problems to be solved in the near future is the reconciliation of geothermal and multi-proxy reconstructions of climatic histories. These different data respond to changes in different yearly seasons. These methodologically and physically different SAT reconstruction schemes can benefit from each other as long as careful data selection allows the comparison.

#### ACKNOWLEDGEMENTS

We are grateful to Dr. V. Cermak, Dr Alan Jessop, Dr. I. Kukkonen and anonymous reviewer for helpful comments on the manuscript. The support of Environment Canada for the first author (J.A.M.) was crucial to the success of this project. The first author would like to acknowledge helpful discussions over the years from Prof. Henry Pollack.

#### REFERENCES

- Archambault, S., and Bergeron, Y. A. (1992). 802 year tree ring chronology from Quebec boreal forest Canadian. *J. For. Res.* **22**, 674–682.
- Baker, D. G., and Ruschy, D. L. (1993). The recent warming in eastern Minnesota shown by ground temperatures. *Geophys. Res. Lett.* **20**, 371–374.
- Beck, A. E. (1977). Climatically perturbed temperature gradients and their effect on regional and continental-heat flow measurements. *Tectonophysics* **41**, 17–39.
- Beck, A. E., and Judge, A. S. (1969). Analysis of heat flow data—I, Detailed observations in a single borehole. *Geophys. J. R. Astron. Soc.* **18**, 145–158.
- Beck, A. E., Shen, P. Y., Beltrami, H., Mareshal, J.-C., Šafanda, J., Sebagenzi, M. N., Vasseur, G., and Wang, K. (1992). A comparison of five different analyses in the interpretation of five borehole temperature data sets. *Global Planet. Change* **98**, 101–112.

- Beltrami, H. (2001). On the relationship between ground temperature histories and meteorological records: a report on the Pomquet station. *Global Planet. Change* **29**, 327–348.
- Beltrami, H. (2002). Climate from borehole data: energy fluxes and temperature since 1500. *Geophys. Res. Lett.* **29(23)**, 2111.
- Beltrami, H., and Mareschal, J.-C. (1992). Ground temperature histories for central and eastern Canada from geothermal measurements: little ice age signature. *Geophys. Res. Lett.* **19(7)**, 689–692.
- Beltrami, H., Chapman, D. S., Archambault, S., and Bergeron, Y. (1995). Reconstruction of high resolution ground temperature histories combining dendrochronological and geothermal data. *Earth Planet. Sci. Lett.* **136**, 437–445.
- Beltrami, H., Wang, J. F., and Bras, R. L. (2000). Energy balance at the Earth's surface: heat flux history in eastern Canada. *Geophys. Res. Lett.* **27**, 3385–3388.
- Beltrami, H., Smerdon, J. E., Pollack, H. N., and Huang, S. (2002). Continental heat gain in the global climatic system. *Geophys. Res. Lett.* **29(8)** 10.1029.
- Birch, F. (1948). The effects of Pleistocene climatic variations upon geothermal gradients. *Am. J. Sci.* **246**, 729–760.
- Blackwell, D. D. (1999). Geothermics in basin analysis—introduction. In “Geothermics in Basin Analysis” (A. Forster, and D. F. Merriam, eds.). Kluwer Academic/Plenum Publishers, Dordrecht/New York, pp. ix–xii.
- Blackwell, D. D., Beardsmore, R. K., Nishimori, R. K., and McMullen, R. J. Jr. (1999). High resolution temperature logs in petroleum setting: examples and applications. In “Geothermics in Basin Analysis” (D. F. Merriam, and A. Forster, eds.). Kluwer Academic/Plenum Publishers, Dordrecht/New York, pp. 1–34.
- Briffa, K. R., Osborn, T. J., Schweingruber, F. H., Harris, I. C., Jones, P. D., Shiyatov, S. G., and Vaganov, E. A. (2001). Low-frequency temperature variations from a northern tree ring density network. *J. Geophys. Res.* **106(D3)**, 2929–2941.
- Cermak, V. (1971). Underground temperature and inferred climatic temperature of the past millennium. *Palaeogeogr. Palaeoclimatol. Palaeoecol.* **10**, 1–19.
- Cermak, V., Bodri, L., and Safanda, J. (1992). Underground temperature fields and changing climate: evidence from Cuba. *Palaeogeogr. Palaeoclimatol. Palaeoecol. (Global Planet. Change Sect.)* **97**, 325–337.
- Cermak, V., Safanda, J., Kresl, M., Dedecek, P., and Bodri, L. (2000). Recent climate warming: surface air temperature series and geothermal evidence. *Stud. Geophys. Geod.* **44**, 430–441.
- Chapman, D. S., Chisholm, T. J., and Harris, R. N. (1992). Combining borehole temperature and meteorological data to constrain past climate change. *Global Planet. Change* **98**, 269–281.
- Clauser, C. (1984). A climatic correction on temperature gradients using surface-temperature series of various periods. *Tectonophysics* **103**, 33–46.
- Clauser, C., and Mareschal, J.-C. (1995). Ground temperature history in Central Europe from borehole temperature data. *Geophys. J. Int.* **121(3)**, 805–817.
- Clauser, C., Giese, P., Huenges, E., Kohl, T., Lehmann, H., Rybach, L., Šafanda, J., Wilhelm, H., Windloff, K., and Zoth, G. (1997). The thermal regime of the crystalline continental crust: implications from the KTB. *J. Geophys. Res.* **102**, 18417–18441.
- Clow, G. D. (1992). The extent of temporal smearing in surface-temperature histories derived from borehole temperature measurements. *Global Planet. Change* **6**, 81–86.
- Correia, A., and Safanda, J. (2001). Ground surface temperature history at a single site in southern Portugal reconstructed from borehole temperatures. *Global Planet. Change* **29**, 155–165.

- Crowley, T. J., and Lowery, T. S. (2000). Northern hemisphere temperature reconstruction. *Science* **289**, 270.
- Dahl-Jensen, D., Mosegaard, K., Gundestrup, N., Clow, G. D., Johnsen, S. J., Hansen, A. W., and Balling, N. (1998). Past temperatures directly from the Greenland ice sheet. *Science* **282**, 268–271.
- Duchkov, A. D., and Devyatkin, V. N. (1992). Reduced geothermal gradients in the shallow West-Siberian Platform. *Global Planet. Change* **98**, 245–250.
- Galushkin, Yu. (1997). Numerical simulation of permafrost evolution as a part of sedimentary basin modeling: permafrost in the Pliocene–Holocene climate history of the Urengoy field in the West Siberian basin. *Can. J. Earth Sci.* **34**, 935–948.
- Guillou-Frottier, L., Mareschal, J.-C., and Musset, J. (1998). Ground surface temperature history in central Canada inferred from 10 selected borehole temperature profiles. *J. Geophys. Res.* **103**, 7385–7397.
- Gullett, D. W., and Skinner, W. R. (1992). “The state of Canada’s climate: temperature change in Canada 1895–1991.” State of Environment Report No. 92-2. Atmospheric Environment Service, Environment Canada, Downsview, Ont., 36 pp.
- Harris, R. N., and Chapman, D. S. (1995). Climate change on the Colorado Plateau of eastern Utah inferred from borehole temperatures. *J. Geophys. Res.* **100**, 6367–6381.
- Harris, R. N., and Chapman, D. S. (2001). Mid-latitude (30°N–60°N) climatic warming inferred by combining borehole temperatures with surface air temperatures. *Geophys. Res. Lett.* **28(5)**, 747–750.
- Harris, R. N., and Gosnold, W. D. (1999). Comparisons of borehole temperature–depth profiles and surface air temperatures in the northern plains of the U.S. *Geophys. J. Int.* **138**, 541–548.
- Hartmann, D. L. (1994). “Global Physical Climatology.” . Academic Press, San Diego, CA, 411 pp.
- Huang, S., and Pollack, H. N. (1998). “Global borehole temperature database for climate reconstruction.” IGBP Pages/World Data Center—A for Paleoclimatology Data Contribution Series No. 1998-044. NOAA/NGDC Paleoclimatology Program, Boulder, CO.
- Huang, S., Pollack, H. N., and Shen, P.-Y. (2000). Temperature trends over the past five centuries reconstructed from borehole temperatures. *Nature* **403**, 756–758.
- IPCC (Intergovernmental Panel on Climate Change), (2001). “Climate Change 2001, The Scientific Basis.” Cambridge University Press, Cambridge, 98 pp.
- Jaeger, J. C. (1965). Application of theory of heat conduction to geothermal measurements. In “Terrestrial Heat Flow” (W. H. K. Lee, ed.), Geophysical Monograph Series, Vol. 8. AGU, Washington, DC, pp. 7–23.
- Jessop, A. M. (1990a). Geothermal evidence of climatic change. *Eos* **71(15)**, 390–391.
- Jessop, A. M. (1990b). “Thermal Geophysics.” . Elsevier, Amsterdam, 306 pp.
- Kane, D. L., Hinkel, K. M., Goering, D. J., Hinzman, L. D., and Outcalt, S. I. (2001). Non-conductive heat transfer associated with frozen soils. *Global Planet. Change* **29**, 275–292.
- Kukkonen, I. (1987). Vertical variation of apparent and paleoclimatically corrected heat flow densities in the central Baltic Shield. *J. Geodyn.* **8**, 33–53.
- Kukkonen, I., and Clauser, C. (1994). Simulation of heat transfer at the Kola deep hole site—implications for advection, heat refraction and paleoclimatic effects. *Geophys. J. Int.* **116**, 409–420.
- Kukkonen, I., and Joeleht, A. (2003). Weichselian temperatures from geothermal heat flow data. *J. Geophys. Res.* **108(B3)**, 2163, doi: 10.1029/2001JB001579.

- Lachenbruch, A. H. (1994). Permafrost, the active layer and changing climate. U.S. Geological Survey Open-File Report 94-694. U.S. Geological Survey, Menlo Park, CA 94025, USA.
- Lachenbruch, A. H., and Marshall, B. V. (1986). Changing climate: geothermal evidence from permafrost in Alaska. *Science* **234**, 689–696.
- Lachenbruch, A. H., Cladouhos, T. T., and Saltus, R. W. (1988). Permafrost temperature and the changing climate. In “Permafrost”, 5th International Permafrost Conference Proceedings, Vol. 3. Tapir Publishers, Trondheim, Norway, pp. 9–17.
- Lachenbruch, A. H., Sass, J. H., Lawver, L. A., Brewer, M. C., Marshall, G. V., Munroe, R. J., Kennelly, J. P. Jr., Galanis, S. P. Jr., and Moses, T. H. Jr. (1988b). Temperature and depth of permafrost on the arctic slope of Alaska. In “Geology and Exploration of the National Petroleum Reserve in Alaska, 1974–1982” (G. Gryc, ed.), US Geological Survey Professional Paper 1399, pp. 645–656.
- Lane, E. C. (1923). Geotherms of the Lake Superior copper country. *Bull. Geol. Soc. Am.* **34**, 703–720.
- Lewis, T. (1998). The effect of deforestation on ground surface temperatures. *Global Planet. Change* **18**, 1–13.
- Lorenc, H. (2000). Studies of the 220 years (1779–1998) air temperature series in Warsaw and evaluation of the century scale tendency. *Materiały Badawcze IMGW, Seria: Meteorologia* **31**, 104.
- Majorowicz, J. A. (1976). Geothermal parameters of the Krzemianka and Udryn region against the background of the earth’s heat flow in NE Poland. *Geol. Rev. (Przegląd Geologiczny, Wyd. Geol. Warszawa)* **10**, 607–613.
- Majorowicz, J. A. (1984). Problems of tectonic interpretation of geothermal field pattern in the platform areas of Poland. *Pol. Acad. Sci. Publ. Inst. Geophys.* **A-13(160)**, 149–166.
- Majorowicz, J. A., and Skinner, W. (1997). Potential causes of differences between ground and air surface temperature warming across different ecozones in Alberta, Canada. *Global Planet. Change* **15**, 79–91.
- Majorowicz, J. A., Safanda, J., Harris, R. N., and Skinner, W. R. (1999a). Large ground surface temperature changes at last three centuries inferred from borehole temperature in the Southern Canadian Prairies, Saskatchewan. *Global Planet. Change* **20**, 227–241.
- Majorowicz, J. A., Garven, G., Jessop, A., and Jessop, P. (1999b). Present heat flow across the Western Canada Sedimentary Basin: the extent of hydrodynamic influence. In “Geothermics in Basin Analysis” (A. Forster, and D. F. Merriam, eds.). Kluwer Academic/Plenum Publishers, Dordrecht/New York, pp. 61–81.
- Majorowicz, J. A., Safanda, J., and Skinner, W. (2002). East to west retardation in the onset of the recent warming across Canada inferred from inversions of temperature logs. *J. Geophys. Res.* **107(B10)**, 2227.
- Majorowicz, J., Safanda, J., Przybylak, R., and Wojcik, G. (2004a). Ground surface temperature history in Poland in the 16th–20th centuries derived from the inversion of geothermal profiles. *Pure Appl. Geophys.* **161(2)**, 351–364.
- Majorowicz, J. A., Skinner, W., and Safanda, J. (2004b). Large ground warming in the Canadian Arctic inferred from inversions of temperature logs. *Earth Planet. Sci. Lett.* **7042**, 1–11.
- Majorowicz, J. A., Skinner, W. R., and Safanda, J. (2004c). Ground surface warming history in Northern Canada inferred from inversions of temperature logs and comparison with other proxy climate reconstructions. *Pure Appl. Geophys.* **162**, in press.
- Mann, M. E., Bradley, R. S., and Hughes, M. (1998). Global scale temperature patterns and climate forcing over the past six centuries. *Science* **392**, 779–787.

- Mann, M. E., Rutherford, S., Bradley, R. S., Hughes, M. K., and Keimig, F. T. (2003). Optimal surface temperature reconstructions using terrestrial borehole data. *J. Geophys. Res.* **108(D7)**, 4203.
- Mareschal, J. C., and Beltrami, H. (1992). Evidence for recent warming from perturbed geothermal gradients: examples from eastern Canada. *Clim. Dyn.* **6**, 135–143.
- Mareschal, J. C., Rolandone, F., and Bienfait, G. (1999). Heat flow variations in deep borehole near Sept-Iles, Quebec, Canada: paleoclimatic interpretation and implication for regional heat flow estimates. *Geophys. Res. Lett.* **26**, 2049–2052.
- Nixon, J. F. (1986). Thermal simulation of subsea saline permafrost. *Can. J. Earth Sci.* **23**, 2039–2046.
- Osborn, T. J., and Briffa, K. R. (2002). Comments on the paper of R.N. Harris and D.S. Chapman mid-latitude (30°N–60°N) climatic warming inferred by combining borehole temperatures with surface air temperatures. *Geophys. Res. Lett.* **29(16)** 10.1029/2001.
- Overpeck, J., Hughen, K., Hardy, D., Bradley, R., Case, R., Douglas, M., Finney, B., Gajewski, K., Jacoby, G., Jennings, A., Lamoureaux, S., Lasca, A., MacDonald, G., Moore, J., Retelle, M., Smith, S., Wolfe, A., and Zielinski, G. (1997). Arctic environmental change of the last four centuries. *Science* **278**, 1251–1256.
- Pollack, H. N., and Huang, S. (2000). Climate reconstructions from subsurface temperatures. *Annu. Rev. Earth Planet. Sci.* **28**, 339–365.
- Pollack, H. N., and Smerdon, J. (2003). Have borehole temperature climate reconstructions been reconciled with multi-proxy reconstructions? *Geophys. Res. Abstr.* **5**, 06345, 2003 EGS/AGU, Nice.
- Pollack, H. N., Shen, P. Y., and Huang, S. (1996). Inference of ground surface temperature history from subsurface temperature data: interpreting ensembles of borehole logs. *Pure Appl. Geophys.* **147**, 537–550.
- Pollack, H. N., Huang, S., and Shen, P.-Y. (2000). Climate change record in subsurface temperatures: a global perspective. *Science* **282**, 279–281.
- Popov, Y. A. (1997). “Optical scanning technology for nondestructive contactless measurements of thermal conductivity and diffusivity of solid matters.” Proceedings of the 4th World Conference on Experimental Heat Transfer, Fluid Mechanics and Thermodynamics, Brussels, Vol. 1, pp. 109–117.
- Primenov, V. P., Popov, Y. A., and Klimanov, V. A. (1996). Vertical variations of heat-flow and paleoclimate. *Izvestiya Phys. Solid Earth* **32(6)**, 547–554.
- Putnam, S. N., and Chapman, D. S. (1996). A geothermal climate change observatory: first year results from Emigrant Pass in Northwest Utah. *J. Geophys. Res.* **101**, 21877–21890.
- Rajver, D., Safanda, J., and Shen, P. Y. (1998). The climate record inverted from borehole temperatures in Slovenia. *Tectonophysics* **291**, 263–276.
- Safanda, J., and Rajver, D. (2001). Signature of the last ice age in the present subsurface temperatures in the Czech Republic and Slovenia. *Global Planet. Change* **29**, 241–257.
- Safanda, J., Correia, A., Majorowicz, J. A., and Rajver, D. (2002). Inverse method of reconstruction of ground surface temperature history from borehole temperatures. In “Geothermal/Dendrochronological Paleoclimate Reconstruction Across Margin of Eurasia” (M. Yamano, T. Nagao, and T. Sweda, eds.), Proceedings 2002 International Matsuyama Conference, Matsuyama, Japan, pp. 163–178.
- Safanda, J., Szweczyk, J., and Majorowicz, J. A. (2004). Geothermal evidence of very low glacial temperatures on a rim of the Fennoscandian ice sheet. *Geophys. Res. Lett.* **31**, L07211.
- Schmidt, W. L., Gosnold, W. D., and Enz, J. W. (2001). A decade of air–ground temperature exchange from Fargo, North Dakota. *Global Planet. Change* **29**, 311–325.

- Shen, P. Y., and Beck, A. E. (1991). Least squares inversion of borehole temperature measurements in functional space. *J. Geophys. Res.* **96**, 19965–19979.
- Shen, P. Y., and Beck, A. E. (1992). Paleoclimate change and heat flow density inferred from temperature data in the Superior Province of the Canadian Shield. *Global Planet. Change* **6**, 143–165.
- Shen, P. Y., Pollack, H. N., Huang, S., and Wang, K. (1995). Effects of subsurface heterogeneity on the inference of climate change from borehole temperature data: model studies and field examples from Canada. *J. Geophys. Res.* **100(B4)**, 6383–6396.
- Skinner, W. R., and Majorowicz, J. A. (1999). Regional climatic warming and associated twentieth century land-cover changes in north-western North America. *Clim. Res.* **12**, 39–52.
- Szewczyk, J. (2002). “Evidences for the Pleistocene–Holocene climatic changes from the deep well temperature profiles from the Polish lowland.” Proceedings of the International Conference on The Earth’s Thermal Field and Related Research Methods, Moscow, pp. 271–275.
- Wang, K. (1992). Estimation of the ground surface temperatures from borehole temperature data. *J. Geophys. Res.* **97**, 2095–2106.
- Zhang, X., Vincent, L. A., Hogg, W. D., and Niitsoo, A. (2000). Temperature and precipitation trends in Canada during the 20th century. *Atmosphere-Ocean* **38**, 395–429.
- Zoth, G., and Haenel, R. (1988). Appendix. In “Handbook of Terrestrial Heat Flow Density Determination” (R. Haenel, L. Rybach, and L. Stegena, eds.). Kluwer Academic, Dordrecht, pp. 449–468.

# INSTABILITY AND STRUCTURAL FAILURE AT VOLCANIC OCEAN ISLANDS AND THE CLIMATE CHANGE DIMENSION

BARBARA H. KEATING<sup>a</sup> AND WILLIAM J. MCGUIRE<sup>b</sup>

<sup>a</sup>*Hawaii Institute of Geophysics and Planetology, University of Hawaii,  
2525 Correa Road, Honolulu, HI, USA*

<sup>b</sup>*Benfield Hazard Research Centre, Research School of Geological and Geophysical Sciences,  
University College London, Gower Street, London WC1E 6BT, UK*

## ABSTRACT

Keating and McGuire (2000) [Island edifice failures and associated tsunami hazards. In "Landslides and Tsunamis", Birkhauser, Boston, pp. 899–956] presented and examined evidence for ubiquitous island edifice failures and their associated tsunami hazards. In this follow-up review, we examine the status of landslide, debris flow and tsunami research and find that significant progress has been made in placing constraints on physical parameters that will facilitate numerical modeling of tsunamis, landslide and debris flow movements. Similarly, physical modeling has provided an important contribution to our understanding of slope failure and debris transport, with many features generated in laboratory experiments clearly identifiable in sonar images of mass wasting events.

In particular, we address published evidence and proposed models supporting the rule of climate change toward the generation of ocean island and continental margin landslides. Evidence presented from the Canary Islands and the Madeira Abyssal Plain is supportive of such a relationship, while that from the Hawaiian archipelago provides a weak argument for this association, primarily due to age-dating limitations. Notwithstanding these, a comparison of the known rainfall pattern for the Hawaiian Islands and the distribution of mapped edifice failures, however, reveal no obvious link between either wet or dry conditions and the disposition of debris avalanches and slumps. Furthermore, contemporary observations from the Hawaiian archipelago show that sub-aerial landslides are common under both wet and dry conditions. A correlation between climate-related sea-level change and continental margin slope failures is supported via the mechanism of methane venting. A comparable link between variations in sea level and instability and collapse at coastal and island volcanoes may also be vindicated by correlation between the intensity of volcanic activity in marine settings and the rate of sea-level change during the late Quaternary.

Our review reiterates strong evidence for abundant slope failures on the flanks of ocean islands. The existence and nature of a climate change link remains, however,

to be firmly established. It is likely that this will need to await better constrained age determinations for submarine slope failures, provided—for example—by an extensive program of ash-layer dating within sequences associated with landslides, slumps and debris flows within the marine environment. We conclude by addressing the hazard implications of future major collapse in the marine environment, drawing attention to increasing evidence for a serious future threat to coastal zones from major landslide-induced tsunamis.

*Keywords:* Climate change, Sea-level change, Slope failure, Island-edifice failure, Gas hydrates, Canary Islands, Hawaii.

## 1. INTRODUCTION

Keating and McGuire (2000) presented evidence for abundant island edifice failures and their associated tsunami hazards. Here we extend that review, reporting on the current status of research into landslides, debris flows, and tsunamis in the marine environment. We draw attention to the paucity of definitive constraints to support modeling studies, describe changes in fundamental approaches to these problems and report progress leading to a better understanding of submarine slope failure. We highlight the need for better age constraints to establish the frequency–size distribution of slope failures and explore models supporting a link between landslides and climate change. In recent years, an increasing and welcome trend has led to the Earth being considered as an integrated physical system within which the geosphere, atmosphere, and hydrosphere interact through a range of cause and effect, and positive and negative feedback systems. Examples include proposed correlations between volcanism and glaciation (e.g., Bray, 1976, 1977; Rampino *et al.*, 1979; Hall, 1982; Nakada and Yokose, 1992; Rampino and Self, 1992, 1993; Sigvaldason *et al.*, 1992), volcanism and rate of sea-level change (Rampino *et al.*, 1979; Wallman *et al.*, 1988; Nakada and Yokose, 1992; McGuire *et al.*, 1997), and ocean island landslides and climate (e.g., Day *et al.*, 1999a; McMurtry *et al.*, 1999).

Published models have been largely developed on the basis of links between geophysical phenomena determined for the late Quaternary; a period characterized by large and dramatic changes in the Earth system as a whole, when the wholesale redistribution of planetary water took place during glacial–interglacial transitions, involving sea-level variations as great as 130 m (Shackleton, 1987) and accompanying large-scale variations in the planet's climate system. Given that the late Quaternary was characterized by the dramatic amplification of many geophysical processes, it is perhaps not surprising that this particularly dynamic

and accessible period of Earth history has provided the evidence upon which recent cause-and-effect models linking volcanism, landsliding, and environmental change have been based. At a time when the planet is once again experiencing rapid climate change, determination of the validity and significance of such correlations is critical, given: (1) their potential hazard impact through tsunami generation and (2) the fact that we have little or no information on the threshold levels beyond which such effects may once again become apparent.

We begin by examining aspects of volcanic edifice instability and the processes that combine together to produce landslides. We review the edifice failures on volcanic ocean islands, describe landslide forms and wherever possible, *quantify* dimensions, volumes, slope angles and changes in properties during transport, then we discuss the concept of facies associated with various intact vs. failed slopes. We review runout and volume relations. The results from laboratory experiments to model debris flows are compared to sonar images of submarine slope. A history of tsunami modeling associated with submarine landslides is reviewed. We suggest the portrayal of simple landslide block modeling employed by some tsunami modelers is contradicted by both experimental observations that show debris flows display complex interactions, changing rheology—particularly when the slope changes, and evidence that the debris flow/turbidite currents erode and incorporate portions of the underlying substrate. We briefly summarize velocity determinations for landslides (sub-aerial and submarine) that suggest velocity observed in nature is often much lower than recent tsunami models employ. While much study has been invested in giant submarine landslides, few smaller submarine landslides have been described, yet the smaller failures are likely to be much more numerous than giant events. Statistical parameters associated with submarine landslides need to be compiled.

This presentation is followed by a review of the observations of climate change affects within the Ocean Basin Environment. We conclude that there seems to be a consensus for increased landslides during wet and humid climate in the Canary Islands. But age dating constraints are not sufficient to bolster a correlation between climate change and landslides around Hawaii. We point out interesting on-going research that suggest the venting of methane from the seafloor may trigger landslides on continental margins.

### 1.1. Volcanic Edifice Instability

From an Earth-system approach, the study of large-scale volcanic slope failures is a strongly interdisciplinary one, encompassing the fields of

volcanology, hydrology, geophysics, engineering geology, sedimentology, and climatology, and calling upon tsunami modelers, sonar imagers, and seismic tomographers—amongst others—to provide additional data that helps us better understand the phenomena and better appreciate associated hazard and risk. Potential for slope instability and failure is enhanced by the fact that actively growing volcanic edifices experience continuous changes in morphology, with the endogenetic (by intrusion) and exogenetic (by extrusion) additions of material leading to oversteepening and overloading (McGuire, 1996). Keating and McGuire (2000) reviewed 22 factors contributing to or involved in the failure process, both in general terms, and for specific volcanoes (Table 1). The single, linking, contributory factor, in both the development of instability and in the initiation of structural failure is, however, gravity.

Instability development and edifice collapse have been evaluated at a number of volcanoes (e.g., Voight *et al.*, 1983a; Paul *et al.*, 1987; Iverson, 1995; Voight and Elsworth, 1997) and have proven to be problematic. Iverson (1995), for example, used a rigid-wedge limit-equilibrium analysis to evaluate if magma injection could be responsible for sector collapse in the Hawaiian islands and concludes, “failure of these gently sloping volcano flanks is problematic”...“if all other factors are constant, driving forces that are too small to displace an ideal, rigid wedge are also too small to displace a deforming volcano flank”. The largest sector likely to be displaced by magma injection is only 3–4 km in length. Iverson (1995) examined other parameters including static buoyancy effects (which appear insufficient to destabilize flank sectors greater than a few kilometers across), and groundwater-seepage (which indicates groundwater flow due to relative sea-level fall produced only a negligible effect since hydraulic head diffusion occurs so rapidly that no significant head gradient could be produced in lithified lava flows). He also addressed the effects of edifice consolidation (within the volcanic pile and underlying clay layer of 10 m) which induced hydraulic gradients that are negligible because the timescale of consolidation is rapid compared to volcano growth (estimated at 300 years). Iverson (1995) concludes that a combination of features, e.g., strong earthquake shaking, thermal stressing, ground water convection, progressive weakening of slip surface materials, and an accumulation of repeated small failure events are likely to be among the most important factors effecting slope failure. Blois-Heulin *et al.* (1995) report on additional limit-equilibrium analyses of wedge-shape slices of the volcano and again conclude that a combination of parameters is required.

Hurlimann *et al.* (2000) analyzed mobility of the La Orotave (Landslide, Tenerife) using limit-equilibrium method and 2-D finite difference techniques, including physical parameters of hydrostatic pore pressure and material strength

TABLE 1. Ocean Island instability—endogenetic failure processes and exogenic failures

Failure Process	Mechanism	Examples
Ocean Island instability—endogenetic failure processes		
1. Unstable foundation—clays	Decoupling along low friction layer	Hawaii
2. Unstable foundations	Decoupling along low friction layer, with ball-bearing like character	Loihi, Savaii
3. Dykes	Physical displacement of flanks of volcano	Koolau Volcano (Oahu, Hawaii)
4. Cumulates	Physical displacement of flanks of volcano	Kilauea (Hawaii), Mt. Etna, Klyucherskoi volcano (Kamchatka)
5. Thermal alteration	Increase in pore pressure; reduction in strength	Hawaii
6. Edifice pore pressure	Liquidation of overpressured sediments	Mururoa, Ritter Volcano, Surtsey Volcano
7. Unbuttressed structure	Creep	Hawaiian Islands
8. Buried faults	Decoupling along pre-existing zone of low friction added overburden	Hilina system (Hawaii), Mururoa, Niue
Ocean Island instability—exogenic failures		
9. Collapse of sub-aerial deposits	Low cohesion material including ball-bearing like horizons, with low-friction surfaces, often dipping seaward	Hawaii, Ritter Island (PNG), Surtsey volcano (Iceland)
10. Collapse of submarine deposits	Low cohesion water-saturated material including ball-bearing like horizons, with low-friction surfaces	Savaii (Samoa)
11. Endo-upwelling	Excess pore pressure	Johnston Island, Mataiva, Niau lagoon (Mururoa), and Tikehau Atoll (Tuamotu chain)
12. Karst megaporosity	Void spaces and rocks of low mechanical strength	Johnston Island, mid-Pacific Mountains, Mururoa Atoll
13. Fractures	Low mechanical strength	Johnston Island, Chapman Seamount, Mururoa Atoll, Horizon Guyot

*Continued*

TABLE 1. Continued

Failure Process	Mechanism	Examples
14. Oversteepening	Low cohesion	Hawaii, Reunion Island, Canary Islands
15. Overloading	High pore pressure; low cohesion	Hawaii
16. Sea level change	Stress changes—foundation stress changes in magma chamber crustal loading/unloading	Hawaii, Pantelleria, Iceland
17. Marine erosion	Changes in pore pressures turbulence physically disrupting sediments and lavas	Hawaii
18. Climate weather—hurricanes	Mass wasting high on volcano turbulence moving low cohesion rocks	Hawaii, Kahe Point, Oahu, Hawaii
19. Glacial response	Crustal loading	Pacific
20. Volcanic activity	Physical displacement of low cohesion material	Hawaii, Mt. St. Augustine, Ritter Volcano
21. Uplift and subsidence	Lithospheric flexure	Cross Seamount, Mehatia, Niue
22. Tectonic seismicity	Physical displacement of low cohesion material	Hawaii, Mururoa
23. Anthropogenic	Physical displacement of low cohesion material	Mururoa

From Keating and McGuire (2000).

and examining dike injection, caldera collapse, and seismicity (but not including thermal effects). Hurlimann *et al.* (1999) carried out a sensitivity analysis employing various material properties and various inclinations of the water table, but found neither weak rocks nor static groundwater pressures alone would initiate a landslide. These analyses require a combination of events such as seismic shock, dike intrusion, or a caldera collapse to destabilize volcanoes. Tinti *et al.* (1997) examined a block-based model for gravitational sliding and found, since the magnitudes of individual driving forces do not exceed failure thresholds it appears a combination of processes is responsible for edifice flank failure.

McGuire (1996) drew attention to the importance of the behavior of the sub-volcanic basement, with both subsidence and uplift beneath the volcano having the potential to accelerate edifice instability. Furthermore, the growth of a volcanic edifice on a sloping or weak (e.g., clay-rich) substrate, strongly favors the development of lateral spreading with all that this entails for the evolution of an associated instability within, below, and around the edifice.

Jiang and LeBlond (1992) modeled the tsunamigenic potential of the coupling of the water mass to a submarine slide and underlying surface, utilizing the physical properties of the landslide (utilizing mud of various rheologies). In the past, poor knowledge of many of these parameters handicapped modeling efforts. Voight (2000) states that studies proposed to better constrain parameters important for hazard analysis (including material zonation, pore pressures, discontinuities, properties, stresses, plastic deformation) are rarely funded. Voight continues: "...others may be difficult or impossible to measure reliably (e.g., rock-mass strength, dynamic loading, the constitute properties of partly crystalline magma)" and: "...complete information on distributions of materials (complex geology), rock mass and magma strength and deformation properties, edifice stresses, and discontinuities cannot be reliably obtained". Similar problems are stressed by Watts and Gardner (2003), who emphasize that: "there are quantities needed to describe landslide constitutive behaviors that are poorly constrained".

Data are increasingly available to support modeling efforts and improve our understanding of the failure process and consequences. We know for example that positive pore pressure within rocks facilitate faulting and displacement and that aborted faults can have dry breccias associated with them, indicating that the absence of positive pore pressure can inhibit failure. Strong thermal alteration weakens rocks and facilitates failure, while low temperature alteration can fill vesicles and fractures with zeolites, reducing permeability and potentially reducing prospect of failure. Steep slopes, rapid growth, and asymmetric shapes are all factors that act to promote instability and structural failure. Other potentially relevant properties remain, however, obscure and poorly constrained,

including failure initiation and mobile-mass de-coupling depths, thicknesses of debris units, and the nature of failure-related faults and discontinuities.

## 2. FACTORS AND MECHANISMS AFFECTING INSTABILITY AND FAILURE AT VOLCANIC OCEAN ISLANDS

Keating and McGuire (2000) reviewed 22 mechanisms (Table 1) involved in the volcanic island instability. Progress has been made in establishing constraints on many of the failure processes and brief summaries of research into mechanisms are discussed here as well as physical properties affecting the failure process.

### 2.1. The Role of Intra-edifice Water

Water contained within a volcanic edifice may generate positive pore pressures capable of facilitating fault initiation and displacement. Elsworth and Day (1999) point out that water table geometries have now been at least partly determined for a number of modern oceanic island volcanoes, including Kilauea (Thomas *et al.*, 1983; Thomas, 1987) and Oahu in Hawaii (Hunt *et al.*, 1988; Hunt, 1997), Tenerife (Plan Hidrologio Insular, Anonymous, 1991) and El Hierro (Navarro and Soler, 1994) the Canary Islands, Fogo in the Cape Verde islands (Bjelm and Svensson, 1982; Martins, 1988; Descloitres *et al.*, 1995) and Piton de la Fournaise volcano on Reunion Island (Coudray *et al.*, 1990). Dike rocks concentrated in rift zones form broadly vertical structures capable of retaining large volumes of water. On water-poor islands, vertical wells and horizontal galleries cut into the dikes tap this source and also provide useful data on the internal structure of the rift zones. The Oahu situation (Fig. 1) is probably typical, with the water table dipping seaward away from the major rift zones and central summit areas (Hunt, 1997; Hunt *et al.*, 1988). An insular fresh water lens floats upon salt water that seeps through the highly porous submarine volcanic edifice. Tidal flushing of brackish water through coastal zones is observed in wells around the periphery of the island. The circulation of seawater through the volcanic edifice below sea level, by convection within edifices, also creates positive interstitial pore pressures (Rougerie *et al.*, 1980, 1991, 1992; Rougerie and Wauthy, 1986, 1988, 1993). Up to 80% of the island of Hawaii (comprising the submarine portion of the volcanoes plus the volume of the island aquifers) can exhibit positive pore pressure capable of facilitating faulting and failure of the edifice. Clague *et al.* (2002) suggest high rainfall, formation of canyons and increased

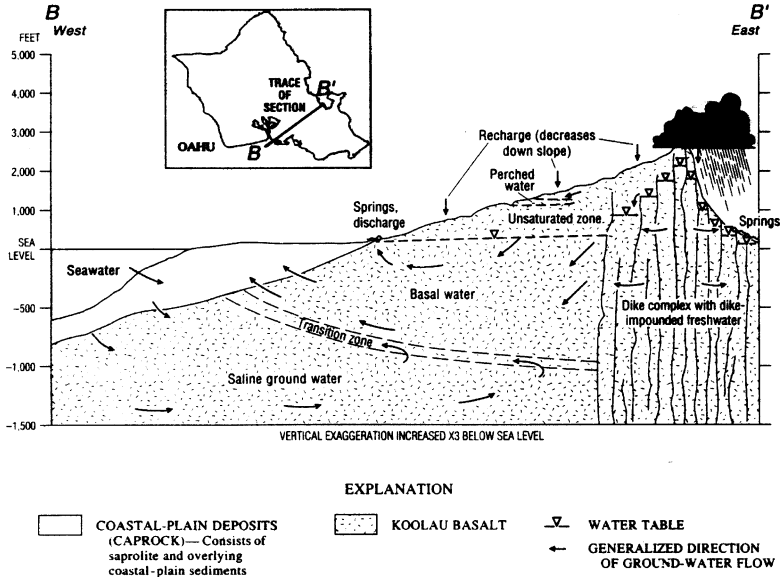


FIG. 1. Profile of Oahu water table illustrating the modes of groundwater occurrence on the island of Oahu, Hawaii (from Hunt, 1997).

groundwater pressure associated with dike intrusions facilitate flank failure. This effect of rainfall is likely, however, to be substantially lower in volcanic islands situated in low rainfall zones such as the equatorial Pacific Ocean (as low as 22 cm/yr; Keating, 1992) or islands or parts of islands located within rain “shadows” (e.g., the western flank of the Cumbre Vieja volcano on La Palma in the Canary Islands or the Hawaiian islands of Lanai and Kahoolawe). The significance of water content in the failure process is highlighted by Day *et al.* (1997), who describe sub-aerial dry breccias exposed in water galleries and outcrops along the San Andres fault system of El Hierro in the Canary Islands. The fault is interpreted by Day *et al.* (1997) and his co-authors as the back-wall of an aborted slide surface that lacked sufficient groundwater pressurization during its development for complete failure. The presence of pseudotachylite testifies to substantial frictional heating as a result of the rapid movement of one rock mass against another, and provides support for the dry-slide scenario. Since dike impounded ground water is potentially highly sensitive to variations in precipitation rates across the summit regions of volcanic ocean islands, a feasible mechanism exists for linking volcanic ocean island collapse and climate change.

A number of authors invoke water as a weakening agent that may be heavily implicated in instability development, and eventually contribute to structural failure through hydrothermal alteration of the edifice (Day, 1996; Elsworth and Day, 1999; van Wyk de Vries *et al.*, 2000; Voight, 2000; Reid *et al.*, 2001; Moon and Simpson, 2002). The effect of elevated fluid pressure is critical, since it facilitates movement along discrete dislocation planes and is an essential prerequisite to the catastrophic failure process. Extremely rapid maturation of a fault is also considered important, reflecting the great deformation rates of highly reactive host rocks that have undergone alteration to clay-rich material. While Mount St. Helens and Mount Rainier (Reid *et al.*, 2001) have been greatly weakened by very corrosive hydrothermal systems, Day (1996 and personal communications, 2001) suggests steam dominated, rather than corrosive alteration (Kilauea-type) systems, may be less responsive to failure since the formation of interstitial zeolite minerals reduces fracture permeability decreasing circulation of hydrothermal fluids.

## 2.2. The Dike Injection Process

Persistent injection of dikes along rift zones is recognized as a key means of promoting edifice instability and is recognized as playing such a role as at Mount Etna (Sicily), Stromboli (Aeolian Islands), and El Hierro (Canary Islands) (McGuire, 1996). On Hawaii, Walker (1986, 1987) measured the individual dikes within the Koolau volcanic complex (East Oahu). At its widest point, 7400 dikes were found with median widths of less than 0.5 m (Walker *et al.*, 1995). Overall extension of the volcano resulting from dike injection is estimated to be over 4 km, with dike confinement leading to the development of positive pore pressures. Because the seaward flanks of coastal volcanoes and volcanic islands are unbuttressed, accommodation of magma intrusion can readily displace the volcanic flanks in this direction, e.g., Smith *et al.* 1999; Cannon *et al.* 2001, Parfitt and Peacock, 2001; Parfitt *et al.* (2002). Morgan *et al.* (2000a,b) and Smith *et al.* (2002) suggest that the submarine bench structures formed at the toe of the Hilina Fault Zone and the Nuuanu avalanche debris flow are the product of cumulative flank displacements that have resulted in imbricate thrusting seen in seismic reflection profiles. These profiles also show a seismically transparent layer underlying displaced blocks, which is interpreted as a layer of pelagic sediment or older turbidites that provided a low-cohesion slip surface that facilitated movement. Scientist debate if dikes cause spreading or spreading causes diking. Both dike injection related spreading and slip along decollements near or below the base of the volcano facilitate flank collapse.

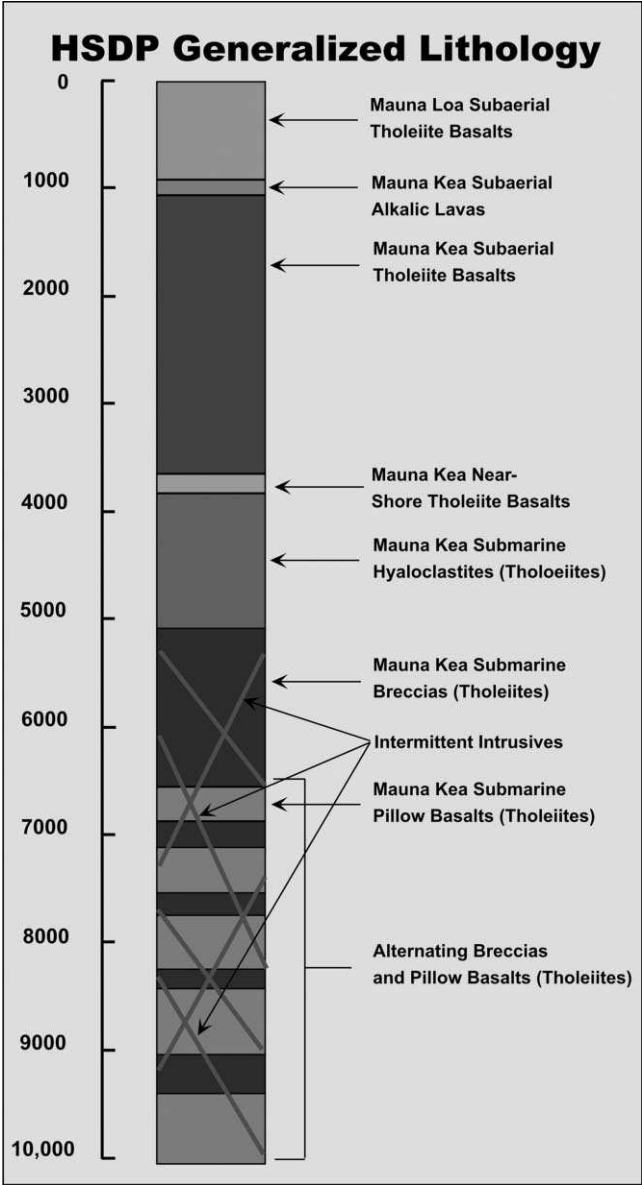
Do earthquake events trigger landslides or do landslides produce the earthquakes? Clearly the magmatic activity and the edifice deformation are interrelated (McGuire, 1996, and references therein). For a discussion of the nature of earthquake studies and “differential slip” on the failed southern slope of Kilauea volcano, see the review by Parfitt and Peacock (2001). Cannon *et al.* (2001) also examine differential slip.

### 2.3. Rock Type

Volcanic edifices, particularly stratocones of andesitic composition are heterogeneous and anisotropic structures, whose material properties are complex and which vary at a range of spatial scales (Voight, 2000). Even compositionally simpler basaltic volcanoes display great variability in terms of lithological and physical properties. The latter was clearly demonstrated during the course of the Hawaii Scientific Drilling Program (1999) which revealed the changing nature of volcanism at a single site. With increasing depth (Fig. 2), Mauna Loa flows give way to Mauna Kea lavas (DePaolo *et al.*, 2001), with the lithology shifting from sub-aerial lava flows to submarine hyaloclastites containing isolated pillow lava. Recent submersible studies on the submarine south flank of Kilauea also recorded a compositional change from alkalic to transitional basalts (Lipman *et al.*, 2000; Sisson *et al.* in Takahashi *et al.*, 2002). At Réunion Island (Indian Ocean), Bachelery *et al.* (1996) describe a change from sub-aerial breccias to debris avalanche deposits on the submarine slopes, while Schmincke and Segsneider (1998) record hyaloclastite lapilli and lithic breccia in cores drilled into the transitional zone (from shallow submarine to sub-aerial deposits) of the southwest flank of Gran Canaria (Canary Islands). Field observations of debris flow lithology and porosity include those of Lee and Edwards (1986), who note diverse rock types, contrasting physical properties and variable water content in gravity-core samples from submarine failure scars.

### 2.4. Rheology

Rheology (rock deformation) varies enormously within a volcanic edifice, both in space and time, and in response to a range of factors including changes in gravitational and tectonic stress regimes, magma intrusion and throughput and environmental effects, during the mass wasting process, temporal changes in rock properties are important. Coussot and Meunier (1996) point out that “mechanical properties such as velocity, flow depth or width, are relevant parameters for classification of slides and flows since they depend on boundary and initial



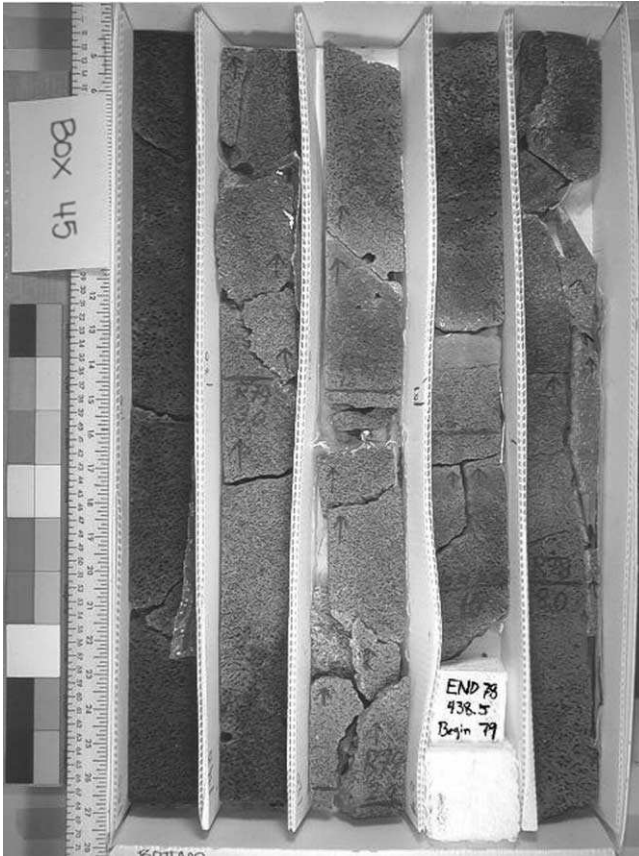


FIG. 2. Continued.

---

FIG. 2. Summary of the preliminary log of rock types from the Hawaii Scientific Drilling Program (HSDP) core hole located in Hilo, Hawaii (Figure from Don Thomas from DePaulo *et al.*, 2001). The stratigraphy begins within Moana Loa sub-aerial basalts at the top of the hole. By 1000 ft the rocks sampled were Moana Kea Sub-aerial lavas. Between 1000 and 2000 ft the rocks changed from alkalic lavas (above) to tholeiitic basalts. Transitional shallow marine materials were encountered between 3500 and 5500 ft. At depth in the core, submarine pillow lavas and breccias were recovered with minor intermittent intrusives.

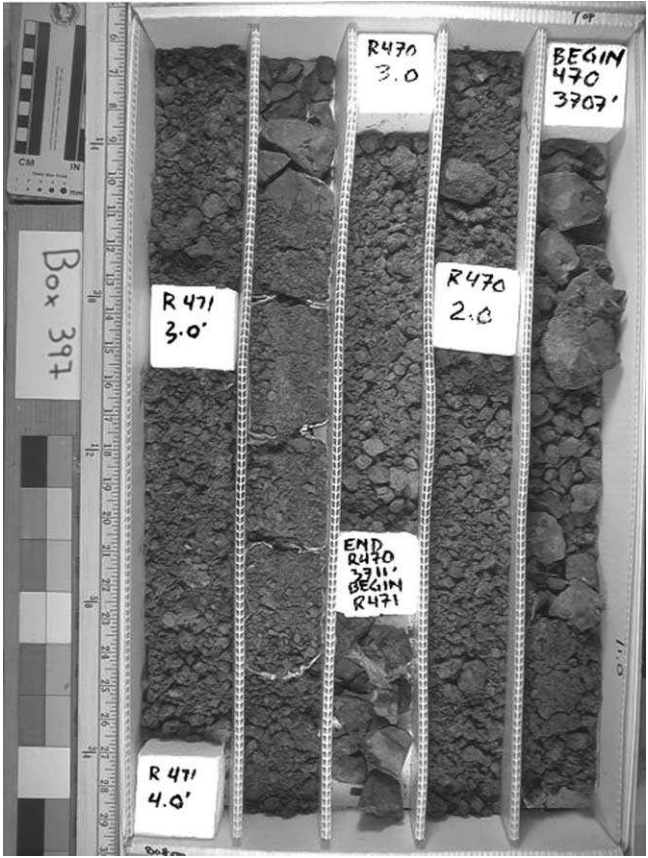


FIG. 2. Continued.

conditions and thus may easily vary from one event to another or during the same event". Studies of changing relationships encountered during mass flow include: Hubl and Steinwendtner (2000), who estimate rheological properties of viscous mass flows (using a conveyor belt approach), Davies (1990), who reports the results of experimental studies of granular flow, using a similar approach, and Coussot and Piau (1996) who addressed changes to the rheology of fine suspensions due to the addition of force-free particles. At Hilo, Hawaii, drill core from a 3 km deep hole reveals a progressive alteration with depth, due to low temperature zeolite minerals filling voids within originally fractured and friable volcanic rocks (e.g., hyaloclastites, *a'a* rubble, and inter-flow rubble; D. Thomas,

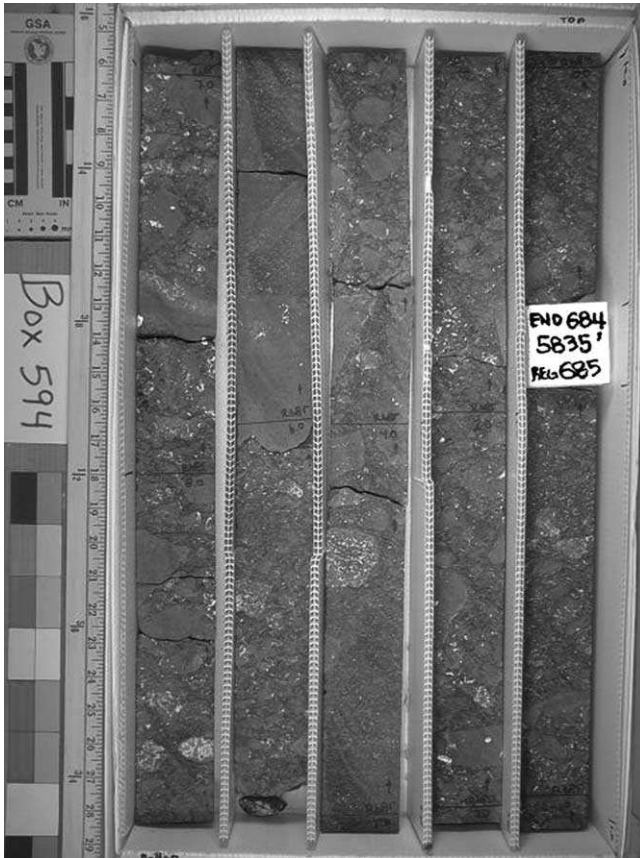


FIG. 2. Continued.

personal communications, 2001) thus altering their physical characteristics, e.g., induration and in particular their permeability. Submarine hyaloclastites often undergo substantial deformation but can prove to be highly indurated.

## 2.5. Rock Density

Improved insight into how volcanic edifices fail requires more information about how rock-mass strength varies, how dynamic loading occurs, how the distribution of materials changes, relevant rheology, and where discontinuities exist. Sampling via drilling projects and seismic modeling helps us to evaluate



FIG. 2. Continued.

these variables. The Hawaii Scientific Drilling Project (HSDP) recovered 500 m of “transitional rocks”, i.e., hyaloclastites, breccias, pyroclastics, rubble, ash, beach and reef deposits representing the shift from submarine to sub-aerial volcanism (Fig. 2) (at depths of 3580–5000 ft in well). Moore (2001) has undertaken wet and dry rock density measurements on the drill core. Such physical measurements are useful for modeling studies, but void spaces between flows or in rubble zones strongly impact gross density distribution and stability within the volcano, which cannot be assessed through individual specimen measurements. Mitchell (2001) used seismic velocity measurements to broadly constrain edifice density and its variation with depth. He estimated that Jasper

Seamount densities, calculated from velocity models using density-slowness regression derived from laboratory samples, exceed  $2.70\text{--}2.75\text{ g/cm}^3$  at  $3.2\text{ km}$  compared to  $2.0\text{ g/cm}^3$ —near the surface (Fig. 3). Remote sensing using magnetic, gravity, and seismic velocity measurements has long been employed on volcanoes around the world, and is extremely valuable in mapping internal heterogeneity, e.g., Hildenbrand *et al.* (1993) aeromagnetic study of Hawaii. Novel information about slope failure processes on volcanic islands and continental margins has arisen, e.g., marine gravity, magnetics, and seismic reflection. These observations constrain internal structure, volumes and source areas. The geophysical studies provide rigorous data that must be reconciled with surface observations. (The geophysical data also provides important links

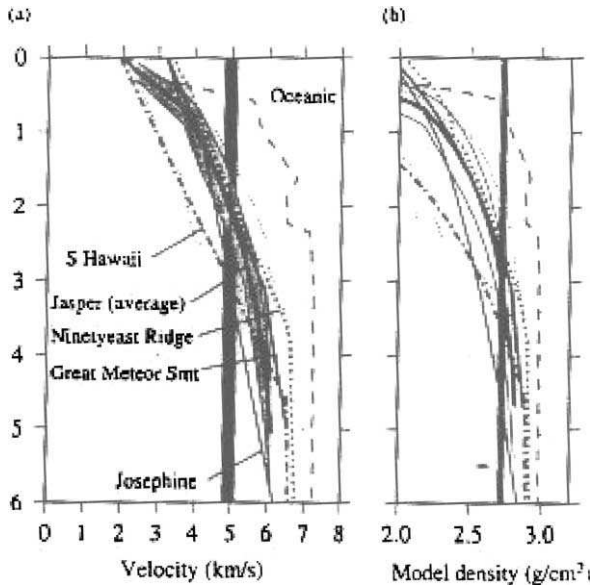


FIG. 3. The left portion of this figure (from Mitchel, 2001; Fig. 17) shows the seismic  $P$ -wave velocity models for several submarine volcanic edifices including: South Hawaii, Jasper Seamount, Ninetyeast Ridge, Great Meteor Seamount, and Josephine Seamount. The dashed line represents  $0.2\text{ Ma}$  fast-spreading ocean crust and the vertical dark shaded line represents an average velocity of  $5.9\text{ Ma}$  oceanic extrusives at ODP Site 504B, with  $10\%$  porosity, for comparison. The Jasper Seamount profile (heavy bold line) with uncertainly bounds can be compared to the profile for the opposite flank of the seamount (light dotted line). The bulk rock density (shown in figure at right) calculated using a density slowness regression from the models (at left in this figure). The horizontal bar represents the typical uncertainty associated with this regression. The shaded line is the expected density of basaltic melt.

between massive slope failures and methane venting.) Due to both time and space considerations, however, a summary of the numerous geophysical studies of volcanoes is not included here.

## 2.6. Landslide Structural Characteristics and Depth of Initiation

Incipient collapse structures have been identified at a limited number of sites worldwide, including the south flank of Kilauea (Hawaii) (Fig. 4), the west flank of the Cumbre Vieja volcano (La Palma, Canary Islands) (Moss *et al.*, 1997; Ward and Day, 2001) and also at Fogo (Cape Verde Islands; Day *et al.*, 1999a–c), Niue Island (South Pacific) (Nunn, 1998, personal communications) and Mururoa Atoll (French Polynesia; see review by Keating, 1998). It would be extremely valuable to be able to better constrain the nature of the faulting, the depth of fault initiation, and the volumes of failed material. Often, however, sonar surveys of volcanic landslides fail to extend into shallow waters, leaving the scarps of many known landslides unstudied. Recent lidar surveys of shallow waters around the Hawaiian Islands and sonar mapping have improved this situation (SHOALS Project; www site: shoals.sam.usace.army.mil/). Furthermore, a detailed knowledge of the thickness of the associated debris

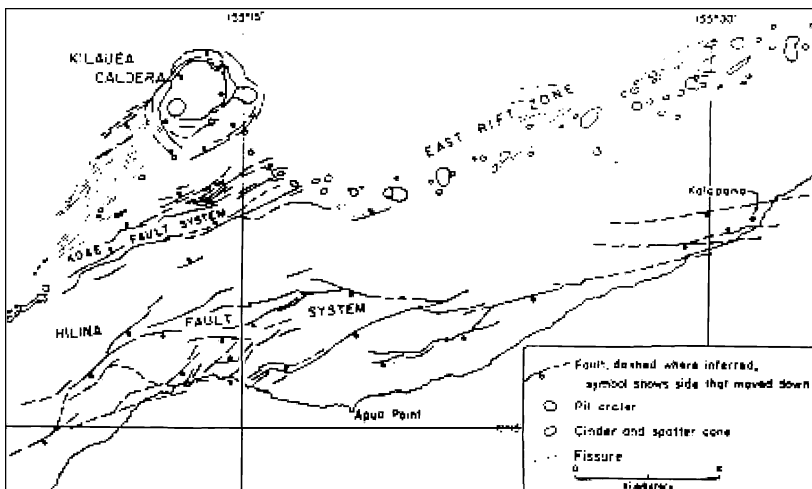


FIG. 4. Map showing the pattern of faults in the Hilina fault system on the southern flank of Kilauea (Fig. 19.21 from MacDonald *et al.*, 1983).

unit is often lacking, either because shipboard seismic profiling fails to penetrate its full depth or because ground-truth sampling is not adequately coupled with sonar imaging. Even where good seismic records exist, it is not always clear if a seismic unit represents an amalgamation of individual failures or a repetition or a stacking resulting from a single event.

Constraints on mass flow thickness can be provided by seismic reflection surveys. Watts *et al.* (1985) conducted a multi-channel seismic survey between the Hawaiian islands of Molokai and Oahu, showing that the moat around the Hawaiian hot spot is filled by hummocky debris. Rees *et al.* (1993), using single-channel seismic reflection data, found a basal unit of pelagic sediment on the sea floor overlain by a thick wedge of lens-shaped units on-lapping the flexural arch. Each unit was characterized by highly chaotic internal reflectivity interpreted as a series of buried landslide deposits. The largest landslide unit was 700 m thick near the axis of the moat, extended 200 km along the bathymetric moat around the islands and contained blocks 100s of meters across, with finer-grained turbidites forming the distal facies. It is possible that the total thickness of landslide debris within the Hawaiian moat may be as great as 2.2 km. It is not known, however, what edifice these rocks are derived from, or when. Leslie *et al.* (2002) described the seismic stratigraphy of the frontal Hawaiian Moat revealed by multi-channel seismic imaging. They identified three distinct seismic facies within the volcanoclastic unit. Additional studies of landslide units and distal volcanoclastic sequence (e.g., Naka *et al.*, 2002; Smith *et al.*, 2002) are yielding important insight into the nature and origin of distal sedimentation. These results are of particular interest because of the absence of turbidite flows linked to the Hilina fault system.

Morgan *et al.* (2000a,b) and Hills *et al.* (2002) used multi-channel seismic reflection profiling to examine the bench-like nature of the Hilina Fault Zone and Nuuanu debris avalanche, revealing imbricate thrusting at the toe of the slope that is interpreted as evidence for incremental displacement of the flank. Swath mapping (P. Campbell, 2000, personal communications) and camera inspections (Wilkins and Keating, 1999, unpublished) on the leeward side of the Waianae (W. Oahu, Hawaii) submarine landslide show concave landslide scarps, covered with low backscatter material (observed using subsea video and interpreted as carbonate sediments), with an occasional outcrop of igneous rock (lacking any cover of sediment and interpreted as post-failure volcanism). Smith *et al.* (2002) discuss new results from seabed mapping for features on Kohala, Mauna Kea volcanoes and Hana Ridge, Hawaii. Moore and Clague (2002) describe the results of sea floor mapping on Nuuanu and Wailau landslides off Oahu. Characterizations of the deposits are made by Yokose; Sherman *et al.*; Clague *et al.*; Shinozaki *et al.*; and Tanaka *et al.* in Takahashi (1978). Lipman *et al.* (2002)

conclude that recurrent landsliding associated with the Hilina bench was characterized by repeated deposition of submarine debris flows that were individually of modest size, rather than chaotic landsliding or large-scale block slumping. The submarine benches adjacent to several Hawaiian rift zones are not well developed in the Canary Islands, instead volcanic cones are present.

At the distal portion of the landslides, the sea floor is covered with a mosaic of variously-sized detrital blocks. Moore and Clague (2002) observed 54 blocks with volume greater than  $1 \text{ km}^3$  in the Nuuanu slide of Oahu. They estimate the total volume of all large blocks at  $1400 \text{ km}^3$  comparable in appearance to images of a debris avalanche published by Labazuy (1996) from Réunion Island (Indian Ocean). Wolfe *et al.* (1993) and Filmer *et al.* (1994) examined the Marquesas Island Chain using seismic reflection and refraction data, finding over 2 km of debris overfilling the bathymetric moat. Single channel seismic profiles reveal that the major portion of the apron consists of volcanoclastic sediments with chaotic internal structure, interpreted as landslide-related debris flows with minor contributions from turbidites, ash falls and eruptive ejecta. Pelagic sediment covers volcanic basement.

A number of recent studies have provided substantial new data on edifice collapse in the Canary Island archipelago. Geisslinger *et al.* (1996) conducted multi-channel seismic profiling between Gran Canaria and Tenerife to map the volcanic apron prior to ocean drilling. Seismic profiles published by Masson *et al.* (1998) illustrate the nature of some of the coherent debris blocks within the Canary debris flow. Funck and Schmincke (1998) used multi-channel seismic reflection to examine the flanks and apron around Gran Canaria (Figs. 5 and 6) and identified a multitude of avalanche and slump features and stratified units on the debris aprons interpreted as interlayered biogenic deposits within primarily volcanic debris, and characterized by strong velocity contrasts. One unit of 180 m thickness displayed several unconformities. A suspected flank failure on the NW flank of Gran Canaria has been correlated with a slide deposit at nearby ODP Site 954, whereas elsewhere along the NW flank another debris unit is characterized by chaotic reflection patterns that are interpreted in terms of a volcanoclastic debris pile at the toe of the steep flank. West of Horgazales Basin (in southwestern Gran Canaria), a series of slump blocks were identified. On the SW side of Gran Canaria mass flow deposits enter the sea, forming a mound or ridge that appears to be the continuation of the sub-aerial flow activity. Funck and Lykke-Andersen (1998a,b) used high resolution reflection seismic profiling to compare three sites on the archipelagic apron north of Gran Canaria with ocean drilling data, and found a pattern of consistently shallowing sources. Schmincke and Segsneider (1998) argue for a shallowing of volcanic source material, evident from an

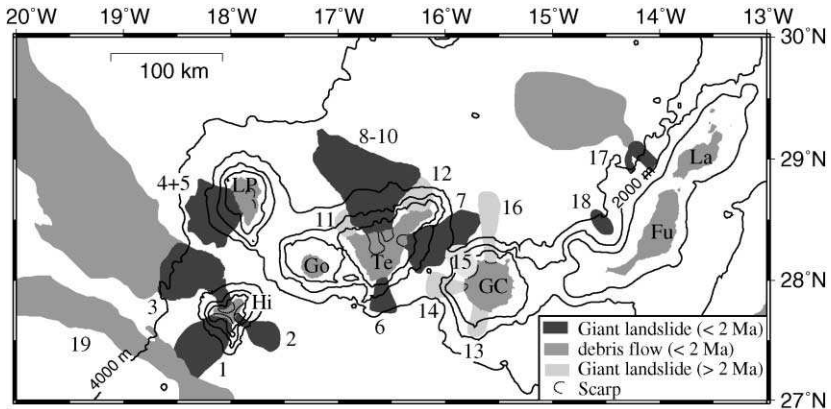


FIG. 5. Map of Canary Island giant landslides (from Krastel *et al.*, 2001a,b; Fig. 4). The numbers identify the landslides described by Krastel *et al.* (2001a,b) including: (1) El Julian debris avalanche, (2) Las Playas debris avalanche, (3) El Golfo debris avalanche and Canary debris flow, (4) Cumbre Nueva debris avalanche, (5) Playa de la Veta debris avalanche complex, (6) Las Bandas del Sur debris avalanche, (7) Gumar debris avalanche, (8–10) Orotava, Icod, and Roques de Garcia debris avalanche, (11) Teno debris avalanche, (12) Anaga debris avalanche, (13) Roque Nublo avalanche. Also shown are the: (14) Horgazales basin, (15) Reentrant at the northwest coast of Gran Canaria, (16) Reentrant at the north coast of Gran Canaria, (17) East Canary ridge avalanche, (18) Jandia debris avalanche, and (19) Saharan debris flow.

increase in shard vesicularity in core samples from Ocean Drilling Sites 953 and 956.

Mehl and Schmincke (1999) report in detail on the sub-aerial Roque Nublo debris avalanche deposit, Gran Canaria. They describe the debris avalanche facies, their characteristics and the rheological interpretation. While the rock unit is sub-aerial it provides important insight into the processes occurring during the formation and transport of debris avalanche materials, the distribution of particles sizes (including mega-blocks greater than 100 m in diameter) and the nature of shearing.

## 2.7. Landslide Form and Dimensions

Moore *et al.* (1989) describe 17 slope failures around the Hawaiian Islands, this number has increased by 66 landslides (longer than 20 km) according to Moore and Clague (2002), some of which—like the Alika debris avalanches—are amalgamations of a series of collapse events. Moore *et al.* (1989) provide volume

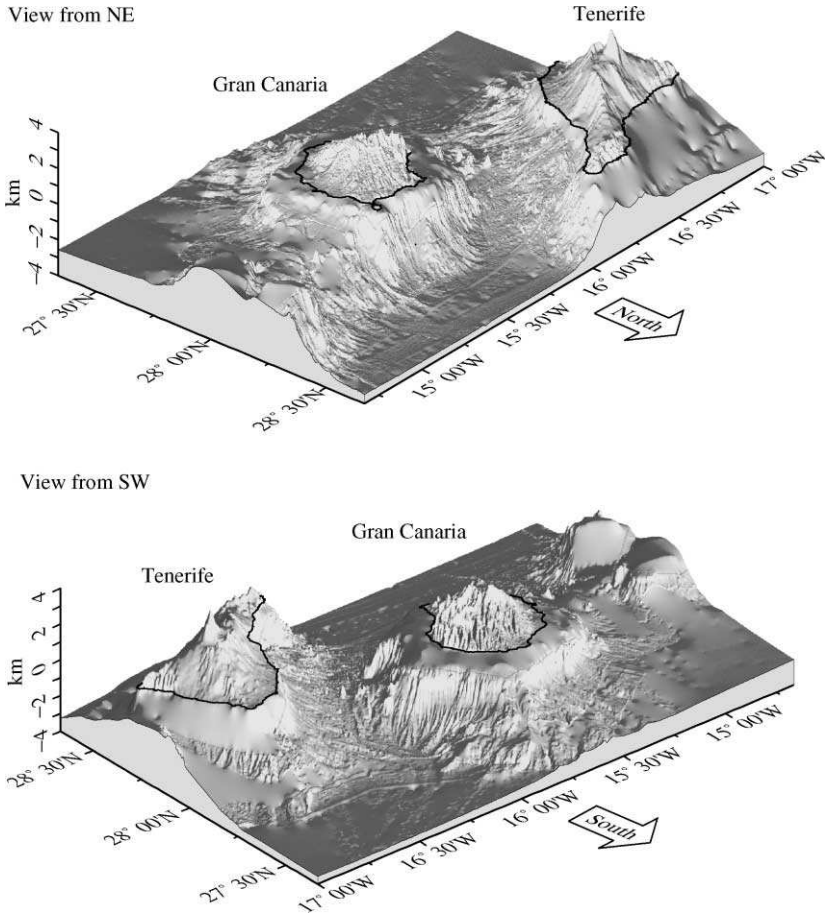


FIG. 6. Three dimensional shaded relief map of the Gran Canaria and Tenerife islands and surrounding sea floor from Krastel *et al.* (2001), Fig. 3; the vertical relief is exaggerated  $7.5 \times$ ). The view (at top) of the islands is from the northeast with illumination from the east-northeast; the image below is a view from the southwest, illuminated from the south. The smooth areas are submarine slopes that were not images by the bathymetric mapping system.

estimates of four of the failures. The volumes of the source volcanoes were calculated by Barger and Jackson (1974) and permit size comparison of debris flows and avalanches with their host volcanoes (Table 2). Both the Nuuanu and Wailau landslide and debris flow volumes appear anomalously large, particularly when compared to results from the Canary Islands, where Schmincke (1990)

TABLE 2. Volumes of selected Hawaiian landslides and their host volcanoes

Debris Unit	Debris Volume (km <sup>3</sup> )	Volcano	Sub-aerial (km <sup>3</sup> )	vol%	Total Volcano (km <sup>3</sup> )	Vol%
Alika DA	400	M. Loa	7500	5.35	42,500	0.94 <sup>a</sup>
Nuuanu DA	5000	Koolau	200	25	20,900	23.9 <sup>a</sup>
Nuuanu DA	3000	Koolau	200	25	20,900	14.3 <sup>b</sup>
Wailau DA	1000	E. Molokai	200	5	16,600	6 <sup>a</sup>
Wailau DA	1000	E. Molokai	200	5	16,600	6 <sup>b</sup>
Hilina Slump	40	Kilauea	700	3.6	19,400	0.2 <sup>a</sup>

DA, debris avalanche.

<sup>a</sup>Based upon Moore *et al.* (1989).

<sup>b</sup>Based upon Satake *et al.* (2002). These values are estimates. Moore and Clague (2002) estimate the volume of mega-blocks and debris avalanche blocks in the Nuuanu landslide at 1400 km<sup>3</sup>. The estimates are likely to be strongly impacted by remobilization which has “masked” older debris fields, so the estimates are likely to be a imprecise and incomplete record.

estimates the El Golfo debris avalanche represented just 3.1% of the volcanic edifice. Estimating the amount removed by subsequent erosion, the volume of the El Golfo landslide failures represents 3.7 and 4.8% of the original edifice. The proximal area of the Canary debris flow lacks prominent headwall scarps, and the debris flow in many areas is only 10 m thick. Gee *et al.* (2001a,b) estimate that four giant Canary Islands landslides (El Golfo, El Julian, San Andres, and Las Palyas) have each removed around 3% of the total edifice volume.

Satake *et al.* (2002) re-analyzed the Nuuanu and Wailau debris avalanches in order to estimate resultant tsunami heights and travel times. They calculate volumes—based upon bathymetric analysis and imagery of the debris units—of 1000 km<sup>3</sup> for the Wailau debris field and 3500 km<sup>3</sup> for the Nuuanu avalanche. Based on bathymetry alone the area of the edifice failure may be overestimated since the landslide model extends the slide to include areas of NE and SE Oahu that appear to be intact volcanic slopes. Likewise, the area of the debris avalanche on the sea floor extends further N–S than the hummocky topography within their bathymetric map. Furthermore, the depth of the slide unit is estimated based upon trial and error, resulting in thicknesses of 330 and 260 m (compared to 200 and 75 m in Moore *et al.*, 1989) with neither estimate constrained by subsurface information. Similarly, the landslide volume for the Wailau debris avalanche is difficult to estimate since very little of the W. Molokai volcano remains above sea level, but it seems likely that part of the collapse of the adjacent W. Molokai Volcano could contribute to the anomalously large volume. Tuscaloosa Seamount sits within the debris field of both and is aligned with the Cretaceous age seamounts on the sea floor adjacent to the Hawaiian Islands. Langford (1969) studied Tuscaloosa Seamount, and suggested, “...on the basis of seismic and bathymetric

evidence, I believe the Tuscaloosa Seamount to be a guyot. Hills at the summit appear to be cones; depressions there appear to be craters. Two rift zones seem to be topographically expressed on the east peak. The moat appears to be due to isostatic adjustment to load. Therefore, I believe the Tuscaloosa Seamount to have formed by constructional volcanism rather than by landsliding". Sediments from the summit of Tuscaloosa have been sampled by box corers and appear, however, to be products of turbidity currents. Samples collected from Shinkai 6500 dive traverses reveal that the seamount is composed of hyaloclastites, consistent with an origin of lateral transport as landslide blocks (Naka *et al.*, 2002), and a seismic reflection line down the axis of the landslide (Moore *et al.*, 2002) strongly suggests that Tuscaloosa is a landslide block. New JAMSTEC multibeam bathymetry is described by Smith *et al.* and Moore and Clague in Takahashi *et al.* (2002). Satake *et al.* (2002) report that the Nuuanu and Wailau debris avalanches represent some of the largest submarine landslides identified to date. With the exception of these two anomalously large debris avalanches, the volume of debris units in the Canary (Schmincke, 1990) and Hawaiian Islands generally make up only a few percent of the volume of the source volcanic edifice. The high volcanic islands in the Hawaiian chain are less than 4.5 My age; the oldest volcanic remnant above sea level becomes submerged by 9 My after its formation, thus, a multitude of landslides are likely to have taken place during this time. While most landslides are likely to be small and volumetrically insignificant, compared to the giant submarine landslides, their number is likely to be immense.

Much new data around the Hawaiian chain has been collected and is still under analysis. The early models for slump and debris avalanche geometries and volumes are now being carefully re-examined. Many "slumps" have been found to be composed of volcanoclastic debris, removed from the islands and accreted to the edges of the volcano flanks (e.g., Lipman *et al.*, 2000; Morgan *et al.*, 2000a) rather than coherent down-dropped portions of the volcanic edifice. While, these observations probably apply to Kilauea, Mauna Loa, Nuuanu and probably Wailau, Laupahoehoe, N. Maui volcanoes, Waianea is a complicated exception.

## 2.8. Slope Angle (Bathymetry)

Siebert (1984) and Murray and Voight (1996) found a correlation between slope angle and frequency of major slope failures on Quaternary island volcanoes, while Labazuy (1996) suggested that rapid and asymmetric growth as on Reunion Island, can cause oversteepening of flanks and induce slope failures. Table 3 summarizes published slope angles for various volcanic edifices.

TABLE 3. Representative submarine slope values

Area	Slope	Reference
Hawaiian waters	19°	Mark and Moore (1987) <sup>a</sup>
Reunion Island	24° (500–1000 m)	Lenat <i>et al.</i> (1989)
Galapagos Islands	6–12°	Rowland (1996)
Canary Islands	18°	Funck and Schmincke (1998). Sub-aerial
Canary Islands	30°	Funck and Schmincke (1998). Submarine

<sup>a</sup>New Bathymetry shows that the slopes vary over a very wide range (Takahashi *et al.*, 2002).

## 2.9. Dynamics

Slope changes, mass changes, resistance, shear (above and below the flow), coherence in material and other factors conspire to slow the movement of landslide debris and change rock properties. Studies such as those of Van Gassen and Cruden (1989) model the changing landslide mass. Kirwan *et al.* (1986) describe time-dependent hydrodynamic modeling of turbidity currents. Experimental studies, such as Marr *et al.* (2001) and others, compare combinations of materials and observe their effects on flow speeds and the nature of debris flow features. Techniques are being developed to measure real-time changes in slide velocities. Arattano and Marchi (2000) report using video to derive velocity distributions along a debris flow surge, while Inaba *et al.* (2000) apply surface velocity computation of debris flows captured on video for vector field measurements. Increasingly, capabilities for real time measurement and estimation of viscosity changes in large-scale tank or flume test are being improved. A better understanding of landslide velocities is critical to tsunami modeling.

## 2.10. Change in Pore Properties Associated with Liquefaction

Kramer (1988) presents examples of slides triggered by coastal liquefaction. Hotta and Ohita (2000) have measured experimental pore water pressures, and suggest excess pore water pressure arises as a consequence of shearing. Denlinger and Iverson (1990) examined liquefaction potential on submarine sediment slopes, and suggest that although pressure gradients required for failure are high, experimentation shows they are easily achieved through compaction (Schwarz, 1982). Shear failure occurs first, but the sediments are already close to liquefaction conditions. Experiments by Marr *et al.* (2001) show that dynamic pore pressure fluctuations induced during sliding produce liquefaction when cohesion is low. Modeling of turbidity flows by Felix (2002) examined

the interaction between velocity, turbulence and sediment distribution. Coarse-grained sediments produced higher velocity gradients and concentration gradients, thickened considerably more and less rapidly, compared to fine-grained sediments.

### 3. POST-FAILURE DEBRIS MOVEMENT

#### 3.1. A Review of Transport Mechanisms

The submarine, liquid-saturated debris flow is one of a member of a suite of failures ranging from dry rock avalanches, and gas-charged pyroclastic flows to submarine edifice collapses (Middleton and Hampton, 1976; Varnes, 1978; Brunsten and Prior, 1984; Johnson and Rodine, 1984; Hampton *et al.*, 1996; Armanini and Michiue, 1997). Slope failures originate at internal fractures (faults and slips) along specific surfaces (Coussot and Meunier, 1996). Within debris flow deposits (particularly submarine flows) the original structure is broken down over long distances as it undergoes extremely large deformations (Mohrig *et al.*, 1999). In slumps, the bulk of the material can undergo relatively small deformations and some internal structures can often be observed in the final deposit (see descriptions of slump of Papua New Guinea associated with the 1998 PNG Tsunami, Tappin *et al.*, 2001, and seismically-induced mudflow in the Santa Barbara Basin, Edwards *et al.*, 1993).

Coussot and Meunier (1996) review the recognition, classification and description of debris flows.<sup>1</sup> They point out that “there is not yet general agreement on classification and flow modeling in the literature. For example different terms are used by geologists to describe the same events (Innes, 1983), and very different approaches to debris flow behavior have been developed (Iverson and Denlinger, 1987)” furthermore, “with debris flow material, the complexity could scarcely be greater since the interactions at a mesoscopic scale are various and complex”. Iverson (1997) warn that “owing to a relative lack of

<sup>1</sup> Koerner (1977); Takahashi (1981); Li *et al.* (1983); Costa (1984); Costa and Williams (1984); Johnson and Rodine (1984); Davies (1986); Pierson (1986); Qian and Wan (1986), O’Brien and Julien (1988), van Steijn (1988), Whipple and Dunne (1992) examine debris flows from various points of view including; field observations, flow characteristics, material behavior, material components, numerical modeling, etc. Other important studies of debris flows include: Sousa and Voigt (1991, 1992), Iverson (1997); Mohrig *et al.* (1999); Frederico (1999); Arattano and Marchi (2000); Hotta and Ohita (2000); Hubl and Steinwendtner (2000); Inaba *et al.* (2000); Iverson *et al.* (2000); Denlinger and Iverson (2001); Iverson and Denlinger (2001) and others. Shanmugam *et al.* (1988) and Shanmugam (1997, 2000) provide a critical perspective on turbidite deposition.

data for rigorous model tests, slide dynamics remain immature compared to slope failure models”.

Debris flows form the focus of a multitude of studies. Important contributions to the field of study include: Morganstern (1967); Moore (1977); Takahashi, (1978, 1980, 1981, 1991); Innes (1983); Costa (1984); Johnson and Rodine (1984); Costa and Wieczorek (1987); Savage (1993); Mulder and Cochonat (1996); Iverson (1997); Iverson *et al.* (1997); Major (1997); Heinrich *et al.* (2001). Iverson (1997) summarizes succinctly “mobilization requires failure of the mass, and sufficient water to saturate the mass, and sufficient conversion of gravitational potential energy to internal kinetic energy to change the style of motion from sliding on a localized failure surface to more widespread deformation that can be recognized as flow”.

Important recent work by Iverson and Vallance (2001) revealed that sub-aerial rock avalanches, debris flows, and pyroclastic flows deform irreversibly as they move downslope. Initial conditions, boundary conditions, and grain comminution and sorting influence pore pressures and cause variations in flow dynamics and deposits. Coussot and Meunier (1996) recognize that hydraulic jumps play a role in debris flow behavior. Piper *et al.* (1999) suggest that these such jumps provide a mechanism to produce a turbidity current that can sustain flow many hours after a slope failure (e.g., that triggered by the 1929 Grand Banks earthquake).

### 3.2. Submarine Mass Movement Classification, Terminology, and Facies Concepts

Varnes (1958) developed a classification of sub-aerial landslides, while Dott (1963) identified several categories of submarine slope instability; falls, slides or slumps, flows and turbidity flows. Moore (1977) suggested modification of the Varnes (1958) classification of sub-aerial landslides, subdividing the main categories, and further updating of the classification scheme was undertaken by Campbell (1975) and Varnes (1978). Marine geologic studies of submarine mass movements, including Middleton and Hampton (1973), Lowe (1979, 1982), and Nardin *et al.* (1979), resulted in several classifications growing from earlier sub-aerial schemes. Prior and Coleman (1984) review submarine mass movement terminologies, and Johnson and Rodine (1984) have suggested useful descriptive terms such as lobes, snouts, lateral levées, medial deposits, and incised channels. Krastel *et al.* (2001a,b) use the term “avalanche complex” to describe an amalgamation of collapse events (a helpful distinction). Cruden and Varnes (1996) suggest a set of definitions of landslide features for mapping. Mulder and Cochonat (1996) review over a hundred different offshore mass movement

deposits described in the literature and devise a classification involving: slides or slumps, plastic flows, or turbidity currents, with subdivisions (plastic flow, liquefied flow) based on cohesionless vs. liquefied flow activity. Within a sub-aerial setting, distinctions can often be made based on velocity that cannot be made in the submarine setting: debris flows (between 0.5 and 10 m/s), landslides (less than few cm/day) and avalanches (greater than 10 m/s). Given current contradictions and confusion over terminology and its usage, it is clear that within the submarine mapping community a concerted effort needs to be made at standardization.

Recently, the distribution and nature of debris flows has been used to define and describe facies surrounding a volcanic edifice. The facies concept is very useful and moves us away from a simple concept of intact vs. failed margins. Schmincke and Sumita (1998) used ocean drilling results to subdivide the volcanic apron around the Canary Islands into several facies. Facies definitions were based upon several drill cores, and an extensive set of geologic studies on the drill core material. They describe a "core facies" that includes intrusive and extrusive volcanic rocks overlain by seismically opaque "flank facies". The flank facies is subdivided into a "hyaloclastite facies" (hyaloclastic lapillistones and breccia) and an outer "volcaniclastic veneer" (of basaltic turbidites and debris flow deposits) up to several 100 m thick, and extending laterally into the slope and basin facies. Sediments above the flank facies include the proximal "slope facies" consisting of slumps, discontinuous bedded units, debris flows, and erosional channels. The distal "basin facies" (Fig. 7) consists of single and grouped seismic reflectors containing volcaniclastics (including ash, debris flows, distal ignimbrites and other volcaniclastic rocks generated by eruptions, erosion, and flank collapse).

Mehl and Schmincke (1999) examined the collapse of the flanks of Roque Nublo stratocone in Gran Canaria. The flank collapse (believed to be triggered by dike intrusion and hydrothermal alteration) involved at least 14 km<sup>3</sup> of debris and covered an area of 180 km<sup>3</sup> on the southern half of the island. The flank collapse occurred sub-aerially but the debris traveled beyond the coastline into the sea. The authors developed a debris avalanche facies system that includes: megablocks, debris avalanche blocks, homogenous facies, shear facies, mixed facies, and debris flow facies.

Ollier *et al.* (1998) studied the volcaniclastic fans associated with Reunion Volcano, recording a proximal fan that included deep-water deltas, debris-avalanche deposits, and slide-included fine-grained sedimentary lobes as well as some erosional features associated with sub-aerial valley outlets. The outer fan (facies) included thick coarse-grained turbidites overlain by a discrete cover

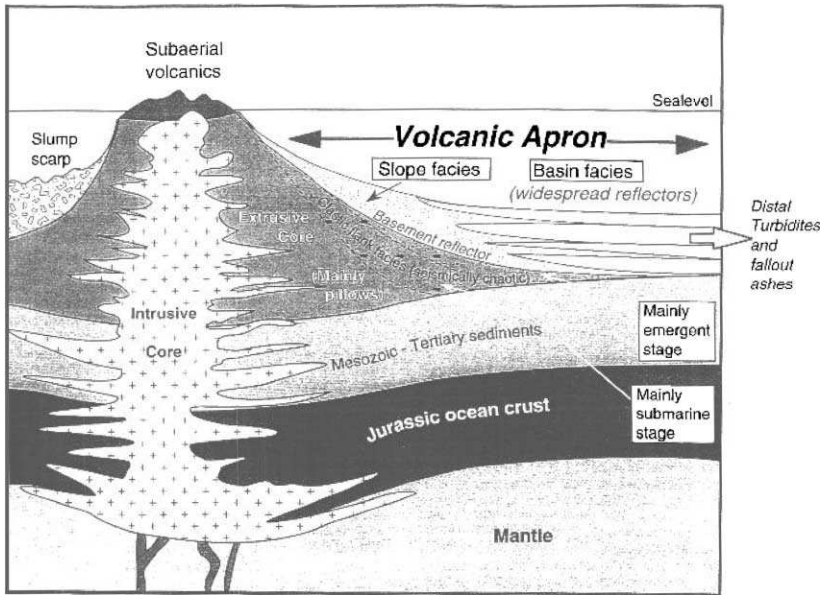


FIG. 7. Schematic drawing of an ocean volcanic edifice and the surrounding clastic apron facies. Based upon the scheme (reproduction of Fig. 7; Schmincke and Sumita (1998).

of hemipelagic/fine-grained turbidites. The basinal area (facies) consists of hemipelagic deposits interbedded with gravelly and sandy turbidite lobes.

Site specific facies descriptions are much more useful for describing submarine relationships between intact and failed slopes than the simple mapping and description of landslides, slumps, and associated phenomena. Submarine canyons are also important features that channelize debris flows and occur along the extensions of sub-aerial canyons and are often marked by accumulation of debris into overbank or levée deposits (see Labazuy, 1996; Krastel *et al.*, 2001a). Channelized debris flows associated with submarine canyons should be incorporated into a comprehensive facies scheme that reflects external as well as internal structure and stratigraphy. The terraces characterized by imbricate internal structures (Morgan *et al.*, 2000a) should also be incorporated within the facies concept approach.

### 3.3. Runout

Gravity dictates that materials from failed slopes move downslope. The conversion from potential energy to kinetic energy also dictates that a large

failure high on a slope will move great distances. Gravity and various physical parameters, including degree of fluidity, pore-pressure dissipation, degree of hydroplaning, determine runout.<sup>2</sup> Sousa and Voigt (1992) outlined the methods used to estimate runout (after catastrophic slope failure).<sup>3</sup> Dade and Huppert (1998) graphically illustrate the relationship between the runout (L/H) and rockfall volume (for non-volcanic, volcanic, and extraterrestrial materials) showing runout increases with the size of the rockfall or debris avalanche (Fig. 8). More specifically, Kilburn and Sorensen (1998) show that for giant landslides (sturzstroms) runout lengths depend on the potential energy available for motion after initial collapse (itself a function of the dimensions of the collapse zone), on the degree of rock fragmentation, and on the rate of momentum loss by fragment collisions in a basal boundary layer. Voight (2000) observed that the percentage of volcanoes that have collapsed correlates with volcano height. Richards and Lorriman (1987) also note that higher cliffs suffer larger landslides and retreat more rapidly because they generate higher shear stresses.

#### 4. TRANSPORT

##### 4.1. Overview of Laboratory Experiments

Physical modeling of slope failures sheds light on the formation of numerous features including hydroplaning, tension cracks, compressional ridges, water-escape features, detached slide blocks, and thickening of debris units associated with changes in slope, scouring of the seafloor, composite failures, channelization and overbank deposition, imbricate beds. Reassuringly, and despite known scaling problems, most of these features are identified in sonar images, seismic surveys and sampling of the sea floor (e.g., Cook *et al.*, 1976; Weaver and

<sup>2</sup> Hutchinson (1986); Cas and Wright (1987); Aksu and Hiscott (1992); Hayashi and Self (1992); Cleary and Campbell (1993); Kilburn and Sorensen (1998); Huang and Garcia (1999); Lee *et al.* (1999); Hurlimann *et al.* (2000) and others.

<sup>3</sup> Sousa and Voigt (1992) outline the methods to estimate runout “a) direct comparison to analogous avalanches, b) the use of empirical relationships such as the ratio of fall height to reach (Scheidegger, 1973; Pariseau and Voight, 1979; Voight *et al.*, 1983a, 1985; Ui, 1983) c) physical scale modeling using analog substances (Hsu, 1975; Voight *et al.*, 1985) and d) the development of theoretical equations for slide dynamics. The latter approach includes point-mass models (Pariseau and Voight, 1979; Pariseau, 1980; Perla *et al.*, 1980; Hungr *et al.*, 1984; McLellan and Kaiser, 1984; Koerner, 1997), sliding block models involving rational calculations of boundary friction (Hutchinson, 1986; Sassa, 1988) and continuum flow models (Lang *et al.*, 1979; Dent and Lang, 1983; Lang and Dent, 1983; Trunk *et al.*, 1986; Sassa, 1988)”.

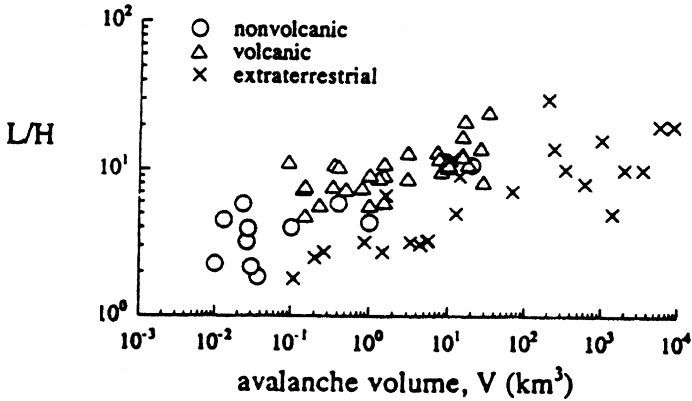


FIG. 8. Relative runout ( $L/H$ ) vs. rockfall volume ( $V$ ) for non-volcanic, volcanic, and extraterrestrial landslides (from Dade and Huppert (1998); Fig. 1).

Kuijpers, 1983; Hill and Tiffin, 1991; Helsley, 1993; Laberg and Vorren, 1993; Garcia, 1996; King *et al.*, 1996; Masson *et al.*, 1998; Schmincke and Sumita, 1998; Lee *et al.*, 1999; Hurlimann *et al.*, 2000; Kuijpers *et al.*, 2001). Laboratory tank experiments have long been used to study landslides, slumping, and debris flows in the marine environment (e.g., Stetson and Smith, 1938). Since confined rheometrical tests cannot give a realistic view of material behavior during surface flow (Coussot and Meunier, 1996), direct flow tests have been expanded to much larger channels (e.g., Iverson *et al.*, 1992, 1997). Denlinger and Iverson (2001) and Iverson and Denlinger (2001) show that small-scale laboratory experiments poorly simulate the dynamics of full-scale flows and such scaled down experiments exhibit effects due to surface tension at the air–water interfaces. Major (1997) reviews both depositional processes in large-scale debris-flow experiments as well as granular flow behavior and grain collision. Imran *et al.* (2001) compare numerical model predictions to laboratory experiments and finds reasonable agreement. Legros (2002) reports that the velocity of well-documented landslides but predictions from fluid absent and granular flow models predict landslides that are much faster and much less responsive to topography than natural ones.

Kneller and Buckee (2000) describe the structure and fluid mechanics of turbidity currents, review recent studies of their geologic implications, and summarize both experimental and mathematical models of gravity currents. Parker (1982) examines the conditions associated with catastrophically erosive turbidity currents. Parker *et al.* (1987) describe experiments on turbidity currents over an erodible bed. Seismic reflection profiles have also been undertaken across

giant landslides on the Ontong-Java Plateau (Berger and Johnson, 1976; Kroenke, 2001, personal communications). Kroenke (2001, personal communications) reports that channelized debris flows produced large isolated remnants with flat tops and steep sides resembling sub-aerial erosional buttes.

The physical modeling experiments of Major (1997), Mohrig *et al.* (1998, 1999) and Marr *et al.* (2001) and others yield intriguing results when compared to sidescan sonar images of submarine slope failures, revealing many common features. As in earlier work, the laboratory experiments of Marr *et al.* (2001), employed a range of coherence from highly coherent plastic flows to non-coherent turbulent suspensions of gravity driven, highly concentrated solid–fluid mixtures. As an experimental mixture is released into a tank of ambient water, it experiences dynamic pressure at the sediment front and shear along the upper boundary at the water–slurry interface. In response, a thickened head region develops in front of the trailing body. The shear stress at the surface of the head results in erosion that entrains sediment in the clear water above the head, forming a subsidiary turbidity current, visibly distinct from the dense debris flow. As an experimental debris flow decelerates, the turbidity current continues, depositing a thin turbidite downslope of the debris flow. The magnitude of the dynamic stresses is a function of flow velocity (Hampton, 1972) and flow velocity is a function of slurry rheology, volume of failed sediment, local bed slope, and bed roughness. The experiments show that strongly coherent debris flows commonly hydroplane, leaving structureless and ungraded deposits showing tension cracks, compression ridges, water-escape structures, detached slide-blocks, and a significant thickening at the base of the slope.<sup>4</sup> Hydroplaning occurs when the dynamic pressure just beyond the head of the gravity flow reaches or exceeds the submerged weight per unit area of the debris flow. Under these conditions a thin layer of ambient water can slip under the head. Hydroplaning occurs in both sub-aqueous debris flows and turbidity currents that are sufficiently swift. The hydroplaning was frequently associated with strongly coherent flows. The increased velocity of the head allowed tension to develop in the tail, and in some cases the hydroplaning head detached (auto-acephalation), traveled beyond the debris flow and stopped motion when hydroplaning ceased. Tension cracks were observed when hydroplaning was absent.

<sup>4</sup> Studies, e.g., Shreve (1968) demonstrate a layer of compressed air trapped beneath a sliding mass enhances mobility. Mohrig *et al.* (1998, 1999) describe experiments on the relative mobility of muddy subaqueous and sub-aerial debris flows and their capability to remobilize antecedent deposits. Mechanical or acoustic fluidization has been described by Howard (1973), Goguel (1978) and Melosh (1979).

Laboratory experiments also show that slide segments detach themselves when vertical tension cracks develop. The slide-block detachment (within a debris avalanche) results in a slow to moderately rapid creep that commonly reinflates the head and remobilizes the flow for a considerable distance. Conspicuous thickening of the flows occurs at slope breaks. The thickening is strongest in coherent flows, and less pronounced in weakly coherent flows. Compression ridges developed in experiments where the slurry collided with previously detached heads. Collision caused compression and buckling of the deposit so that imbricate slices of debris flow were observed when a trailing portion of the tail ramped up and over a detached segment of the debris flow (Sassa, 1988). These imbricate slices left the appearance of multiple depositional events but resulted from a single gravity flow.

Experimentally, runout distance increases with water content of the experimental mixture. When water content is uniform, runout distance decreases with rising clay fraction within the solids. In weakly to moderately coherent debris, grain size sorting occurred in the tail, as the slurry decelerates. Profiles reveal that the bedding shows sharp settling interfaces while strongly coherent flows are ungraded and structureless. Experiments also show that changes of slope result in important changes in debris flows, within which flow velocity decreases and deposition increases when a change in slope angle is encountered.

Dewatering structures (Collinson and Thompson, 1982) associated with venting from the basal coarse deposits have been observed experimentally, with thin plumes of water ejecting into the overlying ambient water shortly after the cessation of motion, and continuing for several minutes. Prior and Coleman (1980) recognized many sea floor features that they correlated with upward fluid flow and saline migration, and examples of this type of discharge are illustrated in Middleton and Hampton (1976). Several publications describing continental margin mass wasting and seabed mechanics are included in Denness (1984), a proceedings volume from an IUTAM/IUGG Symposium, Newcastle, 1983. Paull (2001, personal communications) and Dillon (2001, personal communications) point out that signs of fluid flow on the sea floor are often associated with methane venting. Clearly there is a broad spectrum of discharge possible on the sea floor involving organic breakdown (particularly near the mouths of deltas), hydrocarbon migration, mud volcanoes, gas venting to the surface, gas migration from deep sources along faults, shear-dominated retrogressive slope failure and venting, gas seepage fields, salt dome activity, tectonically driven discharge of pore waters along plate boundaries. These examples reach far beyond gravitational failures and are driven by very different processes.

Experimental models of landslides show that erosion in underlying units takes place during transport of debris flows (Marr, 2000, personal communications).

Kirwan *et al.* (1986) suggest that erosion and deposition are approximately equal during the initial and intermediate slope movement. Theoretical modeling of turbidity currents also calls for erosion during the initial phase of movement and during the intermediate phase of downslope movement. Mohrig *et al.* (1999) observe differences in erosion patterns of turbidity currents in physical models depending on the hardness of the underlying unit.

#### 4.2. Sonar Surveys

Early surveys (e.g., Prior and Coleman, 1980) characterized active slides and flows and provided sonar images of slide and flow features that allowed the authors to identify slope instability hazards to submarine structures such as permanent platforms, jack-up rigs, and pipelines. These early sonar images showed striking examples of “collapse depression features” more recently described as “pockmarks”. The pockmarks occur on otherwise flat sea floor and are generally circular depressions and lack elevated peripheral rims. The distinctive, hummocky, rough surfaces of submarine landslides have led to the identification of numerous other examples, which are documented in the literature.

Since the Hawaiian hot spot is situated at low latitudes (19.50°N) reefs develop quickly on the margins of the volcanoes. Three hundred and sixty seismic reflection profiles within the 200 nautical miles zone extending from the Hawaiian Islands (Keating *et al.*, 1985; Keating, 1994a–d), and crossing the margins of the islands; the profiles show carbonate bank accumulation in excess of 400 m thick (the limit of seismic penetration). Sonar imagery of intact carbonate platforms often reveals a staircase reef configuration (e.g., Campbell and Kroenke, 1994) that reflects changing eustatic sea level and lithospheric flexure during their development. These intact reef-covered slopes can display ancestral canyons cutting across the reef flanks (Campbell, 1994, personal communications). Canyon cutting in relation to landslides is discussed by Clague *et al.* (2002) and Moore and Clague (2002) discuss the distribution of deep canyons relative to landslide features in the Hawaiian Islands. The canyon morphology on the submarine slope of the Canary Islands is described in detail by Krastel *et al.* (2001a). Mehl and Schmincke (1999) suggest deep canyons can preserve debris avalanche materials. Mitchell *et al.* (2002) note that some blocks associated with Hawaiian avalanche deposits are much bigger than those observed within the Canary Islands and suggest many Canary and Hawaiian avalanches are characterized by small debris blocks that may have been constrained as the debris moved down narrow chutes, encouraging interaction between blocks and disintegration. Smith *et al.* (2002) described the submarine volcanic morphology of Kilauea volcano’s (Puna Ridge) SE rift zone.

Slope failures on volcanic edifices leave cusp-shaped coastlines, examples of which include El Hierro (Canary Islands and Tau (Fig. 9; Samoan Islands). Less frequently, a faulted linear margin is observed, for example the southern margin of Johnston Island in the Pacific (Keating, 1987). These flank failures produce broad debris piles on the sea floor that generate a “speckled” pattern in sonar images and real-time bathymetric displays that has proven an extremely useful diagnostic feature for recognizing slope failure deposits (Holcomb and Searle, 1991; Funck and Schmincke, 1998; Krastel *et al.*, 2001b; and many others). Another type of debris covered submarine slope is the scree or talus slope (slope covered by fragmental rock debris, e.g., Carracedo *et al.*, 1999 or massive volcanoclastic breccias (probably derived from progressive mass wasting upslope,

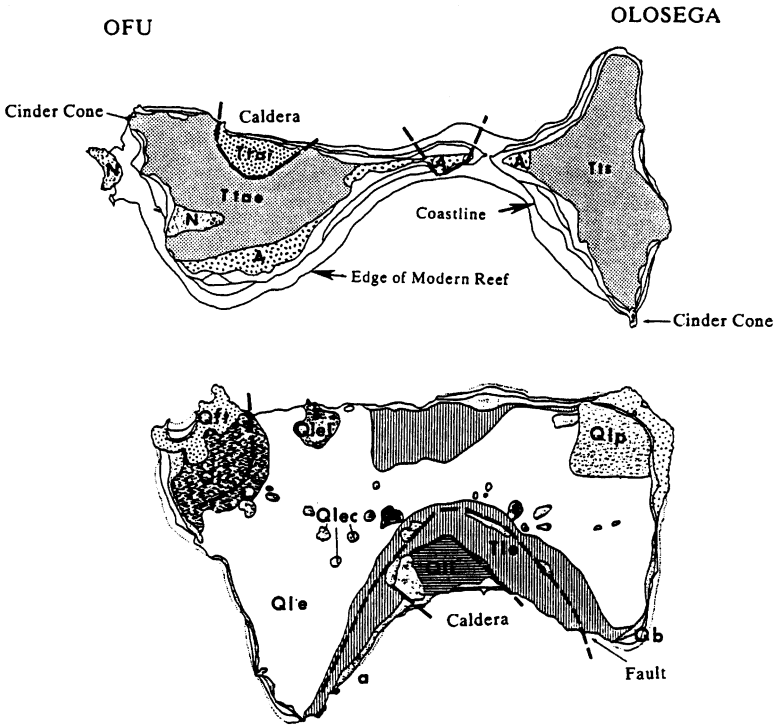


FIG. 9. Geologic maps of the Manua Group within the Samoan Islands. These geologic maps are redrawn from figures by Stice and McCoy (1968). The islands of Ofu and Olosega are shown at top, and the island of Tau is shown at both. In each case, only small portions of the original volcanoes remain above sea level, with much of the caldera lost to the sea.

Smith *et al.*, 2002). The submarine slope adjacent to the coast is covered by material of strong backscatter and granular appearance, interpreted as fragmented lava deposited when lava flows enter the sea and are quenched as coastal ledges fail due to wave activity. This material is not channelized but instead has a blanket-like appearance. A few sites show faulting and a clear potential to fail in the future. The carbonate platforms on many Pacific atolls are faulted (e.g., Johnson Island) and many atoll carbonate banks appear to be undermined by unstable volcanic slopes (e.g., Winterer and Sager, 1995; ODP Leg 143) and are strong candidates for slope failure. Submersible observations on Hawaiian flanks draped by hyaloclastic “slope sediments” that in places are well bedded, and appear indurated. Bedded hyaloclastites have also been dredged extensively from the submarine slopes of the Line Islands in the Central Pacific Basin (Table 4).

#### 4.3. Seismic Surveys

Seismic reflection surveys are of great importance in the study of edifice failures. Studies using this method, of the Nuuanu (Oahu, Hawaii) and Hilina (S. Hawaii) landslides, have shown them to be imbricate failures. The nature of the failures is, however, very different from the imbricate bed architecture discussed in the previous section describing debris transport. Rather than repeated gravity driven (passive) failures, Morgan *et al.* (2000a) and Hills *et al.* (2002) describe seismic profiles that they interpret in terms of a stacking of wedges of material via active volcanic spreading (Fig. 10). The interpreted reflection profiles of the Nuuanu structures reveal internal imbricated bedding (as well as discrete failure blocks called large and small debris avalanche blocks and hydroplaned blocks called mega-blocks by Mehl and Schmincke, 1999). Thus, this margin appears to be a composite of passive (gravity driven failures) and active failure features (wedges of debris at toe of volcano flanks thrust or scrapped up by volcanic spreading/dike injection, see discussion of magma-jacking by Smith *et al.* (1999) and Morgan *et al.* (2002a,b).

### 5. LANDSLIDES AS TSUNAMI GENERATORS

#### 5.1. Introduction and Recent Research Trends

Submarine landslides have long been suspected to cause tsunamis (Milne, 1898; Montessus de Ballore, 1907; Shepard, 1933; Gutenberg, 1939) but the numerical modeling of tsunami associated with submarine landslides (and related processes)

TABLE 4. Sonar studies illuminating slope collapse

Authors	Locations
Ryan (1980, 1982)	Atlantic
Embley (1976, 1980, 1982)	N. Atlantic
Lonsdale (1982)	NE Atlantic
Piper <i>et al.</i> (1988)	Grand Banks (N. Atlantic)
Sonar surveys of submarine landslides on ocean islands and seamounts	
Lonsdale (1986)	Tonga Trench
Hussong (1987)	Oahu (Hawaii)
Keating (1987)	Johnston Island (Central Pacific)
Malahoff (1987)	Loihi (Hawaii)
Lipman <i>et al.</i> (1988)	Alika (Mauna Loa, Hawaii)
Kayen <i>et al.</i> (1989)	Horizon Guyot
Lonsdale (1989)	Kilauea (Hawaii)
Moore <i>et al.</i> (1989)	Hawaiian Ridge
Lenat <i>et al.</i> (1989, 1990)	Réunion
Cochonat <i>et al.</i> (1990)	Réunion
Coulbourn <i>et al.</i> (1991)	Machias Smt. (near Tonga)
Keating and Karogodina (1991a, b)	Savaii, Samoa
Holcomb and Searle (1991)	Ocean Islands (general)
Hill and Tiffin (1991)	Samoa
Kodagali (1991, 1992)	Central Indian Basin
Smoot and King (1992)	N. Pacific Guyots
Masson (1994)	Madeira Abyssal Plain
Masson (1996)	El Hierro (Canary Islands)
Masson <i>et al.</i> (1992)	Sahara Continental Rise
Masson <i>et al.</i> (1993)	Sahara Debris Flow
Natland in Filmer <i>et al.</i> (1994)	Marquesas
Keating (1994a)	Johnston Island, Kiribati
Keating (1994b) and Wessel and Keating (1994)	Cross Seamount. (Hawaii EEZ)
Keating (1994c)	Karin Ridge, Kiribati
Keating (1994d)	Hutchinson Seamount, Kiribati
Keating and Karogodina (1994)	Savaii (Samoa)
Keating <i>et al.</i> (1994)	W. Chapman Seamount (Central Pacific)
Watts and Masson (1995)	Tenerife (Canary Islands)
Weaver <i>et al.</i> (1995)	Canary Basin
Evans <i>et al.</i> (1996)	Storegga Slide (Norway)
Keating (1996)	Atolls and Guyots (C. Pacific)
Labazuy (1996)	Réunion
Wright (1996)	Kermadec Arc
Roberts and Camp (1996)	Canary Islands
Devey <i>et al.</i> (1997)	Foundation Seamounts
Urgeles <i>et al.</i> (1997)	Canary Islands
Keating (1997a,b, 1998)	Line Island, Mururoa (S. Pacific)

Continued

TABLE 4. Continued

Authors	Locations
Weinrebe <i>et al.</i> (1997)	Daikakuji Smt. (Emperors, Pacific)
Kodagali (1998)	Central Indian Basin
Masson <i>et al.</i> (1998)	Canary Islands
Hart <i>et al.</i> (2000)	Samoa Islands
Keating <i>et al.</i> (2000)	Savaii, Samoa
Clouard <i>et al.</i> (2001)	Tahiti (French Polynesia)
Smith <i>et al.</i> (2002)	Puna Ridge (Hawaii)
Takahashi <i>et al.</i> (2002) and others	Hawaiian Islands

Swath Mapping in Exclusive Economic Zone of the continental US and Hawaii (Hampton *et al.*, 1996, for brevity sake, readers are referred to the US Geological Survey GLORIA website for a long list of publications summarizing GLORIA mapping results at: <http://kai.er.usgs.gov/gloria/pubsrefs.html>).

was not begun in earnest until the 1970s. Since then, however, the number of studies of landslide generated tsunami have increased substantially (see Table 5).

The 1998 Papua New Guinea tsunami (Tappin *et al.*, 2001; Watts *et al.*, 2001a,b) triggered much debate within the tsunami community. The tsunami arrival time was not consistent with a seismogenic origin, so modeling shifted to accommodate marine survey observations of offshore slumping, resulting in a complex set of scenarios being generated to explain the tsunami event.

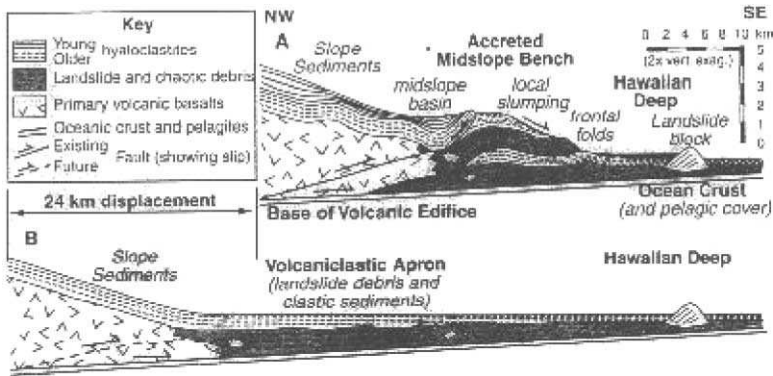


FIG. 10. Profiles of the interpreted structural features on the south eastern flank of Kilauea volcano from Morgan *et al.* (2000a,b); Fig. 5. The image (at top) shows imbricate thrusting of volcanic strata with the bench, rotated sediments in the mid-slope basin, and local slumping of the bench, recycling debris back to the volcanic apron. The profile (at Bottom) shows a reinterpretation, with the recent slope and bench sediments removed. The cumulative flank displacement is estimated to be roughly 24 km. These plots have a 2:1 vertical exaggeration.

TABLE 5. Tsunami and landslide studies (ordered by year)

Authors	
Wiegel (1955)	Lab wave studies submarine movement
Miller (1960)	Giant waves Lituya Bay
Noda (1970)	Landslide-generated water waves (LGWW)
Ben-Menahem and Rosenman (1972)	Amplitudes Submarine Earthquakes
Raney and Butler (1975)	LGWW numerical model (NM)
Striem and Miloh (1976)	Submarine slumping Israel
Murty (1979)	Kitimat Inlet, submarine landslide
Chiang <i>et al.</i> (1981)	Landslide generated waves
Jeffery (1981)	Socio-economic impact in Indonesia
Okusa and Yoshimura (1981)	Possible slope failure due to waves
Edgers and Karlsrud (1982)	Submarine landslides and soil flows
Iwasaki (1982)	WW generated by horizontal bottom motion
Mader <i>et al.</i> (1982)	1975 Kalapana tsunami
Chaudhry <i>et al.</i> (1983)	Reservoir landslide tsunami
Mader (1984)	1975 Kalapana, Hawaii, tsunami
Eissler and Kanamori (1987), Mader (1999)	1975 Kalapana earthquake
Hasegawa and Kanamori (1987)	Grand Banks landslide
Iwasaki (1987)	Submarine landslide tsunami
Townson and Kaya (1988)	Lake Botnen
Gozali and Hunt (1989)	Nearby-landslide tsunami
Kawakatsu (1989)	Landslide, inversion seismic waves
Pelayo and Wiens (1992)	1960 Peru tsunami, slow event
Shuto <i>et al.</i> (1990)	Near field tsunami warning
Gardner-Taggart and Barminski (1991)	Moss Landing landslide/wave
Heinrich (1991)	Nonlinear waves
Ma <i>et al.</i> (1991)	1989 Loma Prieta landslide/tsunami
Harbitz (1992)	Storegga submarine landslide
Heinrich (1992)	Nonlinear sub-aerial/submarine waves
Jiang and LeBlond (1992, 1993, 1994)	Submarine landslide, 3-D NM
Verriere and Lenoir (1992)	Submarine landslide waves
Kraft <i>et al.</i> (1993)	Submarine slide, Puget Sound
Ming and Wang (1993)	Landslide generated waves
Tsuji and Hino (1993)	1792 Shimabara landslide tsunami
Smith and Shepherd (1993)	Tsunami potential Kick'em Jenny
Walker and Bernard (1993)	Tsunami amplitudes
LeBlond and Jones (1994)	Hypothetical 105 ky Lanai
Johnson and Mader (1994)	Hypothetical Lanai landslide/tsunami
Watts and Raichlen (1994)	Underwater landslide generated waves
Imamura and Kikuchi (1994)	1992 Flores Island
Chen <i>et al.</i> (1995)	Landslide and tsunami hazard Vanuatu
Hidayat <i>et al.</i> (1995)	1992 Flores Island

*Continued*

TABLE 5. Continued

Authors	
Imamura <i>et al.</i> (1995)	1992 Flores Island
Wiegel (1955)	Laboratory study
Imamura and Giga (1996)	Subaqueous landslide
Jones and Mader (1996)	105 ka Tsunami propagation
Kulikov <i>et al.</i> (1996)	1994 Skagway tsunami landslide
Pelinovsky and Poplavsky (1996)	Submarine landslide tsunami
Imamura and Giga (1996)	Near-coast tsunami
Smith and Shepherd (1996)	Tsunami potential Kick'em Jenny
Warme and Sandberg (1996)	Impact tsunami
Rzadkiewicz <i>et al.</i> (1997)	Karmsundet landslide
Iwasaki (1987, 1997)	Submarine landslide
Bondevik <i>et al.</i> (1997)	Storegga tsunami
Iwasaki (1997)	Landslide tsunami wave forms
Kowalik (1997)	1958 Lituya Bay
Mader (1997)	1994 Skagway
Tinti <i>et al.</i> (1997)	Block-based gravity sliding
Warme <i>et al.</i> (1997)	Impact, landslide, tsunami
Watts (1997)	Thesis underwater landslides
Geist (1998)	Review local tsunami
Assier-Rzadkiewicz <i>et al.</i> (2000)	1979 Nice landslide tsunami
Heinrich <i>et al.</i> (1998)	Montserrat, Lesser Antilles
Kulikov <i>et al.</i> (1998)	Landslide tsunami Pacific, tides
Titov and Gonzalez (1998)	1998 PNG tsunami
Watts (1998)	Wavemaker curves
Anders and Beget (1999)	Landslides, tsunami, Cook Inlet
Campbell and Nottingham (1999)	1994 Skagway tsunami
Egorov and Osipenko (1999)	Submarine landslide Kamchatka
Grilli and Watts (1999)	Underwater landslides/waves
Kikuchi <i>et al.</i> (1997)	1998 PNG source rupture process
Ma <i>et al.</i> (1999)	1975 Kalapana tsunami
Mader (1999)	1958 Lituya Bay mega-tsunami
Matsuyama <i>et al.</i> (1999)	1998 PNG
McMurtry <i>et al.</i> (1999)	Alika 2 Giant Submarine landslide
Ryan and Davidson (1999)	Tsunami risk assessment, SW Pacific
Satake and Tanioka (1999)	1998 PNG
Sturdivant and McAdoo (1999)	Submarine landslide GIS database
Tanioka (1999)	Far field analysis 1998 PNG
Tappin <i>et al.</i> (1999)	1998 PNG slump
Tinti <i>et al.</i> (1999a,b)	Landslide/tsunami Vulcano Island 1988, Italy
Assier-Rzadkiewicz <i>et al.</i> (2000)	Nice submarine landslide
Borrero <i>et al.</i> (2001)	Submarine landslide Santa Barbara Channel

Continued

TABLE 5. Continued

Authors	
Day <i>et al.</i> (2000a)	Tsunamigenic flank collapse
Driscoll <i>et al.</i> (2000)	Potential tsunami generation
Fryer and Watts (2000)	Near source 1946 Unimak tsunami
Heinrich <i>et al.</i> (2000)	Near field modeling 1998 PNG
Geist (2000, 2001)	1998 PNG
Goldfinger <i>et al.</i> (2000)	S. Oregon Cascadia Margin
Inoue (2000)	1792 Shimabara catastrophe
Keating and McGuire (2000)	Review of island edifice failures
Locat and Lee (2002)	Submarine landslide
Okal (2000)	1998 PNG, t waves, slump
Pelletier <i>et al.</i> (2000)	1999 Vanuatu
Synolakis <i>et al.</i> (2000)	1994 Skagway tsunami
Synolakis <i>et al.</i> (2000)	Slump/tsunami 1998 PNG
Tinti and Bortolucci (2000)	Landslide, tsunami, Stromboli
Watts (2000)	Landslide/tsunami Solid Block Model
Watts <i>et al.</i> (2000a,b)	Amplitude prediction
Caplan-Auerbach <i>et al.</i> (2001)	Hydroacoustic detection landslides
Fritz <i>et al.</i> (2001)	Lituya Bay
Grilli and Watts (2002)	3-D numerical wave tank
Mader (2001a)	La Palma Landslide Tsunami
Mader (2001b)	Lituya Bay mega-tsunami
Okal and Synolakis (2001)	1998 PNG
Ruffman (2001)	Potential slope failure/tsunami comment
Satake and Kato (2001)	Landslide tsunami Oshima-Oshima
Tappin <i>et al.</i> (2001)	1998 PNG tsunami
Tinti <i>et al.</i> (2001)	Shallow water approximation
Von Huene <i>et al.</i> (2001)	Tsunamigenic slope failure
Ward and Day (2001)	La Palma, Canaries
Ward (2001)	Nuuanu, Storegga (1), Norfolk Canyon
Watts (2004)	Probabilistic Landslide/tsunami amplitudes
Watts <i>et al.</i> (2001b)	1998 PNG
Grilli <i>et al.</i> (2002)	Numerical wave tank
Mader and Gitting (2002)	1958 Lituya Bay mega-tsunami
Satake <i>et al.</i> (2002)	Landslide tsunami Oahu and Molokai, HI
Yalciner <i>et al.</i> (2002)	Slope failures, Sea of Marmara
Assier-Rzadkiewicz <i>et al.</i> (2000)	1998 PNG/submarine slumps
Biscontin <i>et al.</i> (2004)	Triggering submarine landslide
Bohannon and Gardner (2004)	Submarine landslide, CA
Fryer <i>et al.</i> (2004)	1946 Aleutian Tsunami
Locat <i>et al.</i> (2004)	Palos Verdes debris avalanche/tsunami
McAdoo and Watts (2004)	Submarine landslide Oregon slope
Murty (2003)	Landslide volume, Tsunami height

Continued

TABLE 5. Continued

Authors	
Ruff (2003)	Energy balance
Terrinha <i>et al.</i> (2003)	Slope instability Portuguese margin
Locat <i>et al.</i> (2004)	Landslide off Palos Verdes, California
Watts <i>et al.</i> (2003)	Wavemaker model

Note: This is a recent compilation that was developed using several computer search programs. We believe the table provides a reasonable compilation of the research but omissions are always likely to occur.

Fishermen in the area of the tsunami inundation reported sea floor changes in their traditional fishing grounds prior to the event, which may be related to venting of hydrocarbon deposits known to exist in this area (Baylis *et al.*, 1997). Future modeling of earthquakes, slumps, and tsunamis should address the possible role of gas venting in the 1998 tsunami event.

Tinti *et al.* (1999a,b) used observations of a slope failure and tsunami at Vulcano Island (Italy) to model tsunami generation and edge waves. The sub-aerial landslide (1988) which was associated with increased fumarolic and seismic activity, occurred on a slope of the volcano where the scars of other slope failures were visible. The study involved simulation of the landslide by means of a Lagrangian-type numerical model within which the slide is a multi-body system, or ensemble of material-deforming blocks interacting together during their motion. The tsunami was simulated according to the Eulerian view by solving the shallow-water approximation to Navier–Stokes equations of fluid dynamics, which incorporated forcing terms dependent on slide motion.

Many other exciting tsunami studies could be cited but for the sake of brevity are not. Tsunami modeling appears to be in a state of flux, particularly relating to the choice of parameters, and a number of questions remain to be addressed. How important to the slide motion is depth averaging and water flow in the reverse direction to the slide motion? How do models based upon landslide center of mass motion, compare with other simple to complex slide models? How critical are assumed slide velocities? Critical reviews and the tests of time will dictate the direction in which modeling proceeds, but current emphasis appears to focus on the simulation of hypothetical events.

## 5.2. Hypothetical Events

The modeling of hypothetical events is particularly important from a hazard and risk perspective, as some outputs are extremely destructive events

of ocean-basin extent. Ward and Day (2001) model the scale and extent of a tsunami generated by the catastrophic failure of the world's most recently activated giant landslide at La Palma. Destabilization of the western flank of the Cumbre Vieja volcano occurred during an eruption in 1949, when part of the flank dropped seaward by up to 4 m along a system of newly opened faults, and recent geodetic measurements suggest that the mass may still be creeping seawards at 1–2 cm every few years (Moss *et al.*, 1997). Using a “geologically-reasonable estimate of landslide motion”, Ward and Day (2001) model a series of collapses ranging in volume from 150 to 500 km<sup>3</sup>, the largest of which generates tsunami capable of crossing the Atlantic Basin and striking the coasts of the Americas with waves in the height range 10–25 m. Similar potential tsunami sources are only now beginning to come to light and are likely to form the foci of future scenario modeling. One is Fogo in the Cape Verde Islands, which, like the Cumbre Vieja, is a particularly steep volcano, with sub-aerial slopes averaging 15° or more and attaining values of 22–28° on the eastern flank. Day *et al.* (1999b) describe a large (9 km), east-facing lateral collapse structure bounded by cliff walls up to 1 km high—the Monte Amarelo collapse—and propose that N–S surface fissuring and east-facing normal faults support contemporary instability of the eastern flank of the currently active Cha das Caldeiras volcano. Ward (2001) modeled the Nuuanu (Hawaii) Slide, the Storrega (Norway) Slide 1, and the Norfolk Canyon Slide (VA, USA).

Mader (2001a) modeled the hypothetical La Palma landslide (proposed by Ward and Day, 2001) using the SWAN code and reached very different conclusions. Mader found a tsunami of small wavelength and period, leading to predicted run up on the east coast of North America of only 3 m. Mader concludes that full Navier–Stokes modeling would predict that the maximum wave amplitude along the east coast of the United States would be about 1 m.

The disparity of results for the hypothetical La Palma landslide tsunami has led portions of the tsunami community to express reservations about island flank failures producing distant tsunami and mega-tsunami (see Tsunami Society Web Site: [www.sthjournal.org/media.htm](http://www.sthjournal.org/media.htm)). Mega-tsunami do, without doubt, occur within enclosed bays and fjords. For example, the 1958 Lituya Bay (Alaska) rock-fall generated tsunami rose 150 m high with water running up the rock face on the opposite site of the bay to an elevation of 450 m. The wave ran over the sand/gravel spit enclosing the bay and was reported to have ran over 30 m high (eyewitness evidence). The period was about 3 min (the same as the La Palma event). The Lituya Bay tsunami was quickly dissipated and was barely observed elsewhere, although this may well reflect the fact that the source was enclosed and the collapse volume was very small compared to the 100s or 1000s of cubic kilometers proposed for tsunamigenic ocean island collapse events.

The Lituya Bay tsunami demonstrates that very high waves can be generated from a landslide near the source (a mega-tsunami) but does not in itself support the propagation of very large tsunami across oceanic distances. Undoubtedly, this is a debate that is likely to continue within the tsunami community for some time.

In the 1980s, Moore and Moore (1984, 1988) hypothesized that a prehistoric slope failure in the Hawaiian Islands produced a “mega-tsunami” that inundated the island of Lanai to an elevation of 365 m. More recently, however, LeBlond and Jones (1994) have questioned if the landslide would have been effective at generating the proposed 105 ka Lanai tsunami. Johnson and Mader (1994) used the model parameters of Johnson and King (1993) for a landslide of 600 km<sup>3</sup> and computed a wave height of 100 m in shallow water near Lanai. Even by doubling the volume of the Alika 2 slide they could not model a tsunami which would approach the run up hypothesized by the Moores. Jones and Mader (1996) modeled the tsunami hypothesized by Moore and Moore (1984, 1988) using SWAN code which solves the non-linear wave equations and employed ETOPO5 topography for the Pacific basin, and increased the landslide to 10 times the area of the Alika landslide off the coast of Hawaii (Moore *et al.*, 1989). Even then, they found the tsunami waves generated by a landslide on the slopes of Hawaii rapidly decayed, with the wave height reaching Australia only having an amplitude of  $\pm 1$  m.

The notion of a mega-tsunami is a recent invention. As such, much remains to be tested about the concept and the types of deposition vs. erosion is associated with it. Exciting debates have already occurred around the concept and much further debate is likely to ensue.

### 5.3. Quantification

Understanding the geologic relationships between landslides and tsunami is critically important, particularly for hazard assessment purposes. [Sessions on landslides and tsunami were organized within the American Geophysical Union (2002, 2003), International Offshore and Polar Engineering Conference (2003) and a NSF-sponsored workshop (2003).] Several recent publications model a subsiding block delimited by two coeval normal faults completely detached from the substrate and moving coherently downslope due to gravity. This portrayal of simple coherent slump movement is contradicted by both experimental observations and field observations that show debris avalanche flows display complex interactions, changing rheology—particularly when the slope changes, and evidence that the debris flow incorporated portions of the underlying substrate (e.g., Mehl and Schminche, 1999). Only in the exceptional case of a

hydroplaning mega-block, is it accurate to describe a landslide as moving downslopes completely detached and simply under the influence of gravity. This notion is an unrealistic simplification of the nature of slope failures and debris movement reviewed in the prior sections. The sources are heterogenous, the failures complex, the debris undergoes significant changes during transport and deposition, and the interactions with the water column are complex.

It has been demonstrated that the larger the volcanic edifice, the longer the runout. McGuire *et al.* (2002) illustrate that volume is an important control on how far a landslide can travel. The general trend shows an increase in landslide length with the square root of landslide volume. While the relationship between edifice size, volume, and runout are very clear, we can see in sonar imagery that the size of slope failures and the length of the runout vary immensely. Some landslides “fluidize” while others simply disaggregate. Important questions that remain to be answered include: Are there many more small landslides than giant ones? How many landslides are rapid, as opposed to slow? What are the statistical relationships, if any, between landslide volume, slope, composition, and runout? VanDine and Bovis (2002) have written a review of Canadian debris flow research which incorporates a bibliography of sub-aerial channelized debris flows (containing 295 citations) and is available electronically. Keefer (2002) reviews the history of landslides caused by earthquakes and points out that only a limited database is available and there is a pressing need for documentation of landslides triggered by earthquakes in a wide variety of environments on a global basis. A review and database for submarine landslide observations such as runout, flow velocity, earthquake rupture duration, and debris flow duration would be extremely enlightening. Schwarz (1982) published such a list of slope failure occurrences. More recent observations will augment this list and increase its value.

Within a sub-aerial setting, distinctions can often be made based on flow velocity that have not been made in the submarine setting; debris flows (move between 0.5 and 10 m/s), creep landslides (less than a few cm/day) and rock avalanches (greater than 10 m/s). These rates reflect differing grain size and rock coherence. The giant landslides mapped around the Hawaiian Islands are generally referred to as avalanches (i.e., fast moving) and slumps (inferred to be slow moving). Moore and Clague (2002) suggest “the sum of the evidence at this time suggests that some form of long-term, creep-induced bulges of Kilauea style presaged the catastrophic failure of both the Nuuanu and Wailau landslides”. Hills *et al.* (2002) observe that the mid-slope bench below the Hilina Fault Zone transforms from thrust sheets up to 2 km thick at the southwest to thinner thrust sheets to the northeast. Thus, there seems to be a change (or lateral transition) from seaward pushing and imbrication of thrust sheets to a stacking of thinner gravitationally driven thrust sheets. Deformation style clearly changes laterally

on the flanks of an oceanic volcano. Deformation style is also likely to change with time. Utilizing sidescan sonar to map gravity-driven debris flows, we have no constraints on how much time is involved in various edifice failures. We lack knowledge of remobilization and amalgamations of landslides that result from compound events. It would seem likely that debris from slumps could continue to move downslope over long periods of time (100s and 1000s of years).

Currently we have few constraints on the duration of earthquake rupture, landslide initiation, or transport processes. A few examples are available, where undersea communication cables have been broken by slope failure events. In the literature, we can find examples of tsunamigenic earthquake rupture durations of 60–150 s (e.g., Geist, 1998), but a comprehensive review of the literature to compare earthquake rupture duration vs. landslide duration (i.e., transport processes recorded from seismic signals, breakage of communication cables, etc.) would be welcome. Slumps (creep-induced bulges) may presage avalanches. Small rock falls may amalgamate into avalanches. Thin slump sheets may fault and become chaotic debris flows.

#### 5.4. New Areas of Tsunami Research

A number of studies of the bolide impact event at the end of the Cretaceous period (K–T boundary event) have reported impact-induced mass wasting, margin collapse, and extensive gravity flow formation, including: Maurrassee and Sens (1991); Kruge *et al.* 1994a,b; Bralower *et al.* (1998); Max *et al.* (1999); Klaus *et al.* (2000); Norris *et al.* (2000); Soria *et al.* (2001); McGuire *et al.* (2002) and others. The impact may have produced mega-waves that left behind tsunami deposits (e.g., Bourgeois *et al.*, 1988; Hildebrand and Boynton, 1990; Albertao and Martins, 1996). Attention is drawn to these studies because this very relevant research is being undertaken by a scientific community distinct from that involved in the study of sedimentation and erosion associated with tsunami inundation (see the review of Dawson and Shi, 2000) with little communication between the two groups.

Mega-tsunami deposits form another focus of relatively new research, and in Hawaii, field studies of supposed mega-tsunami deposits on Lanai have produced surprising results. The studies, carried out by investigators in several disciplines of geology and archaeology, do not support the mega-tsunami hypothesis for their emplacement. Dating studies on the Lanai coral-bearing deposits reveal that they represent several events rather than a single mega-event (Rubin *et al.*, 2000). Furthermore, stratigraphic relationships indicate the deposits consist of a number of units of different ages (Jones, 1993) with significant formation of sub-aerial

soil horizons between submarine coral-bearing units (Keating, 1997a,b; Felton *et al.*, 2000). Field studies also find an intact ancient coral reef at 100 m elevation and horizontal wave cut coral-filled notches within the proposed Lanai inundation zone (Keating and Helsley, 2002). These recent studies suggest that the Lanai deposits reflect island uplift as it passes over the lithospheric flexural arch associated with the Hawaiian hot spot (Wessel and Keating, 1994; Grigg and Jones, 1997; Keating and Helsley, 2002) and offer an argument against the formation of giant tsunami as a result of ocean island collapse. These indicate that a cautious approach is needed in interpreting the emplacement of unexplained coastal deposits by such means. Possible tsunami deposits are also recorded in the Atlantic Ocean, where evidence for a collapse at El Hierro (Canary Islands) dated to around 120 ka may lie in chevron sand ridges and giant boulders visible along east-facing coasts of the Bahamas (Hearty, 1997). These features have also, however, been explained in terms of unprecedented storms (Hearty *et al.*, 1998) and remain problematic.

The subject of slope failures and tsunami is very topical. Much new research has been carried out and new discoveries made within the last 5–10 years. New approaches are being utilized for the study of landslides and tsunami modeling, but landslide-triggered tsunami investigations have a long and complex history, with initial research beginning in the 1950s. Table 5 will allow students to track the development and evolution of landslide-related tsunami modeling.

Landslide velocities used for numerical models of tsunami are often high, e.g., La Palma landslide modeling employed a velocity of 100 m/s (Mader, 2001a) and a velocity of 140 m/s was used to model the Nuuanu Slide (Oahu, HI, Satake *et al.*, 2002). Erishmann and Abele (2001) in “Dynamics of Rockslides and Rockfalls” compare the velocities of well-studied rockslides and rockfalls. Several estimates of landslide velocities are summarized here. For example at Pandemonium Creek (Canada) they assigned a velocity of 38 m/s to the rockslide. Monte Toc in Vaiont Valley, Italy, exhibited evidence of an estimated velocity of 25 m/s. The Blackhawk slide (southern California) was estimated to have a velocity of 76.2 m/s but according to Erishmann and Abele (2001) this is probably “a substantial overestimation”. The Kofels (Austria) rockslide reportedly reached 50 m/s. Va Pola Rockslide (Italy) was assigned maximum velocities from 106 to 74.3 m/s. Valiont Rockslide (N. Italy) that transformed from a creep to a slide with a velocity up to 20 m/s displaced water in front of the rock mass, creating a cascade of water 250 m high. The 1970 Huascarán (Cordillera Blanco, S. America) ice and rockfall is reported to have a velocity between 86 and 96.5 m/s (compare to a free fall velocity over an equal differential altitude of 106 m/s). In addition to the descriptions of these rockslides and rockfall, Erishmann and Abele (2001) provide an instructive discussion of velocity

estimations and point out that velocity calculations are often in error. Schwarz (1982) published velocity estimates for 26 known submarine landslides, with one exception, the velocities were all below 30.5 m/s.

## 6. CLIMATE CHANGE AND LANDSLIDES IN OCEAN BASIN ENVIRONMENTS

### 6.1. Climate Change as a Landslide Trigger

There are two means by which climate change can be held responsible for triggering landslides in ocean basin environments. The first involves direct effects of variations in meteorological parameters, such as precipitation, whereby—for example—changes in patterns of local rainfall over the upper flanks of a volcano may elevate pore-water pressures and raise the potential for edifice instability and failure. Such local meteorological variations are likely to form part of a broader pattern of climate change, as occurred frequently during the late Quaternary, and as is forecast to occur in coming centuries. The second is associated with proxy phenomena (or indirect links) that frequently accompany significant climate change, and in particular the large (> 100 m) changes in sea levels that are closely coupled with glaciation–deglaciation cycles. Day (2001, personal communications) has suggested that climate-related regional controls might be differentiated from those of global extent, such as sea-level change, by diachronous patterns of collapse or even recognition of northern–southern hemisphere distinction. Both regional and global effects have been invoked to explain the triggering of very large landslides from oceanic islands and continental margins

Submarine landslides generated by ocean island volcano collapse or the collapse of continental margins constitutes the largest mass movements on the planet, and both the Nuuanu (Hawaii) volcanic debris avalanche and the Storegga sediment slides off western Norway have volumes in excess of 3000–5000 km<sup>3</sup> (Ward, 2001). Intuitively, it might be expected that one of the most effective ways to trigger large-scale collapse in ocean basin environments would be through large and rapid changes in sea level. For the late Quaternary, sea level variations have been shown to cause significant stress changes along continental margins and in island arcs (Nakada and Yokose, 1992), and are likely also to have triggered increased levels of seismicity and perhaps also volcanism (McGuire *et al.*, 1997). A number of authors (e.g., Weaver and Kuijpers, 1983; Weaver *et al.*, 1995; Maslin *et al.*, 1998; Nisbet and Piper, 1998; Rothwell *et al.*, 1998, 2000) have suggested that submarine sediment slides are most common close to glacial sea-level minima, when slopes loaded

with low-cohesion debris fail in response to seismically triggered dynamic loading (Laberg and Vorren, 1993). Paull *et al.* (1996) suggest there is an increased frequency of continental margin slumping (above gas-hydrate bearing sediments) during sea level minima.

Rothwell *et al.* (1998, 2000) present evidence for mega-turbidite emplacement in the Mediterranean during the low sea-level stand at the height of the last glacial maximum, following a long period of elevated sediment input and accumulation. Kuijpers *et al.* (2001) highlight evidence for slope instability on the Faeroe margin dated at the Pleistocene/Holocene boundary and at the Last Glacial Maximum. These mass-flow events occurred during times of rapid sea-level rise and increased bottom current activity, and glacio-eustatic low stand. Goldstrand (1998) presents evidence for deposition of quartz-rich turbidite deposits derived from Saharan Aeolian sands that migrated onto the exposed continental shelf and shed into the deep sea around the Canary Islands during falls in sea level. Goldstrand also reports several units of shallow marine bioclastic material and foraminifera-rich turbidites corresponding to periods of sea-level fluctuations. Goldstein concludes that large-scale submarine slumping is more active in periods of intensified bottom currents and upwelling. Schmincke and Sumita (1998) interpret the occurrence of thick layers of coarse-grained bioclastic sands (of Pleistocene age) in the Canary Island archipelagic apron as being the product of regression (falling sea level) associated glacial maxima. Ablay and Hurlimann (2000) suggest post-shield landslides on Tenerife correlate with major falls in sea level. They suggest these times corresponded to increased rates of volcanism and coastal erosion and reduced support of the volcanic flanks.

Hawkins (1984) and Taylor (1984) both highlight how unconformity development and contrasting sediment types and permeabilities during periods of sea-level change are liable to promote instability along continental margins. The question of just when this instability is translated into collapse remains, however, questionable. In an analysis of the ages of six North Atlantic continental margin failures, Morton (1993) reveals a scatter of dates between 2000 and 24,000 years (most occurring during the last 16 ky). This supports landslide formation during the period of Holocene sea-level rise rather than during the last low stand. Morton (1993) argues that if continental margins failed when sea levels were at their lowest, then the slides should be buried beneath substantial thickness of late-low stand deposits. This is not borne out by seismic profiles, which document a thin cover of hemipelagic sediments. Eyles and Lagoë (1998) provide examples (Fig. 11) of submarine slump-generated mega-channels in the Yakataga Formation (Gulf of Alaska). But they find little

evidence to suggest the slump activity is systematically related to episodes of sea-level low stand.

The absence of a convincing strong correlation between low sea-level stands and the incidence of landslide formation in ocean basins should not be surprising. The question having to be asked—how would the continental margins and ocean islands know that a sea-level minimum has been reached? It is considerably more likely that both the continental margins and the slopes of ocean island volcanoes will become destabilized and experience failure during the dynamic situation of active sea-level change (upward or downward). The considerable rate of change is rarely appreciated and studies of Holocene coral reef drowning point to post-glacial rises as great as 13.5 m in less than  $290 \pm 50$  yr (Blanchon and Shaw, 1995). As a rule, sea levels during the late Quaternary rose much more rapidly than they fell, partly in response to the catastrophic draining of ice-dammed lakes into the oceans (e.g., Hillaire-Marcel *et al.*, 1981), providing a greater opportunity to destabilize ocean margins and

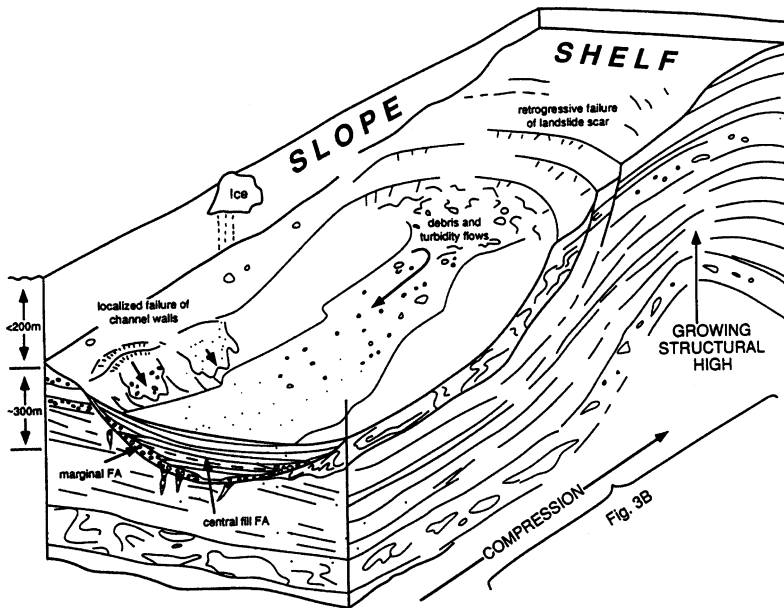


FIG. 11. Schematic block model showing mega-channel formation for the continental margin, in the Icy Bay region of the Gulf of Alaska. This model, from Eyles and Lagoee (1998), shows retrogressive failure along a landslide headwall and localized failure along the walls of the channel.

islands. In support of the impact of rapidly changing sea levels on the geosphere, McGuire *et al.* (1997) showed that for the Mediterranean region there is a convincing statistical correlation between the rate of sea-level change and the numbers of notable explosive volcanic eruptions; a link that is supported by the Greenland ice core record (Zielinski *et al.*, 1997). The same authors propose (Seavol, 1995) that the increase in the incidence of eruptions may be triggered by lateral collapse at island and coastal volcanoes, triggering decompression-related explosive eruptions after the manner of the 1980 Mount St. Helens eruption. They also point to the timing of lateral collapses at the Etna and Stromboli volcanoes, which correlate with rapid changes in sea level. Peripheral erosion associated with sea level rise will act to remove lateral buttressing on the flanks of coastal and island volcanoes promoting slope failures (McGuire *et al.*, 2002).

One of the difficulties with attempting to link collapses at marine volcanoes with changes in sea level lies in the fact that connection might not be directly causal in nature, and both edifice failure and sea-level change may have a common cause. This avenue has been recently explored by Day *et al.* (1999a, 2000a,b), who propose that the common cause might be climate change. They point to the fact that most mid- to low-latitude volcanic ocean islands experienced arid conditions during glacial periods and propose that prevailing water tables are therefore likely to be depressed. This, the authors suggest, would minimize opportunities for new magma to induce pore-fluid pressurization—a dominant mechanism for volcano destabilization during the rift-zone eruptions common at ocean island volcanoes such as those of the Hawaii, Cape Verde and Canary Island archipelagos (e.g., Elsworth and Voight, 1995; Elsworth and Day, 1999). At the same time, the penetration of salt water into the cores of the volcanoes might promote alteration and weaken the structure. During interglacials, in contrast, Day *et al.* (1999a–c) recognize that—for low latitudes—oceanic climates are humid, and ocean island volcanoes at such times are likely to have elevated water tables that are capable of being pressurized by magma intrusion, thereby increasing opportunities for structural failure. The corollary of this is that such collapses are likely to occur during the warming following glacial terminations, when the destabilizing effects of pore-pressure increases are greatest and reinforce the effects of earlier coastal erosion and volcanic core alteration.

Addressing the bigger picture, Day *et al.* (2000b) advocate a correlation between the timing of volcanic ocean island collapses and the precession-forced sea surface temperature (SST) (Fig. 12). They note that as sea levels rise following glacial terminations, so does the low-latitude SST. This sea surface warming is in turn accompanied by changes in the pattern and

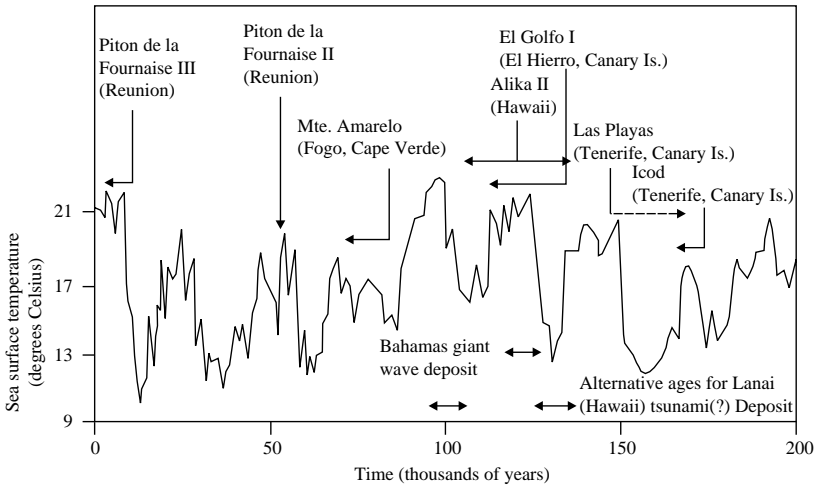


FIG. 12. Ages of oceanic island collapses over the past 200,000 years plotted against the global sea-level and sea-surface temperature change (after Day, personal communication).

characteristics of the trade winds so that they bring increased humidity to low-latitude volcanic islands and increased precipitation on their mid-flanks and summit regions. This, they propose, leads to a rise in the water table on the order of several hundred meters and increased opportunity for collapse as a result of magma intrusion related groundwater pressurization in the core of the volcano (Fig. 13). Day *et al.* (2000a) suggest ocean island collapses having periodicities that reflect the roughly 20,000 Milankovitch precessing forcing of SST maxima at low latitudes.

## 6.2. Gas Hydrates

Increasingly, destabilization of gas hydrates and methane venting have been invoked in the triggering of continental margin landslides (Kayen *et al.*, 1988; Field and Barber, 1993; Kayen and Lee, 1993; Popenoe *et al.*, 1993; Kelley *et al.*, 1994; Paull *et al.*, 1996, 2000, 2002; Abegg and Anderson, 1997; Ashi, 1999; Boe *et al.*, 2000; Max, 2000, 2002; Goldfinger *et al.*, 2002; Helsley, 2002; Keating, 2002; Mienert, 2002; Milkov and Sager, 2002; Shighihara and Imamura, 2002; Watts, 2002). As early as 1977, arguments were made that many slides situated on continental margins might have been

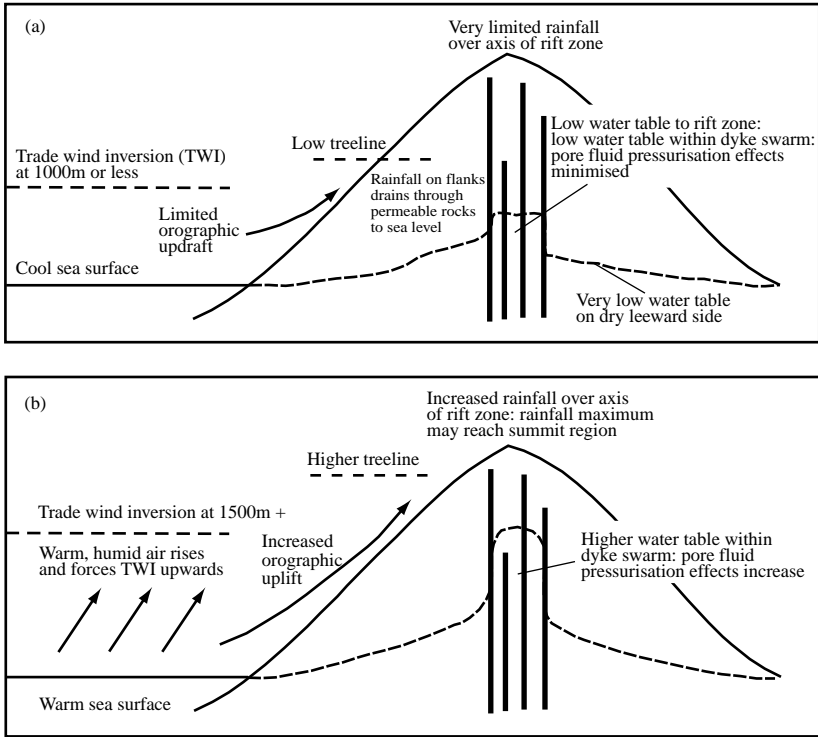


FIG. 13. Increased precipitation on the mid-flanks and summit regions of low-latitude volcanic islands, accompanied by a large rise in water tables, has been advocated as contributing towards a clustering of ocean island collapses during periods when the climate is warm (after Day, personal communication).

triggered by the disassociation of gas hydrate and the venting of methane (Embley and Jacoli, 1977). Since gas hydrates can be destabilized by increases in temperature (as little as  $1^{\circ}\text{C}$ ) and decreases in pressure, it has been suggested that small rises in bottom water temperature or drops in sea level may destabilize the gas hydrate, causing sediment liquefaction and leading to mass failures. Paull *et al.* (1991) have estimated that the first Storegga slide could have released 5 Gt or more of methane. Kennedy *et al.* (2001) suggests gas hydrate destabilization is recorded in Proterozoic rocks.

Considerable scientific effort has been expended on the topic of gas hydrates in marine sediments and methane venting from the sea floor, resulting in the

publication of several special volumes.<sup>5</sup> Modern observations of gas venting show that it greatly disturbs the sea bed producing crater-like features. These can be very large or can occur as small craters or pockmarks covering large fields on the sea floor (North Atlantic: Vogt *et al.*, 1999, Crane, 2001, personal communications; New Zealand margin, Helsley, 2002). At times of lowering sea level, or decreasing bottom water temperature and hydrostatic pressures are likely to trigger the disassociation of gas hydrate and venting of methane from continental margins, disrupting the continental margins and triggering submarine landslides and tsunamis (Ward and Day, 2001). Paull *et al.* (2002) suggest there is an increased continental margin slumping frequency during low stands above gas-hydrate bearing sediments. Vogt and Jung (2002) suggest both late/post glacial bottom-water warming and eustatic sea-level change could affect the methane hydrate stability and explain some submarine slope failures.<sup>6</sup>

### 6.3. Canary Islands

The Canary Islands have constituted an increasing focus for both onshore geological research and offshore marine surveys, and the ubiquity of lateral volcanic collapse within the archipelago has become more apparent. Krastel *et al.* (2001a) report 12 landslides around the Canary Islands, and conclude that large-scale mass wasting is an important process during all phases of magmatic activity (Krastel *et al.*, 2001b). Coastal morphology, landslide-source amphitheatres, aborted landslide basal faults, together with submarine imagery of the landslide deposits and the stratigraphy of turbidite sequences, testify to major collapses on Gran Canaria (e.g., Day, 1996; Funck and Schminke, 1998), Tenerife (e.g., Watts and Masson, 1995), El Hierro (e.g., Carracedo *et al.*, 1999) and La Palma (Carracedo *et al.*, 1999). Studies of the turbidite deposits of the Madeira Abyssal Plain have been used to interpret the geologic history of the African margin and the volcanism of the Canary Islands and Great Meteor-Cruiser Seamount Chain (Pearce and Jarvis, 1992). Weaver and Kuijpers (1983) and Weaver *et al.* (1995)

<sup>5</sup> van Weering *et al.* (1997, Gas in Marine sediments), Special Issue (1992, Continental Shelf Research), Special Issue (1994a, Bulletin of the Geological Society of Denmark), Special Issue (1994b, Geomarine Letters), the NATO Science Committee Special Program Workshop on Marine Slides and other Mass Movements (Saxov and Nieuwenhuis, 1982), the 4th International Conference on Gas in Marine Sediments (Varnes, Bulgaria, 1996), Natural Gas Hydrates (Toulouse, 1996), a MAST/ESF sponsored Gas Hydrate Workshop (Gent Belgium, 1996), a Tsunami Society workshop on Gas Hydrates (Honolulu, 2001).

<sup>6</sup> Additional publications characterizing the slides and debris flows of continental margins include: Stanley and Swift (1976); Bouma *et al.* (1978), Doyle and Pikey (1979), Piper *et al.* (1985); Bugge *et al.* (1987); Kenyon (1987); Aksu and Hiscott (1989); Holder and Bishnoi (2000).

suggested that submarine deposition was influenced by eustasy, particularly low stands of sea level. Contrastingly, Day (personal communications) relates major Canary Island collapses, such as Las Playas and Icod (Tenerife) and El Golfo (El Hierro) to the warmer and wetter phases that characterize periods of post-glacial warming. Lomoschitz *et al.* (2002) suggest periodic landslide activity in the Barranco de Tirajana basin, Gran Canaria, took place during the interglacial when wet and humid climate existed. Hurlimann *et al.* (2001) examined volcanic residual soils and report them as potential slip surfaces and conclude that regional tectonics and climate have a significant influence on the spatial distribution of landslides. Ablay and Hurlimann (2000) conclude that post-shield building landsliding on Tenerife correlate with major sea level falls.

#### 6.4. The Hawaiian Islands and Climate Change

Although almost 70 giant landslides have been identified around the Hawaiian Islands (Moore *et al.*, 1994), with additional landslides reported by Moore and Clague (2002) their ages are poorly constrained. The best age data currently available applies to the Alika 2 submarine landslide, sourced on Hawaii Island (Moore *et al.*, 1999), which McMurtry *et al.* (1999) have dated using a range of methods. Based upon the mean sedimentation rate and the layer thickness of overlying pelagic clay in two cores (extracted less than 1 km from the toe of the landslide), they estimate the age of collapse at  $112 \pm 15$  ky and  $125 \pm 24$  ka. A maximum age of  $127 \pm 5$  ky is estimated from oxygen isotopes analyses from entrained foraminifera in the upper (layer 1) turbidite.

McMurtry *et al.* (1999) also propose a “ball-park” age of 200–250 ka for the earlier Alika 1 collapse, and on the basis of the dates, propose that such giant Hawaiian landslides occurred during warm, wet phases of the Quaternary. As a possible collapse trigger mechanism they suggest that increased ground-water intrusion may lead to more frequent phreatomagmatic eruptions from shallow magma reservoirs. They also make the point that if the trigger is related to increased precipitation, rather than large variations in sea level or other climate-related factors characteristic of the Quaternary, then any future switch to a wetter climate—due, for example to contemporary global warming—might be sufficient to induce future failures. In this context, Nunn (1997, 1999, 2000) reviewed evidence for environmental effects on Pacific islands that provides an insight into how climate change may affect oceanic islands. According to Nunn (2000), during the transition from the Little Climatic Optimum (Medieval Warm Period), a warm period between about 1200 and 700 cal yr BP and the Little Ice Age, a cool, dry period about 600–100 cal yr BP, sea level dropped (possibly in two stages) between 680 and 476 cal yr (AD 1270–1475), the temperature fell by

roughly  $1.5^{\circ}$  (oxygen-isotope analysis), and there was an increase in El Nino frequency (increased precipitation, evidence by increased upland erosion and lowland sedimentation). According to the IPCC 3rd Assessment Report, climate change over the next 100 years is likely to be far more rapid.

### 6.5. Age Dating Correlations

Given the paucity of dates relating to collapses in volcanic archipelagos and around continental margins, and the poor constraints placed upon those few dates that are available (Fig. 14), it is inevitable that at present the link between climate change and ocean basin landslides remains tentative. During the Quaternary, when changes in climate are also accompanied by enormous redistributions of

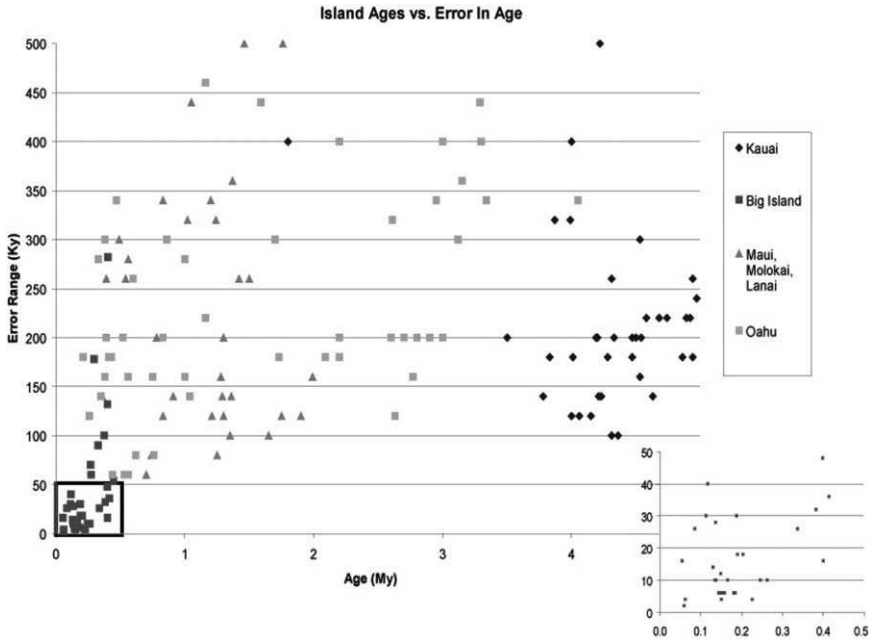


FIG. 14. A plot of the radiometric ages for Hawaiian Islands versus the error range (range + and - in thousand years). The radiometric dates are included in a Summary of Radiometric Ages from the Pacific, IOC Technical Series, v. 32, 1-67, UNESCO, Paris, 1987, compiled by B. H. Keating. A revision of the radiometric age summary for the Hawaiian Islands is underway. The youngest dates, all from subaerial lavas (lower left), have been enlarged in an inset (lower right). With the exception of those ages shown in the inset, the error bars are so large as to preclude assignment to a specific Marine Isotope Stage onset or termination.

planetary water, which themselves may be capable of triggering instability and collapse in oceanic environments, determining a precise mechanistic link is always going to be difficult, if based upon age correlation alone. A summary of the attempts that have been made to accurately and precisely date landslide events in the Hawaiian Islands gives some idea of the problems that are encountered generally in dating large, ancient, collapses in oceanic environments.

Giant flank collapses of the Hawaiian volcanoes have been estimated to occur every 25–100 ky (Lipman *et al.*, 1988, Normark *et al.*, 1993). Normark *et al.* (1993, p. 192) reasoned, in a rather roundabout manner, that since the output of lava by the Hawaiian hot spot is  $0.1 \text{ km}^3/\text{yr}$  (Swanson, 1972) and an average large debris avalanche has a volume of  $1000 \text{ km}^3$ , and then the average periodicity for major landslide events should be 100 ky.

The Wailau debris avalanche (north part of E. Molokai Volcano) was allocated (Normark *et al.*, 1993) an estimated age of 1.4 million years, based upon an age extrapolated for a 1.3 km deep terrace, and assuming the subsidence rate of Molokai is comparable to northern Hawaii. (This may or may not be correct since Molokai is much further away from the hot spot, which is the focus of the lithospheric flexure. And, the degree of lithospheric flexure is greater from the much larger island of Hawaii than the small Molokai Island.) This extrapolation yields an age of 1.17 My. To constrain the maximum age, Normark *et al.* (1993) cite a radiometric age of 1.50 My for the end of the shield building stage of the East Molokai volcano. The northern (failed flank) of Molokai is shown in an aerial view in Fig. 15.

In order to establish an age for the Alike landslide, Normark *et al.* (1993) reasoned “the general youth and location of the Alike phase-2 debris avalanche (fig. 2; Normark *et al.*, 1993) make this mass-movement event the most likely to have caused the 105,000-year-old wave deposits that have been documented on Lanai...”. On Lanai, Moore and Moore (1984) report an uranium series age of 110 ka from Veeh reported by Stearns (1973), combined with three additional determinations of 108, 101, and 134 ka (mathematical average of 112 ka) yet cite an age of the rocks of 105 ka. Deposits on Lanai have subsequently produced a series of ages (Rubin *et al.*, 2000) inconsistent with a single giant wave event and sedimentary evidence indicates the Lanai deposits are associated with island uplift not a giant tsunami (Grigg and Jones, 1997; Felton *et al.*, 2000; Keating and Helsley, 2002). In the Hawaiian Islands and elsewhere, a wide range of approaches have been used to temporally constrain edifice failure, including:

- Dating the youngest lava flows cut by the headwall fault.
- Determining absolute ages for volcanic or carbonate (maximum ages) clasts within the resulting debris deposits.



FIG. 15. Aerial view of the northern (failed flank) of Molokai. The low volcanic peninsula (at the center of the image) is a constructional feature post-dating the edifice failure.

- Dating sediments overlying collapse-related debris deposits on the basis of deposition rates (minimum ages) or a paleomagnetic polarity reversal stratigraphy (if they are older than the last geomagnetic reversal).

At Hawaii, each of these potential means of dating collapses has proved problematical. As at Mauna Loa (Lipman, 1995), headwalls are rapidly buried by continued eruptive activity and therefore become inaccessible. Volcanic clasts in the collapse deposits are often highly altered and as such are poor candidates for conventional radiometric dating. Furthermore, as the depth of the sea floor around the Hawaiian Islands at 4500–5400 m lies below the CCD, coral clasts from the island slopes that reach the sea floor undergo dissolution and recrystallization making them only rarely suitable for Uranium series dating. Sedimentation rates around the Hawaiian Islands vary considerably, and McMurtry *et al.* (1999) report that in the vicinity of the Alika (Phase 2) debris avalanche rates show a 1000-fold range from 1.3 mm/ka to 1.4 m/ka. This is a reflection of the variety of potential inputs into sediment accumulations on debris units, including variable numbers and thicknesses of ash deposits, contributions from subsequent slope failures, regional sedimentation derived from long-term aerosol fallout from the Asian continent, biogenic sedimentation.

Constraining ages on the basis of a dating single grains is always risky, but one of the two age estimates for the Alika II landslide was a maximum age of  $127 \pm 5$  ka estimated from oxygen isotopes results from an entrained foraminifera in the turbidite (McMurtry *et al.*, 1999). Single grains are liable to lab or shipboard contaminations are possible and particularly close to the toe of a turbidite unit can easily be eroded from an underlying unit. Gee *et al.* (1999, 2001a,b) show evidence of dramatic erosional processes associated with the passage of debris flows and turbidity currents on the seafloor on the flank of the Canary Islands. Schmincke and Segsneider (1998) describe ocean drilling results from the flank collapse deposits of the Gran Canaria volcanic apron that provide strong evidence for erosion of soft sediments and incorporation of pre-existing planktonic foraminifera into the basal units of the debris flows. This is likely to be accomplished during turbidite emplacement, during which—for the Canary Basin—organic and volcanic turbidites are shown to have eroded the upper few tens of meters of the sediment column (Weaver, 1994). Weaver *et al.* (1998) also point out that age determinations based upon microfossils are likely to be no more accurate than 50–500 ka based on the accuracy and length of well-established last occurrences marking biostratigraphic zonation boundaries.

Around Hawaii, paleomagnetic dating is hindered by the diagenetic alteration of pelagic red clays, which is so severe that the original magnetization has been altered as post-depositional magnetic grains formed within the sediments (Karlín and Levi, 1983, 1985; Karlín *et al.*, 1987). Helsley (1993) examined the magnetics of ODP Leg 136, located southeast of the Hawaiian islands (on the sea floor outside the Hawaiian Arch). Here the last 400 ka of the stratigraphic record had been removed by turbidity current erosion, and a stable paleomagnetic record was preserved only back to paleomagnetic chron C5. At deeper levels in the hole, the magnetic record was destroyed by diagenetic alteration. Robinson and Sahota (2000) examined the diagenesis in turbiditic sediments from the Madeira Abyssal Plain. They report that magnetic changes occur with an initial stage of suboxic (reductive) diagenesis, following depletion of pore water oxygen and later oxidative diagenesis associated with the slow descent of an oxidation front through the sediment. Weaver *et al.* (1998) describe the progressive development of post-oxic and sulfate-reducing conditions from drilling results on the Madeira Abyssal Plain. Since the magnetic signature of sediments overlying collapse deposits is altered by diagenesis, the direction and polarity will be post-depositional, and therefore indicative of some time younger than the slope failure event.

One potential means of establishing age constraints on turbidites around Hawaii and other volcanic archipelagos would be to undertake radiometric dating on inter-bedded ashes. Garcia (2001, personal communications) indicates this technique has not been tried around the Hawaiian Islands and points out that some of the ashes in Leg 136 drill cores are fresh in appearance and well preserved. Ashes are distributed up to 928 km from the islands (Reim and Halbach, 1982) and as such could provide a valuable tool in developing a much improved collapse stratigraphy for Hawaii. A study of submarine ashes off Réunion Island, Indian Ocean (Fretzdorff *et al.*, 2000) has proven to be a reliable means of dating the main explosive events known from onshore studies.

Even where dates are available, contrasting interpretations by different groups of scientists may result in disagreement about the age of a collapse event. On the Canary Island of El Hierro, for example, Masson (1996) proposed that the El Golfo collapse occurred between 13 and 17 ka BP, based upon correlation of the debris avalanche deposits found on the Madeira Abyssal Plain. To the north of the island turbidite layer "b" (Weaver *et al.*, 1992), which they associate with the collapse, occurs at the boundary between pelagic sediments deposited between oxygen isotope stages 1 and 2 (Urgeles *et al.*, 1997) and dated as 9–15 or 10–17 ka. On shore, however, geologists

noted erosional features indicative of a long period of post-collapse erosion prior to the emplacement of lavas that partially fill the collapse embayment (Carracedo *et al.*, 1999). They also observe multiple generations of scree at the foot of embayment cliffs and perched on the cliffs. There is a K–Ar age difference of 110 ky between lavas present at the top of the El Golfo cliffs and those on the floor of the embayment. Bore holes within the floor of the embayment reveal the presence of an abrasion platform (up to 1.5 km wide) formed in pre-collapse lavas and buried beneath the young lava sequence (Bravo, 1982). It has been inferred that this abrasion surface formed when sea level was close to or above current sea level, during the last interglacial around 100–130 ka BP. This suggests that the formation of El Golfo is much older and provides an argument for its formation during a low sea level stand or during a subsequent rise in sea level (Carracedo *et al.*, 1999).

Day *et al.* (1999a) report that although available age data for giant lateral collapses and associated submarine debris avalanches and mega-turbidites in the Quaternary are limited, there appears to be a consistent link between landslide formation and warmer, more humid, interglacial and interstadial periods. It should be recognized that firm establishment of such a connection must await the arrival of better constrained age data (Day *et al.*, 2000a). During the past 300,000 years, the Earth has experienced three major sea-level oscillations of up to 130 m (Shackleton, 1987), accompanied by complex, dramatic, and global patterns of climate change. Without both more accurate and more precise age assignments for slope failures in the oceanic environment it will continue to be impossible to verify (i) whether or not there is a robust link between environmental change and increased landslide formation, and (ii) whether any such correlation is related to direct changes in climate or to stress variations and other factors relating to sea-level variations. Furthermore, any climatic or proxy-climatic effect may only be a modulating one, superimposed upon a steady background incidence of collapse resulting from dynamic triggers, making it even more difficult to categorically establish any link.

#### 6.6. Arguments for Climate Correlations: Rainfall and Landslides

It has long been known that sub-aerial landslides follow periods of high rainfall (e.g., Terzaghi, 1923, 1943, 1950), and theoretical models examining destabilization associated with steady water flow are reported by Hodge and Freeze (1977) and Iverson and Major (1986). Destabilization associated with

more transient rainfall and recharge has also been described in numerous publications.<sup>7</sup>

On the Hawaiian island of Oahu, several historic landslides have occurred after heavy rainfall. During November 2000, heavy rains (65 cm in 48 h) on the Hilo side of the island of Hawaii, produced 38 landslides that cut the circum-island highway, and caused damage totaling \$23 million US\$. A measurable change in GPS measurements on the SE coast of the island has been observed (Segall, 2001, personal communications, Cervelli *et al.*, 2002), not associated with recorded seismic activity. The event represented an equivalent moment magnitude of 5.7 with a maximum slip velocity of about 6 cm/day, 36 h duration, and is interpreted to have resulted from increased pore pressures along the detachment of the Hilina slump.

Periods of high rainfall do correspond with periods of increased sub-aerial slope failures (see primary references summarized by Iverson, 1986). Clearly extreme storms, strong El Nino effects, and shifts in North Pacific Decadal Oscillations do change the frequency of sub-aerial landslides (Slosson and Larson, 1996; Cannon *et al.*, 1998).

It might thus be reasonable to hypothesize that the largest numbers of volcanic edifice failures around the Hawaiian Islands should be located adjacent to the areas of highest rainfall. To test this hypothesis the rainfall distribution (Rainfall Atlas of Hawaii, 1976; incorporating all Hawaiian rainfall records from 1881 to 1976, Schroeder, 2003, personal communications) was compared (Fig. 16) with the distribution of edifice slope failures around the island (Moore *et al.*, 1989). On the island of Hawaii (the youngest volcanic island in the chain and the center of active volcanism) the greatest rainfall occurs west of Hilo, with in excess of 6 m/yr. Two other loci of activity occur over Kohala Volcano on the northern peninsula where more than 4 m/yr is recorded, and on the slopes of Mauna Loa volcano, above the south shore, where in excess of 3 m/yr of rain is reported.

<sup>7</sup> Fisher (1971); Hutchinson and Bhandari (1971); Williams and Guy (1973); Swanson (1972); Campbell (1975); Pomeroy (1980); Hollingsworth and Kovacs (1981); Leach and Herbert (1982); Kenney and Lau (1984); Sangrey *et al.* (1984); Eyles (1985); Dietrich *et al.* (1986); Chen (1987); Church and Miles (1987); Clark (1987); Iverson and Major (1987); Neary and Swift (1987); Ryan (1988); Einsele (1991); de Campos *et al.* (1992); Diez *et al.* (1996); Diez *et al.* (1999); Iverson (2000); Swanston *et al.* (2003). Groundwater flow and slope failure potential is explored by Iverson and Reid (1992) and Reid and Iverson (1992). Anderson and Sitar (1995) discuss rainfall-induced debris flows. A positive correlation between wet periods and landslide activity has been reported by Pierson *et al.* (1992), Trauth and Strecker (1999) and Pederson *et al.* (2000). Likewise, Iverson *et al.* (1997) suggest that the most important hydrologic distinction between slopes that never fail and those that mobilize to form debris flows is the high water content.

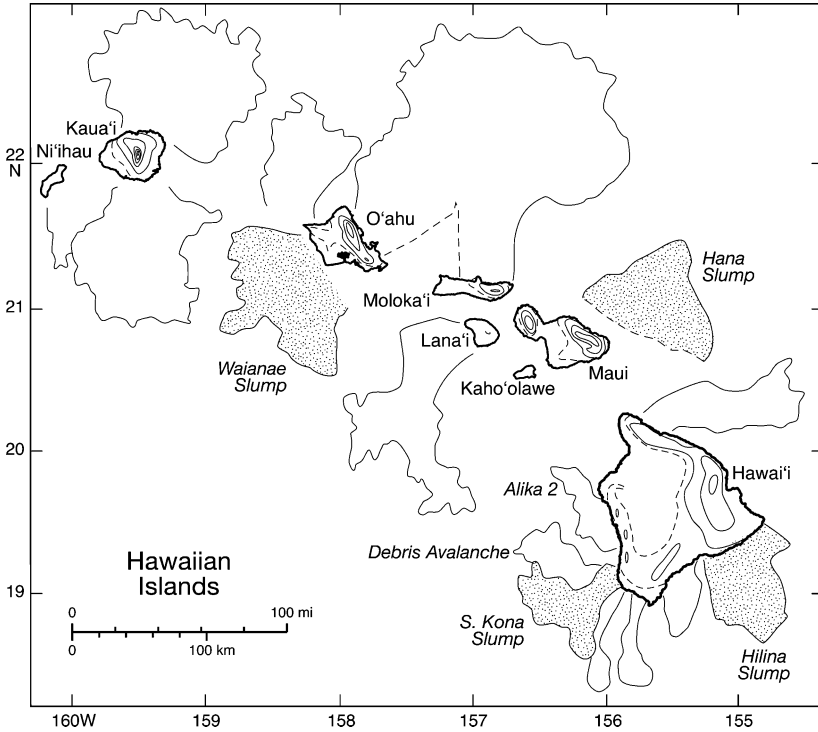


FIG. 16. Map of the main Hawaiian islands showing the mean annual rainfall (1 m contours, in thin solid lines) and locations of slope failures. The rainfall record is based upon observations reported in the Rainfall Atlas of Hawaii (1976). The large slumps (hatched patterns and the debris avalanche deposits outlined by thick solid lines) are after Moore *et al.* (1989). The slumps and debris avalanches occur equally along both the wet and dry sides of the islands.

The next highest rainfall occur on the west slope of Mauna Loa volcano, where recorded values are in excess of 2 m/yr.

With over 6 m/yr of precipitation one would expect to see a concentration of landslides off Hilo, where none are mapped. Smith *et al.* (2002) mapped the Laupahoehoe and Pololu slumps off the east coast of Kohala volcano. The largest number is concentrated on the relatively dry Kona coast as well as the SE segment of the island off the Kilauea volcano coastline and the dry SW coastline. Rainfall is heaviest off the NE flanks of Maui (in excess of 7 m/yr) and Lanai (1 m/yr) and the N side of Molokai (4 m/yr) yet the largest number of landslide debris fields is situated on the S side of the islands. Recent mapping (Eakins and Robinson, 2002)

has identified a Hana slump and Pololu slumps. The large slope failure on the north side of Molokai is the Wailau landslide (Moore and Clague, 2002). On Oahu, rainfall is concentrated over the two volcanic ridges of the Waianae Volcano (west, shown in Fig. 16) and the Koolau Volcano (E. Oahu shown in Fig. 19) with 7 m/yr. Both debris avalanches and slumps are present along both coasts (Moore and Clague, 2002). Kauai, a circular volcano has its rainfall concentrated near the center of the island (with in excess of 11 m/yr, the wettest spot on earth) yet the edifice collapse debris field is concentrated north and south. The heavy rainfall on the peak of Kauai very likely influences stresses on the distal flanks.

An alternate hypothesis might argue that catastrophic debris avalanches should be concentrated in areas of high rainfall and the slower moving slumps would be associated with dry areas. This, however, also fails to explain the edifice collapse distribution, as slumps are equally likely to occur off dry coasts as those characterized by heavy rainfall (Fig. 17). Rainfall does assist landslides failures through seepage along faults and fractures.

During the late 1990–2001 period, the Hawaiian islands have experienced drought conditions, which—perhaps surprisingly—has been associated with increased sub-aerial landslide activity (Public Works, 2000). Jones *et al.* (1984) describe a large (2.5 million m<sup>3</sup>) sub-aerial rock avalanche on the island of Kauai that was not obviously associated with a precipitation event. Rock avalanches are

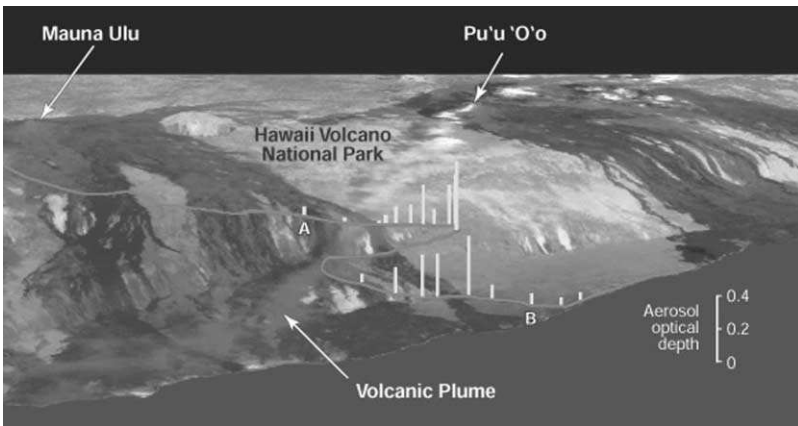


FIG. 17. Shaded relief map of SE Hawaii with lava flows draped upon the topography. The step in the volcanic terrain is the Hilana fault system. The highly reflective lava flows extruded since 1983 appear black and drape over the fault system. At the center of the image is the aerosol plume that originates near Pu'u'u'O'o vent field (Cover Page *Geophys. Res. Lett.*, **29**, 16 from Porter *et al.*, 2002).

known to occur in dry climates, and the characteristics of such events are described by Yarnold (1993).

While these historical incidents represent relatively small and surficial failures, they paint a picture of island slope failures occurring both during wet times and dry times, and having very different failure modes, which may be extended to large edifice failure events. To do this, however, we need to look at climatic patterns and meteorological conditions prevailing at the time of major prehistoric collapse. This topic is strongly debated in the meteorology, paleoclimate, and paleoenvironment communities, with consensus continually changing. The past distribution of rainfall across the islands, *at the time of the collapse needs to be analyzed*. Inevitably, this will require accurate dating of each collapse event and consideration of the prevailing climate in the Pacific Ocean.

## 7. CONCLUSIONS

Keating and McGuire (2000) reviewed island edifice failures and associated tsunamis, showing that evidence for volcanic edifice failures is abundant and continues to grow. Kroenke (2001, personal communications) has completed numerous side-scan sonar surveys for communications cable routes across the Pacific Basin and reports that edifice failures on islands and seamounts are so numerous that it is difficult to miss them. These observations include large-scale sector collapse as well as small landslides and slumps. Kroenke's contention is supported by a study of the shapes of atolls by Stoddart (1950) that showed that only 5 of 99 atolls studied display a circular ring reef. The remaining 94 display polygonal shapes characterized by large, concave bays or linear margins, respectively, and readily explainable in terms of landslide scars and fault scarps. The preponderance of marginal cusps or bays suggests that the number of ancient landslides yet to be mapped on and around atolls and ocean islands is likely to be very large and consequently indicative of frequent slope failures. Cusps and bays far outnumber linear margins, which may indicate that many edifice failures begin with a normal fault at the headwall but are modified as continued retrograde slope failures occur at the margins of the failure, transforming a linear headwall (e.g., the south flank of Johnson Atoll) into a bay. Voight *et al.* (1983), Voight and Elsworth (1997) and Voight (2000) all observe that volcano edifice failure is commonly retrogressive.

As observation brings to light more and more examples of volcanic edifice failure, so further work will be needed in terms of cataloguing and quantifying the characteristics of these important geological events. Increased sampling from the deep sea through cruises aimed at ground-truth sampling and deep ocean drilling

will further improve our knowledge of edifice failures. Similarly crucial, studies aimed at producing reliable dates to constrain the ages of collapse events will significantly improve our knowledge of the frequency of edifice failure, allowing closer examination of proposed links with climate change and a better assessment of the potential tsunami threat.

A comprehensive review of the literature, comparing earthquake rupture duration vs. landslide duration (i.e., transport processes recorded from seismic signals, breakage of communication cables, etc.) would be welcome.

Given the ubiquity of landslides in the marine environment, a critical focus of future study must be improved risk assessment. Cruden and Fell (1997) compiled an edited proceedings volume of an International Workshop on Landslide Assessment that incorporated step-by-step approaches to risk assessment with examples. Dai *et al.* (2002) provide an overview of landslide risk management for sub-aerial landslides. Refice and Capolongo (2002) discuss probabilistic modeling of uncertainties in sub-aerial earthquake-induced landslides. Ward (2001) has represented the principal ingredients of a probabilistic hazard assessment for landslide and tsunami modeling for Hawaii, Norway, and the eastern seaboard of the United States, while Rikitake and Aida (1988) examined tsunami hazard probability in Japan. Small landslides and slips along the south flank of Kilauea volcano have produced some of the largest earthquakes in the history of the islands, generating tsunamis that resulted in deaths and injuries and millions of dollars in property damage. The latest event, a Richter magnitude 7.2 earthquake in 1975, triggered a tsunami with a maximum run-up height of 16 m (at Keauhou Landing), which killed two people and injured 13 others, causing US\$4 million of damage.

If vertical and horizontal slip of a few meters along the Hilina Fault Zone (Fig. 18) can produce such damage, a number of important risk-related questions must be posed: what would be the consequences of a larger displacement or even complete failure of the southern side of the Hilina Fault? How large and how extensive would be the resulting tsunami and what—if any—would be the impact on the one million plus population of Honolulu? Similar questions need to be asked about the threat posed by future collapses on the potentially unstable flanks of other volcanic ocean islands, including Reunion Island's Grand Brulée, the east flank of Pico de Fogo (Cape Verdes) or the western slope of Cumbre Vieja Volcano (La Palma, Canary Islands), and probably others yet to be identified. The critical issue in assessing the future tsunami threat arising from a major collapse of a volcanic island into the ocean appears to be whether or not such a point-source event can generate very large tsunami capable of run-up heights of tens of meters at distances of thousands of kilometers. As previously mentioned, models for the future collapse of the Cumbre Vieja volcano on La Palma output run-up heights along the eastern US that range from 3 m (Mader, 2001a,b) to tens

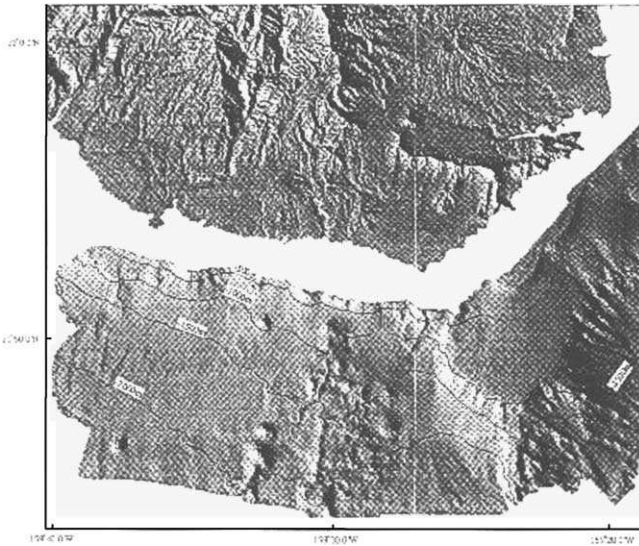


FIG. 18. Shaded relief image of the southern half of the island of Kauai, Hawaii (top half of image) produced from an US Geological Survey image draped on bathymetry offshore. The shallow submarine slope adjacent to the coastline was not imaged thus there is a gap between the two data sets. The constructional gently sloping submarine volcanic margin (lower right) is intact while a hummocky debris flow (failed slope) is evident (at center, bottom).

of meters (Ward and Day, 2001). More recently, Ward and Day (2003) successfully modeled the parameters of the lethal tsunami that resulted from the collapse of the Ritter Island volcano (Papua New Guinea) in 1888 (Johnson, 1987). Such models are likely, however, to continue to give disparate results as they are particularly sensitive to input parameters such as volume, velocity, and the material properties of the landslide. Clearly, the entry of a strongly disaggregated mass into the sea will yield tsunamis with characteristics very different from those generated by a block-slide. Similarly, a slow rupture and displacement vs. a rapid collapse will produce a different tsunami response. To date, most studies have focused on rapid-failure, block slides, for which there is evidence in the geological record (e.g., Day *et al.*, 1997). For completeness, particularly in terms of risk assessment, future studies should address the range of potential collapse scenarios (Fig. 19). A serious assessment of the future risk posed by giant landslides in the submarine environment will only become possible following resolution of the “mega-tsunami” debate and with the

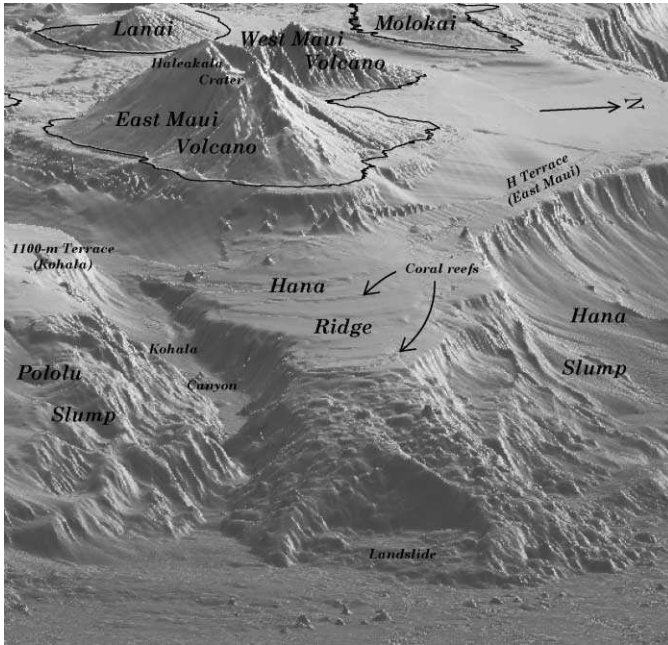


FIG. 19. Shaded relief map showing the digital terrain model for the islands of Lanai, Molokai, and Maui combined with bathymetric models of the seafloor surrounding the islands (map kindly provided by Barry Eakins of the Volcanic Hazards Team of the US Geological Survey). In the lower right corner of the image the large Hana Slump forms a step in the lower slope of the island. This slump block failed but remained largely intact. In the bottom, center, a landslide lies on the extension of the Hana Ridge. The failed material is strongly disaggregated and forms a hummocky pile of debris at the foot of the stop. The Pololu Slump (bottom, left) forms an irregular series of steps that block the Kohala Canyon.

acquisition of far more data on the nature and frequency–size distribution of past collapse events. Only then, will we be able to realistically and soberly address the ensuing risk issues facing communities living on volcanic islands and around the margins of the major ocean basins.

Note: Since this manuscript was submitted several new publications have become available. Readers interested in the topic of landslides and tsunami should review: Yalciner *et al.* (2003), Bardet *et al.* (2003), and Tappin (2004).

Each of these volumes contains numerous papers of interest. We would also recommend that readers review the study relating climate change and landslides with related age dating by Young and Brand (2004).

## ACKNOWLEDGEMENTS

We would like to thank Loren Kroenke, Don Thomas, Mike Garcia, Greg Moore, for examining portions of the manuscript and providing helpful discussions. Review comment by S. Day, and two anonymous reviewers proved extremely helpful in improving the manuscript. Comments from Julia Morgan, Jim Moore, Charles Mader and others have also allowed us to improve the text. Comments by Anne Felton aided in clarifying and shortening the text. Support for this research was provided by the University of Hawaii Sea Grant Program and the Commission of the European Communities DG XII Environmental Programme, Climatology and Natural Hazards Unit. This manuscript is SOEST Contribution #6163.

## REFERENCES

- Abegg, F., and Anderson, A. L. (1997). The acoustic turbid layer in muddy sediments of Eckernfoerde Bay, Western Baltic, methane concentration, saturation and bubble concentration. *Mar. Geol.* **137**, 137–147.
- Ablay, G., and Hurlimann, M. (2000). Evolution of the north flank of Tenerife by recurrent giant landslides. *J. Volcanol. Geotherm. Res.* **113**, 135–159.
- Aksu, A. E., and Hiscott, R. N. (1989). Slides and debris flows on the high-latitude continental slopes of Baffin Bay. *Geology* **17**, 885–888.
- Aksu, A. E., and Hiscott, R. N. (1992). Shingled quaternary debris flow lenses on the north-east Newfoundland Slope. *Sedimentology* **39**, 193–206.
- Albertao, G. A., and Martins, P. P. (1996). A possible tsunami deposit at the Cretaceous–Tertiary boundary in Brazil. *Sediment. Geol.* **104**(1), 189–201.
- Anders, A. M., and Beget, J. E. (1999). Giant landslides and coeval tsunamis in lower Cook Inlet, Alaska. *Geol. Soc. Am. Abstr. Program* **31**(7), 48.
- Anderson, S. A., and Sitar, N. (1995). Analysis of rainfall-induced debris flows. *J. Geotech. Eng.* **121**(7), 544–552.
- Arattano, M., and Marchi, L. (2000). Video-derived velocity distribution along a debris flow surge. *Phys. Chem. Earth, Part B: Hydrol., Oceans Atmos.* **25**(9), 781–784.
- Armanini, A., Michiue, M., eds. (1997). “Recent Developments on Debris Flows.” Springer, Tokyo, pp. 1–226.
- Ashi, J. (1999). Large submarine-landslides associated with decomposition of gas hydrate. *Landslide News* **12**, 17–20 (University of Tokyo Geological Institute, Japan).
- Assier-Rzadkiewicz, S., Heinrich, P., Sabetier, P. C., Savoye, B., and Bourillet, J. F. (2000). Numerical modelling of a landslide-generated tsunami: the 1979 nice event. *Pure Appl. Geophys.* **157**(10), 1707–1727.
- Bachelery, P., Labazuy, P., and Lenat, J. F. (1996). Avalanches de debris sousmarines et subaeriennes a la Reunion. *Comptes Rendus Series II, Sci. de la Terra et des Planetes* **323**(6), 475–482.
- Bardet, J.-P., Synolakis, C. E., Davies, H. L., Imamura, F., and Okal, E. A., eds. (2003). “Landslide Tsunamis: Recent Findings and Research Directions.” Springer-Birkhäuser, Boston, MA.
- Barger, K. E., and Jackson, E. D. (1974). Calculated volumes of individual shield volcanoes along the Hawaiian-Emperor Chain. *J. Res. US Geol. Surv.* **2**(5), 545–550.
- Baylis, S. A., Cawley, S. J., Clayton, C. J., and Savell, M. A. (1997). The origin of unusual gas seeps from onshore Papua New Guinea. *Mar. Geol.* **137**(1–2), 109–120.

- Ben-Menahem, A., and Rosenman, M. (1972). Amplitude patterns of tsunami waves from submarine earthquakes. *J. Geophys. Res.* **17**, 3097–3128.
- Berger, W. H., and Johnson, T. C. (1976). Deep-sea carbonates: dissolution and mass wasting on Ontong-Java Plateau. *Science* **192**, 785–787.
- Biscontin, G., Pestana, J. M., Nadim, F., and Anderson, K. (2004). Seismic triggering of submarine landslides in soft cohesive soil deposits. *Mar. Geol.* **203(3–4)**, 341–354.
- Bjelm, L., and Svensson, C. (1982). *Geophysical investigation on Ilha do Fogo* (including a proposal for geothermal drilling program) Unpublished report, University of Lund, Sweden (cited by Elsworth and Day, 1999).
- Blanchon, P., and Shaw, J. (1995). Reef drowning during the last glaciation: evidence for catastrophic sea level rise and ice-sheet collapse. *Geology* **23**, 4–8.
- Blois-Heulin, C., Belzung, C., and Iverson, R. M. (1995). Can magma-injection and groundwater forces cause massive landslides on Hawaiian volcanoes. *J. Volcanol. Geotherm. Res.* **66**, 295–308.
- Boe, R., Hovland, M., Instanes, A., Rise, L., and Vasshus, S. (2000). Submarine slide scars and mass movements in Karmsundet and Skudenesfjorden, southwestern Norway, morphology and evolution. *Mar. Geol.* **167**, 147–165.
- Bohannon, R. G., and Gardner, J. V. (2004). Submarine landslides of San Pedro Sea Valley, southwest of Long Beach California. *Mar. Geol.* **203(3–4)**, 261–268.
- Bondevik, S. O., Svendsen, J. I., Johnson, G., Mangerud, J., and Kaland, P. E. (1997). The Storegga tsunami along the Norwegian coast, its age and runup. *Boreas* **26(1)**, 29–53.
- Borrero, J., Dolan, J., and Synolakis, C. E. (2001). Tsunami sources within the Eastern Santa Barbara Channel. *Geophys. Res. Lett.* **28**, 643–647.
- Bouma, A. H., Moore, G. T., and Coleman, J. M. (1978). Framework, facies and oil trapping characteristics of the upper continental margin. *Am. Assoc. Pet. Geol. Stud. Geol.* **7**, 1–326.
- Bourgeois, J., Hansen, T. A., Wiberg, T. A., and Kauffman, E. G. (1988). A tsunami deposit at the Cretaceous–Tertiary boundary in Texas. *Science* **241**, 567–570.
- Bralower, T. J., Paul, C. K., and Leckie, R. M. (1998). The Cretaceous–Tertiary boundary cocktail; Chicxulub impact tsunami triggers margin collapse and extensive sediment gravity flows. *Geology* **26(4)**, 331–334.
- Bravo, T. (1982). Formations geológicas en las isla de El Hierro. Inst. Estudios Cnaries Aula Cultura Cabido Insular de Tenerife. 50 Annivers. pp. 85–99.
- Bray, J. R. (1976). Volcanic triggering of glaciation. *Nature* **260**, 414–415.
- Bray, J. R. (1977). Pleistocene volcanism and glacial initiation. *Science* **197**, 251–254.
- Brunsdon, D., and Prior, D. B. (1984). “Slope Instability.” Wiley, New York, pp. 1–441.
- Bugge, T., Befring, S., Belderson, R. H., Eidven, T., Jansen, E., Kenyon, N. H., Holtedahl, H., and Sejrup, H. P. (1987). A giant three-stage submarine slide off Norway. *Geo-Mar. Lett.* **7**, 191–198.
- Campbell, R. H. (1975). Soil slips, debris flows, and rainstorms in the Santa Monica Mountains and vicinity, southern California. *US Geol. Surv. Prof. Paper* **851**, 1–51.
- Campbell, J. K., and Kroenke, L. W. (1994). “Drowned Barrier Reefs and Lagoons South of Molokai and West of Lanai, 1:100,000.” Hawaii Seafloor Atlas. University of Hawaii, Honolulu, Sheet 8.
- Campbell, B. A., and Nottingham, D. (1999). Anatomy of a landslide-created tsunami at Skagway Alaska: November 3, 1994. *Sci. Tsunami Haz.* **19**, 19–47.
- Cannon, S. H., Ellen, S. D., Graham, S. E., Graymor, R. W., Hampton, M. A., Hillhouse, J. W., Howell, D. G., Jayko, A. S., LaHusen, R. L., Lajoie, K. R., Pile, R. J., Ramsey, D. W., Reid, M. E.,

- Richmond, B. M., Savage, W. Z., Wentworth, C. M., and Wilson, R. C. (1998). Slope failure and shoreline retreat during Northern California's latest El Nino. *GSA Today* **8**(8), 1–6.
- Cannon, E. C., Burgmann, R., and Owen, S. E. (2001). Shallow normal faulting and block rotation associated with the 1975 Kalapana Earthquake, Kilauea Volcano, Hawaii. *Bull. Seismol. Soc. Am.* **91**, 1553–1562.
- Caplan-Auerbach, Fox, C. G., and Duennebieer, F. K. (2001). Hydroacoustic detection of submarine landslides on Kilauea volcano. *Geophys. Res. Lett.* **28**(9), 1811–1813.
- Carracedo, J. C., Day, S. J., Guillou, H., and Torrado, J. P. (1999). Giant Quaternary landslides in the evolution of La Palma and El Hierro, Canary islands. *J. Volcanol. Geotherm. Res.* **94**, 169–190.
- Cas, R. A., and Wright, J. V. (1987). "Volcanic successions." Allen & Unwin, London, pp. 1–528.
- Cervelli, P., Segall, P., Johnson, K., Lisowski, M., and Milklius, A. (2002). Sudden aseismic fault slip on the south flank of Kilauea volcano. *Nature* **415**, 1014–1018.
- Chaudhry, H., Mercer, A. G., and Cass, D. (1983). Modeling of slide-generated waves in a reservoir. *J. Hydr. Eng. ASCE* **109**(11), 1505–1520.
- Chen, C.-L. (1987). Comprehensive review of debris flow modeling concepts in Japan. *Geol. Soc. Am. Rev. Eng. Geol.* **7**, 13–29.
- Chen, J. K., Tanylor, F. W., Edwards, R. L., Cheng, H., and Burr, G. S. (1995). Recurrent emerged reef terraces of Yenkahe Resurgent Block Tanna Vanuatu: implications for volcanic, landslide and tsunami hazards. *J. Geol.* **103**, 577–590.
- Chiang, W. L., Divorky, D., Parnicky, P., and Wier, W. (1981). "Numerical Model of Landslide-Generated Waves." Tetra tech Report T-3427. US Department of Commerce, Pasadena, CA, (cited by Heinrich, 1992).
- Church, M., and Miles, M. J. (1987). Meteorological antecedents to debris flows in southwestern British Columbia; some case studies. *Geol. Soc. Am. Rev. Eng.* **7**, 63–79.
- Clague, D. A., Moore, J. G., and Davis, A. S. (2002). Formation of volcanic breccia and hyaloclastite in landslide blocks from the Wailau and Nuuanu Giant Landslides, Hawaii. In "Evolution of Hawaiian Volcanoes: Recent Progress in Deep Underwater Research" (E. Takahashi, P. Lipman, M. Garcia, J. Naka, and S. Aramaki, eds.), American Geophysical Union Monograph **128**, pp. 279–296.
- Clark, G. M. (1987). Debris slide and debris flow historical events in the Appalachians south of the glacial border, reviews in engineering geology. "Debris Flows/Avalanches, Process, Recognition, and Mitigation" (J. E. Costa, and G. F. Wieczorek, eds.), Vol. VII. Geological Society of America, Boulder, CO, pp. 125–138.
- Cleary, P. W., and Campbell, C. S. (1993). Self-lubrication for long runout landslides examination by computer simulation. *J. Geophys. Res.* **98**(B12), 21911–21924.
- Clouard, V., Bonneville, A., and Gilot, P.-Y. (2001). A giant landslide on the southern flank of Tahiti Island, French Polynesia. *Geophys. Res. Lett.* **28**(11), 2253–2256.
- Cochonat, P., Lenat, L. F., Bachelary, P., Boivin, P., Cornaglia, B., Deneil, C., Labazny, P., LeDrezen, E., Lipman, P., Ollier, G., Savoye, B., Vincent, P., and Voisset, M. (1990). Importance des depots gravitaires dans la mise en place d'un systeme volcano-sedimentaire sous-marin (Volcano de la Fournaise, Ilde de la Reunion). *Compute Rendu Acad. Sci.* **311**(Ser. II), 679–686.
- Collinson, J. D., and Thompson, D. B. (1982). "Sedimentary Structures." Allen & Unwin, London, pp. 1–146.
- Cook, H. E., Jenkyns, H. C., and Kelts, K. R. (1976). Sedimentary stratigraphic framework along the Line Islands, equatorial Pacific. *Int. Rep. DSDP* **33**, 849–853.

- Costa, J. E. (1984). Physical geomorphology of debris flows. In "Developments and Applications of Geomorphology" (J. E. Costa, and P. J. Fleisher, eds.). Springer, Berlin, pp. 268–317.
- Costa, J. E., Wiczorek, G. F., eds. (1987). "Debris Flows/Avalanches: Process, Recognition, and Mitigation." Reviews in Engineering Geology 7. Geological Society of America, Boulder, CO, pp. 1–239.
- Costa, J. E., and Williams, G. P. (1984). Debris flow dynamics (videotape). US Geol. Surv. Open File Rep. 84-6606 (22.5 min).
- Coudray, J., Mairine, P., Nicolini, E., and Clerc, J. M. (1990). Approche Hydrogeologique. In "Le volcanisme de La Reunion" (J. F. Lenat, ed.). Publ. Centre de recherches Volcanologiques, Clermont, Ferrand, France, pp. 307–356.
- Coulbourn, W. T., Keating, B. H., Helsley, C. E., and Reed, T. B. (1991). "Machias Seamount, Western Samoa, SeaMARC II Side Scan Sonar Imagery, Bathymetry, Geology, 1:250,000." Pacific Seafloor Atlas. University of Hawaii, Honolulu, HI, Sheet, 22.
- Coussot, P., and Meunier, M. (1996). Recognition and mechanical description of debris flows. *Earth Sci. Rev.* **40**, 209–227.
- Coussot, R., and Piau, J.-M. (1996). The effects of an addition of force-free particles on the rheological properties of fine suspensions. *Int. J. Rock Mech. Min. Sci. Geomech. Abstr.* **33(3)**, 106A.
- Cruden, D. M., and Fell, R. (1997). "Landslide risk assessment." Proceedings of the International Workshop on Landslide Risk Assessment. Balkema, Rotterdam, pp. 1–371.
- Cruden, D. M., and Varnes, D. J. (1996). Landslide types and processes. In "Landslides Investigation and Mitigation." National Academy Press, Washington, DC, pp. 36–75.
- Dade, W. B., and Huppert, H. E. (1998). Long runout rockfalls. *Geology* **26(9)**, 803–806.
- Dai, F. C., Lee, C. F., and Ngal, Y. Y. (2002). Landslide risk assessment and management: an overview. *Eng. Geol.* **64**, 65–87.
- Davies, T. R. H. (1986). Large debris flows: a macro-viscous phenomenon. *Acta Mech.* **63**, 161–178.
- Davies, T. R. H. (1990). Debris-flow surges—experimental simulation. *J. Hydrol. (NZ)* **29**, 18–46.
- Dawson, A. G., and Shi, S. (2000). Tsunami deposits. *Pure Appl. Geophys.* **157(6–8)**, 875.
- Day, S. J. (1996). Hydrothermal pore fluid pressure and the stability of porous, permeable volcanoes. In "Volcano Instability on the Earth and other Planets" (W. J. McGuire, A. P. Jones, and J. Newberg, eds.), Special Publication 110. Geological Society, London, pp. 77–93.
- Day, S. J., Carracedo, J. C., and Guillou, H. (1997). Age and geometry of an aborted rift flank collapse, the San Andres fault system, El Hierro, Canary Islands. *Geol. Mag.* **134(4)**, 523–537.
- Day, S. J., Carracedo, J. C., Guillou, H., and Gravestock, P. (1999a). Recent structural evolution of the Cumbre Vieja volcano, La Palma, Canary Islands: volcanic rift zone reconfiguration as a precursor to volcano flank instability? *J. Volcanol. Geotherm. Res.* **94**, 135–167.
- Day, S. J., McGuire, W. J., Elsworth, D., Carracedo, J. C., and Guillou, H. (1999b). Do giant collapses of volcanoes tend to occur in warm, wet, interglacial periods and if so, why? *Abstract volume, IUGG XXII General Assembly, Birmingham, UK* 174.
- Day, S. J., Heleno de Silva, S. I. N., and Fonseca, J. F. B. D. (1999c). A past giant lateral collapse and present day flank instability of Fogo, Cape Verde Islands. *J. Volcanol. Geotherm. Res.* **94**, 191–218.
- Day, S. J., Watts, P., Fryer, G. J., and Smith, J. R. (2000a). Alternative styles of deformation of the south flank of Kilauea volcano: implications for possible precursors to a future tsunamigenic flank collapse. *EOS, Trans. Am. Geophys. Union* **81(48)**, 749, Session OS24.

- Day, S. J., Elsworth, D., and Maslin, M. (2000b). A possible connection between sea surface temperature variations, orographic rainfall patterns, water table fluctuations and giant lateral collapses of oceanic island volcanoes. Abstract volume, WP251, Western Pacific Geophys. Meet., Tokyo.
- de Campos, M. P., Andrade, M. H. N., and Vargas, E. A. Jr. (1992). "Undersaturated colluvium over rock slide in a forested site in Rio de Janeiro, Brazil." Proceedings of the 6th International Symposium on Landslides. Balkema, Brookfield, VT, pp. 1357–1364.
- Denlinger, R. P., and Iverson, R. M. (1990). Limiting equilibrium, and liquefaction potential in infinite submarine slopes. *Mar. Geotech.* **9**, 299–312.
- Denlinger, R. P., and Iverson, R. M. (2001). Flow of variability fluidized granular masses across three-dimensional terrain 2. Numerical predictions and experimental tests. *J. Geophys. Res.* **106(B1)**, 553–566.
- Denness, B., ed. (1984). "Seabed Mechanics." Graham & Trotman, London, pp. 1–284.
- Dent, J. D., and Lang, T. E. (1983). A biviscous modified Bingham model of snow avalanche motions. *Ann. Glaciol.* **4**, 42–46.
- DePaolo, D. J., Stolper, E., and Thomas, D. M. (2001). Deep drilling into a Hawaiian volcano. *EOS, Trans. Am. Geophys. Union* **82(13)**, 149–155.
- Descloitres, M., Ritz, M., and Mourgues, P. (1995). TDEM soundings for locating aquifers inside the Caldeira of Fogo active volcano, Cape Verde Islands. *Proc. Environ. Eng. Geophys. Soc. Eur. Sec., Environ. Eng. Geophys., Torino, Italy*, 25–27/9/1995, pp. 110–114.
- Devey, C. W., Hekinian, R., Ackerman, D., Binard, N., Francke, B., Hemond, C., Kapsimalis, V., Lorenc, S., Maia, M., Moller, H., Perrot, K., Pracht, J., Rogers, T., Statterger, K., Steinke, S., and Victor, P. (1997). The Foundation Seamount Chain, a first survey and sampling. *Mar. Geol.* **137**, 191–200.
- Dietrich, W., Wilson, C., and Reneau, S. (1986). "Hollows, colluvium and landslides in soil mantled landscapes." Hillslope Processes. Allen & Unwin, Boston, Chapter 17, pp. 362–388.
- Diez, A. G., Salas, L., de Taran, J. R., and Cendrero, A. (1996). Late Quaternary climate change and mass movement frequency and magnitude in the Cantabrian region, Spain. *Geomorphology* **15**, 291–309.
- Diez, A. G., Remondo, J., De Teran, J. R. D., and Cendrero, A. (1999). A morphological approach for the analysis of the temporal occurrence and triggering factors of landslide. *Geomorphology* **30**, 95–113.
- Dott, R. H. (1963). Dynamics of subaqueous gravity depositional processes. *Bull. Am. Petrol. Geol.* **47**, 104–128.
- Doyle, L. J., and Pikey, O. H. (1979). Geology of continental slope. *Soc. Econ. Paleont. Mineral. Spec. Publ.* **27**, 1–374.
- Driscoll, N. W., Weissel, J. K., and Goff, J. A. (2000). Potential for large-scale submarine failure and tsunami generation along the U.S. mid-Atlantic coast. *Geology* **29(5)**, 407–411.
- Eakins, B. W., and Robinson, J. E. (2002). Multibeam Bathymetry of Haleakala Volcano, Maui. In "Eos. Trans. Am. Geophys. Un." Fall Mtg Schedule, T62A-1294 Poster.
- Edgers, L., and Karlsrud, K. (1982). "Soil Flows Generated by Submarine Slides: Case Studies and Consequences." Publication 143. Norway Geotechnical Institute, Oslo, pp. 1–10.
- Edwards, B. D., Lee, H. J., and Field, M. E. (1993). Seismically induced mudflow in Santa Barbara Basin, CA. In "Submarine Landslides, Selected Studies of the US Exclusive Economic Zone" (W. C. Schwab, H. J. Lee, and D. C. Twitchell, eds.), US Geol. Surv. Bull. 2002, pp. 167–175.
- Egorov, O. Yu., and Osipenko, A. B. (1999). Submarine landslide processes in the canyons of the northern part of Kamchatka Bay, East Kamchatka. *Oceanology* **39(4)**, 550–557.

- Einsele, G. (1991). Submarine mass flow deposits and turbidites. In "Cycles and Events in Stratigraphy" (G. Einsele, W. Ricken, and A. Seilacher, eds.). Springer, New York, pp. 313–339.
- Eissler, H. K., and Kanamori, H. (1987). A single-force model for the 1975 Kalapan, Hawaii, earthquake. *J. Geophys. Res.* **92(B6)**, 4827–4836.
- Elsworth, D., and Day, S. J. (1999). Flank collapse triggered by intrusion: the Canarian and Cape Verde archipelagoes. *J. Volcanol. Geotherm. Res.* **94**, 323–340.
- Elsworth, D., and Voight, B. (1995). Dike intrusion as a trigger for large earthquakes and the failure of volcano flanks. *J. Geophys. Res.* **100(B4)**, 6005–6024.
- Embley, R. W. (1976). New evidence for the occurrence of debris flow deposits in the deep sea. *Geology* **4**, 371–374.
- Embley, R. W. (1980). The role of mass transport in the distribution and character of deep-ocean sediments with special reference to the North Atlantic. *Mar. Geol.* **38(1–3)**, 23–50.
- Embley, R. W. (1982). Anatomy of some Atlantic Margin sediment slides and some comments on ages and mechanisms. In "Marine Slides and other Mass Movements" (S. Saxov, and J. K. Nieuwenhuis, eds.). Plenum Press, New York, pp. 189–213.
- Embley, R. W., and Jacobi, R. D. (1977). Distribution and morphology of large submarine sediment slides and slumps on Atlantic continental margins. *Mar. Geotech., Mar. Slope Stability* **2**, 205–228.
- Erishman, T. H., and Abele, G. (2001). "Dynamics of Rockslides and Rockfalls." Springer, Berlin, pp. 1–316.
- Evans, D., King, E. L., Kenyon, N. H., Brett, C., and Wallis, D. (1996). Evidence for long-term instability in the Storegga Slide region off western Norway. *Mar. Geol.* **130**, 281–292.
- Eyles, G. O. (1985). "The New Zealand Land Resource Inventory Erosion Classification." Water and Soil Miscellaneous Publication 85. Soil Conservation Centre, Ministry of Works and Development, Aokautere, Wellington, (cited by Anderson and Sitar, 1995).
- Eyles, C. H., and Lagoe, M. B. (1998). Slump-generated megachannels in the Pliocene–Pleistocene glaciomarine Yakataga Formation, Gulf of Alaska. *Geol. Soc. Am. Bull.* **110(3)**, 395–408.
- Felix, M. (2002). Flow structure of turbidity currents. *Sedimentology* **49(3)**, 397–419.
- Felton, E. A., Crook, K. A. W., and Keating, B. H. (2000). The Hulopoe Gravel, Lanai, Hawaii: new sedimentological data and their bearing on the "Giant Wave" (Mega-Tsunami) emplacement hypothesis. *Pure Appl. Geophys.* **157**, 1257–1284.
- Field, M. E., and Barber, J. H. Jr. (1993). A submarine landslide associated with shallow gas and gas hydrates off Northern California. In "Submarine Landslides: Selected Studies in the U.S. Exclusive Economic Zone" (W. C. Schwab, H. J. Lee, and D. C. Twichell, eds.), US Geol. Surv. Bull. 2002, pp. 151–157.
- Filmer, P. E., McNutt, M. K., Webb, H. F., and Dixon, D. J. (1994). Volcanism and archipelagic aprons in the Marquesas and Hawaiian Islands. *Mar. Geophys. Res.* **16**, 385–406.
- Fisher, R. V. (1971). Features of coarse-grained, high concentrations fluids and their deposits. *J. Sediment. Petrol.* **41**, 916–927.
- Frederico, V. D. (1999). Free-surface flow of hyperconcentrations. *Fluid Dyn. Res.* **24(1)**, 23–26.
- Fretzdorff, S., Paterne, M., Stoffers, P., and Ivanova, E. (2000). Explosive activity of the Reunion island volcanoes through the past 260,000 years as recorded in deep-sea sediments. *Bull. Volcanol.* **62**, 266–277.
- Fritz, H. M., Hager, W. H., and Minor, H.-E. (2001). Lituya Bay Case: rockslide impact and wave run-up. *Sci. Tsunami Haz.* **19(1)**, 3–22.

- Fryer, G. J., and Watts, P. (2000). The 1946 Unimak tsunami: near source modeling confirms a landslide. *EOS, Trans. Am. Geophys. Union* **81(48)**, 748.
- Fryer, G. J., Watts, P., and Pratson, L. F. (2004). Source of the great tsunami of 1 April 1946: a landslide in the upper Aleutian forarc. *Mar. Geol.* **203(3-4)**, 201–218.
- Funck, T., and Lykke-Andersen, H. (1998a). Comparison of seismic reflection data to a synthetic seismogram in a volcanic apron at Site 953. *Proc. ODP, Sci. Rep.* **157**, 3–10.
- Funck, T., and Lykke-Andersen, H. (1998b). Seismic structure of the volcanic apron north of Gran Canaria. *Proc. ODP, Sci. Rep.* **157**, 11–28.
- Funck, T., and Schmincke, H.-U. (1998). Growth and destruction of Gran Canaria deduced from seismic reflection and bathymetric data. *J. Geophys. Res.* **103(B7)**, 15393–15407.
- Garcia, M. O. (1996). Turbidites from slope failure on Hawaiian volcanoes. In “Volcano Instability on the Earth and Other Planets” (W. J. McGuire, A. P. Jones, and J. Newberg, eds.), Special Publication 110. Geological Society, London, pp. 284–292.
- Gardner-Taggart, J. M., and Barminski, R. F. Jr. (1991). Short period wave generation in Moss Landing Harbor caused by offshore landslides induced by the Loma Prieta earthquake. *Geophys. Res. Lett.* **18(7)**, 1277–1280.
- Gee, M. J. R., Masson, D. G., Watts, A. B., and Allen, P. A. (1999). The Saharan debris flow: an insight into the mechanics of long runout debris flows. *Sedimentology* **46**, 317–335.
- Gee, M. J. R., Masson, D. G., Watts, A. B., and Mitchell, N. C. (2001a). Passage of debris currents through a topographic constriction: seafloor erosion and deflection of flow pathways. *Sedimentology* **48**, 1389–1409.
- Gee, M. J. R., Watts, A. B., Masson, D. G., and Mitchell, N. C. (2001b). Landslides and the evolution of El Hierro in the Canary Islands. *Mar. Geol.* **177**, 271–293.
- Geisslinger, A., Hirscheleber, H. B., Schnaubelt, M., Danobeitia, J. J., and Gallart, J. (1996). Mapping the volcanic apron and the upper crust between Gran Canaria and Tenerife (Canary Islands) with seismic profiling. *Geo-Mar. Lett.* **16**, 57–64.
- Geist, E. L. (1998). Local tsunamis and earthquake source parameters. *Adv. Geophys.* **39**, 117–209.
- Geist, E. L. (2000). Origin of the 17 July 1998 Papua New Guinea tsunami: earthquake or landslide? *Seismol. Res. Lett.* **71(3)**, 344–351.
- Geist, E. L. (2001). Reply to comment by E.A. Okal and C.E. Synolakis on “Origin of the 17 July 1998 Papua New Guinea tsunami: earthquake or landslide?” by E.L. Geist”. *Seismol. Res. Lett.* **72(3)**, 367–372.
- Goguel, J. (1978). Scale-dependent rockslide mechanisms, with emphasis on the role of pore fluid vaporation. In “Rockslides and Avalanches. 1. Natural Phenomena” (B. Voight, ed.). Elsevier, Amsterdam, pp. 693–705.
- Goldfinger, C., Kulm, L. D., McNeill, L. C., and Watts, P. (2000). Super-scale failure of the southern Oregon Cascadia margin. *Pure Appl. Geophys.* **157**, 1189–1226.
- Goldfinger, C., Johnson, J. F., and Nelson, C. H. (2002). “Is there a connection between subduction zone earthquakes, submarine landslides and the destabilization of gas hydrates on the central Oregon margin?” Abstracts with Program, Second Tsunami Symposium, May 28–30. The Tsunami Society, Honolulu, unpaginated.
- Goldstrand, P. M. (1998). Provenance and sedimentologic variations of turbidite and slump deposits at Sites 955 and 956. *Proc. ODP, Sci. Res.* **157**, 343–356.
- Gozali, S., and Hunt, B. (1989). Water waves generated by close landslides. *J. Hydr. Res.* **27(1)**, 49–60.
- Grigg, R., and Jones, A. T. (1997). Uplift caused by lithospheric flexure in the Hawaiian Archipelago as revealed by elevated coral deposits. *Mar. Geol.* **141**, 11–25.

- Grilli, S. T., and Watts, P. (1999). Modeling of waves generated by a moving submerged body. Applications to underwater landslides. *Eng. Anal. Bound. Elem.* **23**(8), 645–656.
- Grilli, S. T., and Watts, P. (2002). Development of a 3D numerical wave tank for modeling tsunami generation by underwater landslides. *Eng. Anal. Bound. Elem.* **26**(4), 301–313.
- Grilli, S. T., Vogelmann, S., and Watts, P. (2002). Landslide tsunami prediction in a numerical wave tank. *Ocean Wave Meas. Anal.* **26**(4), 1495–1514.
- Gutenberg, B. (1939). Tsunamis and earthquakes. *Bull. Seismol. Soc. Am.* **29**, 517–526.
- Hall, K. (1982). Rapid deglaciation as an inhibitor of volcanic activity: an hypothesis. *Earth Surf. Proc. Landforms* **7**, 45–51.
- Hampton, M. A. (1972). The role of subaqueous debris flows in generating turbidity currents. *J. Sediment. Petrol.* **42**(4), 775–793.
- Hampton, M. A., Lee, H. J., and Locat, J. (1996). Submarine landslides. *Rev. Geophys.* **34**(1), 33–59.
- Harbitz, C. B. (1992). Model simulations of tsunamis generated by the Storegga slides. *Mar. Geol.* **105**, 1–21.
- Hart, S. R., Staudigel, H., Koppers, A. A. P., Blusztajun, J., Baker, E. T., Workman, R., Jackson, M., Hauri, E., Kurz, M., Sims, K., Fornari, D., Saal, A., and Lyons, S. (2000). Vailulu'u undersea volcano: the New Samoa. *Geochem. Geophys. Geosyst.* **1**, 1–16.
- Hasegawa, H. S., and Kanamori, H. (1987). Source earthquake mechanism of the magnitude of November 1929: double couple or submarine landslide? *Bull. Seismol. Soc. Am.* **77**(6), 1984–2004.
- Hawkins, A. B. (1984). "Introduction, submarine slope failures." *Seabed Mechanics*. Graham & Trotman, London, pp. 51–64.
- Hayashi, J. N., and Self, S. (1992). A comparison of pyroclastic flow and debris avalanche mobility. *J. Geophys. Res.* **97**(B6), 9063–9071.
- Hearty, P. J. (1997). Boulder deposits from large waves during the last interglaciation on north Eleuthera Island, Bahamas. *Quat. Res.* **48**, 326–338.
- Hearty, P. J., Conrad Neumann, A., and Kaufman, D. S. (1998). Chevron ridges and runup deposits in the Bahamas from storms late in oxygen-isotope substage 5e. *Quat. Res.* **50**, 309–322.
- Heinrich, P. (1991). Nonlinear numerical model of landslide-generated water waves. *Int. J. Eng. Fluid Mech.* **4**(4), 403–416.
- Heinrich, P. (1992). Nonlinear water waves generated by submarine and aerial landslides. *J. Wtrwy, Port, Coast. Ocean Eng. ASCE* **118**(3), 249–266.
- Heinrich, P., Mangeney, A., Guibourg, S., Roche, R., Boudon, G., and Cheminee, J.-L. (1998). Simulation of water waves generated by a potential debris avalanche in Montserrat, Lesser Antilles. *Geophys. Res. Lett.* **25**, 3697–3700.
- Heinrich, P., Piatanesi, A., Okal, E., and Hebert, H. (2000). Near-field modeling of the July 17, 1998 tsunami in Papua New Guinea. *Geophys. Res. Lett.* **27**(19), 3037–3040.
- Heinrich, Ph., Piatanesi, A., and Hebert, H. (2001). Numerical modeling of tsunami generation and propagation from submarine slumps. The 1998 Papua New Guinea event. *Geophys. J. Int.* **145**(1), 97–111.
- Helsley, C. E. (1993). Paleomagnetic results from Leg 136. *Proc. ODP, Sci. Res.* **136**, 45–52.
- Helsley, C. E. (2002). "Gas hydrates on the Chatham Rise, New Zealand, and their potential of tsunami generation." Abstracts with Program, Second Tsunami Symposium, May 28–30. The Tsunami Society, Honolulu, unpaginated.
- Hidayat, D., Barker, J. S., and Satake, K. (1995). Seismic source and tsunami generation. *Pure Appl. Geophys.* **144**(3–4), 537.

- Hildebrand, A. R., and Boynton, W. V. (1990). Proximal Cretaceous–Tertiary boundary impact deposits in the Caribbean. *Science* **248**, 843–847.
- Hildenbrand, T. G., Rosenbaum, J. G., and Kauahikaua, J. P. (1993). Aeromagnetic survey of the island of Hawaii. *J. Geophys. Res. B* **98(3)**, 4099–4119.
- Hill, P. J., and Tiffin, D. L. (1991). Marine geology and geophysics of the Western Samoan Exclusive Economic Zone, results of Gloria, SeaMARC II and other shipboard studies. *SOPAC Tech. Rep.* **135**, 1–28.
- Hillaire-Marcel, C., Occhietti, S., and Vincent, J.-S. (1981). Sakami moraine, Quebec: a 500 km long moraine without climate control. *Geology* **9**, 210–214.
- Hills, D. J., Morgan, J. K., Moore, G. F., and Leslie, S. C. (2002). Structural variability along submarine south flank of Kilauea Volcano, Hawaii. In “Hawaiian Volcanoes, Deep Undersea Perspectives” (E. Takahashi, P. W. Lipman, M. O. Garcia, J. Naka, and S. Aramaki, eds.). American Geophysical Union Monograph 128, Washington, DC, pp. 105–124.
- Hodge, R. A. L., and Freeze, R. A. (1977). Groundwater flow systems and slope stability. *Ca. Geotech. J.* **14**, 466–476.
- Holcomb, R. T., and Searle, R. C. (1991). Large landslides from oceanic volcanoes. *Mar. Geotech.* **10**, 19–32.
- Holder, G. D., and Bishnoi, P. R. (2000). Gas hydrates challenges for the future. *Ann. NY Acad. Sci.* **912**, 1–224.
- Hollingsworth, R., and Kovacs, G. S. (1981). Soil slumps and debris flows, prediction and protection. *Bull. Assoc. Eng. Geol.* **18**, 17–28.
- Hotta, N., and Ohita, T. (2000). Pore-water pressure of debris flows. *Phys. Chem. Earth, Part B, Hydrol., Oceans Atmos.* **25(4)**, 381–385.
- Howard, K. (1973). Avalanche mode of motion, implications from lunar examples. *Science* **108**, 1052–1055.
- Hsu, K. J. (1975). Catastrophic debris streams (sturzstroms) generated by rockfalls. *Geol. Soc. Am. Bull.* **86**, 129–140.
- Huang, X., and Garcia, M. H. (1999). Modeling of non-hydroplaning mudflows on continental slopes. *Mar. Geol.* **154**, 131–142.
- Hubl, J., and Steinwendtner, H. (2000). Estimation of rheological properties of viscous debris flow using a belt conveyor. *Phys. Chem. Earth, Part B, Hydrol., Oceans Atmos.* **25(9)**, 751–755.
- Hungr, O., Morgan, G. C., and Kellerhals, R. (1984). Quantitative analysis of debris torrent hazards for design of remedial measures. *Can. Geotech. J.* **23**, 115–126.
- Hunt, C. D. Jr. (1997). “Geohydrology of the Island of Oahu, Hawaii.” US Geol. Surv. Monogr. P1412B, pp. B1–B54.
- Hunt, C. D., Ewart, C. J. Jr., and Voss, C. I. (1988). Region 27, Hawaiian Islands. In “Hydrogeology—The Geology of North America, Vol. 2” (W. Black, J. S. Rosensheim, and P. R. Seabar, eds.). Geological Society of America, Boulder, CO, USA, pp. 255–262.
- Hurlimann, M. (1999). “Geotechnical Analysis of Large Volcanic Landslides. The La Orotava Events of Tenerife, Canary Islands” (Ph.D. thesis), Technical University of Catalonia (UPC), Barcelona, pp. 1–220 (cited in Hurlimann *et al.*, 2000).
- Hurlimann, N., Ledesma, A., and Marti, J. (1999). Conditions favoring catastrophic landslides on volcanoes. *Terra Nova* **11**, 106–111.
- Hurlimann, M., Garcia-Pierrra, J. O., and Ledesma, A. (2000). Causes and mobility of large landslides, application to Tenerife, Canary Islands. *J. Volcanol. Geotherm. Res.* **103**, 121–134.

- Hurlimann, M., Ledesma, A., and Marti, J. (2001). Characterization of a volcanic residual soil and its implication for large landslide phenomena: application to Tenerife, Canary Islands. *Eng. Geol.* **59**, 115–132.
- Husson, D. (1987). Detailed mapping of submarine geology of Oahu, Hawaii, using Sea Mark S system. *EOS, Trans. Am. Geophys. Union* **68(44)**, 1136.
- Hutchinson, J. N. (1986). A sliding-consolidation model for flow-slides. *Can. Geotech. J.* **21**, 115–126.
- Hutchinson, J. N., and Bhandari, R. K. (1971). Undrained loading, a fundamental mechanism of mudflows and other mass movements. *Geotechnique* **21**, 353–358.
- Imamura, F., and Giga, E. C. (1996). Numerical model for wave generation due to subaqueous landslide along a coast. *Sci. Tsunami Haz.* **14(1)**, 13–28.
- Imamura, F., and Kikuchi, M. (1994). Moment release of the 1992 Flores Island earthquake inferred from tsunami and teleseismic data. *Sci. Tsunami Haz.* **12(2)**, 67–76.
- Imamura, F., Gica, E., Takahashi, T., and Shuto, N. (1995). Numerical simulation of the 1992 Flores tsunami, interpretation of tsunami phenomena in northeastern Flores Island and damage at Babi Island. *Pure Appl. Geophys.* **144(3–4)**, 555–568.
- Imran, J., Parker, G., Locat, J., and Lee, H. (2001). 1D numerical model of muddy subaqueous and subaerial debris flows. *J. Hydr. Eng., ASCE* **12(11)**, 959–968.
- Inaba, H., Itakura, Y., and Kasahara, M. (2000). Surface velocity computation of debris flows by vector field measurements. *Phys. Chem. Earth, Part B, Hydrol., Oceans Atmos.* **25(9)**, 741–744.
- Innes, J. L. (1983). Debris flows. *Prog. Phys. Geogr.* **7**, 469–501.
- Inoue, K. (2000). Shimabara-Shigatusaku earthquake and topographic changes by Shimabara catastrophe in 1792, Masuda, Kooiti (prefacer), Mikami, Takehiko (prefacer), Special issue in honor of Professor Michio Nogami, Geographical Report of Tokyo Metropolitan University, **35**, 59–69.
- Iverson, R. M. (1986). Unsteady, nonuniform landslide motion. 1. Theoretical dynamics and the steady datum state. *J. Geol.* **94(1)**, 1–15.
- Iverson, R. M. (1995). Can magma-injection and groundwater forces cause massive landslides on Hawaiian volcanoes? *J. Volcanol. Geotherm. Res.* **66**, 295–308.
- Iverson, R. M. (1997). The physics of debris flows. *Rev. Geophys.* **35**, 245–296.
- Iverson, R. M. (2000). Landslide triggering by rain infiltration. *Water Resour. Res.* **36(7)**, 1897–1910.
- Iverson, R. M., and Denlinger, R. P. (1987). The physics of debris flows—a conceptual assessment. *Proc. Corvallis Symp. Erosion Sed. Pacific Rim, IAHS Publ.* **165**, 155–165.
- Iverson, R. M., and Denlinger, R. P. (2001). Flow of variability fluidized granular masses across three-dimensional terrain 1. Coulomb mixture theory. *J. Geophys. Res.* **106(B1)**, 537–552.
- Iverson, R. M., and Major, J. J. (1986). Groundwater seepage vectors and the potential for hillslope failure and debris flow mobilization. *Water Resour. Res.* **22**, 111543–111548.
- Iverson, R. M., and Major, J. J. (1987). Rainfall, groundwater flow, and seasonal movement at Minor Creek landslide, northwestern California, physical interpretation of empirical relations. *Geol. Soc. Am. Bull.* **99**, 579–594.
- Iverson, R. M., and Reid, M. E. (1992). Gravity-driven groundwater flow and slope failure potential. 1. Elastic effective-stress model. *Water Resour. Res.* **28(3)**, 925–938.
- Iverson, B. M., and Vallance, W. (2001). New views of granular mass flow. *Geology* **29**, 115–118.
- Iverson, R. M., Costa, J. E., and Lattusen, R. G. (1992). Debris-flow flume at H.J. Andrews experimental forest, Oregon, Water Fact Sheet. US Geol. Surv. Open-File Rep. 92-483.
- Iverson, R. M., Reid, M. E., and LaHusen, R. G. (1997). Debris-flow mobilization from landslides. *Annu. Rev. Earth Planet. Sci.* **25**, 85–138.

- Iverson, R. M., Reid, M. E., Iverson, N. R., LaHusen, R. G., Logan, M., Mann, J. E., and Brien, D. L. (2000). Acute sensitivity of landslide rates to initial-soil porosity. *Science* **290**, 513–516.
- Iwasaki, S. (1982). Experimental study of tsunami generated by a horizontal motion of a sloping bottom. *Bull. Earth Res. Inst.* **57**, 239–262.
- Iwasaki, S. (1987). On the estimation of a tsunami generated by a submarine landslide. *Proc. Int. Tsunami Symp.* 134–138.
- Iwasaki, S. (1997). The waveforms and directivity of a tsunami generated by an earthquake and a landslide. *Sci. Tsunami Haz.* **15**, 23–40.
- Jeffery, S. E. (1981). “Our usual landslide: ubiquitous hazard and socioeconomic causes of natural disaster in Indonesia.” Natural Hazard Research Working Paper Series. Working Paper 40. Institute for Behavioral Science, University of Colorado, Boulder, CO, pp. 1–53.
- Jiang, L., and LeBlond, P. H. (1992). The coupling of a submarine slide and the surface waves which it generates. *J. Geophys. Res.* **97(C8)**, 12731–12744.
- Jiang, L., and LeBlond, P. H. (1993). Numerical modeling of an underwater Bingham plastic mudslide and the waves which it generates. *J. Geophys. Res.* **98(C6)**, 10303–10317.
- Jiang, L., and LeBlond, P. H. (1994). Three-dimensional modeling of tsunami generation due to a submarine slide. *J. Phys. Oceanol.* **24**, 559–573.
- Johnson, R. W. (1987). Large-scale volcanic cone collapse: the 1988 slope failure of Ritter volcano, and other examples from Papua New Guinea. *Bull. Volcanol.* **49**, 669–679.
- Johnson, C., and King, D. (1993). Can a landslide generate a 1000 ft tsunami in Hawaii? *12th Big Island Science Conference*, April 29–May 1, 1993.
- Johnson, C., and Mader, C. L. (1994). Modeling the 105 Ka Lanai tsunami. *Sci. Tsunami Haz.* **12**, 33–36.
- Johnson, A. M., and Rodine, J. R. (1984). “Debris Flow, Slope Instability” (D. Brunsten, and D. B. Prior, eds.). Wiley, New York, pp. 257–361.
- Jones, A. T. (1993). “Elevated Coral Deposits in the Hawaiian Islands: A Measure of Island Uplift in the Quaternary” (Ph.D. thesis), Oceanography Department, University of Hawaii, Honolulu, pp. 1–119.
- Jones, A. T., and Mader, C. L. (1996). Wave erosion on the southeastern coast of Australia: Tsunami propagation modeling. *Aust. J. Earth Sci.* **43**, 479–483.
- Jones, B. L., Chinn, S. S. W., and Brice, J. C. (1984). Okokele rock avalanche, island of Kauai, Hawaii. *Geology* **12**, 209–211.
- Karlin, R., and Levi, S. (1983). Diagenesis of magnetic minerals in recent hemipelagic sediments. *Nature* **303**, 327–330.
- Karlin, R., and Levi, S. (1985). Geochemical and sedimentological control on the magnetic properties of hemipelagic sediments. *J. Geophys. Res.* **90**, 10373–10392.
- Karlin, R., Lyle, M., and Health, G. R. (1987). Authigenic magnetite formation in suboxic marine sediments. *Nature* **326**, 490–493.
- Kawakatsu, H. (1989). Centroid single force inversion of seismic waves generated by landslides. *J. Geophys. Res.* **94(B9)**, 12363–12374.
- Kayen, R. E., and Lee, H. (1993). Slope stability in regions of seafloor gas hydrate: Beaufort Sea continental slope. *US Geol. Surv. Bull. B* **B2002**, 97–103.
- Kayen, R., Scholl, D., Kvenvolden, K. A., and Lee, H. (1988). Global change, gas hydrate, and mass wasting of the continental slope. *Ann. Geophys.* **16(Suppl. 1)**, 297, European Geophysical Society Meeting.

- Kayen, R. E., Schwab, W. C., Lee, H. J., Torresan, M. E., Hein, J. R., Quintero, P. J., and Levin, L. A. (1989). Morphology of sea-floor landslides on Horizon Guyot, application of steady-state geotechnical analysis. *Deep-Sea Res.* **36**(12), 1817–1839.
- Keating, B. H. (1987). Structural failure and drowning of Johnston Atoll, Central Pacific Basin. In “Seamounts, Islands, and Atolls” (B. H. Keating, P. Fryer, R. Batiza, and G. W. Boehlert, eds.). American Geophysical Union Monograph 43, Washington, DC, pp. 49–59.
- Keating, B. H. (1992). Insular geology of the Line islands. In “Geology and Offshore Mineral Resources of the Central Pacific Basin” (B. H. Keating, and B. R. Bolton, eds.), Circum Pacific Energy and Mineral Resources Council, Earth Sciences Series 14. Springer, New York, pp. 127–178.
- Keating, B. H. (1994a). “Johnston Island SeaMARC II side scan sonar imagery, bathymetry, 1:100,000 and three dimensional bathymetric model.” Hawaii Seafloor Atlas. SOEST, University of Hawaii, Honolulu, Hi, Sheet 13, pp. 1–17.
- Keating, B. H. (1994b). “Cross Seamount SeaMARC II side scan sonar imagery and bathymetry, 1:100,000, three dimensional bathymetric model, and seismic reflection profiles.” Hawaii Seafloor Atlas. SOEST, University of Hawaii, Honolulu, Hi, Sheet 14, pp. 1–17.
- Keating, B. H. (1994c). “Karin Ridge SeaMARC II side scan sonar imagery, geology, and seismic reflection profiles 1:100,000.” Hawaii Seafloor Atlas. SOEST, University of Hawaii, Honolulu, Hi, Sheet 15, pp. 1–17.
- Keating, B. H. (1994d). “Hutchinson Seamount SeaMARC II side scan sonar imagery, bathymetry and geology, 1:100,000.” Hawaii Seafloor Atlas. SOEST, University of Hawaii, Honolulu, Hi, Sheet 15, pp. 1–17.
- Keating, B. H. (1996). Side-scan images of submarine landslides on the flanks of atolls and guyots. *Mar. Geodesy* **21**(2), 129–146.
- Keating, B. H. (1997a). “Reactivated volcanism within the Central Pacific Line Islands seamount chain.” Transactions of the Fifth Circum-Pacific Energy Mineral Resources Conference. Gulf Publishing Co., Houston, TX, pp. 320–337.
- Keating, B. H. (1997b). Are the coastal gravels on Lanai tsunami deposits? *Abstracts with Program, Cordilleran Section, Kona, Hawaii*. Unpaginated.
- Keating, B. H. (1998). Nuclear testing in the Pacific from a geologic prospective. In “Climate and Environmental Change in the Pacific” (J. Terry, ed.). University of South Pacific, Fiji, pp. 113–144.
- Keating, B. H. (2002). “Introduction to gas-hydrate and landslide workshop.” Abstracts with Program, Second Tsunami Symposium, May 28–30. The Tsunami Society, Honolulu, unpaginated.
- Keating, B. H., and Helsley, C. E. (2002). Ancient shoreline on Lanai, Hawaii: revisited. *Sediment. Geol.* **150**, 3–15.
- Keating, B. H., and Karogodina, I. (1991a). “Savaii, Western Samoa.” Pacific Seafloor Atlas. University of Hawaii, Honolulu, Sheet 20.
- Keating, B. H., and Karogodina, I. (1991b). “Western Samoa, Submarine Features.” Pacific Seafloor Atlas. University of Hawaii, Honolulu, Sheet 21.
- Keating, B. H., and Karogodina, I. (1994). Savaii, Western Samoa, Submarine Features, SeaMARK II Sidescan Sonar Imagery at Original Scale 1,94,000. In “Pacific Seafloor Atlas.”. University of Hawaii, Honolulu, Sheet No. 21.
- Keating, B. H., and McGuire, W. J. (2000). Island edifice failures and associated tsunami hazards. In “Landslides and Tsunamis” (B. H. Keating, C. F. Waythomas, and A. G. Dawson, eds.). Birkhauser, Boston, pp. 899–956.
- Keating, B. H., Helsley, C. E., DeCarlo, E., McMurtry, M., Pringle, M., Campbell, F., Kroenke, L. M., and Jarvis, P. (1985). “Resource assessment of cobalt rich ferromanganese crusts within the

- Hawaiian Exclusive Economic Zone.” Final Report to Minerals Management Bureau. University of Hawaii, Honolulu, pp. 1–220.
- Keating, B. H., Karogodina, I., and Helsley, C. E. (1994). “West Chapman Seamount, Central Line Islands, Kiribati. SeaMARC II side-scan sonar imagery, bathymetry, and geology, 1:250,000.” Pacific Seafloor Atlas. University of Hawaii, Honolulu, Sheet 23.
- Keating, B. H., Helsley, C. E., and Karogodina, I. (2000). Sonar studies of submarine mass wasting and volcanic structures off Savaii Island, Samoa. *Pure Appl. Geophys.* **157**, 1285–1313.
- Keefer, D. K. (2002). Investigating landslides caused by earthquakes—a historical review. *Surv. Geophys.* **26(3)**, 473–510.
- Kelley, J. T., Dickson, S. M., Belknap, D. F., Barnhardt, W. A., and Henderson, M. (1994). Giant sea-bed pockmarks, evidence for gas escape from Belfast Bay, Maine. *Geology* **22**, 59–62.
- Kennedy, M. J., Christie-Blick, N., and Sohl, L. E. (2001). Are Proterozoic cap carbonates and isotopic excursions a record of gas hydrate destabilization following Earth’s coldest intervals? *Geology* **29(5)**, 443–446.
- Kenney, T. C., and Lau, K. C. (1984). Temporal changes in groundwater pressure in a natural slope of nonfissured clay. *Can. Geotech. J.* **21**, 138–146.
- Kenyon, N. H. (1987). Mass-wasting features on the continental slope of northwest Europe. *Mar. Geol.* **74**, 57–77.
- Kikuchi, M., Yamanaka, Y., and Abe, K. (1997). Source rupture process of the Papua New Guinea earthquake of July 17, 1998 inferred from teleseismic body waves. *Earth Planets Space* **51(12)**, 1319.
- Kikuchi, M., Yamanaka, Y., Abe, K., and Morita, Y. (1999). Source rupture process of the Papua New Guinea earthquake of July 17th, 1998, inferred from teleseismic waves. *Earth Planets Space* **51**, 1319–1324.
- Kilburn, C. R. J., and Sorensen, S.-A. (1998). Runout lengths of sturzstroms: the control of initial conditions and of fragment dynamics. *J. Geophys. Res.* **103(B8)**, 17877–17884.
- King, E., Sejrup, H. P., Hafidason, H., Elverhoi, A., and Aarseth, I. (1996). Quaternary seismic stratigraphy of the North Sea Fan, glacially fed gravity flow aprons, hemipelagic sedimentation, and large submarine slides. *Mar. Geol.* **130**, 293–316.
- Kirwan, A. D. Jr., Doyle, L. J., Bowles, W. D., and Brooks, G. R. (1986). Time-dependent hydrodynamic models of turbidity currents analyzed with data from the Grand Banks and Orleansville events. *J. Sediment. Petrol.* **56(3)**, 379–386.
- Klaus, A., Norris, R. D., Hroon, D., and Smit, J. (2000). Impact-induced mass wasting at the K–T boundary; Blake Nose, western Atlantic. *Geology* **28(4)**, 319–322.
- Kneller, B., and Buckee, A. (2000). The structure and fluid mechanics of turbidity currents: a review of some recent studies and their geological implications. *Sedimentology* **47(Suppl. 1)**, 62–94.
- Kodagali, V. N. (1991). Morphologic investigation of “uncharted” seamount from Central Indian Basin, revisited with multibeam sonar system. *Mar. Geodesy* **15**, 37–46.
- Kodagali, V. N. (1992). Slope angle from multibeam sonar data on three seamounts in central Indian Basin. *Proc. Offshore Tech. Conf.* **24(1)**, 463–470.
- Kodagali, V. N. (1998). A pair of seamount chains in the central Indian Basin, identified from multibeam mapping. *Mar. Geodesy* **21(2)**, 147–158.
- Koerner, H. K. (1977). Flow mechanisms and resistances in the debris streams of rockslides. *Int. Assoc. Eng. Geol. Bull.* **26**, 501–505.
- Kowalik, Z. (1997). Landslide-generated tsunami in Skagway, Alaska. *Sci. Tsunami Haz.* **15**, 89–106.

- Kraft, L. M. Jr., Gavin, T. H., and Bruton, J. C. (1993). Submarine flow slide in Puget Sound. *J. Geotech. Eng., ASCE* **118(10)**, 1577–1592.
- Kramer, S. L. (1988). Triggering of liquefaction flow slides in coastal soil deposits. *Eng. Geol.* **26**, 17–31.
- Krastel, S., Schmincke, H.-U., and Jacobs, C. L. (2001a). Formation of submarine canyons on the flanks of the Canary Islands. *Geo-Mar. Lett.* **20**, 160–167.
- Krastel, S., Schmincke, H.-U., Jacobs, C. L., Rihm, R., LeBas, T. P., and Alibes, B. (2001b). Submarine landslides around the Canary Islands. *J. Geophys. Res.* **106(B3)**, 3977–3997.
- Krue, M. A., Crelling, J. C., Montanari, A., Stankiewicz, B. A., and Bensley, D. F. (1994a). Characterization of organic material in Cretaceous–Tertiary boundary strata, Arroyo el Mimbal, Mexico. *LPI Conf.* **827**, 63–64.
- Krue, M. A., Stankiewicz, B. A., Crelling, J. C., Montanari, A., and Bensley, D. P. (1994b). Fossil charcoal in Cretaceous–Tertiary boundary strata: evidence for catastrophic firestorm and megawave. *Geochim. Cosmochim. Acta* **58**, 1393–1397.
- Kuijpers, A., Nielsen, T., Akhmetzhanov, A., de Haas, H., Kenyon, N. H., and van Weering, T. C. E. (2001). Late Quaternary slope instability on the Faeroe margin: mass flow features and timing of events. *Geo-Mar. Lett.* **20**, 149–159.
- Kulikov, E. A., Rabinovich, A. B., Thomson, R. E., and Bornhold, B. B. (1996). The landslide tsunami of November 3, 1994, Skagway Harbor, Alaska. *J. Geophys. Res.* **101(C3)**, 6609–6615.
- Kulikov, E. A., Rabinovich, A. B., Fain, I. V., Bornhold, B. D., and Thomson, R. E. (1998). Tsunami generation by landslide at the Pacific coast of North America. *Oceanology* **38(3)**, 323–328.
- Labazuy, P. (1996). Recurrent landslide events on the submarine flank of Piton de la Fournaise volcano (Reunion Island). In “Volcano Instability on the Earth and Other Planets” (W. J. McGuire, A. P. Jones, and J. Neuberg, eds.), Special Publication 110. Geological Society, London, pp. 295–306.
- Laberg, J. S., and Vorren, T. O. (1993). A late Pleistocene submarine slide on the Bear Island trough mouth fan. *Geo-Mar. Lett.* **13**, 227–234.
- Lang, T. E., and Dent, J. D. (1983). Evaluation of the fluid dynamic properties of mudflows on Mount St. Helens. Final Report prepared for US Department of the Interior, Bureau of Reclamation, Washington, DC, pp. 1–78.
- Lang, T. E., Dawson, K. L., and Martinelli, M. (1979). Application of numerical transient fluid dynamics to snow avalanche flow, part 1, development of computer program, AVALNCH. *J. Glaciol.* **22**, 107–115.
- Langford, S. A. (1969). “The Surface Morphology of the Tuscaloosa Seamount” (Masters thesis), Geology and Geophysics Department, University of Hawaii, Honolulu, pp. 1–12.
- Leach, B., and Herbert, R. (1982). The genesis of a numerical model for the study of the hydrogeology of a steep hillside in Hong Kong. *Eng. Geol. Quart. J.* **15**, 243–259.
- LeBlond, P. H., and Jones, A. T. (1994). Underwater landslides ineffective at tsunami generation. *Sci. Tsunami Haz.* **13(1)**, 25–26.
- Lee, H. J., and Edwards, B. D. (1986). Regional method to assess offshore slope stability. *J. Geotech. Eng.* **112**, 489–509.
- Lee, S. H., Chough, S. K., Black, G. G., Kim, Y. B., and Sung, B. S. (1999). Gradual downslope change in high-resolution acoustic characters and geometry of large-scale submarine debris lobes in Ulleung Basin, East Sea (Sea of Japan) Korea. *Geo-Mar. Lett.* **19**, 254–261.
- Legros, F. (2002). The mobility of long-runout landslides. *Eng. Geol.* **63(3)**, 301–331.

- Lenat, J.-F., Vincent, P., and Bachelery, P. (1989). The off-shore continuation of an active basaltic volcano, Piton de la Fournaise (Reunion Island, Indian Ocean). *J. Volcanol. Geotherm. Res.* **36**, 1–36.
- Lenat, J.-F., Bachelery, P., Bonneville, A., Galdeano, A., Labazuy, P., Rousset, D., and Vincent, P. (1990). Structure and morphology of the submarine flank of an active basaltic volcano: Piton de la Fournaise (Reunion Island, Indian Ocean). *Oceanol. Acta* **10**, 211–223, (Special volume).
- Leslie, S. C., Moore, G. F., Morgan, J. K., and Hills, D. J. (2002). Seismic stratigraphy of the frontal Hawaiian moat: implications for sedimentary processes at the leading edge of an oceanic hotspot trace. *Mar. Geol.* **184**, 143–162.
- Li, J., Yuan, J., Bi, C., and Luo, D. (1983). The main features of the mudflow in Jiang-Jia Ravine. *Z. Geomorphol.* **27**, 325–341.
- Lipman, P. W. (1995). “Declining growth of Mauna Loa during the last 100,000 years: rates of lava accumulation versus gravitational subsidence.” *Mauna Loa Revealed, Structure, Composition, History and Hazards*. American Geophysical Union Monograph 92, Washington, DC, pp. 45–80.
- Lipman, P., Normark, W., Moore, J., Wilson, J., and Gutmacher, G. (1988). The giant submarine Alika debris slide, Mauna Loa, Hawaii. *J. Geophys. Res.* **93**, 4279–4299.
- Lipman, P. W., Sisson, T., Ui, T., and Naka, J. (2000). Ancestral growth of Kilauea volcano: submarine alkalic through tholeiitic shield-stage development and landsliding on the offshore south flank of Hawaii Island. *Geology* **28**, 1079–1082.
- Lipman, P. W., Sisson, T. W., Ui, T., Naka, J., and Smith, J. R. (2002). Ancestral growth of Kilauea volcano and instability of its south flank. In “Hawaiian Volcanoes, Deep Undersea Perspectives” (E. Takahashi, P. W. Lipman, M. O. Garcia, J. Naka, and S. Aramaki, eds.). American Geophysical Union Monograph 128, Washington, DC, pp. 161–192, CD.
- Locat, J., and Lee, H. J. (2002). Submarine landslides: advances and challenges. *Can. Geotech. J.* **39**, 193–212.
- Locat, J., Lee, H., Locat, P., and Imran, J. (2004). Numerical analysis of the mobility of the Palos Verdes debris avalanche, California, and implications for the generation of tsunamis. *Marine Geology* **203(3-4)**, 269–280.
- Lomoschitz, A., Meco, J., and Corominas, J. (2002). The Barranco de Tirajana basin, Gran Canaria (Spain). A major erosive landform caused by large landslides. *Geomorphology* **42(1)**, 117–130.
- Lonsdale, P. (1982). Sediment drifts in the northeast Atlantic and their relationship to the observed abyssal currents. *Bull. Inst. Geol. Bassin Aquitaine Bordeaux* **31**, 141–150, (cited by Hurlimann *et al.*, 2000).
- Lonsdale, P. (1986). A multibeam reconnaissance of the Tonga Trench axis and the intersection with the Louisville guyot chain. *Mar. Geophys. Res.* **8**, 295–327.
- Lonsdale, P. (1989). A geomorphological reconnaissance of the submarine part of the East Rift zone of Kilauea volcano. *Bull. Volcanol.* **51**, 123–144.
- Lowe, D. R. (1979). Sediment gravity flows, their classification and some problems of application to natural flows and deposits. In “Geology of Continental Slopes” (L. J. Doyle, and O. H. Pikey, eds.), Soc. Econ. Pal. Mineral. Sp. Pub. 27, pp. 75–82.
- Lowe, D. R. (1982). Sediment gravity flows, II. Depositional models with special reference to the deposits of high-density turbidity currents. *J. Sediment. Petrol.* **52**, 279–297.
- Ma, K.-F., Satake, K., and Kanamori, H. (1991). The origin of the tsunami excited by the 1989 Loma Prieta earthquake: faulting, or slumping. *Geophys. Res. Lett.* **18(4)**, 637.
- Ma, K.-F., Kanamori, H., and Satake, K. (1999). Mechanism of the 1975 Kalapana, Hawaii, earthquake inferred from tsunami data. *J. Geophys. Res.* **104**, 13153–13167.

- MacDonald, G. A., Abbot, A. T., and Peterson, F. L. (1983). "Volcanoes in the Sea: The Geology of Hawaii." 2nd ed. University of Hawaii Press, Honolulu, pp. 1–517.
- Mader, C. L. (1984). A landslide model for the 1975 Hawaii tsunami. *Sci. Tsunami Haz.* **2**, 71.
- Mader, C. L. (1997). Modeling the 1994 Skagway tsunami. *Sci. Tsunami Haz.* **15**, 41.
- Mader, C. L. (1999). "Modeling the 1958 Lituya Bay Tsunami." *Science of Tsumani Hazards*, \*Vol. 17, pp. 57–67.
- Mader, C. L. (2001a). Modeling the La Palma landslide tsunami. *Sci. Tsunami Haz.* **19**, 160.
- Mader, C. (2001b). Modeling the 1958 Lituya Bay mega-tsunami. *Sci. Tsunami Haz.* **17**, 57.
- Mader, C. L., and Gitting, M. L. (2002). Modeling the 1958 Lituya Bay mega tsunami. *Sci. Tsunami Haz.* **20**, 241.
- Mader, C. L., Tangora, R. E., and Nichols, B. D. (1982). A model of the 1975 Hawaii tsunami. *Nat. Sci. Haz.* C-1.
- Major, J. J. (1997). Depositional processes in large-scale debris-flow experiments. *J. Geol.* **105**, 345–366.
- Malahoff, A. (1987). Geology of the summit of Loihi submarine volcano. In "Volcanism in Hawaii" (R. W. Decker, T. L. Wright, and P. H. Stauffer, eds.), US Geol. Surv. Prof. Paper 1350, pp. 133–144.
- Mark, R. K., and Moore, J. G. (1987). Slopes of the Hawaiian ridge. In "Volcanism in Hawaii" (R. W. Decker, T. L. Wright, and P. H. Stauffer, eds.), US Geol. Surv. Prof. Paper 1350, pp. 101–108.
- Marr, J. G., Harff, P. A., and Shanumugan, G. (2001). Experiments on subaqueous sandy gravity flows: the role of clay and water content in flow dynamics and depositional structure. *Geol. Soc. Am. Bull.* **113**(11), 1377–1386.
- Martins, V. C. (1988). Preliminary geothermal investigations in Cape Verde. *Geothermics* **17**, 521–530.
- Maslin, M., Mikkelsen, N., Vilela, C., and Haq, B. (1998). Sea-level and gas-hydrate-controlled catastrophic sediment failures of the Amazon Fan. *Geology* **26**, 1107–1110.
- Masson, D. G. (1994). Late Quaternary turbidity current pathways to the Madeira abyssal plain and some constraints on turbidity current mechanisms. *Basin Res.* **6**, 17–33.
- Masson, D. G. (1996). Catastrophic collapse of the flank of El Hierro about 15,000 years ago, and the history of large flank collapses in the Canary Islands. *Geology* **24**, 231–234.
- Masson, D. G., Kidd, R. B., Gardner, J. V., Huggett, Q. J., and Weaver, P. P. E. (1992). Saharan continental rise, facies distribution and sediment slides. In "Geologic Evolution of Atlantic Continental Rises" (C. W. Poag, and P. C. de Graciansky, eds.). Van Nostrand Reinhold, New York, pp. 327–343.
- Masson, D. G., Huggett, Q. J., and Brunnsden, D. (1993). The surface texture of the Saharan debris flow deposit and some speculations on submarine debris flow processes. *Sedimentology* **40**(3), 583–598.
- Masson, D. G., Canals, M., Alonso, B., Urgeles, R., and Huhnerbach, V. (1998). The Canary debris flow, source area morphology and failure mechanisms. *Sedimentology* **45**(2), 411–432.
- Matsuyama, M., Walsh, J. P., and Harry, Y. (1999). The effect of bathymetry on tsunami characterization at Sissano Lagoon, Papua New Guinea. *Geophys. Res. Lett.* **26**, 3513–3516.
- Maurrassee, F. J. M. R., and Sens, G. (1991). Impact tsunami and the Haitian Cretaceous–Tertiary boundary layer. *Science* **252**, 1690–1693.
- Max, M. (2000). Gas hydrates: challenges for the future. *Ann. NY Acad. Sci.* **912**, 1–187.
- Max, M. (2002). "Mass flow in marine sediment: physical causes and possible examples from the geologic record." Abstracts with Program, Second Tsunami Symposium, May 28–30. The Tsunami Society, Honolulu, unpaginated.

- Max, M., Dillon, W. P., Nishimura, C., and Hurdle, B. G. (1999). Sea-floor methane blow-out and global fires storm at the Cretaceous Tertiary boundary. *Geo-Mar. Lett.* **18(4)**, 285–291.
- McAdoo, B. G., and Watts, P. (2004). Tsunami hazard from submarine landslides on the Oregon continental slope. *Mar. Geol.* **203(3/4)**, 235–245.
- McGuire, W. J. (1996). Volcano instability: a review of contemporary themes. In “Volcano Instability on the Earth and Other Planets” (W. J. McGuire, A. P. Jones, and J. Newberg, eds.), Special Publication 110. Geological Society, London, pp. 77–93.
- McGuire, W. J., Howarth, R. J., Firth, C. R., Solow, A. R., Pullen, A. D., and Saunders, S. J. (1997). Correlation between rate of sea-level change and frequency of explosive volcanism in the Mediterranean. *Nature* **389**, 473–476.
- McGuire, B., Mason, I., and Kilburn, C. (2002). “Natural Hazards and Environmental Change.” Oxford University Press, New York, pp. 1–187.
- McLellan, P., and Kaiser, P. K. (1984). “Application of a two-parameter model to rock avalanches of the Mackenzie Mountains.” Proceedings of the 4th International Symposium on Landslides, Toronto, Canada, pp. 559–565.
- McMurtry, G. M., Herrero-Bevera, E., Cremer, M. D., Smith, J. R., Resig, J., Sherman, C., and Torreson, M. E. (1999). Stratigraphic constraints on the timing and emplacement of the Alika 2 giant Hawaiian submarine landslide. *J. Volcanol. Geotherm. Res.* **94**, 35–58.
- Mehl, K. W., and Schmincke, H.-U. (1999). Structure and emplacement of the Pliocene Roque Nublo debris avalanche deposit, Gran Canaria, Spain. *J. Volcanol. Geotherm. Res.* **94(1–4)**, 105–134.
- Melosh, H. J. (1979). Acoustic fluidization, a new geologic process? *J. Geophys. Res.* **84**, 8097–8113.
- Middleton, G. V., and Hampton, M. A. (1973). Sediment gravity flows, mechanics of flow sand deposition. In “Turbidites and Deep Water Sedimentation. Short Course Lecture Notes.” Society of Economic Paleontologists and Mineralogists. Pacific Section, pp. 1–38.
- Middleton, G. V., and Hampton, M. A. (1976). Subaqueous sediment transport and deposition by sediment gravity flows. In “Marine Sediment Transport and Environmental Management” (D. J. Stanley, and D. J. P. Swift, eds.). American Geological Institute/Wiley, Alexandria, VA/New York, pp. 197–218, Chapter 11.
- Mienert, J. (2002). “The Storegga submarine landslides: what do we observe and what do we model?” Abstracts with Program, Second Tsunami Symposium, May 28–30. The Tsunami Society, Honolulu, unpaginated.
- Milkov, A. V., and Sager, W. W. (2002). “Global distribution and significance of natural gas hydrate.” Abstracts with Program, Second Tsunami Symposium, May 28–30. The Tsunami Society, Honolulu, unpaginated.
- Miller, D. J. (1960). Giant waves at Lituya Bay, Alaska. *US Geol. Surv. Prof. Paper* **354-C**, 51–83.
- Milne, J. (1898). “Earthquakes and Other Earth Movements.” Paul, Trench, Truber & Co., London.
- Ming, D., and Wang, D. (1993). Studies on waves generated by landslides. *Proc. XXV Congr. IAHR, Tech. Session C*, 1–8.
- Mitchell, N. C. (2001). Transition from circular to stellate forms of submarine volcanoes. *J. Geophys. Res.* **106(B2)**, 1987–2003.
- Mitchell, N. C., Masson, D. G., Watts, A. B., Gee, M. J. R., and Urgeles, R. (2002). The morphology of the submarine flanks of volcanic ocean islands—a comparative study of the Canary and Hawaiian hotspot islands. *J. Volcanol. Geotherm. Res.* **115**, 83–107.
- Mohrig, D., Whipple, K. X., Honzo, M., Ellis, C., and Parker, G. (1998). Hydroplaning of subaqueous debris flows. *Geol. Soc. Am. Bull.* **110(3)**, 387–394.

- Mohrig, D., Elverhøi, A., and Parker, G. (1999). Experiments on the relative mobility of muddy subaqueous and subaerial debris flows and their capacity to remobilize antecedent deposits. *Mar. Geol.* **154**(1), 117–129.
- Montessus de Ballore, F. (1907). Le science seismologique; les tremblements de terra; avec une preface par M. Ed. Suess, A. Colin, Paris, pp. 1–579.
- Moon, V., and Simpson, C. J. (2002). Large-scale mass-wasting in ancient volcanic materials. *Eng. Geol.* **64**(1), 41–64.
- Moore, D. G. (1977). Submarine slides. In “Rockslides and Avalanches. 1. Natural Phenomena” (B. Voight, ed.), Developments in Geotechnical Engineering, Vol. 14A. Elsevier Scientific Pub. Co., New York, pp. 563–604.
- Moore, J. G. (2001). Density of basalt core from Hilo drill hole, Hawaii. *J. Volcanol. Geotherm. Res.* **112**, 221–230.
- Moore, J. G., and Clague, D. A. (2002). Mapping of the Nuuanu and Wailau landslides in Hawaii. In “Hawaiian Volcanoes Deep Underwater Perspective” (E. Takahashi, P. W. Lipman, M. O. Garcia, J. Naka, and S. Armaki, eds.). American Geophysical Union Monograph 128, Washington, DC, pp. 223–244, CD.
- Moore, J. G., and Moore, G. W. (1984). Deposit from a giant wave on the island of Lanai, Hawaii. *Science* **226**, 1312–1314.
- Moore, G. W., and Moore, J. G. (1988). Large-scale bedforms in boulder gravel produced by giant waves in Hawaii. *Geol. Soc. Am. Spec., Paper* **229**, 101–110.
- Moore, J. G., Clague, D. A., Holcomb, R. T., Lipman, P. W., Normark, W. R., and Torresan, M. E. (1989). Prodigious submarine landslides on the Hawaiian ridge. *J. Geophys. Res.* **94**, 17465–17484.
- Moore, J. G., Normark, W. R., and Holcomb, R. T. (1994). Giant Hawaiian landslides. *Science* **264**, 46–47.
- Moore, J. G., Normark, W. R., and Gutmacher, C. E. (1999). Major landslides on the submarine flanks of Mauna Loa volcano, Hawaii. In “Landslides of the World” (K. Sassa, ed.). Japan Landslide Society, Kyoto University Press, Kyoto, pp. 385–390.
- Moore, G. F., Coombs, M. L., Clague, D. A., Moore, J. G., and Takahashi, E. (2002). New data from the Waianae slump southwest of Oahu Island, Hawaii. *Am. Geophys. Union Program* 168, Talk T62A-1301.
- Morgan, J. K., Moore, G. F., Hills, D. J., and Leslie, S. (2000a). Overthrusting and sediment accretion along Kilauea’s mobile south flank, Hawaii: evidence for volcanic spreading from marine seismic reflection data. *Geology* **28**(7), 667–670.
- Morgan, J. K., Moore, G. F., Hills, D. J., Smith, J. R., Lipman, P., Naka, J., and Ui, T. (2000b). Correlation of recent R/V Ewing Marine seismic reflection data and Kaiko and Shinkai submarine observations over the south flank of Kilauea Volcano, HI. *EOS, Trans. Am. Geophys. Union* **8**(6), 22.
- Morganstern, N. R. (1967). Submarine slumping and the initiation of turbidity currents. *Mar. Geotech.* 189–210.
- Morton, R. A. (1993). Attributes and origins of ancient submarine slides and filled embayments, examples from the Gulf Coast basins. *Am. Assoc. Petrol. Geol. Bull.* **77**(6), 1064–1081.
- Moss, J. L., McGuire, W. J., and Page, D. (1997). Ground deformation monitoring of a potential landslide at La Palma, Canary Islands. *J. Volcanol. Geotherm. Res.* **94**(1–4), 251–265.
- Mulder, T., and Cochonat, P. (1996). Classification of offshore mass movements. *J. Sediment. Res.* **66**(1), 43–57.

- Murray, J. B., and Voight, B. (1996). Slope stability and eruption prediction on the eastern flank of Mt. Etna. In "Volcano Instability on the Earth and Other Planets" (W. J. McGuire, A. P. Jones, and J. Neuberg, eds.), Special Publication. Geological Society, London, pp. 111–114.
- Murty, T. S. (1979). Submarine slide-generated water waves in Kitimat Inlet, British Columbia. *J. Geophys. Res.* **84(C12)**, 7777–7779.
- Murty, T. S. (2003). Tsunami wave height dependence on landslide volume. *Pure Appl. Geophys.* **160(10–11)**, 2147–2153.
- Naka, J., Kanamatsu, T., Lipman, P., Sisson, T., Tsuboyama, N., Morgan, J., Smith, J. R., and Ui, T. (2002). Deep-sea volcanoclastic sedimentation around the southern flank of Hawaii island. In "Evolution of Hawaiian Volcanoes: Recent Progress in Deep Underwater Research" (E. Takahashi, P. Lipman, M. Garcia, J. Naka, and S. Aramaki, eds.). American Geophysical Union Monograph 128, Washington, DC, pp. 29–50.
- Nakada, M., and Yokose, H. (1992). Ice age as a trigger of active Quaternary volcanism and tectonism. *Tectonophysics* **212**, 321–329.
- Nardin, T. R., Hein, F. J., Gorsline, D. S., and Edwards, B. D. (1979). A review of mass movement processes and acoustic characteristics and contrasts in slope and base-of-slope systems versus canyon-fan-basin floor systems. In "Geology of Continental Slopes" (L. J. Doyle, and O. H. Pikey, eds.), Special Publication 27. Society of Economic Paleontologists and Mineralogists, pp. 61–73.
- Navarro, J. M., and Soler, C. (1994). El Agua en El Hierro. Resumen del avance del plan hidrológico de la Isle de El Hierro. *Resumen Excmo.* Cabildo Insular de El Hierro Y Consejería de Obras Publicas Vivenda y Agua, Santa Cruz de Tenerife, pp. 1–59.
- Neary, D. G., and Swift, L. W. J. (1987). Rainfall thresholds for triggering a debris avalanching event in the southern Appalachian Mountains. In "Reviews in Engineering Geology, Vol. VII—Debris Flows/Avalanches, Process, Recognition and Mitigation" (J. E. Costa, and G. F. Wieczorek, eds.). Geological Society of America, Boulder, CO, pp. 81–92.
- Nisbet, E. G., and Piper, D. J. W. (1998). Giant landslides. *Nature* **392**, 329–330.
- Noda, E. K. (1970). Water waves generated by landslides. *J. Wtrwy Harbors, Coast. Eng. ASCE* **96(WW4)**, 835–855.
- Normark, W. R., Moore, J. G., and Torresan, M. E. (1993). Giant volcano-related landslides and the development of the Hawaiian Islands. In "Submarine Landslide, Selected Studies in the U.S. Exclusive Economic Zone" (W. C. Schwab, H. J. Lee, and D. C. Twichell, eds.). US Geol. Surv. Bull. 2002, pp. 184–196.
- Norris, R. D., Firth, J., Blusztajn, J. S., and Ravizza, G. (2000). Mass failure of the North Atlantic margin triggered by the Cretaceous–Paleogene bolide impact. *Geology* **29(12)**, 1119.
- Nunn, P. D. (1997). Late Quaternary environmental changes on Pacific islands; controversy, certainty and conjecture. *J. Quat. Sci.* **12(5)**, 443–450.
- Nunn, P. (1998). Personal communications.
- Nunn, P. D. (1999). "Environmental Change in the Pacific Basin Chronologies, Causes, Consequences." Wiley, New York, pp. 1–357.
- Nunn, P. D. (2000). Illuminating sea level fall around AD 1200–1510 (730–440 cal yr BP) in the Pacific Islands: implications for environmental change and cultural transformation. *NZ Geogr.* **56**, 4–12.
- O'Brien, J. S., and Julien, P. Y. (1988). Laboratory analysis of mudflow properties. *J. Hydr. Eng.* **114**, 877–887.
- Okal, E. A. (2000). T waves from the 1998 Sandaun PNG sequence: definitive timing of the slump. *EOS, Trans. Am. Geophys. Union* **81(48)**, 142.

- Okal, E. A., and Synolakis, C. E. (2001). Comment on "Origin of the 17 July 1998 Papua New Guinea tsunami: earthquake or landslide?" By E.L. Geist. *Seismol. Res. Lett.* **72**, 362–366.
- Okusa, S., and Yoshimura, M. (1981). Possibility of submarine slope failure due to waves. *Tokai Univ. Bull.* **14**, 227–234, (in Japanese).
- Ollier, G., Cochonat, P., Lenat, J.-F., and Labazuy, P. (1998). Deep-sea volcanoclastic sedimentary systems: example of La Fournaise volcano, Reunion Indian Ocean. *Sedimentology* **45**(2), 293–330.
- Parfitt, E. A., and Peacock, D. C. P. (2001). Faulting in the southern flank of Kilauea Volcano, Hawaii. *J. Volcanol. Geotherm. Res.* **106**, 265–284.
- Parfitt, E. A., Gregg, T. K. P., and Smith, D. K. (2002). A comparison between subaerial and submarine eruptions at Kilauea Volcano, HI: implications for the thermal viability of lateral feeder dikes. *J. Volcanol. Geotherm. Res.* **13**, 213–242.
- Pariseau, W. G. (1980). Rockslides and avalanches; basic principles and perspectives in the realm of civil and mining operations. In "Rockslide and Avalanches, 2" (B. Voight, ed.), Engineering Sites. Elsevier, Amsterdam, pp. 1–92.
- Pariseau, W. G., and Voight, B. (1979). Rockslides and avalanches; basic principles and perspectives in the realm of civil and mining operations. In "Rockslides and Avalanches. 2. Engineering Sites" (B. Voight, ed.). Elsevier, Amsterdam, pp. 1–92.
- Parker, G. (1982). Conditions for the ignition of catastrophically erosive turbidity currents. *Mar. Geol.* **46**, 307–327.
- Parker, G., Garcia, M. H., Fukushima, Y., and Yu, W. (1987). Experiments on turbidity currents over erodible beds. *J. Hydr. Res.* **25**, 123–147.
- Paul, A., Gravier, J. P., and Boudon, J. (1987). A numerical model for simulating deformation of Mt. St. Helens volcano. *J. Geophys. Res.* **92**, 10299–10312.
- Paull, C. K. (2001). Personal communications.
- Paull, C. K., Ussler, W. III, and Dillion, W. P. (1991). Is the extent of glaciation limited by marine gas-hydrates? *Geophys. Res. Lett.* **18**, 423–434.
- Paull, C. K., Buelow, W. J., Ussler, W. III, and Brorowski, U. S. (1996). Increased continental marine slumping frequency during sea-level low-stands above gas-hydrate-bearing sediments. *Geology* **24**, 143–146.
- Paull, C., Bohrmann, G., Brewer, P., Cochonat, P., Collett, T., Edwards, N., Hovland, M., Johnson, A., Kvenrolden, K., Matsumoto, R., Sloan, D., Trehu, A., and Westbrook, G. (2000) Excerpts from the Final Report of JOIDES Gas Hydrate Program. *Joides J.* **26**(2-2000), 33–39.
- Paull, C., Ussler, W. III, Maher, N., Greene, H. G., Rehder, G., Lorenson, T., and Lee, H. (2002). Pockmarks off Big Sur, California. *Mar. Geol.* **181**(4), 323–335.
- Pearce, T. J., and Jarvis, I. (1992). Composition and provenance of turbidite sands: Late Quaternary, Madeira Abyssal Plain. *Mar. Geol.* **109**, 21–51.
- Pederson, J., Pazzaglia, F., and Smith, G. (2000). Ancient hillslope deposits, missing links in the study of climate controls on sedimentation. *Geology* **28**, 27–30.
- Pelayo, A. M., and Wiens, D. A. (1992). Tsunami earthquakes; slow thrust-faulting accretionary wedge. *J. Geophys. Res. B* **97**, 15321–15337.
- Pelinovsky, E., and Poplavsky, A. (1996). Simplified model of tsunami generation by submarine landslides. *Phys. Chem. Earth* **21**(1–2), 13–17.
- Pelletier, B., Regnier, M., Calmanr, S., Pillet, R., Cabioch, G., Lagabrielle, Y., Bore, J. M., Caminade, J. P., Lebellegard, P., Cristopher, I., and Temakon, S. (2000). The Ambrym-Pentecost (Vanuatu) earthquake of November 26, 1999 (magnitude 7.5); preliminary data on seismicity and associated

- tsunami and crustal displacements. *Comptes Rendes de l'Academie des Sciences (Series II)* **331(1)**, 21–28.
- Perla, R., Cheng, T. T., and McClung, D. M. (1980). A two-parameter model of snow avalanche motion. *J. Glaciol.* **6**, 197–207.
- Pierson, T. C. (1986). Flow behavior of channelized debris flows, Mount. St. Helens, Washington. In “Hillslope Processes” (A. D. Abrahams, ed.). Allen & Unwin, Boston, pp. 269–296.
- Pierson, T. C., Ellen, S. D., and Iverson, R. M. (1992). “Shallow landsliding during intense rainfall, Oahu, Hawaii.” Proceedings of the Sixth International Symposium on Landslides. Balkema, Rotterdam, Netherlands.
- Piper, D. J. W., Farre, J. A., and Shore, A. (1985). Late Quaternary slumps and debris flows on the Scotian slope. *Geol. Soc. Am. Bull.* **96**, 1508–1517.
- Piper, D. J. W., Shor, A. N., and Clarke, J. E. H. (1988). The 1929 “Grand Banks” earthquake, slump, and turbidity current. *Geol. Soc. Am. Spec. Paper* **229**, 77–92.
- Piper, D. J. W., Cochonot, P., and Morrison, M. L. (1999). The sequence of events around the epicenter of the 1929 Grand banks earthquake, initiation of debris flows and turbidity current inferred from sidescan sonar. *Sedimentology* **46(1)**, 79–97.
- Pomeroy, J. S. (1980). Storm induced debris avalanching and related phenomena in the Johnstown area, with reference to other studies on the Appalachians. *US Geol. Surv. Prof. Paper* **1191**, 1–24.
- Popenoe, P., Schmuck, E. A., and Dillon, W. P. (1993). The Cape Fear landslide; slope failure associated with salt diapirism and gas hydrate decomposition. *US Geol. Surv. Bull.* **B2002**, 40–53.
- Porter, J. N., Norton, K. A., Mougini-Mark, P. J., Lienert, B., Sharma, S. K., Lau, E., Sutton, A. J., Elias, T., and Oppenheimer, C. (2002). Sun photometer and lidar measurements of the plume from the Hawaii Kilauea Volcano Pu’u’O’o vent. Aerosol flux and SO<sub>2</sub>. *Geophys. Res. Lett.* **29(6)**, 30, Cover figure, DOI10.1029/2002GLO14749.
- Prior, D. B., and Coleman, J. M. (1980). Active slides and flows in unconsolidated marine sediments on the slopes of the Mississippi Delta. In “Marine Slides and Other Mass Movements” (S. Saxov, and J. K. Nieuwenhuis, eds.). Plenum Press, New York, pp. 21–49.
- Prior, D. B., and Coleman, J. M. (1984). Submarine slope instability. In “Slope Instability” (D. Brunnsden, and D. B. Prior, eds.). Wiley, New York, pp. 419–455.
- Public Works. (2000). Bypass road constructed of sand, coral and a cellular system. *Public Works* **131(9)**, 48.
- Qian, N., and Wan, Z. (1986). A critical review of the research on the hyperconcentrated flow. *China Int. Res. Training Center Erosion Sediment. Publ., China* (cited in Coussot and Meunier, 1996).
- Rainfall Atlas of Hawaii. (1976). State of Hawaii Department of Land and Natural Resources Report, R76, pp. 99–151.
- Rampino, M. R., and Self, S. (1992). Volcanic winter and accelerated glaciation following the Toba super-eruption. *Nature* **359**, 50–52.
- Rampino, M. R., and Self, S. (1993). Climate-volcanism feedback and the Toba eruption of ~74,000 years ago. *Quat. Res.* **40**, 269–280.
- Rampino, M. R., Self, S., and Fairbridge, R. W. (1979). Can rapid climate change cause volcanic eruptions? *Science* **206**, 826–828.
- Raney, D. C., and Bulter, H. L. (1975). “A Numerical Model for Predicting the Effects of Landslide-generated Water Waves.” US Army Engineer Waterways Experiment Station Report, H-75-1. US Department of Commerce, Springfield, VA, (cited by Heinrich, 1992).

- Rees, B., Detrick, R. S., and Coakley, B. (1993). Seismic stratigraphy of the Hawaiian flexural moat. *Geol. Soc. Am. Bull.* **105**, 189–205.
- Refice, A., and Capolongo, D. (2002). Probabilistic modeling of uncertainties in earthquake-induced landslide hazard assessment. *Comput. GEO Sci.* **28**, 735–749.
- Reid, M. E., and Iverson, M. M. (1992). Gravity-driven groundwater flow and slope failure potential. 2. Effects of slope morphology, material properties, and hydraulic heterogeneity. *Water Resour. Res.* **28(3)**, 939–950.
- Reid, M. E., Sisson, T. W., and Brien, D. L. (2001). Volcano collapse promoted by hydrothermal alteration and edifice shape, Mt. Rainier, Washington. *Geology* **29(9)**, 779–782.
- Relm, E., and Halbach, P. (1982). Hawaiian derived volcanic ash layers in equatorial N.W. Pacific sediments. *Mar. Geol.* **50**, 25–40.
- Richards, K. S., and Lorrimer, N. R. (1987). Basal erosion and mass movement. In “Slope Stability” (M. G. Anderson, and K. S. Richards, eds.). Wiley, New York, pp. 331–357.
- Rikitake, T., and Aida, I. (1988). Tsunami hazard probability in Japan. *Bull. Seismol. Soc. Am.* **78(3)**, 1268–1278.
- Roberts, J. A., and Cramp, A. (1996). Sediment stability on the western flanks of the Canary Islands. *Mar. Geol.* **134**, 13–30.
- Robinson, S. G., and Sahota, J. T. S. (2000). Rock-magnetic characterization of early, redoximorphic diagenesis in turbiditic sediments from the Madeira Abyssal Plain. *Sedimentology* **47**, 367–394.
- Rothwell, R. G., Thomson, J., and Kahler, G. (1998). Low sea-level emplacement of a very large late Pleistocene ‘megaturbidite’ in the western Mediterranean Sea. *Nature* **392**, 377–380.
- Rothwell, R. G., Reeder, M. S., Anastasakis, G., Stow, D. A. V., Thomson, J., and Kahler, G. (2000). Low sea-level stand emplacement of megaturbidites in the western and eastern Mediterranean sea. *Sediment. Geol.* **135**, 75–88.
- Rougerie, F., and Wauthy, B. (1986). Le Concept d’Endo-upwelling dans le fontionement des Atolls Oasis. *Oceanol. Acta* **9**, 133–148.
- Rougerie, F., and Wauthy, B. (1988). “The endo-upwelling concept: a new paradigm for solving an old paradox.” Proceedings of the 6th International Coral Reef Symposium, Papeete, Tahiti **3**, pp. 21–26.
- Rougerie, F., and Wauthy, B. (1993). The endo-upwelling concept, from geothermal convection to reef construction. *Coral reefs* **12**, 19–30.
- Rougerie, F., Gros, R., and Bernadac, M. (1980). La lagoon de Mururoa (archipel de Tuamotu), Esquisses de caracteristiques et des changes avec l’Ocean. (*Rapport ORSTROM, Papeete*) *Section Oceanographic* 16.
- Rougerie, F., Andre, C. H., and Jean-Baptiste, P. H. (1991). Helium-3 inside atoll barrier reef interstitial water: a clue for geothermal endo-upwelling. *Geophys. Res. Lett.* **18**, 109–112.
- Rougerie, F., Fagerstrom, J. A., and Andre, C. (1992). Geothermal endo-upwelling: a solution to the reef nutrient paradox? *Cont. Shelf Res.* **12**, 758–798.
- Rowland, S. K. (1996). Slopes, lava flow volumes, and vent distributions on Volcano Fernandina, Galapagos Islands. *J. Geophys. Res.* **101**, 27657–27672.
- Rubin, K. H., Fletcher, C. H., and Sherman, C. (2000). Fossiliferous Lanai deposits formed by multiple events rather than a single giant tsunami. *Nature* **408**, 675–681.
- Ruff, L. J. (2003). Some aspects of energy balance and tsunami generation by earthquakes and landslides. *Pure Appl. Geophys.* **160(10–11)**, 2156–2176.
- Ruffman, A. (2001). Potential for large-scale submarine slope failure and tsunami generation along the US Mid-Atlantic coast: comment. *Geology* **29(10)**, 967.

- Ryan, W. B. F. (1980). Tectonic significance of Atlantic carbonate platform escarpments. *Int. Geol. Congr.* **26(2)**, 539.
- Ryan, W. B. F. (1982). Imaging of submarine landslides with wide-swath sonar. In "Marine Slides and Other Mass Movements" (S. Saxov, and J. K. Nieuwenhuis, eds.). Plenum Press, New York, pp. 175–188.
- Ryan, M. P. (1988). The mechanisms and three dimensional internal structure of active magmatic systems: Kilauea Volcano, Hawaii. *J. Geophys. Res.* **93**, 4213–4248.
- Ryan, J., and Davidson, J. (1999). Contemporary assessment of tsunami risk and implications for early warnings for Australia and its island territories. *Sci. Tsunami Haz.* **17(2)**, 107–125.
- Rzadkiewicz, A. S., Mariotti, C., and Heinrich, P. (1997). Numerical simulation of submarine Karmsundet landslides and their hydraulic effects. *J. Waterway, Coast. Ocean Eng. ASCE* **123(4)**, 149–157.
- Sangrey, D. A., Harrop-Williams, K. O., and Klaiber, J. A. (1984). Predicting ground-water response to precipitation. *Am. Soc. Civ. Eng. J. of Geotech. Eng.* **110**, 957–975.
- Satake, K., and Kato, Y. (2001). The 1741 Oshima-Oshima eruption: extent and volume of submarine debris avalanche. *Geophys. Res. Lett.* **28(3)**, 427–430.
- Satake, K., and Tanioka, Y. (1999). Sources of tsunami and tsunamigenic earthquakes in subduction zones. *Pure Appl. Geophys.* **154(3–4)**, 467–483.
- Satake, K., Smith, J. R., and Shinozaki, K. (2002). Volume estimate and tsunami modeling for the Nuanu and Wailau landslides. In "Evolution of Hawaiian Volcanoes: Recent Progress in Deep Underwater Research" (E. Takahashi, P. Lipman, M. Garcia, J. Naka, and S. Aramaki, eds.). American Geophysical Union Monograph 128, Washington, DC, pp. 333–346.
- Sassa, K. (1988). "Geotechnical model for the motion of landslides." Proceedings of the 5th International Symposium on Landslide, Lausanne, Switzerland, pp. 37–55.
- Savage, S. B. (1993). Mechanics of debris flows in hydraulic engineering. *93 Proc. Hydr. Div., Am. Soc. Civ. Eng.* **2**, 1402–1407.
- Saxov, S., and Nieuwenhuis, J. K. (eds.) (1982). Marine slides and other mass movements. *NATO Conference Series IV, Marine Sci.*, **6**, 1–353.
- Scheidegger, A. E. (1973). On the prediction of the reach and velocity of catastrophic landslides. *Rock Mech.* **5**, 231–236.
- Schmincke, H.-U. (1990). "Geology and Geological Field Guide of Gran Canaria." Pluto Press, Kiel, (cited by Urgeles *et al.*, 1997), pp. 1–212.
- Schmincke, H.-U., and Segsneider, B. (1998). Shallow submarine to emergent basaltic shield volcanism of Gran Canaria: evidence from drilling into the volcanic apron. *Proc. ODP, Sci. Rep.* **157**, 141–181.
- Schmincke, H.-U., and Sumita, M. (1998). Tephra event stratigraphy and emplacement of volcanoclastic sediments, Mogan and Fataga stratigraphic intervals. Part II: origin and emplacement of volcanoclastic layers. *Proc. ODP, Sci. Rep.* **157**, 267–292.
- Schwarz, H.-U. (1982). Subaqueous slope failures—experiments and modern occurrences. In "Contributions to Sedimentology" (H. Fuchtbauer, A. P. Lisitzyn, J. D. Milliman, and E. Siebold, eds.). Schweizerbartsche Verlagsbuchhandlung, Stuttgart, pp. 1–116.
- Seavolc (1995). Sea-level change and the stability and activity of coastal and island volcanoes. Environment Programme Contract EV5V-CT92-0170 Final Report. Commission of the European Communities, Brussels.
- Shackleton, N. J. (1987). Oxygen isotopes, ice volume and sea level. *Quat. Sci. Rev.* **6(3–4)**, 183–190.

- Shackleton, N. N., Berger, A., and Peltier, W. R. (1990). An alternative astronomical calibration of the lower Pleistocene time scale based on ODP Site 677. *Roy. Soc. Edinburgh Trans. Earth Sci.* **81**, 251–261.
- Shanmugam, G. (1997). The Bouma sequence and the turbidite mind sea. *Earth Sci. Res.* **2(4)**, 201–229.
- Shanmugam, G. (2000). 50 Years of the turbidite paradigm (1950s–1990s): deep-water processes and facies models—a critical perspective. *Mar. Petrol. Geol.* **17(2)**, 285–342.
- Shanmugam, G., Moiola, R. J., and Sales, J. K. (1988). Duplex-like structures in submarine fan channels, Ouachita mountains, Arkansas. *Geology* **16**, 229–232.
- Shepard, F. P. (1933). Depth changes in Sagami Bay during the great Japanese earthquake. *J. Geol.* **41**, 527–536.
- Shigihara, Y., and Imamura, F. (2002). “Numerical simulation with 2-layer model for landslide-induced tsunami.” Abstracts with Program. Second Tsunami Symposium, May 28–30. The Tsunami Society, Honolulu, unpaginated.
- SHOALS, www site: shoals.sam.usace.army.mil/.
- Shreve, R. L. (1968). “The Blackhawk Landslide.” Special Paper 108. Geological Society of America, Boulder, CO, pp. 1–47.
- Shuto, N., Goto, N., and Imamura, F. (1990). Numerical simulation as a means of warning for near-field tsunami. *Coast. Eng. Jpn* **33(2)**, 173–193.
- Siebert, L. (1984). Large volcanic debris avalanches: characteristics of source areas, deposits and associated eruptions. *J. Volcanol. Geotherm. Res.* **22**, 163–197.
- Sigvaldason, G. E., Annertz, K., and Nilsson, M. (1992). Effects of glacier loading/deloading on volcanism: post-glacial volcanic production rate of the Dyngjufjoll area, central Iceland. *Bull. Volcanol.* **54**, 385–392.
- Slosson, J. E., and Larson, R. A. (1996). Slope failures in southern California: rainfall threshold, prediction, and human causes. *Int. J. Rock Mech. Min. Sci. Geomech. Abstr.* **33**, 241A–242A.
- Smith, M. S., and Shepherd, J. B. (1993). Preliminary investigations of the tsunami hazard of Kick'em Jenny submarine volcano. *Mar. Haz.* **7**, 257–277.
- Smith, M. S., and Shepherd, J. B. (1996). Tsunamiogenic landslides at Kick'em Jenny. In “Volcano Instability on the Earth and Other Planets” (W. J. McGuire, A. P. Jones, and J. Neuberg, eds.), Special Publication 10. Geological Society, London, pp. 115–124.
- Smith, J. R., Malahoff, A., and Shor, A. N. (1999). Submarine geology of the Hilina slump and morpho-structural evolution of Kilauea volcano, Hawaii. *J. Volcanol. Geotherm. Res.* **94(1–4)**, 59–88.
- Smith, J. R., Satake, K., Morgan, J. K., and Lipman, P. W. (2002). Submarine landslides and volcanic features on Kohala and Mauna Kea volcanoes and the Hana Ridge, Hawaii. In “Hawaiian Volcanoes Deep Underwater Perspective” (E. Takahashi, P. W. Lipman, M. O. Garcia, J. Naka, and S. Armaki, eds.), American Geophysical Union Monograph 128, Washington, DC, pp. 11–28, CD.
- Smoot, N. C., and King, R. E. (1992). 3-D secondary surface geomorphology of submarine landslides on NW Pacific plate guyots. *Geomorphology* **6**, 157–174.
- Soria, J. M., Alfaro, P., Fernandez, J., and Viseras, C. (2001). Quantitative subsidence-uplift analysis of the Bajo Segura Basin (eastern Betic Cordillera, Spain); tectonic control on the stratigraphic architecture. *Sediment. Geol.* **140(3–4)**, 271–289.
- Sousa, J., and Voigt, B. (1991). Continuum simulation of flow failures. *Geotechnique* **41(4)**, 515–538.
- Sousa, J., and Voigt, B. (1992). Computational flow modeling for long-runout landslide hazard assessment, with an example from Clapiere Landslide, France. *Bull. Assoc. Eng. Geol.* **24(2)**, 131–150.

- Special Issue. (1992). *Continental Shelf Res.* **12**(10).
- Special issue. (1994a). *Bull. Geol. Soc. Denmark.* **41**, Part 1.
- Special Issue. (1994b). *Geo-Mar. Lett.*, **14**(2/3).
- Stanley, S. P., and Swift, D. J. P. (1976). "Marine Sediment Transport and Environmental Management." Wiley, New York, pp. 1–602.
- Stearns, H. T. (1973). Potassium–argon ages of lavas from the Hawi and Pololu Volcanic Series, Kohala Volcano, Hawaii: discussion. *Geol. Soc. Am. Bull.* **84**, 3483–3484.
- Stetson, H. C., and Smith, J. F. (1938). Behavior of suspension currents and mud slides on the continental slope. *Am. J. Sci.* **35**, 1–13.
- Stice, G. D., and McCoy, R. W. Jr. (1968). The geology of the Manua Islands, Samoa. *Pacif. Sci.* **22**, 426–457.
- Stoddart, D. R. (1950). The shape of atolls. *Mar. Geol.* **3**, 369–383.
- Striem, H. L., and Miloh, M. T. (1976). Tsunamis induced by submarine slumping off the coast of Israel. *Int. Hydrogr. Rev.* **53**(2), 41–55.
- Sturdivant, N., and McAdoo, B. G. (1999). A web-based GIS database of submarine landslides. *Geol. Soc. Am. Abstr. Program* **31**(7), 81.
- Swanson, D. A. (1972). Magma supply rate at Kilauea volcano, 1952–1971. *Science* **175**, 163–170.
- Swanston, D. N., Ziemer, R. R., and Janda, R. J. (1983). Influence of climate on progressive hillslope failure in Redwood Creek Valley, northwestern California. *US Geol. Surv. Open File Rep.* **83–259**, 1–42.
- Synolakis, C. E., Bardet, J.-P., Borrero, J. C., Davies, H. L., Okal, E. A., Silver, E. A., and Sweet, S. (2000). The slump origin of the 1998 Papua New Guinea tsunami. *Proc. Math. Phys. Eng. Sci.* **8A**(458), 763–789.
- Takahashi, T. (1978). Mechanical characteristics of delta flows. *J. Hydr. Div.* **104**, 1153–1169.
- Takahashi, T. (1980). Debris flow on prismatic open channel. *J. Hydr. Div. Am. Soc. Civ. Eng.* **106**, 381–396.
- Takahashi, T. (1981). Debris flow. *Ann. Rev. Fluid Mech.* **12**, 57–77.
- Takahashi, T. (1991). "Debris Flow." IAHR Monograph Series. Balkema, Rotterdam, pp. 1–156.
- Takahashi, E., Lipman, P. W., Garcia, M. O., Naka, J., and Armaki, S. (2002). Hawaiian volcanoes deep underwater perspective. *Am. Geophys. Union Monogr.* **128**, 1–418, CD.
- Tanioka, Y. (1999). Analysis of the far-field tsunamis generated by the 1999 Papua New Guinea earthquake. *Geophys. Res. Lett.* **26**(22), 3393–3396.
- Tappin, D., ed. (2004). Submarine-slump-generated tsunamis. *Marine Geology* (special issue). **203**(3–4), 1–386.
- Tappin, D. R., Matsumoto, T., Watts, P., Sakate, K., McMurtry, G., Matsuyama, M., Lefoy, T., Tsuji, Y., Kanamatsu, T., Lus, W., Iwabachi, Y., Yeh, H., Matsuyama, W., Lefoy, Y., Tsuji, Y., Hill, P., Crook, K., Anton, L., and Walsh, J. P. (1999). Sediment slump likely caused 1998 Papua New Guinea tsunami. *EOS, Trans. Am. Geophys. Union* **80**, 329–340.
- Tappin, D. R., Watts, P., McMurtry, G. M., Lefoy, Y., and Matsumoto, T. (2001). The Sissano, Papua New Guinea tsunami of July 1998—offshore evidence on the source mechanism. *Mar. Geol.* **175**, 1–23.
- Taylor, R. F. (1984). "Introduction liquefaction of seabed sediments triaxial test simulations." Seabed Mechanics. Graham & Trotman, London, pp. 131–148.
- Terrinha, P., Pinheiro, L. M., Henriot, J.-P., Matias, L., Ivanov, M. K., Monteiro, J. H., Akhmetzhanov, A., Volkonskaya, A., Cunha, T., Shaskin, P., and Rovere, M. (2003). Tsunamigenic–seismogenic structures, neotectonics, sedimentary processes and slope instability on the southwest Portuguese Margin. *Mar. Geol.* **195**, 55–73.

- Terzaghi, K. (1923). Die Berechnung der Durchlassigkeitsziffer des Tones aus dem Verlauf der hydrodynamischen Spannungserscheinungen, Sitzungsberichte, der Akademie der Wissenschaften in Wien, Mathematisch-naturwissenschaftliche Klasse, Part 2a, **132**(3–4).
- Terzaghi, K. (1943). "Theoretical Soil Mechanics." Wiley, New York, pp. 1–510.
- Terzaghi, K. (1950). Mechanisms of landslides. In "Application of Geology to Engineering Practice" (S. Paige, ed.). Geological Society of America, Boulder, CO, pp. 83–123.
- Thomas, D. (1987). A geochemical model of the Kilauea east rift zone. In "Volcanism in Hawaii" (R. W. Decker, T. L. Wright, and P. H. Stauffer, eds.), Paper 1350. US Geol. Surv., pp. 1507–1525.
- Thomas, D. M., Cox, M. E., Hellsley, C. E., Kauahikaua, J. P., Lienert, B. R., Mattice, M. D., Thomas, T. L., produced by NGDC/NAOO for US Dept. of Energy. (1983). "Geothermal Resources of Hawaii." Hawaii Institute of Geophysics Map, Pub. US Government Printing Office, Washington, DC.
- Tinti, S., and Bortolucci, E. (2000). Analytical investigation on tsunamis generated by submarine slides. *Annali di Geofisica* **43**(3), 519–536.
- Tinti, S. E., Bortolucci, E., and Vannini, C. (1997). A block-based theoretical model suited to gravitational sliding. *Nat. Haz.* **16**, 1–28.
- Tinti, S., Bortolucci, E., and Armigliato, A. (1999a). Numerical simulation of the landslide-induced tsunami of 1988 on Vulcano Island, Italy. *Bull. Volcanol.* **61**, 121–137.
- Tinti, S., Bortolucci, E., and Romagnoli, C. (1999b). Modeling a possible Holocene landslide-induced tsunami at Stromboli Volcano, Italy. *Phys. Chem. Earth, Part B, Hydrol., Oceans Atmos.* **24**(5), 423–429.
- Tinti, S., Bortolucci, E., and Chiavettieri, C. (2001). Tsunami excitation by submarine slides in shallow water approximation. *Pure Appl. Geophys.* **158**(4), 759–798.
- Titov, V., and Gonzalez, F. (1998). Numerical study of the July 17, 1998 Papua New Guinea tsunami. In "Tsunami Research at the End of a Critical Decade" (G. T. Hebenstreit, ed.). Kluwer Academic Press, Dordrecht, pp. 197–207.
- Townson, J. M., and Kaya, Y. (1988). Simulations of the waves in Lake Botnen created by the Tissa landslide. *Proc. Inst. Civ. Eng.* **85**(2), 145–160.
- Trauth, M. H., and Strecker, M. R. (1999). Formation of landslide-dammed lakes during a wet period between 40,000 and 25,000 B.P. on northwestern Argentina. *Palaeogeogr. Palaeoclimatol. Palaeoecol.* **153**, 277–287.
- Trunk, F. J., Dent, J. D., and Land, T. E. (1986). Computer modeling of large rock slides. *J. Geotech. Eng.* **112**, 348–360.
- Tsuji, Y., and Hino, T. (1993). Damage and inundation height of the 1792 Shimabara landslide tsunami along the coast of Kumamoto prefecture. *Bull. Earthq. Res. Inst. Tokyo* **68**(2), 91–176.
- Tsunami Society Web Site. [www.sthjournal.org/media.htm](http://www.sthjournal.org/media.htm).
- Ui, T. (1983). Volcanic dry avalanche deposits, identification and comparison with non-volcanic debris stream deposits. *J. Volcanol. Geotherm. Res.* **18**, 135–150.
- Urgeles, R., Canals, M., Baraza, J., Alonso, B., and Masson, D. G. (1997). The most recent megaslides on the Canary Islands, the El Golfo Debris Avalanche and the Canary Debris Flow. *J. Geophys. Res.* **102**, 20305–20323.
- VanDine, D. F., and Bovis, M. (2002). History and goals of Canadian debris flow research. A review. *Nat. Haz.* **26**, 67–80.
- Van Gassen, W., and Cruden, D. M. (1989). Momentum transfer and friction in the debris of rock avalanches. *Can. Geotech. J.* **26**, 623–628.

- van Steijn, H. (1988). Debris flows involved in the development of Pleistocene stratified slope deposits. *Z. Geomorphol. NF* **71**, 45–58, (cited by Coussot and Meunier, 1996).
- van Weering, T. C. E., Klaver, G. T., and Prin, R. A. (1997). Gas in marine sediments—an introduction. *Mar. Geol.* **137**, 1–3.
- van Wyk de Vries, B., Kerle, N., and Petley, D. (2000). Sector collapse at Casita volcano, Nicaragua. *Geology* **28**(2), 167–170.
- Varnes, D. J. (1958). Landslide types and processes. In “Landslides and Engineering Practice” (E. B. Eckel, ed.), Highway Research Board Special Report 29.
- Varnes, D. J. (1978). Slope movement types and processes. In “Landslides Analysis and Control” National Acad. Science, Transportation Research Board, Special Report 176, pp. 1–33.
- Verriere, M., and Lenoir, M. (1992). Computation of waves generated by submarine landslides. *Int. J. Numer. Methods Fluids* **14**, 403–421.
- Vogt, P. R., and Jung, W.-Y. (2002). Holocene mass wasting on upper non-Polar continental slopes—due to post-glacial ocean warming and hydrate dissociation. *Geophys. Res. Lett.* **29**(9) 55-1–55-4.
- Vogt, P. R., Crane, K., Sundvor, E., Hjelstuen, B. O., Gardner, J., Bowles, F., and Cherkashev, G. (1999). Ground-truthing 11- to 12-kHz side-scan sonar imagery in the Norwegian-Greenland Sea: part II: probable diapirs on the Bear Island fan slide valley margins and the Voring Plateau. *Geo-Mar. Lett.* **19**, 111–130.
- Voight, B. (2000). Structural stability of andesite volcanoes and lava domes. *Philos. Trans. R. Soc. London* **358**, 1663–1703.
- Voight, B., and Elsworth, D. (1997). Failure of volcano slopes. *Geotechnique* **47**, 1–31.
- Voight, B., Janda, R. J., Glicken, H., and Douglass, P. M. (1983). Nature and mechanics of the Mount St. Helens rockslide-avalanche of 18 May 1980. *Geotechnique* **33**, 243–273.
- Voight, B., Janda, R. J., Glicken, H., and Douglass, P. M. (1985). Reply to discussion on “Nature and mechanics of Mt. St. Helens rockslide-avalanche of 18 May 1980”. *Geotechnique* **35**, 357–368.
- Von Huene, R., Ranero, C. R., and Watts, P. (2001). Instability and tsunamigenic potential at convergent margins. *EOS, Trans. Am. Geophys. Union, Fall Meet. Program H22G-04*, 147.
- Walker, G. P. L. (1986). Koolau dike complex, Oahu, intensity and origin of a sheeted Dike complex high in a Hawaiian volcanic edifice. *Geology* **14**, 310–313.
- Walker, G. P. L. (1987). The Dike complex of Koolau Volcano, Oahu: international structure of a Hawaiian rift zone. In “Hawaiian Volcanism” (R. W. Decker, T. L. Wright, and P. H. Stauffer, eds.), US Geol. Surv. Prof. Paper 1350. US Government Printing Office, Washington, DC, pp. 961–993.
- Walker, D. A., and Bernard, E. N. (1993). Comparison of T-phase spectra and tsunami amplitudes for tsunamigenic and other earthquakes. *J. Geophys. Res. C, Oceans* **98**, 12557–12565.
- Walker, G. P. L., Eyre, P. R., Spengler, R., Knight, M. D., and Kennedy, K. (1995). Congruent dike-widths in large basaltic volcanoes. In “Physics and Geochemistry of Dikes” (G. Baer, and A. Heimann, eds.). Balkema, Rotterdam, pp. 35–40.
- Wallman, P. C., Mahood, G. A., and Pollard, D. D. (1988). Mechanical models for correlation of ring-fracture eruptions at Pantelleria Strait of Sicily, with glacial sea-level drawdown. *Bull. Volcanol.* **50**, 327–339.
- Ward, S. N. (2001). Landslide tsunami. *J. Geophys. Res.* **106**(6), 11201–11216.
- Ward, S. N., and Day, S. (2001). Cumbre Vieja volcano—potential collapse and tsunami at La Palma, Canary Islands. *Geophys. Res. Lett.* **28**(17), 3397–3400.

- Ward, S. N., and Day, S. (2003). Ritter Island volcano—lateral collapse and the tsunami of 1888. *Geophys. J. Int.* **154**, 891–902.
- Warme, J. E., and Sandberg, C. A. (1996). Alamo megabreccia: record of a Late Devonian impact in southern Nevada. *GSA Today* **6**, 17.
- Warme, J. E., Kuehner, H.-C., and Oberbeck, V. R. (1997). Carbonate platform landslide and multiple tsunami triggered by asteroid or comet impact, Devonian, Nevada. Geological Society of America, Cordilleran Section, 93rd annual meeting Kailua-Kona, HI, United States, May 21–23. *Abstr. Programs—Geol. Soc. Am.* **29(5)**, 73.
- Watts, P. (1997). “Water Waves Generated by Underwater Landslides” (Ph.D. thesis), California Institute of Technology, Pasadena, CA.
- Watts, P. (1998). Wavemaker curves for tsunamis generated by underwater landslides. *J. Wtrwy, Port, Ocean Eng. ASCE* **124(3)**, 127–137.
- Watts, P. (2000). Tsunami features of solid block underwater landslides. *J. Wtrwy Port, Ocean Eng.* **126(3)**, 144–151.
- Watts, P. (2002). “Probability distributions and sensitivity analysis of gas hydrate induced landslides and tsunamis.” Abstracts with Program, Second Tsunami Symposium, May 28–30. The Tsunami Society, Honolulu, unpaginated.
- Watts, P. (2004). Predictions of landslide analysis of gas hydrate induced landslides and tsunami off southern California. *Mar. Geol.* **203(3-4)**, 235–245.
- Watts, P. (2004). Probabilistic predictions of landslide tsunamis off southern California. *Mar. Geol.* **203(3/4)**, 281–301.
- Watts, A. B., and Masson, D. G. (1995). A giant landslide on the north flank of Tenerife, Canary Islands. *J. Geophys. Res.* **100**, 24487–24498.
- Watts, P., and Gardner, J. V. (2003). Landslide tsunami scenario off California, landslide tsunami scenario off Palos Verdes, California, ASCE Preprint.
- Watts, P., and Raichlen, F. (1994). Water waves generated by underwater landslides. *Seismol. Res. Lett.* **65**, 1, (abstract).
- Watts, A. B., TenBrink, U. S., Buhl, P., and Brocher, T. M. (1985). A multichannel seismic study of lithospheric flexure across the Hawaiian-Emperor seamount chain. *Nature* **315**, 105–111.
- Watts, P., Grilli, S. T., and Synolakis, C. E. (2000a). Predicting tsunami amplitudes. *Am. Geophys. Union Fall Meet. Detailed Sessions Program* 314.
- Watts, P., Imamura, F., and Grilli, S. T. (2000b). Comparing model simulations of three benchmark cases. *Sci. Tsunami Haz.* **28(2)**, 107–124.
- Watts, P., Borrero, J. C., Tappin, D. R., Bardet, J.-P., Grilli, S. T., and Synolakis, C. (2001a). Novel simulation technique on the 1998 Papua New Guinea tsunami. In “Tsunami Research at the End of a Critical Decade” (G. T. Hebenstreit, ed.). Kluwer Academic Press, Dordrecht, pp. 193–208.
- Watts, P., Matsuyama, M., and Tappin, D. R. (2001b). Potential landslide tsunamis near Aitape, Papua New Guinea. *ITS 2001 Proc.* 425–436, Session 2, Number 2–11.
- Watts, P., Tappin, D. R., Grilli, S. T., Kirby, J. T., and Fryer, G. J. (2003). Landslide tsunami case studies using a Boussinesq model and a fully nonlinear tsunami generation model. *Nat. Hazards Earth Syst. Sci.* **3(5)**, 39–402.
- Weaver, P. P. E. (1994). Determination of turbidity current erosional characteristics from reworked coccolith assemblages, Canary Basin, north-east Atlantic. *Sedimentology* **41**, 1025–1038.
- Weaver, P. P. E., and Kuijpers, A. (1983). Climatic control of turbidite deposition on the Madeira Abyssal Plain. *Nature* **306**, 360–363.

- Weaver, P. P. E., Rothwell, R. G., Ebbing, J., Gunn, D., and Hunter, P. M. (1992). Correlation, frequency of emplacement and source directions of megaturbidites on the Madeira Abyssal Plain. *Mar. Geol.* **109**, 1–20.
- Weaver, P. P. E., Masson, D. G., Gunn, D. E., Kidd, R. B., and Maddison, D. A. (1995). Sediment mass wasting in the Canary Basin. In “Atlas of Deep Water Environments, Architectural Style in Turbidite Systems” (K. T. Pickering, R. N. Hiscott, F. Kenvon, F. Ricci Lucci, and R. D. A. Smith, eds.). Chapman & Hall, London, pp. 287–296, (cited by Masson *et al.* 1998).
- Weaver, P. P. E., Jervis, I., Lebreiro, S. M., Abes, B., Baraza, J., Howe, R., and Rothwell, R. G. (1998). Neogene turbidite sequence on the Madeira Abyssal Plain: basin filling and diagenesis in the deep ocean. *Proc. ODP, Sci. Res.* **157**, 619–634.
- Weinrebe, W. O., Connor, J., and Kopp, C. (1997). High resolution morphology of Daikakuji Seamount-Hawaiian Emperor chain bend. *EOS, Trans. Am. Geophys. Union* **78(Suppl. 46)**, 726.
- Wessel, P., and Keating, B. H. (1994). Vertical tectonic history of Cross Seamount. *J. Geophys. Res.* **99(B2)**, 2747–2756.
- Whipple, K., and Dunne, T. (1992). The influence of debris-flow rheology on fan morphology, Owens Valley, California. *Geol. Soc. Am. Bull.* **104**, 887–900.
- Wiegel, R. L. (1955). Laboratory studies of gravity waves generated by the movement of a submarine body. *EOS, Trans. Am. Geophys. Union* **36(5)**, 759–774.
- Williams, G. P., and Guy, H. P. (1973). Erosional and depositional aspects of Hurricane Camille in Virginia, 1969. *US Geol. Surv. Prof. Paper* **804**, 1–80.
- Winterer, E. L., and Sager, W. W. (1995). Synthesis of drilling results from the mid-Pacific mountains: regional context and implications. *Proc. ODP, Sci. Res.* **143**, 497–535.
- Wolfe, C. J., McNutt, M. K., and Detrick, R. S. (1993). The Marquesas archipelagic apron: seismic stratigraphy and implications for volcano growth, mass wasting, and crustal underplating. *J. Geophys. Res.* **99**, 13591–13608.
- Wright, I. C. (1996). Volcaniclastic processes on modern submarine arc stratovolcanoes, sidescan and photographic evidence from the Rumble IV and V volcanoes, southern Kermadec Arc (SW Pacific). *Mar. Geol.* **136**, 21–39.
- Yalciner, A. C., Alpar, B., Altinok, Y., Ozbay, I., and Imamura, F. (2002). Tsunamis in the Sea of Marmara—historical documents for the past, model the future. *Mar. Geol.* **190**, 445–463.
- Yalciner, A. C., Pelinovsky, E. N., Okal, E., and Synolakis, C., eds. (2003). Submarine Landslides and Tsunamis. NATO Science Series IV, Earth and Environmental Sciences, Vol. 21. Kluwer Academic, Dordrecht, The Netherlands, pp. 1–328.
- Yarnold, J. C. (1993). Rock-avalanche characteristics in dry climates and the effect of flow into lakes, insights from mid-Tertiary sedimentary breccias near Artillery Peak. *Geol. Soc. Am. Bull.* **105**, 345–360.
- Yokose, H. (2002). Landslide of northeastern Oahu, Hawaii: SHINKAI 6500 submersible investigation. In “Evolution of Hawaiian Volcanoes: Recent Progress in Deep Underwater Research” (E. Takahashi, P. Lipman, M. O. Garcia, J. Naka, and S. Aramaki, eds.). American Geophysical Union Monograph 128, Washington, DC, pp. 245–262, CD.
- Young, A. G., and Brand, J. R. (2004). Age-dating of slope failures on the Sigsbee Escarpment, using the past to paint a clear picture of the slope stability hazard at BP’s Atlantic and Mad Dog developments. *Sea Technol.* **45(9)**, 30–35 (e-mail: oceanbiz@sea-technology.com).
- Zielinski, G. A., Mayewski, P. A., Meeker, L. D., Gronvold, K., Germani, M. S., Whitlow, S., Twickler, M. S., and Taylor, K. (1997). Volcanic aerosol records and tephrochronology of the summit, Greenland ice cores. *J. Geophys. Res.* **102**, 26625–26640.

**This page is intentionally left blank**

## INDEX

### A

Age dating, 177, 230, 242  
Asperity, 11–13, 23, 25, 42, 66, 102, 104  
Asymmetrical structures, 82

### B

Barriers to fluid flow, 66, 102, 103  
Bear Creek, CA, 88  
Big Hole fault, 91  
Blueberry fault, 90  
Borehole temperatures as proxy, 26,  
78–80, 82, 87, 113, 115, 116, 127,  
129–131, 133, 134, 137, 140, 142, 144,  
147–149, 165, 168, 169  
Borehole temperatures, 26, 78–80, 82, 87,  
113, 115, 116, 127, 129–131, 133, 134,  
137, 140, 142, 144, 147–149, 165, 168,  
169  
Boundary fractures, 89  
Breccia, 66, 72, 74, 75, 76, 78, 81, 82, 85,  
91, 92, 102, 181, 183, 185, 187, 190,  
202, 209  
Brittle, 67, 69, 70, 82, 95

### C

Calcite veins, 74  
Canary Islands, 176, 177, 179, 182, 183,  
192, 194, 196, 197, 199, 202, 208, 211,  
223, 228, 233, 240  
Carboneras Fault, 82, 83  
Cataclasis, 78, 81, 82  
Characteristic displacement, 96, 97, 99,  
102, 103  
Chelungpu fault, 85, 88  
Chi-Chi earthquake, 86, 88  
Climate research, 113

Coefficient of dynamic friction, 97  
Conduits to fluid flow, 81  
Constrained comminution, 74, 91  
Continental heat, 8, 11, 12, 27, 114, 116,  
122, 128, 148, 149, 152, 154, 155, 169,  
175, 177, 191, 207, 211, 212, 222–224,  
226, 228, 230  
Coulomb criterion, 100  
Crack damage, 77  
Crustal deformation, 2, 4, 6, 7, 25, 40, 42,  
45, 46, 49, 51, 57

### D

Debris flows, 176, 177, 194, 196, 199,  
200–203, 205, 206, 207, 213, 219, 220,  
228, 233  
Deformation bands, 90, 91  
Deformation mechanisms, 67, 69  
Dike Injection and volcanic spreading,  
181, 184, 210  
Dip-slip fault, 83  
Displacement weakening rheology, 66  
Domains, 88  
Drilled and cored faults, 66  
Ductile, 47, 69, 70, 95  
Dynamic friction, 97  
Dynamical loading, 92

### E

Earthquake arrest, 2–7, 11–13, 22, 25, 26,  
46, 48, 57, 73, 92, 95, 97, 98, 102, 103,  
184, 213, 216, 219, 240  
Earthquake nucleation, 103  
Earthquakes, 2–7, 11–13, 22, 25, 26, 46,  
48, 57, 73, 92, 95, 97, 98, 102, 103, 184,  
213, 216, 219, 240  
Elastico-frictional regime, 67

Entrada and Navajo Sandstones, 90

Exhumed faults, 102

## F

Failed branching, 93

Fault core, 72–75, 77, 78, 81, 82, 85, 89, 96, 102, 103

Fault growth, 103

Fault lubrication, 88

Fault mechanics, 103

Fault structure, 71, 82

Fault zone formation, 88, 89, 94

Fault zones, 66, 67, 83, 85, 89, 94, 95, 103, 104

Fractal fragmentation, 91, 103

Fractal size distributions, 74, 89, 91, 92, 103

Fracture density, 75, 77, 87, 91

Fracture energy, 66, 98, 99, 100, 102, 103

Fracture mechanics model, 99

Fracture probability, 91

Fragmentation, 74, 75, 91–93, 103, 204

Friction instability, 66, 96, 97

Friction, 6, 47, 56, 57, 66, 92, 94–97, 102, 103, 179, 183, 213

Frictional resistance, 6, 66

Frictional strength, 96

## G

Gain and energy fluxes ???

Gas hydrate, 176, 226–228

Geodetic observations, 2, 8, 14, 23, 26, 27, 40, 46, 49, 56, 57

Global warming, 114, 115, 229

Gouge and breccia zone, 74–76, 81, 85

Granular, 72, 74, 96, 103, 188, 205, 210

Granulated gouge, 65

Great Alaska Earthquake of 1964, 7

Grinding limit, 92

Ground temperatures, 118, 119, 122, 134, 154, 165

## H

Hawaii, 176–179, 182–185, 187–189, 191–195, 197–199, 208, 210, 211, 213, 218–221, 225, 229–231, 233, 234, 236–238, 240, 241, 243

Heat flow, 56, 95, 114, 116, 121, 125–128, 130–132, 141, 143, 144, 160

## I

Impact events, 1, 177, 190, 213, 214, 220, 225, 241

Initial stress, 3, 13, 28, 35, 57, 78, 97, 119, 121, 160, 164, 201, 204, 208, 221, 234

## J

Joints, 88

## L

Landslide-generated tsunamis, 213

Lateral heterogeneities, 101

Loading system, 96

Locked-in slip, 98

## M

Magnitude zero earthquakes, 65

Marine, 2, 176, 179, 187, 191, 201, 205, 212, 223, 225, 227, 228, 230, 240

Median Tectonic Line, 78, 81

Mega-tsunami, 213–215, 217, 218, 220, 243

Mesosopic damage elements, 77

Minimum size earthquake, 96

Models, 2, 7, 8, 13, 22, 37, 38, 45–47, 51–53, 57, 103, 114, 118, 119, 132, 144, 145, 150, 176, 177, 190, 191, 198, 201, 205, 207, 208, 213, 216, 221, 235, 240–242

Mylonization, 82

**N**

Nojima Fault, 78–81, 95  
 Normal faults, 83–85, 91, 101, 217, 218  
 Normal stress reduction, 92

**O**

Off-fault damage, 67, 92, 100, 101, 103  
 Off-fault damage, 65, 67, 92, 101, 103  
 Out-of-plane branching, 93

**P**

Particle-size distributions, 74  
 Passing-Wrinkle Pulse  
 Peak strength, 23, 25, 35, 36, 40, 74, 77, 97, 198, 237  
 Permeability, 81, 82, 102, 125, 181, 184, 189  
 Plastiductile regime  
 Poissonian distribution, 91  
 Pore fluids, 65, 102, 128, 178–182, 184, 199, 201, 204, 207, 222, 225, 227, 234, 236,  
 Pore pressures, 179, 181, 182, 184, 201, 236  
 Post-yield, 99  
 Postseismic rebound, 7, 47  
 Prince William Sound Earthquake, 16  
 Prominent slip surface, 96, 100, 102, 103  
 Propagating dislocation, 97  
 Propagating slip-pulse, 92  
 Pseudotachylyte, 94, 95, 183  
 Punchbowl fault, 67, 69, 70–73, 76–78, 83  
 Punchbowl formation, 69

**R**

Rainfall, 182, 183, 222, 228, 235–239  
 Reactivation of preexisting joints, 88  
 Regional climate change, 157  
 Regional climate variability, 157  
 Regional stress angle, 157  
 Relict structure, 74, 92

Residual strength, 8, 17, 97, 229  
 Reverse faults, 22, 83  
 Rheological stiffness, 96  
 Risk, 131, 178, 213, 216, 233, 240–242  
 Rosin-Ramler distribution, 91  
 Roughness of fault surfaces, 93  
 Runout, 177, 203–205, 207, 213, 219  
 Rupture Propagation, 98, 104  
 Rupture velocity, 100  
 Ryoike mylonite, 82

**S**

Sambagawa schist, 82  
 Same-sized neighbors, 91  
 San Gabriel fault, 67, 69, 70, 74–76, 92, 95, 104  
 San Rafael Desert, Utah, 90  
 Sea level change, 179  
 Seafloor, 177, 204, 233, 242  
 Secondary faulting, 100  
 Seiche, ???  
 Seismogenic depth, 66, 67, 104  
 Self-similarity, 93  
 Shear localization, 75, 89, 91, 92, 103  
 Shear resistance, 96  
 Shear rupture, 93  
 Sierpinski gasket, 91  
 Simulated fault gouge, 66  
 Size distribution of fault gouge, 69, 91, 176, 243  
 Slip pulse, 92, 98, 100  
 Slip surface, 22, 80, 85, 90, 91, 96, 100, 102, 103, 178, 184, 229  
 Slip-weakening curve, 98  
 Slip-weakening distance  
 Slipping patch, 96, 97  
 Small faults, 88, 89  
 Smallest earthquake, 103  
 Solid earth geophysics, 46  
 Southcentral Alaska seismicity, 1, 2, 4, 5, 7–13, 17, 19, 26, 31, 32, 34, 40, 45, 49, 54, 56, 57

Splay fractures, 89, 91  
 Static friction, 97  
 Stick-slip friction, 66, 96, 97  
 Strain accumulation, 7, 31, 41, 46–48, 51, 53  
 Strain hardening mechanism, 90  
 Strain localization, 74, 81  
 Strike-slip fault, 8, 67, 69, 70, 72, 81, 102, 104  
 Strike-slip friction instability, 3, 8, 9, 23, 24, 49, 52, 65–67, 69, 72, 102, 104  
 Subduction zone seismotectonics 1, 2, 4, 7, 9, 11–13, 42, 45, 46, 57  
 Submarine landslides, 177, 198, 208, 210, 211, 213, 222, 228  
 Subsidiary faulting, 4, 24, 46, 48, 77, 85  
 Surveys, 14, 20, 27, 28, 31, 37, 38, 40, 192, 193, 204, 208, 210, 211, 228, 239

### T

Textural Classification, 68  
 Thermal pressurization, 102, 103  
 Transport, 11, 85, 125, 131, 177, 195, 198, 200, 204, 207, 210, 219, 220, 240  
 Triangular slip profiles, 101

Tsunami deposits, 220, 221  
 Tsunami research, 220

### U

Ultracataclasite, 72–76, 78, 82, 83, 85, 87, 91, 94  
 Ultramylonite, ???  
 Underwater landslides, 213  
 Underwater slumps, 213, 214

### V

Velocity strengthening (stable) friction, 92  
 Velocity weakening (unstable) friction, 66, 74, 92  
 Velocity weakening rheology, 66  
 Volcanic edifice instability, 177

### W

Wall rock, 66, 72, 74, 75, 82, 85, 92

### Z

Zones of deformation bands, 77, 78